Karlsruhe Series in Photonics & Communications, Vol. 2

Ayan Maitra

Nonlinear Resonators for All-Optical Signal Processing

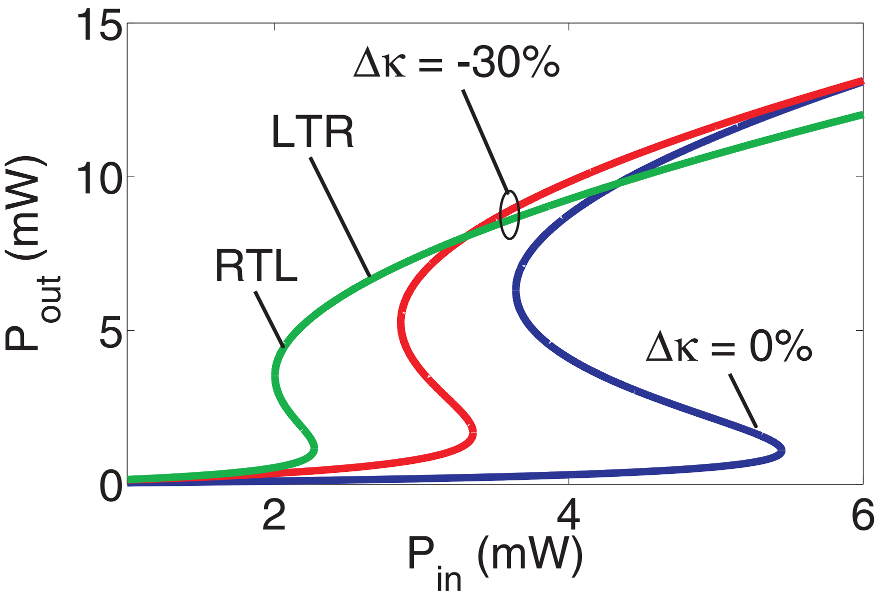

universitätsverlag karlsruhe

Ayan Maitra

Nonlinear Resonators for All-Optical Signal Processing

Karlsruhe Series in Photonics & Communications, Vol. 2
Edited by Prof. J. Leuthold and Prof. W. Freude

Universität Karlsruhe (TH), Institute of High-Frequency and Quantum Electronics (IHQ),
Germany

Nonlinear Resonators for All-Optical Signal Processing

by
Ayan Maitra

universitätsverlag karlsruhe

Dissertation, Universität Karlsruhe (TH)
Fakultät für Elektrotechnik und Informationstechnik, 2007

Impressum

Universitätsverlag Karlsruhe
c/o Universitätsbibliothek
Straße am Forum 2
D-76131 Karlsruhe
www.uvka.de

SOME RIGHTS RESERVED

Dieses Werk ist unter folgender Creative Commons-Lizenz
lizenziert: http://creativecommons.org/licenses/by-nc-nd/2.0/de/

Universitätsverlag Karlsruhe 2009
Print on Demand

ISSN: 1865-1100
ISBN: 978-3-86644-150-7

Nonlinear Resonators for All-Optical Signal Processing

Zur Erlangung des akademischen Grades eines

DOKTOR-INGENIEURS

von der Fakultät für
Elektrotechnik und Informationstechnik
der Universität Karlsruhe (TH)
genehmigte

DISSERTATION

von

Ayan Maitra, M. Sc., M. Tech.
geb. in Kolkata, Indien

Tag der mündlichen Prüfung	12.06.2007
Hauptreferent	Prof. Dr.-Ing. Dr. h. c. W. Freude
1. Korreferent	Prof. Dr. sc. nat. J. Leuthold
2. Korreferent	Prof. Dr. rer. nat. U. Lemmer

Dedicated to the memory of my father…

Zusammenfassung — Abstract

Nichtlineare resonante Komponenten zur voll-optischen Signalverarbeitung

Diese Dissertationsschrift untersucht resonante nichtlineare Strukturen, die sich zur voll-optischen Signalverarbeitung in optischen Nachrichtensystemen eignen. Eine herausragende Eigenschaft dieser Strukturen ist ihre bistabiles Transmissionsverhalten, so daß sie als optische Flip-Flops genutzt werden können. Bisher waren bistabile Komponenten in ihrer Verwendung eingeschränkt durch die kleinen nichtlinearen Koeffizienten der meistgenutzten optischen Materialien (vor allem Glasfasern) Die Schaltschwelle konnte nur mit sehr hohen optischen Leistungen überschritten werden, was eine gerätetechnisch einfache und wirtschaftlich günstige Umsetzung bisher verhinderte.

In der vorliegenden Arbeit werden neue, komplexer strukturierte Entwürfe von optischen Komponenten vorgestellt, die bei niedrigeren optischen Leistungen schalten. Dies gelingt durch den Einsatz von modifizierten Gittern räumlich veränderlicher Bandlücke, durch Gitter mit räumlichem Chirp der Gitterperiode und durch die Einführung einer Gitter-Asymmetrie. Die vorgelegten Daten basieren auf den Materialien InP and Silizium (speziell Silizium auf einem niedrigerbrechenden Substratglas, Si auf SiO_2, SOI).

Weiter werden aktive und passive periodische Wellenleiterstrukturen untersucht und eine generalisierte Theorie zu ihrer Beschreibung entwickelt, die nicht-reziproke Transmission und Reflexion einschließt. Insbesondere ergibt sich, daß allgemeine nichtlineare Resonatoren ohne Inversionssymmetrie sich nicht-reziprok nach Art einer „optischen Diode“ verhalten und damit als integrierbare optische Richtungsleitungen („Isolatoren“) einsetzbar sind.

Diese verallgemeinerte Beschreibung läßt sich auf eine Vielfalt von Nichtlinearitäten anwenden, z. B. auf Nichtlinearitäten in Kerr-Medien, Halbleiterverstärkern (semiconductor optical amplifiers, SOA), Materialien mit Zwei-Photonen-Absorption (two-photon absorption, TPA), Metamaterialien mit negativen Brechzahlen, auf sättigbare Absorber sowie auf Stoffe mit Kombinationen der genannten nichtlinearen Effekte. Weiter sind Resonatoren beschreibbar, die durch Defekte in photonischen Kristallen erzeugt werden. Erstmalig in dieser Arbeit wird eine SOA-basierte periodische Struktur mit verteilter Rückkoplung (distributed feedback, DFB) auf ihr Schaltverhalten hin untersucht.

SOI-Wellenleiter können mit CMOS-Prozessen hergestellt werden und sind daher besonders attraktiv. Die hohe Feldkonzentration im stark führenden Wellenleiter erzeugt hohe Feldstärken bei mäßigen Eingangsleistungen und bewirkt dadurch besonders große nichtlineare Wechselwirkungen, was zur voll-optischen Signalverarbeitung vorteilhaft genutzt werden kann. Allerdings beschränkt die in Silizium früh einsetzende Zwei-Photonen-Absorption die zulässigen optischen Eingangsleistungen. Hier wird ein Entwurf vorgestellt, der diesen Nachteil in einen Vorteil verkehrt: Ein durch Zwei-Photonen-Absorption nichtlinear-verlustbehafteter Resonator ohne Inversionssymmetrie kann in seiner Reflektivität geschaltet werden, wobei ein großes Extinktionsverhältnis erreicht wird.

Schließlich wird eine neuartige Anordung für ein voll-optisches Flip-Flop beschrieben, wobei Haltestrahl und SET-Signal in gleicher Richtung propagieren, während Haltestrahl und RESET-Signal gegenläufig sind.. Bei dieser Anordnung ist ein ko-propagierender „negativer“ RESET-Lichtimpuls nicht erforderlich.

Abstract

Nonlinear resonant structures are studied to explore their optical signal-processing capability and seek to advance their application to optical communication networks.

Bistability is observed in nonlinear resonant structures which can be utilized to realize an all-optical flip-flop. However, owing to the very small value of the nonlinear coefficient in most optical materials (including silica fibers), the power required to observe bistability (the switching threshold) is very high. Unless the power requirement can be somehow reduced, these devices will remain unsuitable for commercial applications. New designs based on stopband tapered, chirped gratings with asymmetrically placed phase shift regions were proposed. This reduces the switching threshold for bistable switching operations. High index-contrast waveguide structures with sidewall corrugations based on InP and silicon on insulator (SOI) are proposed for device realization.

We have studied active and passive waveguide-based periodic structures and developed the general theory describing the nonreciprocal transmission and reflection behaviour of a resonator having structural asymmetries. It predicts that any resonator structure lacking inversion symmetry will exhibit “optical diode” like non-reciprocal transmission property. This generalised description is applicable to a wide variety of nonlinearities, e.g. Kerr-type, semiconductor optical amplifier (SOA), two-photon absorption (TPA). This formulation can be extended to negative-index material, saturable absorbers or combined nonlinear effects.

This simplified formulation can be used in predicting non-reciprocity and is also applicable to photonic crystal based resonators. The non reciprocal behaviour is explored for potential application as non-magnetic isolator. We predict the nonreciprocal property of SOA based periodic structure for the first time.

Silicon has attracted a great deal of attention for optoelectronic applications due to its potential for forming inexpensive, monolithic integrated optical components. The strong optical confinement offered by SOI waveguides enhances nonlinear optical interactions, such as Raman and Kerr effect, in a chip-scale device. This opens numerous possibilities in using silicon as a material for all-optical signal processing. However, this functionality is impaired by TPA, which can severely degrade the performance of a device. Here we propose a scheme combining the advantages of a high extinction ratio inherent in a Fabry-perot resonator with the fast TPA nonlinearity readily available in silicon. By optically tuning the reflectivity of a silicon-based asymmetric Fabry-Perot resonator through TPA inside the cavity, we switch between an impedance-matched condition with low reflectivity, and a high-reflectivity state. This leads to a high extinction ratio larger than 20 dB for the reflected signal.

Further, we propose a new scheme for waveguide Bragg grating based all-optical flip-flop operation where the holding beam and the SET signals are co-propagating inside the device, while the RESET signals are counter-propagating inside the device. In this scheme the so called negative RESET pulse is not needed.

Table of contents

Zusammenfassung — Abstract i
Table of contents v
List of figures vii
List of tables xv
List of symbols and acronyms xvii
1 Introduction and outline 1
  1.1 Motivation 1
  1.2 Achievements of the present work 3
  1.3 Outline 3
2 Theoretical foundation 5
  2.1 Maxwell's equations 5
  2.2 Linear coupled mode theory 7
    2.2.1 CW solution in linear case 10
  2.3 Nonlinear coupled mode equations (NLCME) 12
    2.3.1 NLCME for passive Kerr-type of devices 12
      2.3.1.1 Scaling relations in nonlinear coupled mode equation 15
    2.3.2 NLCME for carrier induced nonlinearity 15
      2.3.2.1 Carrier density rate equation 17
      2.3.2.2 Small-signal steady-state solution for active waveguide grating 18
  2.4 Generalized coupled mode theory and the gain rate equation 19
  2.5 Summary 22
3 Analysis of uniform periodic structures 23
  3.1 Optical bistability: steady state analysis 23
    3.1.1 Introduction 23
    3.1.2 Physical process of bistability in Kerr type nonlinear medium 24
      3.1.2.1 Elliptic function formalism for Kerr-type nonlinearity 26
    3.1.3 Active device 28
      3.1.3.1 Transfer matrix method (TMM) 28
  3.2 Optical bistability: Time dependent analysis 30
    3.2.1 CW signal propagation in a Kerr-type medium 30
    3.2.2 Pulse propagation in a Kerr-type grating 34
    3.2.3 Bistability and comparison with quasi-steady state calculation 36
    3.2.4 Flip-flop operation for a passive device 36
    3.2.5 Flip-flop operation for an active device 40
  3.3 Summary 43
4 Novel isolator design 45
  4.1 General theory leading to nonreciprocal behaviour 45
    4.1.1 Kerr-type nonlinear medium in the cavity 50
    4.1.2 SOA type nonlinear medium in the cavity 59
    4.1.3 Comparison of different types of nonlinearity 61
  4.2 Asymmetric periodic structures 62

4.3 Stopband tapered waveguide Bragg grating 62
  4.3.1 Numerical simulations of an active structure 63
  4.3.2 Numerical simulations of passive structure 64
4.4 Effect of chirp and other asymmetries in an active device 68
4.5 Asymmetrically phase shifted structure 70
  4.5.1 Exact solution of NLCME........ 70
  4.5.2 Non-reciprocal behaviour........ 72
4.6 Summary 74
5 Lowering of switching threshold........ 75
5.1 Passive stopband tapered waveguide Bragg grating 75
5.2 Active Stopband tapered waveguide Bragg grating 79
5.3 Asymmetrically phase shifted structure 80
5.4 Asymmetric Fabry-Perot resonator 80
5.5 Summary 81
6 Nonlinear FDTD simulation........ 83
6.1 Introduction 83
  6.1.1 Asymmetric waveguide Bragg grating........ 84
  6.1.2 FDTD analysis of WBG 85
  6.1.3 Stable state of nonlinear WBG........ 91
  6.1.4 Pulsative state of nonlinear WBG 92
  6.1.5 Chaotic state of nonlinear WBG 93
6.2 Summary 95
7 Signal processing in periodic structure 97
7.1 Four-wave-mixing in ST-WBG 97
7.2 High extinction ratio switching using two-photon absorption in a silicon waveguide resonator 99
7.3 Summary 102
Appendix A: List of parameters used for SOA-DFB simulation 109
Appendix B: Numerical method 111
B.1 Transfer matrix method........ 111
B.2 Generalized transfer matrix method........ 113
B.3 Finite difference method 117
B.4 Implicit Runge-Kutta method........ 119
B.5 Summary 121
Acknowledgements 123
Resume 125

List of figures

Figure 2-1 : Schematic diagram showing the variation of the refractive index as a function of position *z* inside the grating of length *L* 8

Figure 2-2 : Dispersion relation of a linear periodic structure, Eq. (2.33). The solid line represents the band diagram of a period structure of infinite length. The dotted line represents the dispersion relation for the free photon. The region $|\delta| \leq \kappa$ defines the stopband. 11

Figure 2-3 : Reflection and transmission spectra for two values of κL. The solid (red) curve is for $\kappa L = 5$, while the dashed (blue) curve is for $\kappa L = 2$. (a) Transmissivity. (b) Reflectivity. (c) Transmission phase. (d) Reflection phase. 11

Figure 2-4 : Power dependent transmission curve for a Kerr type nonlinear periodic structure. The solid (blue) line shows the transmission curve in the linear case, while the dotted (red) line shows the non-linear transmission curve. 15

Figure 2-5 : Small-signal transmission curve for an active DFB structure for different values of the length normalized gain g_0L. 19

Figure 2-6 : Nonlinear effect on dispersion diagram of Kerr type nonlinear periodic structures for the linear case ($\Gamma = 0$) (see solid blue curves), and two nonlinear cases ($\Gamma \neq 0$) (see the dotted blue lines and the solid red lines). 22

Figure 3-1 : Typical hysteresis curve with the different region of interest 23

Figure 3-2 : Schematic diagram showing the stopband (shaded grey region) as a function of position *z* inside the grating of length *L*. The solid lines (blue) depict the band edges for the grating. The dashed red line depicts the detuning parameter corresponding to the CW signal 24

Figure 3-3 : (a) Power dependent bend in the transmission curve as calculated from NLCME (same as in Figure 2-4) (b) Schematic variation of the transmissivity of the grating with different input intensities. The arrow indicates the direction of increasing input intensity from black → red → blue. The dotted green line depicts the detuning coefficient corresponding to the input signal. The slope of the curve also changes significantly with increasing input intensity. For the results from a detailed calculation see Figure 2-4 25

Figure 3-4 : S-curves for $\kappa L = 5$, $\delta_0 L = 4.75$, $\Gamma L = 0.1$ cm^2/GW showing the dependence of (a) transmissivity, and (b) reflectivity on input intensity. 28

Figure 3-5 : Flowchart for calculation of the field distribution using TMM for active device. 29

Figure 3-6 : Schematic waveguide Bragg grating. 30

Figure 3-7 : Linear transmission curve showing the operating frequency (normalized detuning coefficient) and the transmission resonance 31

Figure 3-8 : Time dependent (a) transmissivity and (b) reflectivity curve for a normalized detuning coefficient of $\delta_0 L = 4.75$, $\Gamma L = 0.1$ cm^2/GW. In both the curves the dashed black line represents the results for the linear case; the red curves represents the results of the nonlinear case with normalized input intensity of $A_0^2 \Gamma L = 0.1$; the blue curve represents the results of the nonlinear case with normalized input intensity of

$A_0^2\Gamma L = 0.256$. The time is expressed in units of the transit time T_r of the signal through the device........ 31
Figure 3-9 : (a) Steady-state power distribution inside the grating; the red and the blue curves are for a normalized detuning coefficient of $\delta_0 L = 4.75$, $\Gamma L = 0.1$ cm^2/GW with normalized input intensity of $A_0^2\Gamma L = 0.1$, and $A_0^2\Gamma L = 0.256$ respectively. (b) Temporal and spatial variation of intensity inside grating for a normalized input intensity $A_0^2\Gamma L = 0.256$. (c) Temporal and spatial variation of flux density inside the grating for a normalized input intensity $A_0^2\Gamma L = 0.256$. The time is expressed in units of the transit time T_r of the signal through the device........ 32
Figure 3-10 : Time dependent transmissivity showing pulsating behaviour for a normalized input power of (a) $A_0^2\Gamma L = 0.484$; (b) $A_0^2\Gamma L = 0.676$. In both cases the red and blue curves are for a normalized detuning coefficient of $\delta_0 L = 4.75$ and $\delta_0 L = 4.85$ respectively. (c) Temporal and spatial variation of intensity inside grating for a normalized detuning coefficient of $\delta_0 L = 4.75$. The time is expressed in units of the transit time T_r of the signal through the device........ 33
Figure 3-11 : Propagation of Gaussian input pulse in a nonlinear waveguide Bragg grating with $\kappa L = 5$, $\Gamma L = 0.1$ cm^2/GW for a normalized detuning coefficient $\delta_0 L = 4.75$ corresponding to the carrier frequency of the pulse. The black lines show the input Gaussian signal. The blue lines in the left and the middle column show the transmitted and reflected intensities, respectively. The column on the right shows the corresponding temporal and spatial intensity variation inside the grating. Different rows represent different pulse FWHM (I) FWHM = T_r; (II) FWHM = $20\times T_r$; (III) FWHM = $33\times T_r$.; (IV) FWHM = $103\times T_r$. In (I) the pulse is spectrally much wider with respect to the grating's stopband; hence the grating acts as a nonlinear filter. As the spectra of the input signal become narrower from top to bottom the signal more and more resembles a CW like behaviour; moreover the average power of the pulse increases from top to bottom. Increase in the average power induces a large nonlinear shift of the bandgap of the grating and hence the input field penetrates deeper into the structure. The horizontal green dashed line in (IV) represents the up-switching threshold 0.256/(ΓL) of the device. The green (red) dot represents the up (down)-switching threshold. The time is expressed in units of the signal's transit time T_r of the signal through the device........ 35
Figure 3-12 : Input-output bistable curve with $\kappa L = 5$, $\delta_0 L = 4.75$, $\Gamma L = 0.1$ cm^2/GW. The green dashed line shows results from the calculation in steady-state while the black solid line shows the results from the time dependent calculation, which shows a transient at the up-switching threshold........ 36
Figure 3-13 : Schematic flip-flop operation by modulating input signal........ 37
Figure 3-14 : Schematic flip-flop operation with co-propagating SET and counter propagating RESET signal........ 37
Figure 3-15 : (a) schematic intensity distribution inside the grating in the high transmitting state. The green arrow indicates the location of local minimum. (b) The temporal and spatial dynamics of the intensity distribution inside the grating during the RESET

operation the magenta arrow indicates the time at which the RESET signal enters the device 38

Figure 3-16 : AOFF operation with co-propagating SET and counter propagating RESET signals. SET and RESET signals are Gaussian pulses of peak intensity $A\max^2 \Gamma L = 0.36$, FWHM of $15\times Tr$ and pulse repetition rate of $75\times Tr$. All signals (SET, RESET, and CW) are at the same frequency (the corresponding detuning coefficient is $\delta_0 L = 4.75$). (a) SET signal. (b) RESET signal. (c) Transmitted signal. (d) Reflected signal. The transmission (or reflection) state of the device changes from low to high (or from high to low) in presence of SET signal. The reverse happens in presence of a RESET signal. (e) Temporal and spatial variation of intensity distribution inside grating. In presence of the SET signal the device moves from the low to the high transmission state, having more energy stored in the grating. In presence of the RESET signal the device moves from the high to the low transmission state, having less energy stored in the grating. The time is expressed in units of the transit time T_r of the signal through the device. 39

Figure 3-17 : AOFF operation in SOA-DFB using signals at same wavelength for the f device parameters $L = 300$ µm, $\kappa L = 3$, $g_0 L = 1.2$. All the signals (CW holding beam and the SET/RESET signal) have an identical normalized detuning coefficient of $\delta_0 L = 6.76$. The CW holding beam power is 20 µW. Super Gaussian of order two SET/RESET signal pulses with FWHM of 2 ns are used. (a) The deviation from the mean holding beam power is 10 µW. (b) Temporal dynamics of the output power. 41

Figure 3-18 : AOFF operation in SOA-DFB using signals at different wavelength for $L = 300$ µm, $\kappa L = 3$, $g_0 L = 1.2$. The CW holding beam power is 0.1 mW. Super Gaussian of order two SET (RESET) signal pulses with FWHM of 2 ns are used with peak power of 0.1 mw (1 mW). The detuning coefficient $\delta_0 L = 1$ ($\delta_0 L = 7.9$) is used for the SET (RESET) signals, while for the CW signal the detuning coefficient is $\delta_0 L = 6.56$ 41

Figure 3-19 : Temporal dynamics of the low-to-high switching operation for the for $L = 300$ µm, $\kappa L = 3$, $g_0 L = 1.2$. with SET peak power of 1.2 mW. The dynamic shows that the output is latched to an intermediate state during the duration of the pulse and switches to the high transmitting state. 42

Figure 3-20 : Steady state bistable curves for $L = 300$ µm, $\kappa L = 3$, $g_0 L = 1.2$. with SET peak power of 1.2 mW. with peak SET power of 1.2 mW. The green (black) curve is the bistable curve in absence (presence) of the SET pulse. 43

Figure 4-1 : Schematic diagram showing a nonlinear periodic structure. The green and the red arrow indicates the left-to-right and right-to-left direction of propagation. 46

Figure 4-2 : Variation of power enhancement (PE) in the cavity as a function of phase detuning ϕ. Linear lossless case, $\alpha_{\text{int}} L = 0$, for different values of $R_1 = 0.99$ (red), 0.85 (blue), 0.32 (magenta), with $R_2 = 0.99$. (a) LTR & (b) RTL propagations. 47

Figure 4-3 : Variation of power enhancement (PE) in the cavity as a function of phase detuning ϕ. Linear case with linear loss coefficient, $\alpha_{\text{int}} L = -0.3$, for different values of $R_1 = 0.99$ (red), 0.85 (blue), 0.32 (magenta), with $R_2 = 0.99$. (a) LTR & (b) RTL propagations. 48

Figure 4-4 : Variation of reflectivity R of AFPR as a function of phase detuning ϕ. Linear case with linear loss coefficient, $\alpha_{\text{int}} L = -0.3$, for different values of $R_1 = 0.99$ (red), 0.85 (blue), 0.32 (magenta), with $R_2 = 0.99$. (a) LTR & (b) RTL propagations. 48

Figure 4-5 : Schematic waveguide structure with two sidewall corrugated DBR mirrors forming an asymmetric Fabry-Perot resonator. 50

Figure 4-6 : Graphical solution of equation (4.3) for a AFPR with $R_1 = 0.85$, $R_2 = 0.95$, $L = 100$ μm, $\gamma = 3.5$ cm^{-1}W^{-1} in the lossless case $\alpha_{\text{int}} L = 0$ for (a) $\phi = 0$ and (b) $\phi = -0.3\pi$ The black dotted line is for the power corresponding to down-switching threshold, dashed line for the up-switching threshold, while the solid line corresponding to the power in the bistable region. $P_{\text{ref}} = (\gamma L)^{-1}$ 51

Figure 4-7 : The variation of the output power with respect to the input power of an AFPR with $L = 100$ μm, $\gamma = 3.5$ cm^{-1}W^{-1}, and $R_1 = R_2 = 0.99$ (red), 0.95 (blue), 0.90 (magenta) and 0.75 (green), $\alpha_{\text{int}} = 1$ dB/cm, $\phi = -0.1\pi$ for (a) LTR and (b) RTL propagating signals. $P_{\text{ref}} = (\gamma L)^{-1}$. 52

Figure 4-8 : Variation of the input power and detuning (corresponding to the offset from frequency resonance), specifying a bistable (shaded) region which is bounded by the up- and down-switching thresholds for different reflectivity combinations, and for different linear loss coefficients. The left column shows the lossless case, $\alpha_{\text{int}} = 0$ for (A) $R1 = R2 = 0.99$; (a) $R1 = R2 = 0.95$. The right column represents the lossy case with linear loss coefficient $\alpha_{\text{int}} = 1$ dB/cm (B) $R1 = R2 = 0.99$; (b) $R1 = R2 = 0.95$. In all the curves the following device parameters are valid $L = 100$ μm, $\gamma = 3.5$ cm^{-1}W^{-1}, the reference power is $P_{\text{ref}} = (\gamma L)^{-1}$. 53

Figure 4-9 : Variation of the input power and detuning ϕ (corresponding to the offset from frequency resonance), specifying a bistable (shaded) region which is bounded by the up- and down-switching thresholds. Lossy case, with loss coefficient $\alpha_{\text{int}} = 1$ dB/cm, $L = 100$ μm, $\gamma = 3.5$ cm^{-1}W^{-1}. The reference power is $P_{\text{ref}} = (\gamma L)^{-1}$. for (A) $R_1 = 0.99$, $R_2 = 0.95$; (B) $R_1 = 0.99$, $R_2 = 0.90$; (a) $R_1 = 0.95$, $R_2 = 0.90$; (b) $R_1 = 0.95$, $R_2 = 0.85$. The LTR and RTL propagating cases are depicted by green and red shaded areas, respectively. The marked regions show the isolation region. 54

Figure 4-10 : Graphical solution of NL-AFPR for a specific input power of $P_{\text{in}} = P_{\text{ref}}$ (black dotted line) in absence of linear loss, $\alpha_{\text{int}} = 0$ with $R_1 = 0.85$, $R_2 = 0.95$, $L = 100$ μm, $\gamma = 3.5$ cm^{-1}W^{-1} for three different phase detuning, $\phi = 0$ (red), -0.15π (blue), -0.3π (magenta). (a) LTR and (b) RTL propagating cases. 55

Figure 4-11 : Bistable curves of a NL-AFPR in absence of linear loss, $\alpha_{\text{int}} = 0$ with $R_1 = 0.85$, $R_2 = 0.95$, $L = 100$ μm, $\gamma = 3.5$ cm^{-1}W^{-1} for three different phase detuning, $\phi = 0$ (red), -0.15π (blue), -0.3π (magenta). (a) LTR and (b) RTL propagating cases. The black dotted line correspond to a certain input power of $P_{\text{in}} = P_{\text{ref}}$. 55

Figure 4-12 : Graphical solution of NL-AFPR for a specific input power of $P_{\text{in}} = P_{\text{ref}}$ (black dotted line) in presence of linear loss, $\alpha_{\text{int}} = 1$ dB/cm with $R_1 = 0.85$, $R_2 = 0.95$, $L = 100$ μm, $\gamma = 3.5$ cm^{-1}W^{-1} for three different phase detuning, $\phi = 0$ (red), -0.15π (blue), -0.3π (magenta). (a) LTR and (b) RTL propagating cases. 56

Figure 4-13 : Bistable curves of a NL-AFPR in presence of linear loss, α_{int} = 1dB/cm with $R_1 = 0.85$, $R_2 = 0.95$, L = 100 µm, γ = 3.5 cm^{-1}W^{-1} for three different phase detuning, ϕ = 0 (red), –0.15π (blue), –0.3π (magenta). (a) LTR and (b) RTL propagating cases. The black dotted line correspond to a certain input power of $P_{\mathrm{in}} = P_{\mathrm{ref}}$ 56

Figure 4-14 : Isolator behaviour for phase detuning ϕ = –0.15π with parameter as on Figure 4-13. if the device is operated at input power lying inside the rectangular box, then for RTL operation the transmissivity T is low, and is high for LTR operation. 56

Figure 4-15 : Influence of TPA on the transmission properties of a NL-AFPR. Variation of the input power and detuning ϕ (corresponding to the offset from frequency resonance), specifying a bistable (shaded) region which is bounded by the up- and down-switching thresholds. with $R1$ = 0.85, $R2$ = 0.95, L = 100 µm. The red and green shaded region represents the bistable region for RTL and LTR propagating signals. TPA is neglected in (A) and (B) while in (a), and (b) TPA is included. The left column is for the lossless (linear) case, α_{int} = 0 dB/cm, while the right column is for linear loss of α_{int} = 1 dB/cm. $P_{\mathrm{ref}} = (\gamma L)^{-1}$ 57

Figure 4-16 : Nonreciprocal behaviour of a SOA-based AFPR. The left column show the variation of the input power and detuning ϕ (corresponding to the offset from frequency resonance), specifying a bistable (shaded) region which is bounded by the up- and down-switching thresholds of an NL-AFPR with SOA in the cavity. The right column show the corresponding variation of maximum isolation ratio with detuning ϕ. 60

Figure 4-17 : Influence of different types of nonlinearity on (a) the nonlinear gain/loss and (b) the nonlinear phase shift for different values of cavity power. 61

Figure 4-18 : Different type of asymmetries in grating structures. (a) Stopband tapered; (b) Chirped; (c) Asymmetrically placed phase shifted structure. 62

Figure 4-19 : (a) Stopband-tapered waveguide Bragg grating (ST-WBG) of length L. Schematic stopband dependence on z with band edges for uniform grating (– – –), and for ST-WBG (upper and lower boundaries of shaded region), and detuning parameter δ_0 of CW input signal (——). (b) Schematic ST-WBG with varying sidewall corrugations. 63

Figure 4-20 : Variation of the switching up and down switching thresholds for (a) $\Delta\kappa$ = 0 %; (b) $\Delta\kappa$ = –10 %; (c) $\Delta\kappa$ = –20 %; (d) $\Delta\kappa$ = –30 %. The red and the green curves are for the LTR and RTL propagating cases respectively. 64

Figure 4-21 : Nonreciprocal behaviour for an active device with $\Delta\kappa$ = –15 % and $\delta_0 L$ = 4.75 64

Figure 4-22 : Nonreciprocal behaviour for an passive device with $\Delta\kappa$ = –15 % and $\delta_0 L$ = 4.75 65

Figure 4-23 : Nonreciprocal behaviour for a passive device with $\Delta\kappa$ = –15 % and $\delta_0 L$ = 4.75 showing nonreciprocal transmission behaviour. (a) and (b) shows the temporal and spatial variation of intensity inside grating for a the LTR and RTL propagating cases. (c) Temporal dynamics of the transmitted power for LTR and RTL propagations............... 66

Figure 4-24 : Impulse responses showing nonreciprocal behaviour for a passive device with $\Delta\kappa$ = –15 % and $\delta_0 L$ = 4.75. 67

Figure 4-25 : Impulse responses showing nonreciprocal behaviour for the same parameters considered in the Figure 4-24. 67

Figure 4-26 : Schematic of locally-averaged refractive index as a function of z, CW frequency $\omega_0 = \omega_T^{RTL}$. Low power (—, Linear Δn_G), nonlinear RTL (—) and LTR operation (—).Horizontal dashed lines for spatial average navg over total grating length labelled with respective transmission resonance frequencies ω_T (– –), ω_T^{LTR} (– –), ω_T^{RTL} (– –).Lower-left inset: Power transmission near upper band edge. Top right inset: Intensity for RTL (←) and LTR (→) operation. 68

Figure 4-27 : Nonreciprocal behaviour for an active device with $\Delta\kappa = +30$ %, $C_\Lambda = -30$ % and $\Delta J = 0$ %, $\delta_0 L = 5.5$, $g_0 L = 1.2$ 69

Figure 4-28 : Variation of the up and down switching threshold for an active device with (a) $\Delta\kappa = -10$ %, $C_\Lambda = +20$ % and $\Delta J = 0$ %. (b) $\Delta\kappa = -10$ %, $C_\Lambda = +30$ % and $\Delta J = 0$ %. (c) $\Delta\kappa = -30$ %, $C_\Lambda = +30$ % and $\Delta J = 0$ %. (d) $\Delta\kappa = -10$ %, $C_\Lambda = +20$ % and $\Delta J = -10$ %, $g0L = 1.2$. 69

Figure 4-29 : Schematic of periodic structure with a $\lambda/4$ phase-shift at location $z = L_1$ 70

Figure 4-30 : (a) Variation of the transmissivity with normalized input power for $\kappa L = 4$ and $\delta_0 L = 0$, and for symmetric (solid line) and asymmetric $\lambda/4$ phase-shifted structures (broken lines). (b) Bistable curves for the same structure with $\delta_0 L = -0.70$. Reference power $P_{\mathrm{ref}} = 1.3$ W. 73

Figure 4-31 : Transmission curve for a $\lambda/4$ phase-shifted structure at location $z = L_1$ for different values of input power showing a direction dependent bending of the transmission curve. (a) Variation of the transmissivity with normalized detuning for $\kappa L = 4$ with $P_{\mathrm{In}}/P_{\mathrm{ref}} = 0.01$, and (b) with $P_{\mathrm{In}}/P_{\mathrm{ref}} = 0.04$. The solid blue line represents the transmissivity of the structure in the linear case. Reference power $P_{\mathrm{ref}} = 1.3$ W. 73

Figure 5-1 : Schematic diagram showing the variation of the stopband as a function of position z inside the grating of length L. The dashed lines give the band edges for a uniform grating. The lines bounding the shaded region show the stopgap variation for a ST-WBG. The solid line gives the detuning parameter of the CW input signal. The marked regions show the so called “opaque” and “transparent” regions of the grating, corresponding to the CW signal. 76

Figure 5-2 : Bistable curves for different tapering coefficients. 76

Figure 5-3 : The threshold switching power for the ST-FBG, which decreases linearly with the negative tapering coefficient for detuning coefficients $\delta_0 L = 4.75$ and $\delta_0 L = 4.6$. 77

Figure 5-4 : Low transmission state: a) Energy density inside the grating for different tapering coefficients, $\Delta\kappa = 0\%$ (—) and $\Delta\kappa = -10\%$ (−♦−). The energy density is normalised to the peak value. (b) *Upper-band edge* of the stopgap for the uniform grating, with $\Delta\kappa = 0\%$. The solid line gives the upper-band edge for $n_2^I = 0$, the dashed line shows the local band edge. c) upper band edge for the ST-WBG, with $\Delta\kappa = -10\%$. The horizontal dotted line shows the detuning $\delta_0 L$. 78

Figure 5-5 : High transmission state: a) Energy density inside the grating for different tapering coefficients, $\Delta\kappa = 0\%$ (—) and $\Delta\kappa = -10\%$ (−♦−). The energy density is normalised to the peak value. (b) *Upper-band edge* of the stopgap for the uniform grating, with

$\Delta\kappa = 0\%$. The solid line gives the upper-band edge for $n_2^I = 0$, the dashed line shows the local band edge. c) upper band edge for the ST-WBG, with $\Delta\kappa = -10\%$. The horizontal dotted line shows the detuning $\delta_0 L$. 78

Figure 5-6 : S-curves of ST-DFB SOA for different tapering coefficients Δκ, where the normalized gain coefficient $g_0L = 1.2$, the normalized internal loss $\alpha_{\text{int}}L = 0$, and the normalized detuning coefficient $\delta_0 L = 6.5$. 79

Figure 5-7 : Variation of the up and down switching threshold with the detuning coefficient for the same parameters consider in Figure 5-6 80

Figure 5-8 : S-curve of asymmetrically phase shifted structure for different value of L_1 for RTL propagation. 80

Figure 5-9 : Graphical solution of NL-AFPR with $L = 100$ µm, $\alpha_{\text{int}} = 0$ dB/cm. The red line represents the case of $R_1 = 0.95$, $R_2 = 0.95$. The blue line represents the case of $R_1 = 0.95$, $R_2 = 0.32$. The green line represents the case of $R_1 = 0.32$, $R_2 = 0.95$. The black dotted line corresponding to $P_{\text{In}} = P_{Avg}$. TPA is neglected. 81

Figure 6-1 : Schematic configuration of the waveguide Bragg grating having an asymmetric stopband; (a) the top view, and (b) the cross section of the waveguide. In the analysis the structure is approximated by a slab waveguide having an effective refractive index of the stacked structure. The ports for signal detection are located at a half hight of the InGaAsP core and at $(x, z) = (0,0)$ and $(0, L_0)$. (c) An example of the upper band-edge frequency variation realized by the third-order polynomial $g(z')$ for $W_g = 0.1$ μm 85

Figure 6-2 : Transmission spectra for the 100Λ-long waveguide Bragg gratings of uniform amplitudes of sidewall modulation. W_g in legend is in μm. 86

Figure 6-3 : Comparison of the calculated transmission spectra for 200-Λ-long asymmetric gratings with the maximum modulation $W_g = 0.1$ μm and $W_g = 0.20$ μm. The upper frequency band edges are 208.20 THz for $W_g = 0.1$ μm, and 214.08 THz for $W_g = 0.20$ μm 87

Figure 6-4 : Switching for the LTR and RTL configuration of a 235Λ-long waveguide with $W_g = 0.1$ μm at 207.9 THz operating frequency ($\Delta f = 0.3$ THz). Maximum incident field value is 5.25 × 107 V/m at 100 ps. Right vertical axis shows the normalized permittivity change by the nonlinearity. 88

Figure 6-5 : Electric field for 200 Λ-long RTL configuration (positive variation) with $W_g = 0.1$ µm at 207.85 THz operating frequency. (a) Off-state at 90 ps, and (b) on-state at 130 ps. 89

Figure 6-6 : Switch-on threshold electric field and power versus the length of the waveguide grating for the RTL (positive) configuration with $Wg = 0.1$ μm and 0.2 μm. The error bars are the uncertainty due to the step increment of the incident field variation............ 90

Figure 6-7 : Switching for the LTR and RTL configuration of a 220Λ-long waveguide with $Wg = 0.20$ µm at 214.03 THz operating frequency ($\Delta f = 0.05$ THz). Maximum incident field is 2.6×10^7 V/m at 75 ps. Minimum switch-on threshold is $E_{\text{th}}^{(\text{on})} = 1.05\times10^7$ V/m (equivalent light power $P_{\text{th}}^{(\text{on})} = 77$ mW) for RTL. 91

Figure 6-8 : An example of the stable switching state for a uniformly modulated WBG of 200 Λ in length, $W_g = 0.15$ μm at operating frequency 209.40 THz ($\Delta f = 0.15$ THz). The

maximum field is 1.75×107 V/m. Switch-on occurs at $E_{th}{}^{(on)} = 1.6\times107$ V/m (equivalent light power $P_{th}{}^{(on)} = 170$mW) ... 93
Figure 6-9 : Stable state electric field for 200 Λ-long uniform grating. Wg = 0.15 μm, 209.40 THz, 1.75×107 V/m. (a) Off-state at 20 ps, and (b) on-state at 60 ps ... 93
Figure 6-10 : An example of the pulsative time signal for a uniformly modulated WBG of 220 Λ in length, $W_g = 0.2$ μm at operating frequency 214.03 THz ($\Delta f = 0.05$ THz). The maximum incident field is 5.25×10^7 V/m. Transition to the pulsative state occurs at incident field $E = 3.2\times10^7$ V/m (equivalent light power $P = 720$ mW). ... 94
Figure 6-11 : (a) Optical Kerr model for $f_{op} = 206.5$ THz ($\Delta f = 0.2$ THz), with Lorentz dispersion with the damping factor $\delta p = 1.0\times10^{14}$ rad/s. Calculation stopped at 5 ps. (b) SCP model for fop = 200.3 THz ($\Delta f = 0.2$ THz), with the damping factor $\delta p = 1.0\times10^{13}$ rad/s. Calculation still continues after 10 ps ... 95
Figure 7-1a,b : Schematic of locally-averaged refractive index as a function of z, CW frequency $\omega_0 = \omega_T{}^{RTL}$. Low power (—, Linear Δn_G), nonlinear RTL (—) and LTR operation (—).Horizontal dashed lines for spatial average navg over total grating length labelled with respective transmission resonance frequencies ω_T (– –), ωTLTR (– –), $\omega_T{}^{RTL}$ (– –).Lower-left inset: Power transmission near upper band edge. Top right inset: Intensity for RTL (←) and LTR (→) operation. ... 98
Figure 7-2 : Scheme of switching operation using reflective AFPR ... 100
Figure 7-3 : Effect of including TPA on reflectivity of AFPR for different parameters. (a) Dependence of the reflectivity ϕ or $R_1 = 32\%$, $R_1 = 99\%$. (b) & (e) Dependence of reflectivity on the input power and for the phase detuning in an AFPR with $R_1 = 32\%$, $R_1 = 99\%$ and $R_1 = 50\%$, $R_1 = 85\%$ respectively; (c) & (f) Dependence of P_{avg} in the cavity for the parameters used in (b) & (e). (d) Dependence of reflectivity R on power for $R_1 = 32\%$, $R_1 = 99\%$. ... 101
Figure 7-4 : Effect of neglecting TPA on reflectivity of AFPR for different parameters. Dependence of reflectivity on input power, and on phase detuning in an AFPR with (a) $R_1 = 32\%$, $R_2 = 99\%$; (b) $R_1 = 50\%$, $R_2 = 85\%$. ... 101
Figure B-1 : Schematic GTMM ... 114
Figure B-2 : Flowchart for calculation of the field distribution using GTMM for passive device. ... 116
Figure B-3 : Flowchart for numerical solution using TMM. ... 117
Figure B-4 : Finite difference method ... 119
Figure B-5 : Implicit Runge-Kutta method. ... 120

List of tables

Table B1 : Values of the coefficients used in integration and extrapolation procedure. 120

List of symbols and acronyms

Constants

c	speed of light in vacuum	2.99792458×10^{8} m/s
$\hbar$	reduced Planck constant	1.05459×10^{-34} Js
h	Planck constant	6.62618×10^{-34} Js
π	pi	3.141592
e	elementary charge	1.60219×10^{-19} C
ε_0	permittivity of free space	8.854188×10^{-12} As/V/m
μ_0	permeability of free space	$4\pi\times10^{-7}$ Vs/Am
z_0	vacuum wave impedence	377 Ω

Symbols

α_{H}-factor	linewidth enhancement factor / Henry factor, Eq. (2.46)
α_{int}	linear loss coefficient
a	differential gain
A_0	input signal amplitude, Eq. (3.19)
A_f	forward propagating field
A_b	backward propagating field
A_{eff}	effective area, Eq. (2.43)
α_2	two-photon absorption coefficient
C_Λ	chirp coefficient
δ	detuning coefficient, Eq. (2.26)
$\delta_{\mathrm{eff}}^{f}$	forward effective self-coupling coefficient
$\delta_{\mathrm{eff}}^{b}$	backward effective self-coupling coefficient
$\overline{\delta}$	mean of forward and backward effective self-coupling coefficient
Δ_{eff}	difference of forward and backward effective self-coupling coefficient
$\Delta\kappa$	tapering coefficient
ΔJ	current tapering coefficient

Δn_{G}	refractive index modulation of grating
ϕ_{res}	phase shift corresponding to the resonance frequency in Fabry-perot resonator
ϕ	phase detuning of the operating signal from ϕ_{res}
F_T	transmitted flux (unit W)
$\mathbb{F}$	cavity finesse
J_{c}	current density
$\kappa_f^{(\mathrm{NL})}$	forward effective nonlinear coupling coefficient
$\kappa_b^{(\mathrm{NL})}$	backward effective nonlinear coupling coefficient
g_0	single pass gain coefficient of an SOA
γ	nonlinear coefficient (unit $\mathrm{cm}^{-1}\ \mathrm{W}^{-1}$)
Γ	nonlinear coefficient (unit $\mathrm{cm\ W}^{-1}$)
Γ_{conf}	field confinement factor of SOA
k_0	propagation constant in vacuum
κ	coupling coefficient
Λ	period of grating
L	length of the device/cavity
λ_{B}	Bragg wavelength
n_2^I	Kerr nonlinear coefficient (unit $\mathrm{cm}^2\mathrm{W}^{-1}$)
N	carrier density
N_0	carrier density at transparency
Ω	phase shift in the grating
P_{G}	total power inside the grating/resonator
P_{Avg}	average power in the cavity
ω_{B}	angular Bragg frequency

Acronyms

AFPR	asymmetric Fabry-Perot resonator
AOFF	all-optical flip-flop
CME	coupled mode equation

CMT	coupled mode theory
CW	continuous wave
DFB	distributed feedback
DBR	distributed Bragg reflector
ER	extinction ration
FBG	fiber Bragg grating
FDTD	finite-difference time domain
FE	field enhancement
FFT	fast Fourier transform
FP	Fabry-Perot resonator
FT	Fourier transform
FWHM	full-width-half-maximum
FWM	four-wave mixing
GNLCME	generalized nonlinear coupled mode equations
IR	isolation ratio
LTR	left to right
NLCME	nonlinear coupled mode equation
NLWBG	nonlinear waveguide Bragg grating
ODE	ordinary differential equation
PDE	partial differential equation
Q-factor	resonator quality factor
RTL	right to left
SOA	semiconductor optical amplifier
SPM	self phase modulation
ST-WBG	stopband tapered waveguide Bragg grating
SVEA	slowly varying envelope approximation
TMM	transfer matrix method

TPA	two-photon absorption
XGM	cross-gain modulation
XPM	cross-phase modulation
WBG	waveguide Bragg grating
WC	wavelength conversion
WDM	wavelength division multiplexing

1 Introduction and outline

With the growth of data traffic in telecommunication networks, the demands of photonic transmission systems are subjected to permanent rise. Photonics networks are useful in transferring information efficiently through high capacity optical fibers. However, till date most of the signal processing including amplification, retiming, multiplexing and demultiplexing as well as routing is done in the electrical domain. This requires optical-electrical-optical (OEO) conversions in intermediate nodes of the network. With the growing need for high speed data transfer this may lead to a speed bottleneck.

All-optical compact signal processing devices are thus a growing need in the present communications industry. Of particular interest are all-optical flip-flops, logic gates, and wavelength converters using compact semiconductor devices. These devices can be used for optical signal regeneration, for optical signal monitoring, and for optical packet header processing.

All-optical packet or burst switched networks are promising solutions for situations which require high data-rates. In such networks all the signal processing can be done in the optical domain bypassing OEO conversions. One of the main requirements of such packet or burst-switched network is processing of optical labels or optical headers in the optical domain. All-optical flip-flops are thus extremely useful in such networks. An optical flip-flop is a device which can temporarily store the input/output information, and processes it with other control signals, all in the optical domain. These types of devices are essentially a bistable device with two stable states of operations. The state of such a device can be changed with an optical control signal.

In an all-optical fiber transmission line several connectorized optical components are present, and various backscattered signals are generated from the end faces of these components. This scattered light can enter the source and destabilize it, thereby creating unwanted feedback. Optical feedback degrades the signal-to-noise ratio and consequently the bit-error probability (usually called bit error “rate” BER), thus resulting in poor transmission performance. Isolators are thus indispensable devices for eliminating these backscattering. Isolators with compact size which can be integrated on a chip are of high demand.

1.1 Motivation

Bistability in a nonlinear device with a feedback is first proposed by Gibbs [22]. Later Winful et. al. [75] has predicted a bistable state of operation in a nonlinear Bragg grating exploiting the Kerr effect. This opens a wide possibility of all-optical signal processing. However the power requirements to observe bistability were too high, due to a low value of nonlinear coefficient. Previous studies, which have focused on nonlinear periodic structures, considered Kerr-type nonlinearities, where the intensity dependence of the refractive index shifts the stopband to lower frequencies and leads to a dispersive bistability. Owing to the very small value of the nonlinear coefficient in most optical materials, the power required to observe any detectable shift in the stopband (the switching threshold) is very high. A few remedies have been proposed that use materials with higher nonlinearities such as semiconductors, or exploit a resonant field enhancement to increase the nonlinear effects, thereby lowering the threshold power, but also the extinction ratio.

Here we report about an alternative design which exhibits low switching power, shows an isolator-like functionality, and can be integrated on a chip with other optical components. The design is based on a stopband-tapered waveguide Bragg grating (ST-WBG), where the stopband width is linearly changed along the length of the grating. Further, we describe all-optical switching properties in a stopband tapered distributed feedback (ST-DFB) SOA. Here, the gain saturation is accompanied by a nonlinear change of refractive index, in which the carrier-induced nonlinearity is $\sim 10^7$ higher than with usual Kerr-based nonlinearities.

The nonreciprocity or direction-dependent transmission property or “optical diode”-like behaviour in a nonlinear periodic structure was first proposed by Scalora and Dowling [62], [63]. They used thin film based multilayered quasi-periodic structures with varying thickness or nonlinearity. Afterwards many researchers have proposed nonreciprocal behaviours in nonlinear resonator structures, but in all these publications the general description of the origin of such behaviour was lacking. Moreover, in all the cases only Kerr-type of nonlinearities was explored.

Here we summarize the possible limitations of using nonlinear resonator based all-optical signal processing:

- Low bandwidth
- Speed limited by material properties (for active device).
- Moderately fast, switching time generally limited by the resonator response time

However, there are some possible advantages also which should be considered:

- Low power requirement (for active devices).
- Possible amplification.
- Wavelengths compatible to present-day’s photonics network.
- Compact size and integratability
- Resonance enhancement of nonlinear effects.

In this thesis we explore the nonlinear resonator structures and seek to enhance their performance by suitable design. We discuss possible methods for reducing the threshold switching power for bistable flip-flop operations. Further, we explore nonreciprocal phenomena, and utilize them to construct an isolator.

1.2 Achievements of the present work

- Extensive numerical study of nonlinear periodic structure using coupled mode theory and FDTD. The active and passive type of nonlinearity is explored in the same framework. Generalized couple mode theory is introduced, and comparative studies have been made for different types of nonlinearities.

- New designs based on gratings which are stopband tapered, chirped or having asymmetrically placed phase shift are proposed. This reduces the switching threshold for bistable switching operations. High index contrast waveguide structure with sidewall corrugations based on InP and SOI are proposed for device realization. We also propose a high extinction ratio switching operation based on an asymmetric Fabry-Perot resonator exploiting two-photon absorption.

- A general theory of nonreciprocal transmission and reflection for a resonator structure is introduced. It predicts that any resonator structure lacking inversion symmetry exhibit "optical diode" like non-reciprocal transmission. This theory is applicable to a wide variety of nonlinearities like Kerr, SOA, TPA, carrier-plasma effects. The formulation can be extended to negative-index material, saturable absorbers or combined nonlinear effects. This simple formulation can be used in predicting non-reciprocal properties. It is applicable to photonic crystal based resonators and can be also extended to ring resonators. For the first time, the nonreciprocity of an SOA-DFB is predicted. A direction dependent FWM efficiency is predicted for the first time. The FWM performance is compared with results of ring resonator experiments.

- A specific all-optical switching scheme utilizing a Bragg grating is proposed for the first time. This scheme realizing an all-optical flip-flop by combining a holding beam and a SET signals co-propagating inside the device, while the RESET signal is counter-propagating to the holding beam. In this setup the so called negative RESET pulse is not needed.

1.3 Outline

In Chapter 2 we introduce the theoretical foundation of the thesis. A brief introduction to the coupled mode theory is given. In this chapter a generalized coupled mode equation (GNLCME) is introduced which helps in describing the active and passive periodic structures in the same framework.

In Chapter 3 we introduce the different analytical and numerical techniques to solve the GNLCME. For passive Kerr-type media we discuss the analytical solution using elliptic functions. The time dependent solution of GNCME is also discussed and the results are compared with the analytic solution in the steady state. A general description of bistable behaviour is given and a comparative study is done between Kerr-type and carrier induced nonlinearities.

A new scheme of all-optical flip-flop operation utilizing a counter-propagating SET and RESET signal are discussed along with their potential advantages.

In Chapter 4 we discuss the nonreciprocal devices and propose a simplified model of an asymmetric Fabry-Perot resonator (AFPR) to understand and predict the direction dependent non-reciprocal transmission behaviour. We discuss the general principle which leads to this novel behaviour and discuss the general condition to observe such effects. We have discussed different types of asymmetrical structures including stopband-tapered waveguide Bragg gratings in active and passive media, as well as Bragg gratings with an asymmetrically placed $\lambda/4$ phase shift in the context of passive devices. The effect of chirp and a spatial variation of the current density on this nonreciprocal behaviour are discussed.

In Chapter 5 we propose a possible geometrical variation of the resonator structures leading to a lowering of the switching threshold. We discuss different types of resonator structures each in context with different types of nonlinearities.

In Chapter 6 we report on the finite-difference in time-domain (FDTD) simulation of high index-contrast waveguide Bragg gratings with sidewall corrugation. The nonreciprocal behaviour and lowering of switching threshold as predicted in Chapter 4 and 5 are verified with an extensive numerical study.

In Chapter 7 we report on wavelength conversion using four-wave mixing (FWM) in a Kerr-type waveguide Bragg grating. We discuss the effect of stopband tapering on the FWM conversion efficiency. We also discuss about a high extinction ratio switching operation in an AFPR using TPA.

2 Theoretical foundation

2.1 Maxwell's equations

The propagation of optical fields in periodic structure is governed by Maxwell's equations. In SI-units these equations are given by

$$\operatorname{curl}\vec{E} = -\frac{\partial\vec{B}}{\partial t}, \tag{2.1}$$

$$\operatorname{curl}\vec{H} = \frac{\partial\vec{D}}{\partial t} + \vec{J}, \tag{2.2}$$

$$\operatorname{div}\vec{D} = \rho, \tag{2.3}$$

$$\operatorname{div}\vec{B} = 0, \tag{2.4}$$

where $\vec{E}$ and $\vec{H}$ are the electric and magnetic field vectors, respectively. $\vec{D}$ is the electric displacement and $\vec{B}$ is the magnetic induction. In the absence of free charges, as is common for optical materials, the current density $\vec{J}$ and the charge density ρ are both zero. With the electric polarization $\vec{P}$, the magnetization $\vec{M}$, the permittivity ε_0 of free space, and the magnetic permeability μ_0 of free space we define the constitutive relations:

$$\begin{aligned}\vec{B} &= \mu_0\vec{H} + \vec{M},\\ \vec{D} &= \varepsilon_0\vec{E} + \vec{P}.\end{aligned} \tag{2.5}$$

Since typical optical materials are non-magnetic, we assume $\vec{M} = 0$ and thus $\vec{B}$ is proportional to $\vec{H}$. We assume the medium to be invariant with respect to time shifts, and that the polarization $\vec{P}$ does not depend on the magnetic field. It can be shown that $\vec{P}$ can be written as a Volterra series [61] with influence function tensors[1] $\vec{\chi}^{(m)}$ [7],

$$\begin{aligned}\vec{P}(\vec{r},t) = {} & \varepsilon_0\int_{-\infty}^{+\infty}\vec{\chi}^{(1)}(t-t_1)\vec{E}(\vec{r},t_1)dt_1\\ & +\varepsilon_0\int\int_{-\infty}^{+\infty}\vec{\chi}^{(2)}(t-t_1,t-t_2)\vdots\vec{E}(\vec{r},t_1)\vec{E}(\vec{r},t_2)dt_1dt_2\\ & +\varepsilon_0\int\int\int_{-\infty}^{+\infty}\vec{\chi}^{(3)}(t-t_1,t-t_2,t-t_3)\vdots\vec{E}(\vec{r},t_1)\vec{E}(\vec{r},t_2)\vec{E}(\vec{r},t_3)dt_1dt_2dt_3\\ & +\cdots\ .\end{aligned} \tag{2.6}$$

Further, we assume that the material under consideration is isotropic. With this assumption we can write the polarization $\vec{P}$ as the sum of the linear $\vec{P}_L$ and nonlinear polarization $\vec{P}_{NL}$ as

$$\vec{P}(\vec{r},t) = \vec{P}_{\mathrm{L}}(\vec{r},t) + \vec{P}_{\mathrm{NL}}(\vec{r},t), \tag{2.7}$$

$$\vec{P}_{\mathrm{L}}(\vec{r},t) = \varepsilon_0\int_{-\infty}^{+\infty}\vec{\chi}^{(1)}(t-t_1)\vec{E}(\vec{r},t_1)dt_1, \tag{2.8}$$

---

[1] $\vec{\chi}^{(m)}$ is a tensor of rank $m + 1$, with $m = 1, 2, \ldots$.

$$\begin{aligned}\vec{P}_{\mathrm{NL}}\left(\vec{r},t\right)&=\varepsilon_0\int\int_{-\infty}^{+\infty}\overleftrightarrow{\chi}^{(2)}\left(t-t_1,t-t_2\right)\vdots\vec{E}\left(\vec{r},t_1\right)\vec{E}\left(\vec{r},t_2\right)dt_1dt_2\\&+\varepsilon_0\int\int\int_{-\infty}^{+\infty}\overleftrightarrow{\chi}^{(3)}\left(t-t_1,t-t_2,t-t_3\right)\vdots\vec{E}\left(\vec{r},t_1\right)\vec{E}\left(\vec{r},t_2\right)\vec{E}\left(\vec{r},t_3\right)dt_1dt_2dt_3\\&+\cdots\ .\end{aligned}\qquad(2.9)$$

We assume that the nonlinear part $\vec{P}_{NL}$ is sufficiently small and can be treated as a small perturbation of the linear part $\vec{P}_L$, i.e.,

$$\left|\vec{P}_{\mathrm{NL}}\left(\vec{r},t\right)\right|\ll\left|\vec{P}_{\mathrm{L}}\left(\vec{r},t\right)\right|.\qquad(2.10)$$

Both $\vec{E}\left(t,\vec{r}\right)$ and $\vec{P}\left(t,\vec{r}\right)$ are assumed to be quasi-monochromatic with equal optical centre angular frequency ω_0. We define the susceptibility tensors $\tilde{\overleftrightarrow{\chi}}^{(m)}$ as the Fourier transform of the influence function tensors. If the operating frequency is far away from any material resonances, the influence function tensor can be approximated by a product of delta functions[2]:

$$\overleftrightarrow{\chi}^{(m)}=\tilde{\overleftrightarrow{\chi}}^{(m)}\left(\omega_1,\omega_{2,}...,\omega_m\right)\prod_{j=1}^{m}\delta\left(t-t_j\right).\qquad(2.11)$$

This assumption is valid as long as the pulse width is greater than 100 fs [4]. With this instantaneous response of the susceptibility, the polarization in the time domain becomes

$$\begin{aligned}\vec{P}\left(\vec{r},t\right)&=\vec{P}_L\left(\vec{r},t\right)+\vec{P}_{NL}\left(\vec{r},t\right)\\&=\varepsilon_0\left(\tilde{\overleftrightarrow{\chi}}^{(1)}\cdot\vec{E}\left(\vec{r},t\right)+\tilde{\overleftrightarrow{\chi}}^{(2)}:\vec{E}^2\left(\vec{r},t\right)+\tilde{\overleftrightarrow{\chi}}^{(3)}\vdots\vec{E}^3\left(\vec{r},t\right)+\cdots\right).\end{aligned}\qquad(2.12)$$

For isotropic materials however the tensors become diagonal and can be reduced to scalar functions [4]. Depending on the symmetry class of the material, some of the higher order susceptibilities can be further simplified or they even vanish for certain symmetries. For an operating frequency far away from any material resonances, the intrinsic dispersion of the material is also assumed to be small compared to the dispersion induced by the periodic structures[3]. Therefore, we neglect any time- or frequency-dependence in the susceptibilities. It should be noted, that the dispersion and the absorption of a material are related by the Kramers-Kronig relations [30]. So in the frequency region of interest we assume for passive media a small loss and a nearly constant refractive index. This will not be true outside this region. For active materials, we allow a gain which influences the refractive index via the Henry-factor α_{H} (see Section 2.3.2 on page 15).

We proceed by inserting Eq. (2.12) into Eq. (2.5) yielding

$$\vec{D}\left(\vec{r},t\right)=\varepsilon_0\tilde{\overleftrightarrow{\varepsilon}}\left(\vec{r}\right)\vec{E}\left(\vec{r},t\right)+\vec{P}_{NL},\qquad(2.13)$$

where the linear dielectric function $\tilde{\overleftrightarrow{\varepsilon}}\left(\vec{r}\right)$ is given by

---

[2] This approximation leads to constant susceptibility tensor in the frequency range of interest [4].

[3] It can be shown that the grating induced dispersion is a few orders of magnitude higher than the material dispersion [5].

$$\tilde{\varepsilon}(\vec{r}) = 1 + \tilde{\chi}^{(1)}. \tag{2.14}$$

Note that periodic structure can be described as a composite system, so all the susceptibilities and therefore the dielectric function $\tilde{\varepsilon}$ are assumed to depend on the coordinate $\vec{r}$. The linear refractive index $\tilde{n}$ can be related to the dielectric function by $\tilde{\varepsilon} = \tilde{n}^2$.

By taking the curl of Eq. (2.1) and combining it with equation (2.7) and (2.13), one can eliminate $\vec{B}$ and $\vec{D}$ in favour of $\vec{E}$ and $\vec{P}$ to obtain the nonlinear wave equation in a weakly inhomogeneous medium[4]

$$\text{curl curl } \vec{E} - \frac{\varepsilon(\vec{r})}{c^2}\frac{\partial^2 \vec{E}}{\partial t^2} = \mu_0 \frac{\partial^2 \vec{P}_{\text{NL}}}{\partial t^2}, \tag{2.15}$$

where $c^2 = 1/(\mu_0 \varepsilon_0)$ is the velocity of light in vacuum. We consider Cartesian coordinate system. Further, we consider a linearly polarized light propagating along the z–axis. So by choosing the polarization parallel to the x–axis, we only have to consider one component of the electric field vector $\vec{E} = E_x \hat{e}_x$. From equation (2.12) it is obvious that the same applies for the polarization. In the following we consider only the scalar quantities. We drop the x-subscripts both for the fields and susceptibility[5] and the vector wave equation (2.15) simplifies to the scalar wave equation,

$$\nabla^2 E - \frac{\varepsilon(\vec{r})}{c^2}\frac{\partial^2 E}{\partial t^2} = \mu_0 \frac{\partial^2 P_{\text{NL}}}{\partial t^2}. \tag{2.16}$$

The above equation gives the general description of plane waves in a nonlinear medium with spatial varying dielectric constant. In the following sections we will consider different linear and nonlinear periodic structures which are characterized by $\varepsilon(\vec{r})$.

2.2 Linear coupled mode theory

To obtain the wave equation for a weakly varying periodic structure it is more convenient to work in the Fourier domain [4] assuming a time dependence of exp(−iωt). So we write the wave equation (2.16) in the Fourier domain neglecting any nonlinear polarization P_{NL},

$$\nabla^2 \tilde{E} - \tilde{\varepsilon}(\vec{r},\omega)\frac{\omega^2}{c^2}\tilde{E} = 0, \quad k_0 = \frac{\omega}{c}. \tag{2.17}$$

The quantities $\tilde{E}$ and $\tilde{\varepsilon}$ are the Fourier transforms of the electric field E and the dielectric function ε. The quantity k_0 represents the vacuum propagation constant.

For a linear waveguide (i.e., for a medium which is homogeneous along z) the solution of the above equation (2.17) would take the form,

$$\tilde{E}(\vec{r},\omega) = F(x,y)\left[\tilde{A}_f(\omega)\exp\left(\mathrm{i}\beta(\omega)z\right) + \tilde{A}_b(\omega)\exp\left(-\mathrm{i}\beta(\omega)z\right)\right]. \tag{2.18}$$

---

[4] In a weakly homogenous medium we assume grad (ln ε) ≈ 0.

[5] In an isotropic material the susceptibility tensor is diagonal and the diagonal terms of $\chi^{(1)}$ and $\chi^{(3)}$ can be written as χ_{xx} and χ_{xxxx} respectively. We drop the subscript of the susceptibility in the scalar approximation.

Here $F(x, y)$ denotes the transverse field distribution[6]. The above solution describes two independent waves with propagation constant propagation constant β at angular frequency ω, moving in opposite directions. Here we have denoted the constant field amplitude $\tilde{A}_f$ for the forward and $\tilde{A}_b$ for the backward propagating wave, respectively.

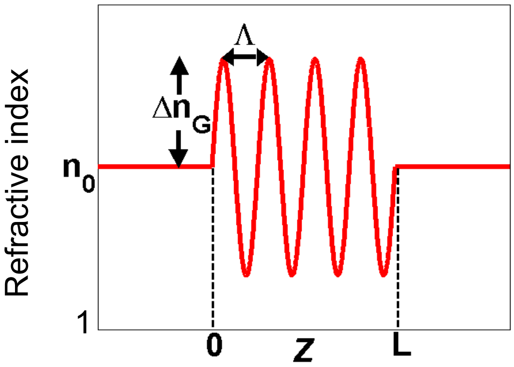

Figure 2-1 : Schematic diagram showing the variation of the refractive index as a function of position z inside the grating of length L

We consider only 1D periodic structures (e.g. fiber Bragg gratings (FBG) or semiconductor distributed feedback structures (DFB)) where the dielectric constant is assumed to be periodic along the z-direction. Further, we assume the media are lossless. We model the dielectric constant of a grating as described in Ref. [4], [5]. In such a periodic structure the dielectric constant can be written in terms of a spatial Fourier series with period Λ as

$$\varepsilon(z) = \hat{\varepsilon}_0 + \sum_{\substack{m=-\infty \\ m\neq 0}}^{\infty} \hat{\varepsilon}_m \exp\left(\frac{i2\pi m z}{\Lambda}\right). \tag{2.19}$$

Here $\hat{\varepsilon}_0, \hat{\varepsilon}_m$ are the spatial Fourier components of $\varepsilon(z)$. We assume that the dominant effect results from the first order spatial Fourier coefficients $\hat{\varepsilon}_{\pm 1}$. Further as we have neglected any absorption, i.e., $\varepsilon(z)$ in our case is real and we can use $\hat{\varepsilon}_{-1} = \hat{\varepsilon}_1^*$ to write

$$\varepsilon(z) \approx \hat{\varepsilon} + 2\Re(\varepsilon_1)\cos\left(\frac{2\pi z}{\Lambda}\right). \tag{2.20}$$

Here $\Re(\varepsilon_1)$ denotes the real part of ε_1. For small values of $\Re(\varepsilon_1)$ (i.e., for a small refractive index variation, $(\Delta n_G)^2 << 1$) we write the expression for the real effective refractive index $n = \beta / k_0$ of the grating as

$$n(z) = n_0 + \Delta n_G \cos\left(\frac{2\pi z}{\Lambda}\right). \tag{2.21}$$

The schematic variation of the refractive index as a function of z inside the grating of length L is shown in Figure 2-1.

---

[6] We normalize the unit such that the quantity $F(x, y)$ is dimensionless.

Now, if Δn_{G} is zero, the general solution of the wave equation (2.17) in the linear case is written as in Eq. (2.18).

If the index modulation Δn_{G} is small, the solution of the wave equation can be still written in the same form as Eq. (2.18), but the amplitudes $\tilde{A}_f$ and $\tilde{A}_b$ become weakly dependent on z and ω. So we make the ansatz [5],

$$\tilde{E}(\vec{r},\omega)=F(x,y)\left[\tilde{A}_f(z,\omega)\exp(\mathrm{i}\beta_B z)+\tilde{A}_b(z,\omega)\exp(-\mathrm{i}\beta_B z)\right]. \tag{2.22}$$

Here the quantity $\beta_B=\pi/\Lambda$ is the Bragg wave number for the first-order grating (see Eq. (2.21)). The Bragg condition can be written as

$$\beta_B=\frac{n_0}{c}\omega_B=\frac{\pi}{\Lambda}. \tag{2.23}$$

Furthermore we assume that the amplitudes (or to be more precise, the envelopes) $\tilde{A}_{f,b}$ vary slowly in space. With the vacuum propagation constant k_0 we assume

$$\left|\frac{\partial^2\tilde{A}_{f,b}}{\partial z^2}\right|\ll 2k_0\left|\frac{\partial\tilde{A}_{f,b}}{\partial z}\right|. \tag{2.24}$$

This method is known as the slowly varying envelope approximation (SVEA) [1]. Using SVEA, and keeping only the nearly phase-matched terms, and neglecting all spatial second derivatives, we obtain the following set of coupled differential equations

$$\begin{aligned}+\frac{\partial\tilde{A}_f}{\partial z}&=+\mathrm{i}\delta(\omega)\tilde{A}_f+\kappa\tilde{A}_b,\\-\frac{\partial\tilde{A}_b}{\partial z}&=+\mathrm{i}\delta(\omega)\tilde{A}_b+\kappa\tilde{A}_f.\end{aligned} \tag{2.25}$$

The real quantity δ, called the detuning coefficient, is a measure of the detuning from the Bragg angular wavenumber and is defined as

$$\delta(\omega)=\frac{n_0}{c}(\omega-\omega_{\mathrm{B}})\equiv\beta(\omega)-\beta_{\mathrm{B}}. \tag{2.26}$$

It can be seen from the above equations, that the forward and backward propagating modes are no longer independent but are coupled together via the coupling term κ, which is know as a coupling coefficient and is given by

$$\kappa=\frac{\omega_{\mathrm{B}}\Delta n_{\mathrm{G}}}{2c}=\frac{\pi\Delta n_{\mathrm{G}}}{\lambda_{\mathrm{B}}}. \tag{2.27}$$

To obtain the coupled mode equations (CME) in the time domain, we assume that the total field in the time domain can be written as

$$E(\vec{r},t)=F(x,y)\left[A_f(z,t)\exp(\mathrm{i}\beta_B z)+A_b(z,t)\exp(-\mathrm{i}\beta_B z)\right]\exp(-\mathrm{i}\omega_0 i)+\text{c.c.}. \tag{2.28}$$

Here "c.c." denotes the complex conjugate. We can expand the propagation constant β in a Taylor series about ω_0,

$$\begin{aligned}\beta(\omega) &= \beta + \frac{\mathrm{d}\beta}{\mathrm{d}\omega}(\omega-\omega_0) + \frac{1}{2}\frac{\mathrm{d}^2\beta}{\mathrm{d}\omega^2}(\omega-\omega_0)^2 + \cdots \\ &\approx \beta + \frac{1}{v_g}(\omega-\omega_0),\end{aligned} \tag{2.29}$$

and retain the leading-order terms to obtain the coupled mode equations in the time domain as

$$\begin{aligned}+\mathrm{i}\left(\frac{\partial A_f}{\partial z} + \frac{1}{v_g}\frac{\partial A_f}{\partial t}\right) + \kappa A_b = 0, \\ -\mathrm{i}\left(\frac{\partial A_b}{\partial z} - \frac{1}{v_g}\frac{\partial A_b}{\partial t}\right) + \kappa A_f = 0.\end{aligned} \tag{2.30}$$

We define $v_g = \mathrm{d}\omega/\mathrm{d}\beta$ as the group velocity

2.2.1 CW solution in linear case

In this section, we discuss the CW solutions of Eq. (2.25). We consider the following trial solution

$$\begin{aligned}\tilde{A}_f(z) = A_1\exp(\mathrm{i}qz) + A_2\exp(-\mathrm{i}qz), \\ \tilde{A}_b(z) = B_1\exp(\mathrm{i}qz) + B_2\exp(-\mathrm{i}qz),\end{aligned} \tag{2.31}$$

where q needs to be determined from the boundary conditions. The quantities A_1, A_2, B_1 and B_2 are constants. The trial solution is a true solution of Eq. (2.25) only if the following four relations are valid:

$$\begin{aligned}(q-\delta)A_1 = \kappa B_1, \qquad (q+\delta)B_1 = -\kappa A_1, \\ (q-\delta)B_1 = \kappa A_2, \qquad (q+\delta)A_2 = -\kappa B_2.\end{aligned} \tag{2.32}$$

These equations are satisfied for nonzero values of the constants A_1, A_2, B_1 and B_2 if the possible values of q obey the dispersion relation (see Figure 2-2)

$$q^2 = \delta^2 - \kappa^2. \tag{2.33}$$

The above expression gives the dispersion relation of the grating in a 1D infinitely long structure. The stopband is defined by $|\delta| \le \kappa$ (see Figure 2-2). A signal at any frequency lying in the stopband is unable to propagate inside the structure, thus the structure is “opaque” to the incoming signal. In other words, the propagation constant of the field inside the stopband is imaginary leading to the decay of the incoming radiation along the direction of propagation. For $|\delta| \ge \kappa$, waves can propagate, and the grating is “transparent”. In Figure 2-2 the dotted lines represents the situation for free photons; they can be obtained by inserting $\kappa = 0$ in Eq. (2.33).

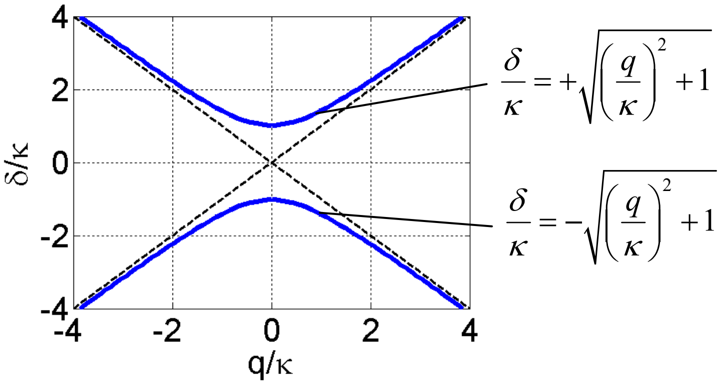

Figure 2-2 : Dispersion relation of a linear periodic structure, Eq. (2.33). The solid line represents the band diagram of a period structure of infinite length. The dotted line represents the dispersion relation for the free photon. The region $|\delta| \leq \kappa$ defines the stopband.

For a grating of finite length the situation changes but still maintains the same qualitative behaviour. In such a structure of length L one can calculate [13] the reflectivity R and the transmissivity T utilizing Eq. (2.33),

$$\begin{aligned} R &= \left|\frac{\tilde{E}_b(0)}{\tilde{E}_f(0)}\right|^2 = \left|\frac{\mathrm{i}\kappa\sin(qL)}{q\cos(qL) - \mathrm{i}\delta\sin(qL)}\right|^2, \\ T &= \left|\frac{\tilde{E}_f(L)}{\tilde{E}_f(0)}\right|^2 = \left|\frac{q\exp(+\mathrm{i}\delta L)}{q\cos qL - \mathrm{i}\delta\sin qL}\right|^2. \end{aligned} \tag{2.34}$$

The reflectivity and the transmissivity for the structures characterized by a grating constant

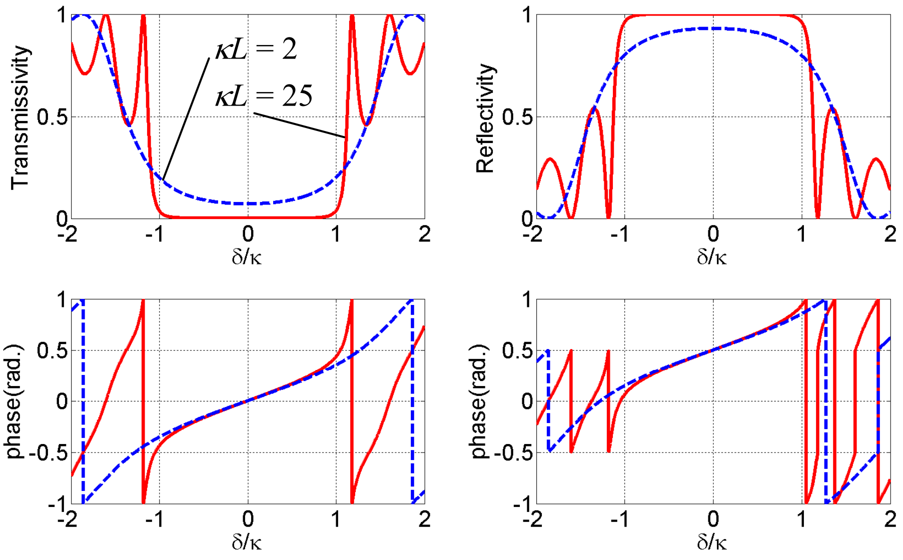

Figure 2-3 : Reflection and transmission spectra for two values of κL. The solid (red) curve is for $\kappa L = 5$, while the dashed (blue) curve is for $\kappa L = 2$. (a) Transmissivity. (b) Reflectivity. (c) Transmission phase. (d) Reflection phase.

of $\kappa L = 3$ (blue dotted line) and $\kappa L = 5$ (red solid line) are plotted in Figure 2-3. We can see from the plots that as the grating constant κL increases the transmissivity and the reflectivity curves become steeper near the transmission resonance (i.e., at $T = 1$ or $R = 0$). Moreover the peak reflectivity of the periodic structure at the Bragg frequency (the corresponding detuning coefficient is $\delta = 0$) approaches 100 % (as observed in a truly periodic structure). Specifically for $\kappa L > 3$ the reflectivity at Bragg resonance is above 99 %. The maximum reflectivity occurs at the centre of the stopband ($\delta = 0$) and can be calculated using (2.34) as

$$R_{\max} = R(\delta = 0) = \tanh^2(\kappa L). \tag{2.35}$$

2.3 Nonlinear coupled mode equations (NLCME)

The coupled mode theory (CMT) described in the previous sections can be easily extended to include nonlinearities. We start from the full nonlinear wave equation (2.16) with the nonlinear polarization given by Eq. (2.12). In the following two subsections we present the derivation of the nonlinear coupled mode equations. Here we consider two different kinds of nonlinearities, i.e., Kerr-type nonlinearities, and carrier induced nonlinearity.

For a material with odd inversion symmetry, the second order susceptibility coefficient $\chi^{(2)}$ must vanish. This type of symmetry is observed for an isotropic material as well as for a large number of common crystals like Si and Ge. As SiO_2 is a symmetric molecule, the same symmetry is observed for glass fibers. So for the device based on this kind of materials the leading nonlinear term is $\chi^{(3)}$. This effect is also known as Kerr effect. In such materials the nonlinear effect is virtually instantaneous.

We can have another class of nonlinearity due to injection of external charge carriers. With the injection of the external carrier the refractive index of the material changes and from the Kramers-Kronig relation it influences the imaginary part of the refractive index, which can be simply modelled introducing the Henry or alpha-factor α_H [25]. This kind of nonlinearity is generally observed in semiconductor optical amplifiers. The injection of carriers induces a large change in the refractive index; hence a periodic structure made up of active[7] elements will have higher nonlinearities, ~ 10^7 times higher in comparison to the Kerr-type material based passive optical devices [50]. However, the carrier induced nonlinearity is limited by the bottle-neck of carrier relaxation. So we always have a trade-off between the higher nonlinearity and speed limitations.

2.3.1 NLCME for passive Kerr-type of devices

In this section we derive the nonlinear coupled mode equation for Kerr-type nonlinear periodic structures. We assume that the influence of the change of the nonlinear refractive index is sufficiently small in comparison to the background refractive index. This approximation leads to treat the nonlinear contribution as a perturbation; hence similar to the procedure described in Section 2.2 we start with the linear solution of the CME and introduce nonlinearity as a perturbation. So with the similar argument we can say, if the carrier frequency is sufficiently far away from any material resonances, the susceptibility does not vary strongly with frequency. For this range, the waveguiding can be described by an effective index, which we assume to be frequency independent. This means the material dispersion is neglected, an assumption which is justified provided the propagation length is sufficiently short, which is the case for all our devices. We only consider the leading order nonlinear term $\chi^{(3)}$. With these assumptions, the nonlinear polarization (2.12) simplifies to

---

[7] Active elements are defined as materials which show gain or absorption due to charge carrier injection.

$$P_{\mathrm{NL}}(z,t)=\varepsilon_0\chi^{(3)}E^3(z,t), \tag{2.36}$$

The effective refractive index n in this case can be written as a function of the direction of propagation z, and of the magnitude of the electric field intensity I:

$$n(z)=n_0+\Delta n_{\mathrm{G}}(z)\cos\left(\frac{2\pi}{\Lambda}z\right)+n_2^I I. \tag{2.37}$$

In the above equation the first term on the right-hand side is the linear refractive index. The second term gives the periodic variation of the refractive index in the direction of propagation, where we have considered only the dominant spatial component with period Λ. The last term in equation (2.37) gives the contribution from the material nonlinearity, with nonlinear coefficient n_2^I. The quantity n_2^I is a measure of the nonlinear coefficient n_2, expressed in units of intensity [37] and can be explicitly written as

$$n_2^I=\frac{3Z_0}{4n}\Re\left[\chi^{(3)}\right]. \tag{2.38}$$

Here the quantity Z_0 is the vacuum wave impedance.

We do the same analysis as done for the linear case, i.e., we neglect any polarisation effects, and denote the slowly varying envelopes of the forward and backward travelling waves as A_f and A_b, respectively. In the following, the carrier angular frequency is ω_0, $k_0 = n_0\omega_0/c$ is the propagation constant, $k_{\mathrm{B}} = \pi/\Lambda$ is the Bragg wavenumber corresponding to the Bragg wavelength $\lambda_{\mathrm{B}} = 2n_0\Lambda$, and c is the speed of light in vacuum. The electric field inside the grating can be written as:

$$\begin{aligned}E(z,t)=C_n\left[A_f(z,t)\exp(\mathrm{i}\beta_B z)+A_b(z,t)\exp(-\mathrm{i}\beta_B z)\right]\\ \times\exp(-\mathrm{i}\omega_0 t)\quad .\end{aligned} \tag{2.39}$$

The normalization constant C_{n} is chosen such that $|A_{f,b}|^2$ gives the intensity of the forward and backward waves in units of W/cm^2.

Inserting the coupled mode ansatz (2.39) into equation (2.30) and neglecting all the terms not matched in phase, assuming weak nonlinearities, applying SVEA, and only keeping the leading order terms, we are finally left with

$$\begin{aligned}
&+\frac{\partial A_f}{\partial z}+\frac{1}{v_g}\frac{\partial A_f}{\partial t}=\mathrm{i}\delta A_f+\mathrm{i}\kappa A_b+\mathrm{i}\Gamma\left(\left|A_f\right|^2+2\left|A_b\right|^2\right)A_f,\\
&-\frac{\partial A_b}{\partial z}+\frac{1}{v_g}\frac{\partial A_b}{\partial t}=\mathrm{i}\delta A_b+\mathrm{i}\kappa A_f+\mathrm{i}\Gamma\left(\left|A_b\right|^2+2\left|A_f\right|^2\right)A_b.
\end{aligned} \tag{2.40}$$

Here v_g is the group velocity, and the nonlinear coupling coefficient Γ is defined as:

$$\Gamma=\frac{2\pi n_2^I}{\lambda_B}. \tag{2.41}$$

The nonlinear terms with a factor "2" in front are the cross-phase modulation terms, while the other nonlinear terms are called self-phase modulation terms. While the above derivation of the coupled mode equations was more of an approximate approach, rigorous methods do exist and can be found in [29]. Coupled mode theory can also be extended to deep gratings, where the assumption $\Delta n_\mathrm{G} << n_0$ no longer holds [29]. The NLCME are useful in describing the response of a finite-length structure, while avoiding the difficulties involved in solving the full-vectorial wave equations. In general, the coupled mode equations must be solved numerically. Figure 2-4 shows the power dependent transmission curve of a periodic structure. With increase in power the transmission curve move (see red curve Figure 2-4) to the lower frequency side (or lower value of the detuning coefficient). It is observed that the transmission curve is mostly influenced near the transmission resonance.

The nonlinear coefficient Γ (unit cm/W) can be related to the nonlinear coefficient γ (unit 1/(cm W)) defined with respect to the effective area of A_eff [4] as

$$\Gamma=\gamma A_\mathrm{eff}. \tag{2.42}$$

Here the effective area is defined as [4]

$$A_\mathrm{eff}=\frac{\left[\int\limits_{-\infty}^{-\infty}\int\limits_{-\infty}^{\infty}\left|F(x,y)\right|^2\mathrm{d}x\mathrm{d}y\right]^2}{\int\limits_{-\infty}^{-\infty}\int\limits_{-\infty}^{\infty}\left|F(x,y)\right|^4\mathrm{d}x\mathrm{d}y}. \tag{2.43}$$

Here $F(x, y)$ is the transverse field distribution. The above definition is valid for a weakly guiding medium; for a high index contrast waveguide this definition should be modified to include the more accurate calculations [36].

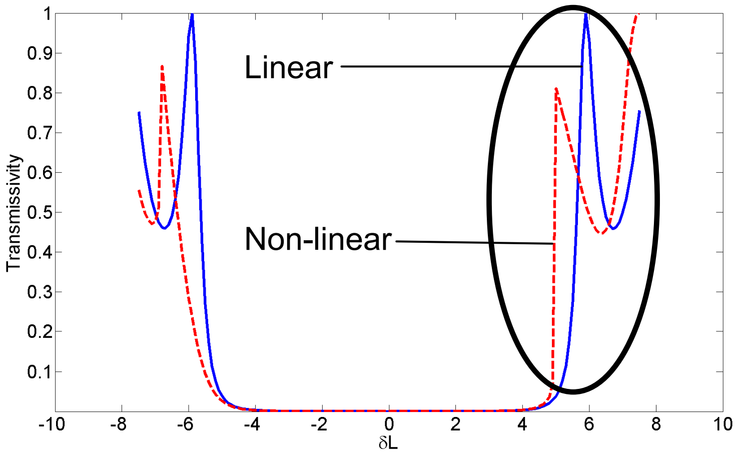

Figure 2-4 : Power dependent transmission curve for a Kerr type nonlinear periodic structure. The solid (blue) line shows the transmission curve in the linear case, while the dotted (red) line shows the non-linear transmission curve.

2.3.1.1 Scaling relations in nonlinear coupled mode equation

The NLCME (2.40) remains unchanged if we choose any arbitrary scale factor of a_1 and a_2 such that the following relations are valid [68]

$$\begin{gathered}\kappa = a_1\tilde{\kappa}, \quad \delta = a_1\tilde{\delta}, \quad z = \frac{\tilde{z}}{a_1}, \quad t = \frac{\tilde{t}}{a_1}, \\ \Gamma = a_2{}^2\tilde{\Gamma}, \quad A_{f,b} = \frac{\sqrt{a_1}}{a_2}\tilde{A}_{f,b}.\end{gathered} \tag{2.44}$$

So if a simulation is performed with a certain value of κL and ΓL the same results can be applied to different structures using proper scale factors a_1 and a_2.

2.3.2 NLCME for carrier induced nonlinearity

In an active material like with a semiconductor optical amplifier (SOA) another type of nonlinearity is observed. Due to injection of carriers in a semiconductor this type of material offers gain to the incoming optical signal. In this section we derive the nonlinear coupled mode theory for carrier induced nonlinearity.

We consider the equation (2.25) and (2.26), where the angular wavenumber $\beta = nk_0$ contains contributions particular to active semiconductor media. In particular, the refractive index in SOAs is dependent on the carrier density N. To make this apparent, we express the effective refractive index $n = n_b + n_a$ by a background part n_b and a contribution from the SOA active region n_a. Both the real n'_a and imaginary n''_a parts of $n_a = n'_a + \mathrm{i}\, n''_a$ depend on the carrier density. The Henry-factor α_H represents the ratio of the change in the real part of the refractive index $\Delta n'_a$ to a given change in the imaginary part $\Delta n''_a$ is expressed as [25]:

$$\alpha_H = \frac{\Delta n'_a}{\Delta n''_a} = -2k_0\frac{\Delta n_a}{\Delta g}, \tag{2.45}$$

where we have introduced the power gain $g = -2k_0\, n''_a$. Expanding the gain $g = (\mathrm{d}\, g/\mathrm{d}N)\, [N - N_0]$ and the refractive index $n = n_0 + (\mathrm{d}\, n/\mathrm{d}N)\, [N - N_0]$ as linear functions of the carrier density N, evaluated at transparency $N = N_0$, the α_H–factor becomes in the small signal case

$$\alpha_H = -2k_0 \left. \frac{\mathrm{d}n/\mathrm{d}N}{\mathrm{d}g/\mathrm{d}N} \right|_{N=N_0} . \tag{2.46}$$

In the following we assume that α_H does not depend on the carrier density N_0; this common approximation greatly simplifies the theoretical analysis of bistability [2], but possibly hides actual behaviour since the carrier density can take on a range of values between transparency and lasing threshold during bistable switching. In any medium, the real and imaginary parts are coupled, and the strength of this coupling can be calculated using the Kramers-Kronig relations. In active semiconductors, this coupling is very strong; the gain saturation is accompanied by significant changes in the refractive index. In all the simulation results presented here we assume a constant α_H–factor. Though for ultra-fast nonlinearities in SOAs the assumption of constant α_H–factor does not hold strictly [74], we still assume it to be constant for simplicity.

Changes in the refractive index with carrier density are most often attributed to a carrier-induced shift of the gain spectrum, and gain compression. A change in carrier density also affects the refractive index through free-carrier absorption [28], but this effect is usually dominated by the gain contribution. The refractive index also depends on temperature, but we operate at speeds (> 10 MHz) where sluggish temperature effects average out. We define β_b as the background modal wavenumber, the wavenumber β for DFB SOAs can be written using the α_H–factor as

$$\beta = \beta_b - \mathrm{i}\frac{g}{2}\left(1 - \mathrm{i}\alpha_H\right) + \mathrm{i}\frac{\alpha_\mathrm{int}}{2}, \tag{2.47}$$

We can expand the background wavenumberβ_b in a Taylor series about ω_0, and high-order terms are neglected since they produce little change for pulses passing through the small length (~ 300 μm) of the SOA. We can do the similar analysis as in section 2.2 and write the coupled mode equation in the time domain as,

$$\begin{aligned} +\frac{\partial A_f}{\partial z} + \frac{1}{v_g}\frac{\partial A_f}{\partial t} &= \mathrm{i}\,\kappa_f^{(\mathrm{NL})} A_f + \mathrm{i}\,\kappa A_b, \\ -\frac{\partial A_b}{\partial z} + \frac{1}{v_g}\frac{\partial A_b}{\partial t} &= \mathrm{i}\,\kappa_b^{(\mathrm{NL})} A_b + \mathrm{i}\,\kappa A_f, \end{aligned} \tag{2.48}$$

where,

$$\kappa_f^{(\mathrm{NL})} = \kappa_b^{(\mathrm{NL})} = \delta - \mathrm{i}\frac{g}{2}\left(1 - \mathrm{i}\alpha_H\right) + \mathrm{i}\frac{\alpha_\mathrm{int}}{2}. \tag{2.49}$$

The detuning parameter can be defined similarly to (2.26) as

$$\delta = \beta_b - \beta_B = \frac{2\pi n_b}{\lambda} - \frac{\pi}{\Lambda} = \frac{2\pi n_b}{\lambda} - \frac{2\pi n}{\lambda_B}, \tag{2.50}$$

The gain term g in the time domain is evaluated at the optical-signal frequency ω_0,

$$g(x,y,z,t) = \Gamma_{\text{conf}} g_{\text{mat}} = \Gamma_{\text{conf}} a\left[N(x,y,z,t) - N_0\right],. \tag{2.51}$$

We define Γ_{conf} as the optical confinement factor, and N_0 is the transparency carrier density; $a = \mathrm{d}g/\mathrm{d}N$ is the differential gain.

2.3.2.1 Carrier density rate equation

The carrier density N is the density of electron-hole pairs, and is based on the assumption of charge neutrality between the conduction-band electrons and valence-band holes [6]. For time scales longer than the intraband relaxation time (~ 0.05 ps), the dynamics of the carrier density in both SOAs and semiconductor lasers has been modelled by a rate equation [6]

$$\frac{\mathrm{d}N}{\mathrm{d}t} = \frac{J_c}{ed} - \frac{N}{\tau} - \frac{a}{\hbar\omega}\left(N - N_0\right)I. \tag{2.52}$$

The right-hand side consists of various mechanisms that create or eliminate electron-hole pairs. The first term represents electrical injection of carriers, where J_c is the injected current density and e is the electric elementary charge. The second term accounts for spontaneous and non-radiative recombination mechanisms, where τ is the carrier recombination lifetime. Although this lifetime is dependent on the carrier density (through spontaneous emission and Auger recombination) we neglect this dependence to simplify our analysis [46]. The final term accounts for stimulated recombination of electron-hole pairs by the optical signal, where $\hbar$ is the reduced Planck's constant, and I is the optical intensity average over a few optical periods $2\pi/\omega$.

The spatial dependence of the intensity I along the propagation direction z is expressed by the total power at z, $\sigma\left(\left|A_f\right|^2 + \left|A_b\right|^2\right)$, the confinement factor Γ_{conf} and the active cross-sectional area Wd, namely

$$I = \frac{\Gamma_{\text{conf}}\sigma}{Wd}\left(\left|A_f\right|^2 + \left|A_b\right|^2\right), \tag{2.53}$$

where N is now understood to be averaged over the transverse dimension, and the optical confinement factor Γ_{conf} and the mode cross section σ are given in terms of the transverse field distribution $F(x, y)$ by

$$\begin{aligned} \Gamma_{\text{conf}} &= \int_0^W \int_0^d dxdy \left|F(x,y)\right|^2 \Big/ \sigma, \\ \sigma &= \int_{-\infty}^{+\infty} \int_{-\infty}^{+\infty} dxdy \left|F(x,y)\right|^2. \end{aligned} \tag{2.54}$$

As the carrier density enters the coupled mode equations through the modal gain g, it is convenient to write the gain rate equation using (2.52) and (2.51) averaged over the active cross-section as

$$\tau \frac{\mathrm{d}g}{\mathrm{d}t} = g_0 - \left[1+\bar{P}\right]g. \tag{2.55}$$

The small-signal value of the gain is $g_0 = \Gamma_{\text{conf}} a N_0 \left(\bar{J}_c - 1\right)$, and $\bar{J}_c = J_c \tau / e d N_0$ gives the current density normalized to its value required to achieve transparency. The normalized optical power $\bar{P}$ is given by

$$\bar{P} = \frac{\left[\left|A_f(z)\right|^2 + \left|A_b(z)\right|^2\right]\sigma}{P_{\text{sat}}} = \frac{P_f + P_b}{P_{\text{sat}}}, \quad P_{\text{sat}} = \frac{\hbar\omega W d}{\tau a \Gamma_{\text{conf}}}, \tag{2.56}$$

where $P_f = \sigma|A_f|^2$ and $P_b = \sigma|A_b|^2$ are the optical powers of the individual field envelopes, and P_{sat} defines the saturation power. The gain rate equation (2.55) also provides the information about the phase change experienced by the signal via the α_{H}-factor.

2.3.2.2 Small-signal steady-state solution for active waveguide grating

The NLCME's (2.48) for carrier induced nonlinearity can be simplified to a great extent for the small-signal case (i.e., for $P \ll P_{\text{sat}}$) and for input signals that vary much slower than the inverse of the carrier lifetime τ, such that the steady-state is achieved. So in the steady-state, the small-signal approximation of the governing equation can be written from (2.48) and (2.55) as

$$g = g_0 / \left(1+\bar{P}\right), \tag{2.57}$$

$$+\frac{\mathrm{d}A_f}{\mathrm{d}z} = \mathrm{i}\kappa_f^{(\text{NL})} A_f + \mathrm{i}\kappa A_b, \tag{2.58}$$

$$-\frac{\mathrm{d}A_b}{\mathrm{d}z} = \mathrm{i}\kappa_b^{(\text{NL})} A_b + \mathrm{i}\kappa A_f. \tag{2.59}$$

For sufficiently low power we can even write $g \approx g_0$. With this simplification the gain dependent detuning $\kappa_{f,b}^{(\text{NL})}$ becomes a constant quantity independent of the input field intensities. So we can use the same analysis as used in Section 2.2.1 and the equations can be solved exactly. Figure 2-5 shows the typical transmission curve obtained from the solution of the above equations for the parameters as described in 0. For $g_0 = 0$, the solution exactly matches the solution for a passive linear device, which proves the validity of our formulation.

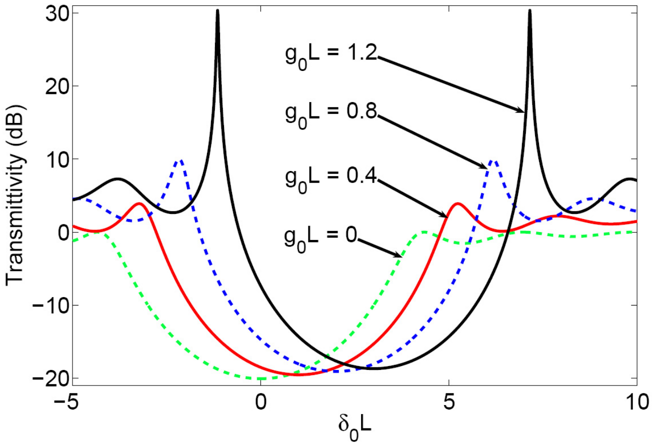

Figure 2-5 : Small-signal transmission curve for an active DFB structure for different values of the length normalized gain g_0L.

2.4 Generalized coupled mode theory and the gain rate equation

The similarity in the governing equation for two different types of nonlinearities as considered in previous sections leads us to formulate a general coupled mode equation, which can be used in describing the features of both type of nonlinearity in the same framework. We introduce a forward $\kappa_f^{(\mathrm{NL})}$ and backward nonlinear coupling coefficient as $\kappa_b^{(\mathrm{NL})}$ and write the generalized coupled mode equations and gain rate equations as [16]:

matrh

$$\begin{aligned} +\frac{\partial A_f}{\partial z}+\frac{1}{v_g}\frac{\partial A_f}{\partial t} &= \mathrm{i}\delta A_f+\mathrm{i}\kappa A_b+\mathrm{i}\kappa_f^{(\mathrm{NL})}A_f, \\ -\frac{\partial A_b}{\partial z}+\frac{1}{v_g}\frac{\partial A_b}{\partial t} &= \mathrm{i}\delta A_b+\mathrm{i}\kappa A_f+\mathrm{i}\kappa_b^{(\mathrm{NL})}A_b, \\ \tau\frac{\mathrm{d}g}{\mathrm{d}t} &= g_0-\left[1+\bar{P}\right]g. \end{aligned} \tag{2.60}$$

We define

$$\kappa_f^{(\mathrm{NL})}=\begin{cases}\Gamma\left(\left|A_f\right|^2+2\left|A_b\right|^2\right)+\mathrm{i}\dfrac{\alpha_{\mathrm{int}}}{2}, \\ -i\dfrac{g}{2}\left(1-i\alpha\right)+\mathrm{i}\dfrac{\alpha_{\mathrm{int}}}{2}\end{cases}\qquad \kappa_b^{(\mathrm{NL})}=\begin{cases}\Gamma\left(\left|A_b\right|^2+2\left|A_f\right|^2\right)+\mathrm{i}\dfrac{\alpha_{\mathrm{int}}}{2}, & \text{(passive)} \\ -\mathrm{i}\dfrac{g}{2}\left(1-i\alpha\right)+\mathrm{i}\dfrac{\alpha_{\mathrm{int}}}{2}. & \text{(active)}\end{cases} \tag{2.61}$$

α_{int} is a linear loss term[8]. The equations above are useful in explaining the general features of nonlinearity in a periodic structure. We will be discussing these similarities in the subsequent chapters. Thus $\kappa_{f,b}^{(\mathrm{NL})}=0,\ g_0=0$ describes a linear periodic structure with no gain or loss. It is important to note that the nonlinear coupling coefficients $\kappa_{f,b}^{(\mathrm{NL})}$ contribute to the so-called self-coupling coefficient. So we can define an effective self-coupling coefficient $\delta_{\mathrm{eff},f}$ for the forward and $\delta_{\mathrm{eff},b}$ for the backward propagating waves as

---

[8] The loss term has been phenomenologically added to account for loss mechanisms such as free-carrier absorption and scattering.

$$\begin{aligned}\delta_{\mathrm{eff},f} &= \delta + \kappa_{fb}^{(\mathrm{NL})},\\ \delta_{\mathrm{eff},b} &= \delta + \kappa_{bf}^{(\mathrm{NL})}.\end{aligned} \tag{2.62}$$

These self-coupling coefficients are dependent on the input power as can be seen from Eq. (2.61). For a given average power in an active device these effective self coupling coefficients are same. With an increase in power (lower gain) the detuning coefficient shifts to a lower value (compare Figure 2-5).

For a Kerr-type nonlinear medium this change is more complicated. The magnitude of the self-coupling is different for the forward and the backward propagating wave, as can be seen from the following equations

$$\begin{aligned}\delta_{\mathrm{eff},f} &= \delta + \Gamma\left(\left|A_f\right|^2 + 2\left|A_b\right|^2\right) + \mathrm{i}\frac{\alpha_{\mathrm{int}}}{2},\\ \delta_{\mathrm{eff},b} &= \delta + \Gamma\left(\left|A_b\right|^2 + 2\left|A_f\right|^2\right) + \mathrm{i}\frac{\alpha_{\mathrm{int}}}{2}.\end{aligned} \tag{2.63}$$

We can write the difference and mean value of the forward and the backward effective self-coupling coefficient using (2.42)

$$\begin{aligned}\Delta_{\mathrm{eff}} &= \delta_{\mathrm{eff},f} - \delta_{\mathrm{eff},b} = -\Gamma\left(\left|A_f\right|^2 - \left|A_b\right|^2\right)\\ &= -\gamma F_T,\end{aligned} \tag{2.64}$$

$$F_T = A_{\mathrm{eff}}\left(\left|A_f\right|^2 - \left|A_b\right|^2\right). \tag{2.65}$$

$$\begin{aligned}\bar{\delta}_{\mathrm{eff}} &= \frac{\delta_{\mathrm{eff},f} + \delta_{\mathrm{eff},b}}{2}\\ &= \delta + \frac{3\Gamma}{2}\left(\left|A_f\right|^2 + \left|A_b\right|^2\right) + \mathrm{i}\frac{\alpha_{\mathrm{int}}}{2}\\ &= \delta + \frac{3\gamma}{2}P_{\mathrm{G}} + \mathrm{i}\frac{\alpha_{\mathrm{int}}}{2}.\end{aligned} \tag{2.66}$$

$$P_{\mathrm{G}} = A_{\mathrm{eff}}\left(\left|A_f\right|^2 + \left|A_b\right|^2\right). \tag{2.67}$$

Here we have introduced the local transmitted flux (F_T) and the local power (P_{G}) inside the grating. For some qualitative analysis we can see that for Kerr type nonlinearity the shift in the bandgap (related to the shift in the effective detuning coefficient) is different for forward and backward propagating waves. For materials with positive nonlinearity, i.e., $n_2^I > 0$ $(\gamma > 0)$, the relation $\delta_{\mathrm{eff},b} > \delta_{\mathrm{eff},f}$ is valid for a positive-valued transmitted flux ($F_T > 0$). The mean value of the effective self-coupling coefficients is found to increase with the power inside the grating (P_{G}).

Nonlinear dispersion curve for Kerr-type gratings: To do some qualitative analysis in the CW limit we drop the time derivatives and we assume

$$A_f = u_f \exp(\mathrm{i}qz), \qquad A_b = u_b \exp(\mathrm{i}qz), \tag{2.68}$$

where u_f and u_b are assumed to be constant along the grating length [5]. Substituting (2.68) in (2.60) and defining $u = u_b/u_f$ we get

$$q = -\frac{\kappa\left(1-u^2\right)}{2u} - \frac{\gamma P_{\mathrm{G}}}{2}\frac{\left(1+u^2\right)}{\left(1+u^2\right)}, \qquad \delta = -\frac{\kappa\left(1+u^2\right)}{2u} - \frac{3\gamma P_{\mathrm{G}}}{2}. \tag{2.69}$$

The above equations describe the nonlinear dispersion curves. In terms of the forward and the backward effective-self-coupling coefficients it can be similarly written as

$$q^2 + q\left(\delta_{eff}^{f} - \delta_{eff}^{b}\right) + \left(\kappa^2 - \delta_{eff}^{f}\delta_{eff}^{b}\right) = 0. \tag{2.70}$$

We can see that for the linear case (Γ = 0) the effective self coupling coefficients are identical and the above set of equations reduces to expression (2.33) in the linear case.

Figure 2-6 shows the different qualitative dispersion curves for different power levels for linear and nonlinear cases. The solid blue curve represents the dispersion diagram for linear case (e.g. see Figure 2-2), the blue dotted curves and the red curves are the nonlinear dispersion curves for low power and high power respectively. It can be seen from the curves that with an increase in power the dispersion curve shifts towards the lower frequency side and above some critical power level $P_c = 2\kappa/\gamma$ [5] a loop is formed in the upper branch of the dispersion curve which gives the onset of the bistability. But it is to be noted that the critical power level calculated from (2.69) is not very accurate, due to the oversimplified approximation used in (2.68), nevertheless this analysis gives a qualitative understanding of the physics of nonlinear Kerr type periodic structures.

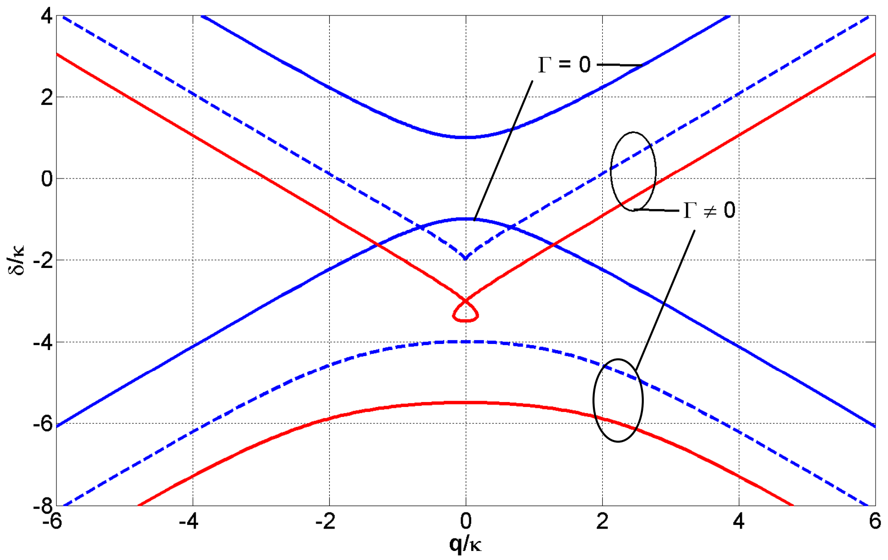

Figure 2-6 : Nonlinear effect on dispersion diagram of Kerr type nonlinear periodic structures for the linear case (Γ = 0) (see solid blue curves), and two nonlinear cases (Γ ≠ 0) (see the dotted blue lines and the solid red lines).

2.5 Summary

In this chapter we have derived the nonlinear coupled mode equations describing nonlinear periodic structures starting from Maxwell's equations. We have used the following assumptions in deriving those equations which are summarized as follows:

- We have assumed a weakly homogeneous material.
- The material dispersion is neglected in comparison to the grating-induced dispersion.
- A weak nonlinearity is assumed so that it can be treated as a perturbation.
- In the active medium the α_H factor is assumed to be constant

As a new result we have introduced a generalised nonlinear coupled mode equation which is useful in describing the active and the passive periodic structure in the same framework. We will compare the effect from active and passive periodic structures in subsequent chapters. We have also introduced the effective self-coupling coefficients which have its usefulness when comparing with the linear model. This also helps in numerical simulation of the active and passive periodic structure using similar numerical techniques. The effective self coupling coefficient can be used in explaining the nonlinear change in the transmission. The different value of forward and backward effective self coupling coefficient for passive nonlinear structure leads to different qualitative behaviour of the bistable range of operations in comparison with the active device.

3 Analysis of uniform periodic structures

In this chapter we discuss the steady-state and time dependent behaviour of uniform periodic structures. We discuss the physical process leading to bistable behaviour in the presence of nonlinearity. Different types of nonlinearity are discussed in the framework of a generalized couple mode theory [Section 2.4].

3.1 Optical bistability: steady state analysis

3.1.1 Introduction

A system is said to be optically bistable if it has two stable output states for the same value of the input over some range of input values. The schematic representation of the input-output characteristic of a bistable system is shown by the blue line in Figure 3-1. The quantity 'X' represent the input value (e.g. input intensity, wavelength, biasing current for an optical system) and 'Y' stands for the output value (e.g. transmitted intensity, reflected intensity, group-delay). It is evident from the figure that for any input value X_0, between X_{up} and X_{down}, the system has two possible stable states Y_{low} and Y_{high}. The unstable state of the system is shown by the blue dotted line in Figure 3-1. If the input quantity X is increased gradually from low to high value it follows the lower branch (region I in Figure 3-1) of the blue curve in Figure 3-1 till it reaches the value of X_{up}. If the input quantity is further increased the output jumps to the upper branch (region II in Figure 3-1) and continue to follows the upper branch. On the other hand if the quantity X is initially at high value ($> X_{\mathrm{up}}$), and we reduce it gradually it follows the upper branch of the blue curve till it reaches the value of X_{down} and then folds back to the lower branch (see the down-arrow in Figure 3-1). So depending upon its history the system

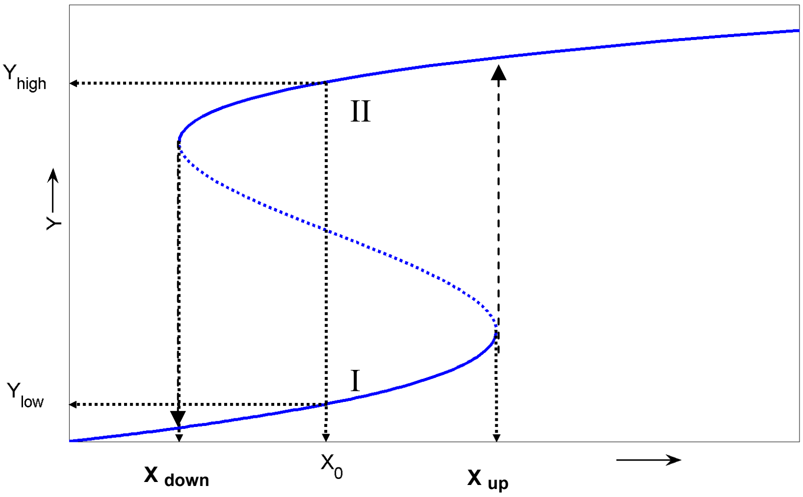

Figure 3-1 : Typical hysteresis curve with the different region of interest

preferentially stays either in the high (Y_{high}) or in the low (Y_{low}) output state if the quantity X lies between X_{up} and X_{down}. The extinction ratio for such a bistable structure can be defined as

$$\text{ER} = \left.\frac{Y_{\text{high}}}{Y_{\text{low}}}\right|_{X_0} . \tag{3.1}$$

We describe this steady-state transfer function as a “hysteresis curve” until otherwise specified. This unique feature of bistability is of utmost importance in designing devices like all-optical flip-flops [16] [18] [26] [48] [49] [56] and logic gates. They have potential application in the area of optical regeneration, decision circuits and in optical packet header processing. Bistability is observed in nonlinear systems with a feedback mechanism [22]. The periodic structures considered in the previous chapters have an inherent feedback mechanism through Bragg reflection. In the following sections we analyze the steady state response of such nonlinear periodic structures. We discuss the physics of different types of optical bistability for different types of nonlinearity (2.60).

3.1.2 Physical process of bistability in Kerr type nonlinear medium

As discussed in Section 2.3.1 the refractive index at each point in the grating is modified by the field intensity I through the nonlinear refractive index coefficient n_2^I,

$$n(z) = n_0 + \Delta n_G(z)\cos\left(\frac{2\pi}{\Lambda}z\right) + n_2^I I. \tag{3.2}$$

The intensity dependence of refractive index leads to the variation of the band edges and for some specific values of the signal detuning parameter (δ_0) the output intensity is bistable with respect to the input intensity.

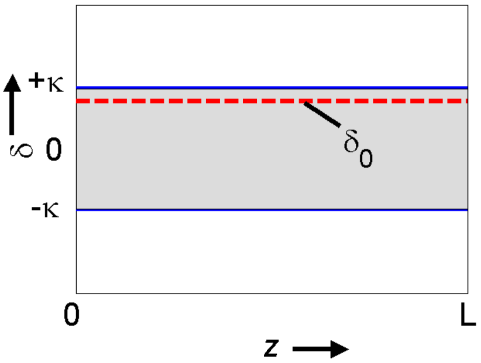

Figure 3-2 : Schematic diagram showing the stopband (shaded grey region) as a function of position z inside the grating of length L. The solid lines (blue) depict the band edges for the grating. The dashed red line depicts the detuning parameter corresponding to the CW signal

We consider an input signal with a frequency lying in the stop-band of the linear grating (i.e. for $|\delta_0| < \kappa$). A schematic transmission curve near the transmission resonance is shown in Figure 3-3 (similar to the transmission curve in Figure 2-3 and Figure 2-4). Here we use a schematic approach to explain the bistable behaviour of the system. In the low intensity limit, the incoming wave intensity does not appreciably alter the refractive index of the medium, and decays exponentially along the propagation direction. In a finite grating structure the exponential tail reaches the back of the grating, leading to nonzero but low transmission. So the amount of energy stored in the grating is quite small. With the increase in input intensity, the nonlinear contribution increases and the transmission resonance is shifted to the lower frequency side (or to lower value of the detuning coefficient, see Figure 3-3). So the penetration depth increases resulting in an increase of the transmission coefficient. Signals at different detuning coefficients experience different transmissivity, and thus have different penetration depth inside the grating. So in the presence of nonlinearity different parts of the transmission curve are influenced differently leading to a considerable change in the slope of the transmission curve near the transmission maximum. This trend continues as the input intensity is further increased until the up-switching threshold is reached, where the transmission resonance frequency nearly equals the signal frequency, and the slope of the curve becomes very steep. As a result, the internal optical intensity is increased even more via resonant field enhancement, taking advantage of the steep slope. This leads to a positive feedback for the internal power which in turn moves the transmission resonance to lower frequencies than the signal frequency. This results in a jump in the transmitted intensity as shown at X_{up} in Figure 3-1.

The reverse process occurs at the down-switching threshold. A gradual reduction of the input intensity shifts the transmission resonance to the higher frequency side (or higher value of the detuning coefficient) and the transmission resonance frequency returns back towards the signal frequency. A subsequent lowering of the incident intensity moves the transmission maxima to higher frequencies than the signal frequency, and hence the internal energy decreases and the system return to the low transmission state. So the bistable switching in a nonlinear periodic structure occurs via a positive feedback involving the intensity dependent refractive index, transmission, and the energy stored in the grating.

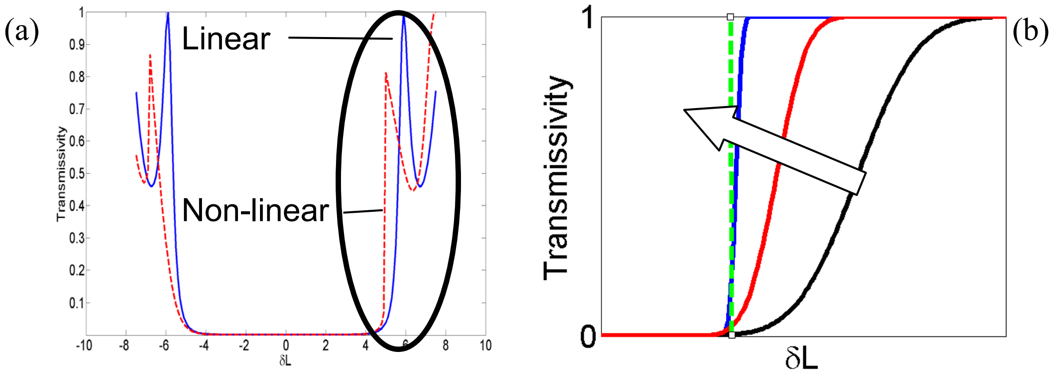

Figure 3-3 : (a) Power dependent bend in the transmission curve as calculated from NLCME (same as in Figure 2-4) (b) Schematic variation of the transmissivity of the grating with different input intensities. The arrow indicates the direction of increasing input intensity from black → red → blue. The dotted green line depicts the detuning coefficient corresponding to the input signal. The slope of the curve also changes significantly with increasing input intensity. For the results from a detailed calculation see Figure 2-4

3.1.2.1 Elliptic function formalism for Kerr-type nonlinearity

We calculate the steady-state intensity distribution along the NL-WBG using the methods as described by Winful et al. [75]. This method exactly solves the steady-state NLCME in terms of elliptic functions and allows us to write a compact expression relating the input and the output intensity. If we consider the equilibrium state, where the intensity distribution inside the grating is stationary, the time dependent part of the NLCME (2.40) can be dropped and we can simplify those equations,

$$\begin{aligned} +\frac{\mathrm{d}A_f}{\mathrm{d}z} &= \mathrm{i}\delta A_f + \mathrm{i}\kappa A_b + \mathrm{i}\Gamma\left(\left|A_f\right|^2 + 2\left|A_b\right|^2\right)A_f, \\ -\frac{\mathrm{d}A_b}{\mathrm{d}z} &= \mathrm{i}\delta A_b + \mathrm{i}\kappa A_f + \mathrm{i}\Gamma\left(\left|A_b\right|^2 + 2\left|A_f\right|^2\right)A_b. \end{aligned} \tag{3.3}$$

We separate the amplitude and the phase part of the forward and the backward field envelopes by $A_f = A_+ \exp(\mathrm{i}\phi_+)$ and $A_b = A_- \exp(\mathrm{i}\phi_-)$. Substituting these expressions in Eq. (3.3) and equating the real and the imaginary part the following set of equations is obtained,

$$+\frac{\mathrm{d}A_+}{\mathrm{d}z} = +\kappa A_- \sin(\psi), \tag{3.4}$$

$$-\frac{\mathrm{d}A_-}{\mathrm{d}z} = -\kappa A_+ \sin(\psi), \tag{3.5}$$

$$+A_+\frac{\mathrm{d}\phi_+}{\mathrm{d}z} = +\kappa A_- \cos(\psi) + \Gamma\left[A_+{}^2 + 2A_-{}^2\right]A_+, \tag{3.6}$$

$$-A_-\frac{\mathrm{d}\phi_-}{\mathrm{d}z} = +\kappa A_+ \cos(\psi) + \Gamma\left[A_-{}^2 + 2A_+\right]A_-. \tag{3.7}$$

Here the quantity ψ is defined as $\psi = 2\delta z + \phi_+ - \phi_-$. From the above set of equations we can find the following conserved quantities,

$$F_T = A_{\mathrm{eff}}\left[A_+^2(z) - A_-^2(z)\right], \tag{3.8}$$

$$G/A_{\mathrm{eff}} = 2\kappa A_+(z)A_-(z)\cos\psi(z) + \left[2\delta + 3\Gamma A_-{}^2(z)\right]A_+{}^2(z). \tag{3.9}$$

The quantity F_T is the transmitted flux as in Section 2.4 on page 19. The first conserved quantity can be obtained in a rather simple way combining equation (3.4) and (3.5). The conservation of the transmitted flux F_T in a lossless medium in the steady-state can also be predicted from Poynting's theorem [30]. The second conserved quantity can not be understood intuitively. The two conserved quantities together with equation (3.4)–(3.7) thus describe the nonlinear system. We further assume a non-reflective boundary condition at the interface at $z = L$, i.e.,

$$A_-(L) = 0. \tag{3.10}$$

With this assumption the transmitted flux can be written as

$$\begin{aligned} F_T &= A_{\mathrm{eff}}\left[A_+^2(L)-A_-^2(L)\right] \\ &= A_{\mathrm{eff}}A_+^2(L). \end{aligned} \tag{3.11}$$

The above expression leads to a simplification of the conserved quantity *G*,

$$G = 2\delta F_T. \tag{3.12}$$

If we replace ψ using Eq. (3.4) then we can write,

$$\begin{aligned} \kappa^2 A_+^2\left[1-\left(\frac{1}{\kappa A_-}\frac{\mathrm{d}A_+}{\mathrm{d}z}\right)^2\right] &= A_-^2\left[\delta+\frac{3}{2}\Gamma A_+^2\right]^2 \\ \left(\frac{L}{2}2A_+\frac{\mathrm{d}A_+}{\mathrm{d}z}\right)^2 &= A_-^2\left[(\kappa L)^2 A_+^2 - A_-^2\left(\delta L+\frac{3}{2}\Gamma L A_+^2\right)^2\right] \\ \left(\frac{L}{2}\frac{\mathrm{d}A_+^2}{\mathrm{d}z}\right)^2 &= \left[(\kappa L)^2 A_+^2 - \left(A_+^2-A_T^2\right)\left(\delta L+\frac{3}{2}\Gamma L A_+^2\right)^2\right]A_-^2. \end{aligned} \tag{3.13}$$

We introduce a reference power by $A_c^2 = 4A_{\mathrm{eff}}\lambda n_0/(3\pi n_2 L) = A_{\mathrm{eff}}8n_0^2/(3\Gamma L)$, and define the normalized flux for the forward wave as $J(z)=\left[A_+(z)/A_c\right]^2$, the normalized transmitted flux as $\tilde{F}_T = \left[F_T/A_c^2\right]$. So Eq. (3.13) can be written in a normalized form as,

$$\begin{aligned} \left(\frac{L}{2}\frac{\mathrm{d}J}{\mathrm{d}z}\right)^2 &= \left(J-\tilde{F}_T\right)\left[(\kappa L)^2 J-\left(J-\tilde{F}_T\right)(\delta L+2J)^2\right] \\ &= P(J). \end{aligned} \tag{3.14}$$

The above differential equation is the reduced form of the NLCME in steady-state. The integration of Eq. (3.14) is a standard elliptic problem whose solution depends on the parameters $\kappa L, \delta L, \tilde{F}_T$. The solution[9] can be written in terms of the roots J_i for $i = 1, 2, 3, 4$ of the polynomial *P*(*J*) on the right hand side of equation (3.14) as,

$$J(z) = J_3 - \frac{J_3-J_2}{1-\dfrac{J_1-J_2}{J_1-J_3}\mathrm{sn}^2(u,s)}. \tag{3.15}$$

with the abbreviations

$$\begin{aligned} u &= 2\left[(J_1-J_3)(J_0-J_2)\right]^{1/2}, \\ s &= 2\left[(J_1-J_2)(J_3-J_4)\right]^{1/2}/u, \end{aligned} \tag{3.16}$$

In general we can write,

$$J(z) = \mathrm{f}\left(\kappa L, \delta L, \Gamma L, \tilde{F}_T\right). \tag{3.17}$$

---

[9] For more general description of elliptic function, see Byrd and Friedman[8]

The above function relates the input intensity in terms of the output intensity and thus gives the transfer function of a nonlinear periodic structure. In strict mathematical sense it is possible to invert the above equation to write the output as a function of input, but we avoid such a complicated method and rather calculate the input intensity for a given output intensity. This does not represent the actual physical situation, but is useful in calculating the hysteresis curves and analyzing the results.

We consider a structure with $\kappa L = 5$ as the normalized coupling coefficient. In Figure 3-4 (a), we plot the relation given by Eq. (3.15), relating the input and output intensity, for a normalized detuning parameter $\delta_0 L = 4.75$.

We can do a similar analysis and calculate the reflectivity of the structure. The reflectivity of the structure also shows bistable behaviour as expected but the shape of the curve is different from the previous case. We plot the reflectivity of the same structure in Figure 3-4(b), for the same normalized detuning parameter $\delta_0 L = 4.75$ as before.

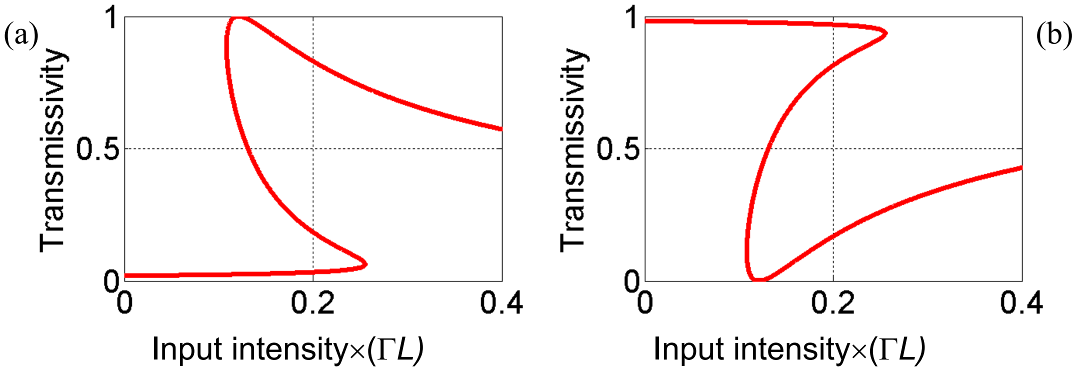

Figure 3-4 : S-curves for $\kappa L = 5$, $\delta_0 L = 4.75$, $\Gamma L = 0.1$ cm^2/GW showing the dependence of (a) transmissivity, and (b) reflectivity on input intensity.

3.1.3 Active device

In this section we discuss the steady state analysis for a uniform periodic structure with a carrier-induced nonlinearity. For this class of nonlinearity we also observe optical bistability similar to that observed for Kerr-type nonlinearity. As discussed before carrier induced nonlinearity is $\sim 10^7$ higher than that in a Kerr-type medium. So we expect a much lower switching power for bistability than for a Kerr-type medium.

3.1.3.1 Transfer matrix method (TMM)

For steady state analysis we drop the time dependent terms both in the coupled mode equation and the gain rate equations and rewrite the GNLCME as in Eq. (2.60). We divide the grating length into M subsections. To obtain a unique solution, we reverse the direction of calculation. The fields at the input facet is calculated by inverted transfer matrices starting from the output facet [47],

$$\begin{bmatrix} A_f(0) \\ A_b(0) \end{bmatrix} = \underline{T}^{-1}(g_1)\underline{T}^{-1}(g_2)\cdots\underline{T}^{-1}(g_M)\begin{bmatrix} A_f(L) \\ A_b(L) \end{bmatrix}. \tag{3.18}$$

The quantity g_m gives the gain in the m^{th} section. The coefficients of the matrix $\underline{T}$ can be found in see Appendix B.1. Since these coefficients depend on the input fields we use an iterative approach (see Appendix B.1) to find the stable solutions. To summarize the methods we use the following flow-diagram Figure 3-5 to calculate the steady state response.

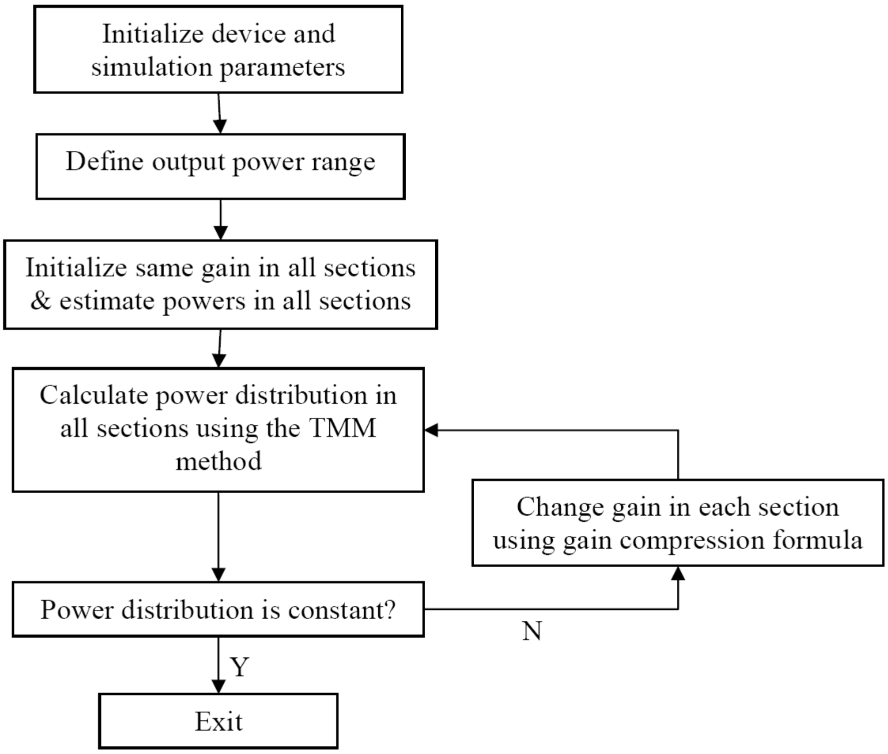
Initialize device and simulation parameters
Define output power range
Initialize same gain in all sections & estimate powers in all sections
Calculate power distribution in all sections using the TMM method
Change gain in each section using gain compression formula
Power distribution is constant?
N
Y
Exit

Figure 3-5 : Flowchart for calculation of the field distribution using TMM for active device.

3.2 Optical bistability: Time dependent analysis

The steady state solution of the GNLCME in the previous sections give a good understanding of the bistable device operations, but this analysis relies on CW input signals. Here we explore the temporal dynamics and pulse propagation through the nonlinear waveguide Bragg grating (WBG). Time dependent simulation gives a rich variety of phenomena which cannot be observed from the steady state solutions.

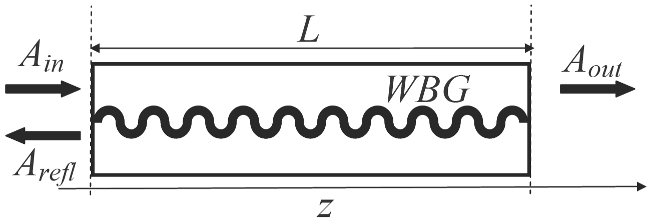

Figure 3-6 : Schematic waveguide Bragg grating.

3.2.1 CW signal propagation in a Kerr-type medium

We numerically study the time dependent solution of the nonlinear coupled mode equations using an implicit finite-difference scheme (see Appendix B.3). In the schematic waveguide Bragg grating as in Figure 3-6, a continuous wave is incident from the left end of the WBG, i.e., at $z = 0$. The boundary conditions are

$$\begin{aligned} A_f(0,t) &= A_0, \\ A_b(L,0) &= 0. \end{aligned} \tag{3.19}$$

In our calculations the input signal is not applied instantly to avoid numerically generated shock [61]. Rather, we gradually increase the transition from $A_0(0) = 0$ to $A_0(2T_r) = A_0$ using a smooth transition function given by a 9th order polynomial. All time units are expressed in terms of the transit time $T_r = L/v_g$ of the signal through the device, and all the intensities are expressed in units of $(\Gamma L)^{-1}$. In all the results that follow, we use a uniform grating with $\kappa L = 5$, $\Gamma L = 0.1$ cm^2/GW as described in [38][67][69] for a silica based fiber. We have used the detuning coefficient $\delta_0 L = 4.75$ unless otherwise specified. The detuning coefficient is chosen such that the device is in a low transmitting state (−18 dB) in the linear case (see red dashed line in Figure 3-7). The grating's transmission resonance at the detuning coefficient of $\delta L = 5.9$ is marked by a dashed green line. These results can also be used to describe devices with different nonlinearities and other material parameters with suitable scaling relations (see Section 2.3.1.1 on page 15). The hysteresis curve calculated from the steady-state solution for the same set of parameters is given shown before in Figure 3-4.

The refractive index at each point in the grating is modified by the field intensity through the nonlinear refractive index, which leads to a variation of the band edges. We will refer to the modified (detuned) band edges as the local band edges in the following. Different regions of the bistable curve can be understood by considering the dynamic behaviour of these local band edges within the grating.

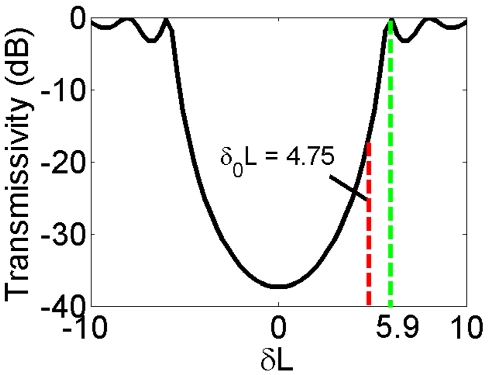

Figure 3-7 : Linear transmission curve showing the operating frequency (normalized detuning coefficient) and the transmission resonance.

In Figure 3-8(a) and (b) we plot the time dependent changes of the transmissivity and reflectivity of the WBG for different intensities of the input CW signal. As discussed in Section 3.1.2 in the low intensity limit, an incoming signal does not appreciably alter the position of the local band edges, and decays exponentially (see red curve in Figure 3-9(a)) if its frequency lies within the stopband ($|\delta| < \kappa$). In a finite grating structure the exponential tail reaches the back of the grating, leading to non-zero but low transmission. In this region the influence of the material nonlinearity on the transmission is very small. To quantify this we start at an arbitrarily chosen low normalized intensity of $A_0^2\,\Gamma L = 0.1$. From our numerical simulation we found that for $A_0^2\,\Gamma L = 0.1$ the output settles down at a state of low transmission after an initial jump (see red curve in Figure 3-8). The transient behaviour for the linear case is plotted by the dashed black line in Figure 3-8. At low intensity levels the linear and the nonlinear curves are almost indistinguishable.

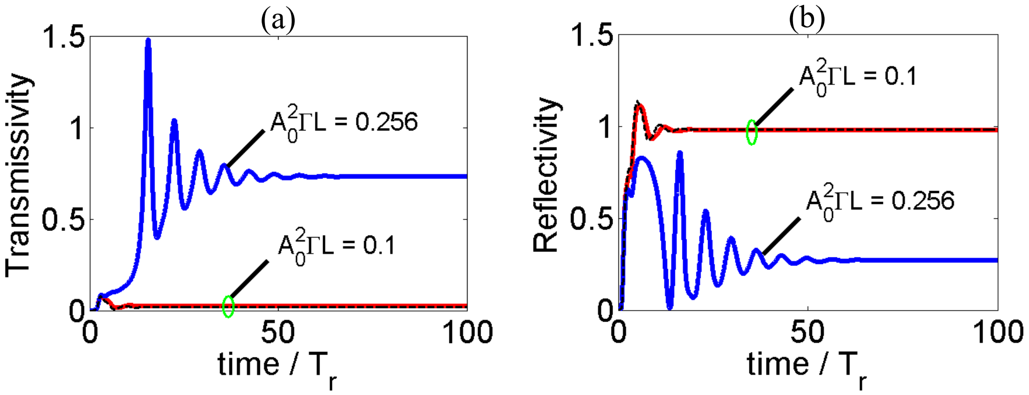

Figure 3-8 : Time dependent (a) transmissivity and (b) reflectivity curve for a normalized detuning coefficient of $\delta_0 L = 4.75$, $\Gamma L = 0.1$ cm^2/GW. In both the curves the dashed black line represents the results for the linear case; the red curves represents the results of the nonlinear case with normalized input intensity of $A_0^2\Gamma L = 0.1$; the blue curve represents the results of the nonlinear case with normalized input intensity of $A_0^2\Gamma L = 0.256$. The time is expressed in units of the transit time T_r of the signal through the device.

With the increase in input intensity, the local band edges are shifted to a lower frequency and so the penetration depth of the signal into the stopband increases, leading to an increase in the transmission coefficient.

For an input intensity above the up-switching threshold (e.g. $A_0^2\,\Gamma L = 0.256$), the nonlinear contribution dominates and a peak in intensity develops near the front of the grating, due to a large local shift of the stopband. In the time domain, this peak in intensity moves towards the centre of the structure and shows a relaxation-oscillatory behaviour before finally stabilizing around the centre of the grating, as seen in Figure 3-9(b). The transmissivity and reflectivity also shows similar relaxation-oscillatory behaviour before stabilizing at a constant value (see the blue curve Figure 3-8). The amount of energy stored in the grating in this case is significantly larger than that stored in the low-transmission case. The steady-state intensity distribution for such case is shown in Figure 3-9 (a).

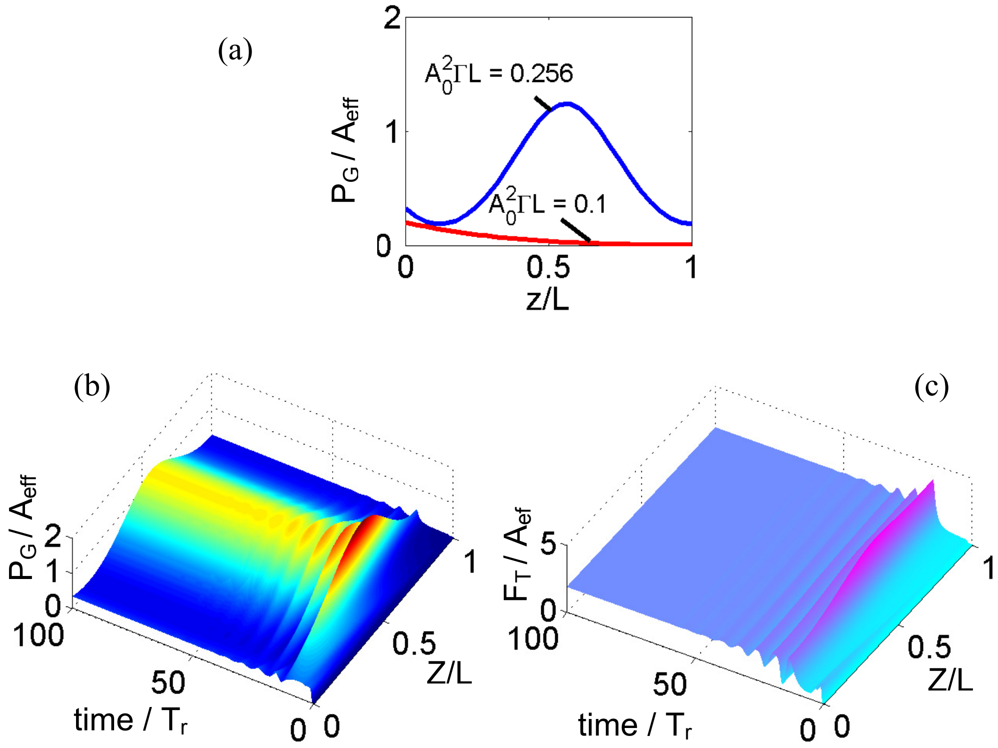

Figure 3-9 : (a) Steady-state power distribution inside the grating; the red and the blue curves are for a normalized detuning coefficient of $\delta_0 L = 4.75$, $\Gamma L = 0.1$ cm^2/GW with normalized input intensity of $A_0^2\Gamma L = 0.1$, and $A_0^2\Gamma L = 0.256$ respectively. (b) Temporal and spatial variation of intensity inside grating for a normalized input intensity $A_0^2\Gamma L = 0.256$. (c) Temporal and spatial variation of flux density inside the grating for a normalized input intensity $A_0^2\Gamma L = 0.256$. The time is expressed in units of the transit time T_r of the signal through the device.

It can be shown from the NLCME (2.40) that the following relation is valid

$$\frac{\partial F_T}{\partial z} = -\frac{\partial\left(P_{\mathrm{G}}/v_g\right)}{\partial t}. \tag{3.20}$$

The quantity F_T is the transmitted flux, and the quantity P_{G} is the local power inside the grating as defined before as in Section 2.4 on page 19. The above equation can be interpreted as a continuity equation. The term on the left hand side represents the transmitted flux, while the expression on the right hand side represents the rate of decrease of energy inside the grating. As the system evolves in time there is a dynamic exchange of energy between the material and the field leading to a relaxation oscillatory behaviour of the output. In the steady state the time derivative on the right hand side becomes zero leading to constant flux inside the grating. In our numerical simulation we consider the system to be in a state of dynamic equilibrium when the transmitted flux becomes constant. The temporal dynamics of the transmitted flux for normalized input intensity of $A_0^2\,\Gamma L = 0.256$ is shown in Figure 3-9 (c). We observe a relaxation-oscillatory behaviour which finally settles down to a constant flux distribution inside the grating.

As the input intensity is increased (e.g. $A_0^2\,\Gamma L = 0.484$), the local upper-band edge continues to shift to lower frequencies, and even more power is coupled to the grating. The increased power in the grating is then released in terms of a pulsating output as can be seen from Figure 3-10 (a). A strong relaxation oscillation is observed in this case. For as increased input power of $A_0^2\,\Gamma L = 0.676$ the output becomes nearly periodic and we can observe strong pulsating behaviour due to modulation instability. The pulsation frequency depends upon the input intensity and the detuning coefficient $\delta_0 L$ associated with the input CW signal frequency (see the blue and the red curve in Figure 3-10(a) and (b)). The energy distribution inside the grating varies faster than in the low power cases (compare Figure 3-9(b) and Figure 3-10 (c).

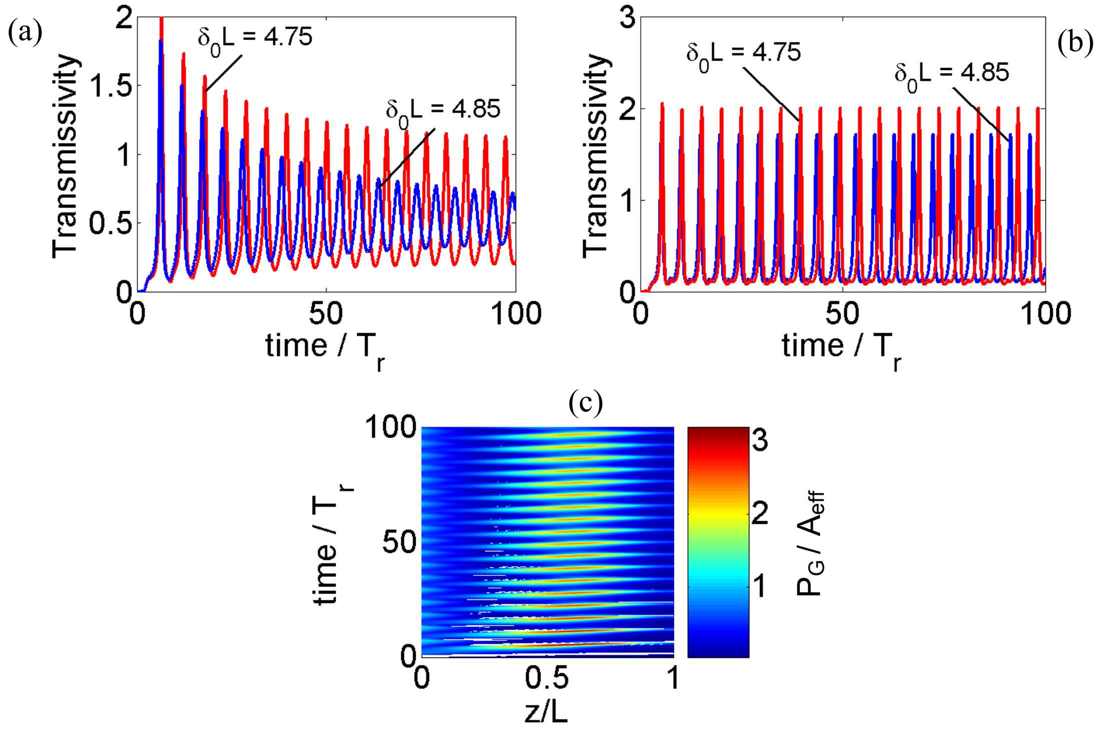

Figure 3-10 : Time dependent transmissivity showing pulsating behaviour for a normalized input power of (a) $A_0^2\Gamma L = 0.484$; (b) $A_0^2\Gamma L = 0.676$. In both cases the red and blue curves are for a normalized detuning coefficient of $\delta_0 L = 4.75$ and $\delta_0 L = 4.85$ respectively. (c) Temporal and spatial variation of intensity inside grating for a normalized detuning coefficient of $\delta_0 L = 4.75$. The time is expressed in units of the transit time T_r of the signal through the device.

3.2.2 Pulse propagation in a Kerr-type grating

We now extend our study from CW signals to pulses of finite duration. We choose the same parameters of the grating as before with $\kappa L = 5$, $\Gamma L = 0.1$ cm^2/GW, and a normalized detuning coefficient $\delta_0 L = 4.75$, corresponding to the central frequency of the pulse. Due to finite bandwidth of the signal pulse the different frequency components of the signal experience different transmission slopes as can be seen from Figure 3-7. We plot the temporal dynamics of different Gaussian pulses with normalized peak intensity $A_0^2 = 0.4 / (\Gamma L)$, and with different FWHM, in Figure 3-11. The black curves represent the intensity of the input Gaussian pulse while the blue curve represents the transmitted (reflected) pulses in the left (middle) column. All intensities are normalized to $A_0^2\,\Gamma L = 0.4$. The corresponding transverse variation of the intensity distribution inside the grating for different values of pulse FWHM are depicted the right column of Figure 3-11.

For a very narrow temporal pulse the spectrum is large in comparison to the grating stopband, and thus for such a pulse the grating acts as a nonlinear filter. For a pulse with FWHM of T_r the input pulse is mostly reflected and the pulse shape is distorted due to nonlinear filtering. The peak of the transmitted pulse is delayed as can be seen from Figure 3-11(a-I). As the temporal pulse width is increased to $20\times T_r$ ($33\times T_r$) the spectrum becomes narrower and the effect of the bandgap becomes increasingly important. With the increase in temporal pulse width thus the signal resembles more and more the behaviour of a CW signal (compare with Figure 3-8 and Figure 3-11 (II) & (III)) and it shows strong relaxation oscillation in transmission (see Figure 3-11(a-II) – (a-III)) and reflection (see Figure 3-11(a-II) – (a-III)). A sharp switching threshold is also observed from Figure 3-11 (b-II) – (b-III). The corresponding dynamics of the intensity distribution inside the grating is depicted in Figure 3-11 (c-II) – (c-IIII).

We now inject a very long temporal pulse (FWHM of $10^3\times T_r$), which essentially behaves as a quasi-CW signal with respect to the grating's transmission spectrum. The corresponding transmitted and the reflected signal are plotted in Figure 3-11 (a-IV) and (b-IV), respectively. We observe that above a certain normalized input power of $A_0^2\,\Gamma L = 0.256$ the device jumps to a high transmitting state (see the green dashed line in Figure 3-11(a-IV) and (b-IV)). This is comparable to the up-switching threshold obtained from the CW calculation (see blue curve in Figure 3-8(a)). The device stays in the high transmitting state even after the power is reduced below $A_0^2\,\Gamma L = 0.256$. The device finally switches to the low transmitting state around $A_0^2\,\Gamma L = 0.1$, which corresponds to the down-switching threshold (see the red dot line in Figure 3-11 (a-IV) and (b-IV)). This shows that the system has a memory and the term hysteresis used previously is justified here. We see that in the high transmitting state certain amount of energy is stored inside the grating, and the power distribution resembles the power distribution inside a linear grating at transmission resonance. From the time dependent calculation we can extract the information about the hysteresis curve as shown in Figure 3-12. A transmissivity of one is obtained near the down-switching threshold.

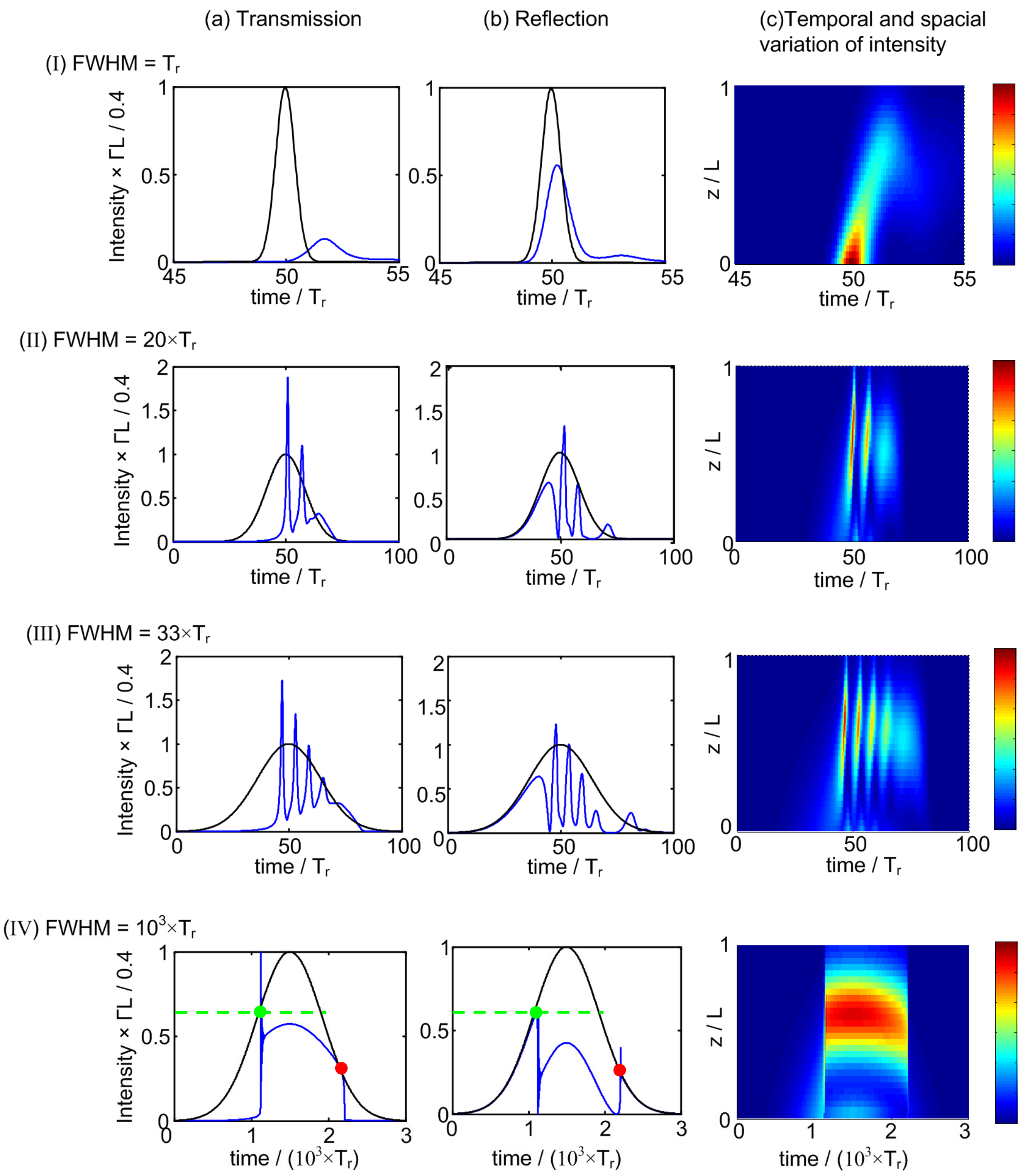

Figure 3-11 : Propagation of Gaussian input pulse in a nonlinear waveguide Bragg grating with $\kappa L = 5$, $\Gamma L = 0.1$ cm^2/GW for a normalized detuning coefficient $\delta_0 L = 4.75$ corresponding to the carrier frequency of the pulse. The black lines show the input Gaussian signal. The blue lines in the left and the middle column show the transmitted and reflected intensities, respectively. The column on the right shows the corresponding temporal and spatial intensity variation inside the grating. Different rows represent different pulse FWHM (I) FWHM = T_r; (II) FWHM = 20×T_r; (III) FWHM = 33×T_r.; (IV) FWHM = 103×T_r. In (I) the pulse is spectrally much wider with respect to the grating's stopband; hence the grating acts as a nonlinear filter. As the spectra of the input signal become narrower from top to bottom the signal more and more resembles a CW like behaviour; moreover the average power of the pulse increases from top to bottom. Increase in the average power induces a large nonlinear shift of the bandgap of the grating and hence the input field penetrates deeper into the structure. The horizontal green dashed line in (IV) represents the up-switching threshold 0.256/(ΓL) of the device. The green (red) dot represents the up (down)-switching threshold. The time is expressed in units of the signal's transit time T_r of the signal through the device.

Moreover by increasing the pulse width the average power of the pulse is also increased. Increasing the average power of the pulse in turn induces a large change in the bandgap due to nonlinear effects and hence the field penetrates deeper inside the grating structure.

3.2.3 Bistability and comparison with quasi-steady state calculation

To test the accuracy of our time dependent model we made a comparative study with the accurate steady-state calculation using elliptic functions. In our calculations a long Gaussian pulse of FWHM of $10^3\times T_r$ (same as in Figure 3-11(IV)) is launched. For such a long pulse the signal behaves essentially as a CW signal. From the transmission signal it is possible to calculate the bistable curve of such a device for that detuning coefficient. The result of this calculation is depicted by the black curve in Figure 3-11. Earlier we have calculated the bistable curve for the same device for the same operating condition from the steady-state analytic calculation (see Figure 3-4(a)). The bistable curve calculated from the steady-state analytic calculation is again plotted (see the green dashed line) in Figure 3-11. The bistable curves calculated from two different method show excellent agreement as can be seen from Figure 3-11. The discrepancy near the up-switching threshold occurs due to the strong relaxation oscillatory behaviour observed when the device changes from the low to the high transmitting state. If we use a pulse with longer duration, this deviation reduces. This agreement validates our numerical simulation of NLCME.

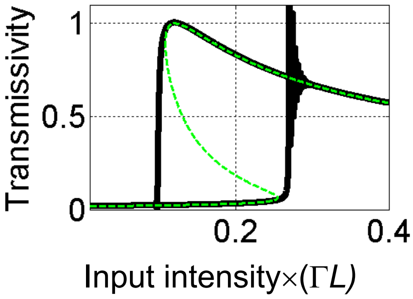

Figure 3-12 : Input-output bistable curve with $\kappa L = 5$, $\delta_0 L = 4.75$, $\Gamma L = 0.1$ cm^2/GW. The green dashed line shows results from the calculation in steady-state while the black solid line shows the results from the time dependent calculation, which shows a transient at the up-switching threshold.

3.2.4 Flip-flop operation for a passive device

The bistability of the output power with respect to the input power of a nonlinear waveguide Bragg grating can be utilised for an all-optical flip-flop (AOFF). Figure 3-13 shows a schematic operation of such an all-optical flip-flop. We consider a CW holding beam with certain input power near the centre of the bistable region (see the solid line in Figure 3-13). At this operating point the device has two possible output states defined by P_{on} and P_{off}. By modulating the holding signal we can switch the state of the device from low to high state and vice versa. Instead of modulating the input CW signal directly it is also possible to perform an

AOFF operation by injecting a positive[10] (or negative) SET (or RESET) control pulse with same central frequency as of the CW signal.

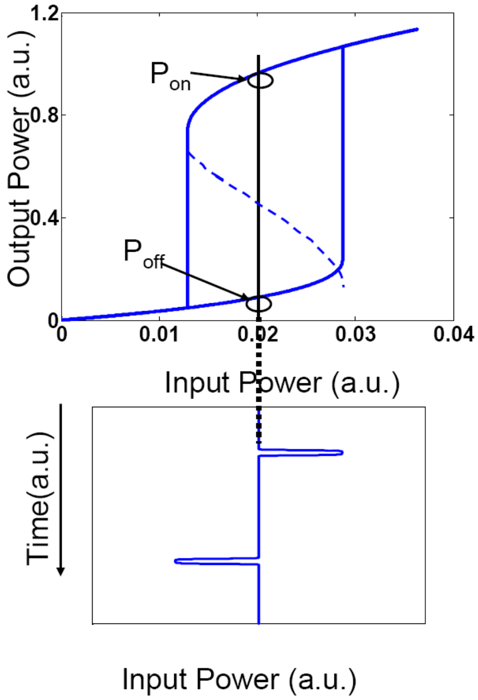

Figure 3-13 : Schematic flip-flop operation by modulating input signal.

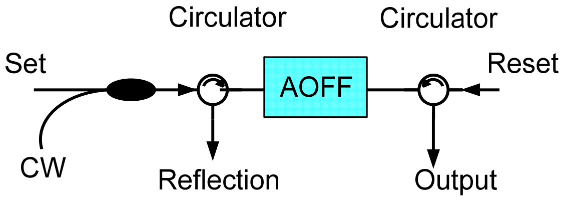

Figure 3-14 : Schematic flip-flop operation with co-propagating SET and counter propagating RESET signal.

Here we propose a new scheme for AOFF operation where the SET and the RESET signals are injected from the front (i.e., at $z = 0$) and back (i.e., at $z = L$) of the grating. Thus in this scheme the holding beam and the SET signals are co-propagating inside the device, while the RESET signal is counter-propagating with the holding beam (see Figure 3-14). In this scheme the so called negative RESET pulse is not needed.

We consider a case in which a CW holding beam with normalized intensity $A_0^2 \Gamma L = 0.196$ and detuning coefficient $\delta_0 L = 4.75$ is injected from the left of the AOFF device. Now we inject a sequence of input pulses (see Figure 3-16(a)) from the left side, co-propagating with the holding beam. From the right side we inject a sequence of input pulses (see Figure 3-16 (b)), counter-propagating with the CW holding beam. The co-propagating signal applied from the left side is used for the 'SET' operation, i.e., to change the transmission of the device from low to high. The counter-propagating signal applied at the right side is used for the 'RESET' operation, i.e., to change the transmission of the device from high to low. We consider the SET and the RESET pulse as a Gaussian pulse of peak intensity $A_{\max}{}^2\,\Gamma L = 0.36$ and FWHM

---

[10] The positive and negative are referred relative to the CW input power.

To understand the working principle of this scheme we look the field distribution inside the grating in the high transmitting state (similar to Figure 3-9) in Figure 3-15.(a) The green arrow indicate local minimum near the front end of the grating (i.e., at $z = 0$). If we inject a RESET pulse from the forward direction it in turn moves this minimum towards the center of the grating. We now consider a counter-propagating RESET signal which is injected from the back of the grating. With this injection the local minima moves towards the front of the grating and if the input power is sufficient enough it pushes the minima out of the grating leading to a transition to the low transmitting state. We depict the schematic of the temporal and spatial distribution of intensity inside the grating in Figure 3-15(b) the horizontal arrow indicates the temporal location of counter-propagating RESET pulse. We see this counter-propagating pulse sweeps away the energy stored in the grating towards the front end. This type of RESET operation is only possible with a counter-propagating signal.

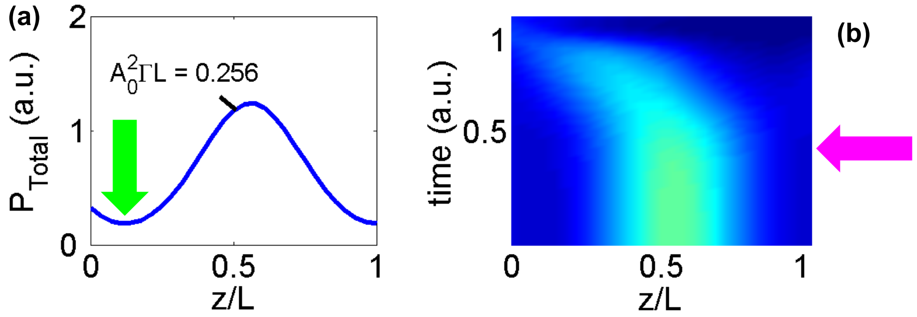

Figure 3-15 : (a) schematic intensity distribution inside the grating in the high transmitting state. The green arrow indicates the location of local minimum. (b) The temporal and spatial dynamics of the intensity distribution inside the grating during the RESET operation the magenta arrow indicates the time at which the RESET signal enters the device

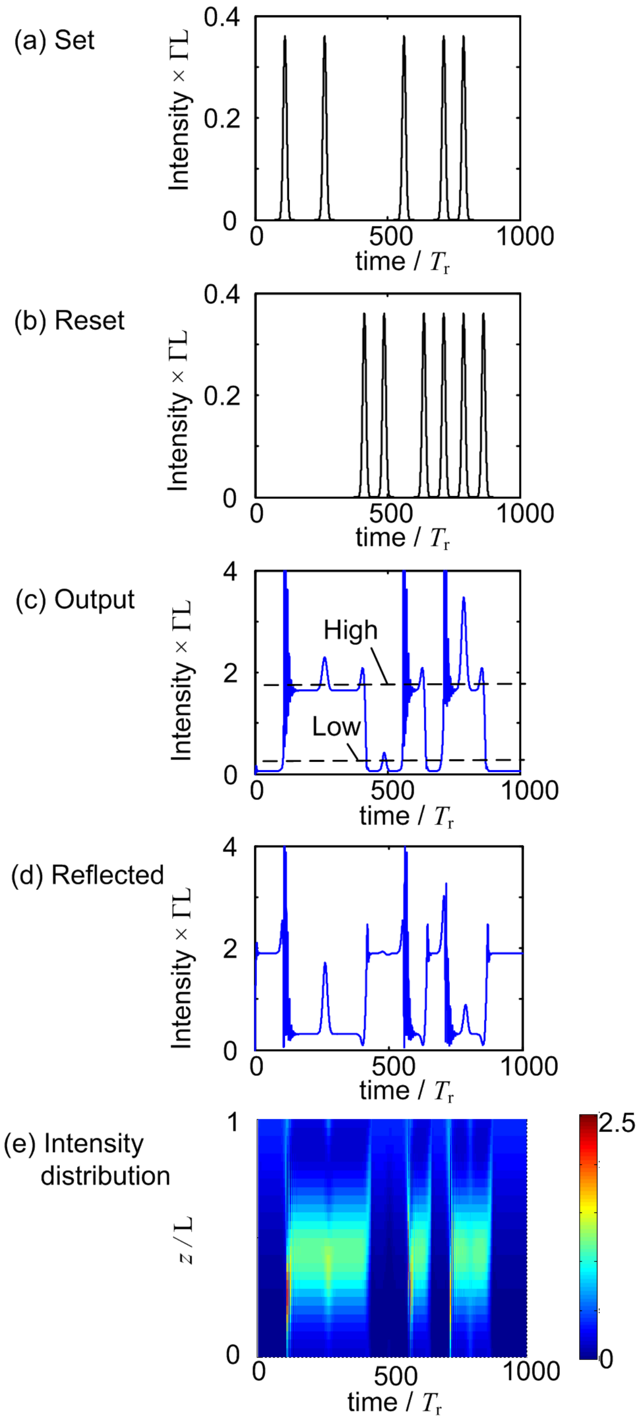

Figure 3-16 : AOFF operation with co-propagating SET and counter propagating RESET signals. SET and RESET signals are Gaussian pulses of peak intensity $A\max^2\ \Gamma L = 0.36$, FWHM of 15×Tr and pulse repetition rate of 75×Tr. All signals (SET, RESET, and CW) are at the same frequency (the corresponding detuning coefficient is $\delta_0 L = 4.75$). (a) SET signal. (b) RESET signal. (c) Transmitted signal. (d) Reflected signal. The transmission (or reflection) state of the device changes from low to high (or from high to low) in presence of SET signal. The reverse happens in presence of a RESET signal. (e) Temporal and spatial variation of intensity distribution inside grating. In presence of the SET signal the device moves from the low to the high transmission state, having more energy stored in the grating. In presence of the RESET signal the device moves from the high to the low transmission state, having less energy stored in the grating. The time is expressed in units of the transit time T_r of the signal through the device.

of 15×T_r and pulse repetition rate of 75×T_r. All signals (SET, RESET, and CW) are at the same frequency (the corresponding detuning coefficient is $\delta_0 L = 4.75$). Figure 3-16 (c) shows the transmission, while Figure 3-16 (d) shows the reflection of the AOFF. It can be seen that the device stays in its high (low) transmission state even after the SET (RESET) pulse duration. The transition from the low to the high transmission state has 5.5×T_r switching time and around 25×T_r of ringing time. The transition from the high to the low transmission state has 6.6×T_r switching time with almost zero ringing time. Figure 3-16 (e) shows the corresponding dynamics of the power distribution inside the grating. In presence of the SET signal the device moves from the low to the high transmission state, having more energy stored in the grating. In presence of the RESET signal the device moves from the high to the low transmission state, having less energy stored in the grating.

To get some actual device parameters and to estimate the actual power and time scale for such an operation we consider an InP based device with $\kappa L = 5$, $L = 600$ µm. The power for the CW signal is calculated to be 85 mW and the peak power of the SET/RESET signals are 15 mW, and the transition time for up-switching (down-switching) is 36 ps (42 ps). The power levels are still high for realistic device applications. The high switching power can however be reduced using highly nonlinear materials or by proper designing the geometry of the device. In chapter 5 we will discuss a possible method to reduce the threshold switching power.

3.2.5 Flip-flop operation for an active device

In this section we discuss the flip-flop operation in a semiconductor optical amplifier based distributed feedback (SOA-DFB) structure. We use the so-called transfer matrix method (TMM) (see Appendix B.1) as discussed by [47]. This method relies on an iterative solution of GNLCME, Eq. (2.60), using transfer matrices.

As introduced before flip-flop operation of a bistable device can be done by modulating a holding beam (signal) power (see Figure 3-13). We consider AOFF operation in SOA-DFB using signals at same wavelength for the following device parameters: $L = 300$ µm, $\kappa L = 3$, $g_0 L = 1.2$. All the signals (CW holding beam and the SET/RESET signal are at identical normalized detuning coefficient of $\delta_0 L = 6.76$. The CW holding beam power is 20 µW. Super Gaussian (of order two) SET/RESET signal pulses with FWHM of 2 ns are used. The corresponding input and output powers are plotted in Figure 3-16 (a) and (b) respectively. Comparing with the passive structure (as in the previous section) we see that by using an active medium the switching power is substantially reduced. However the switching operation is rather slow and is limited by the carrier lifetime of the material.

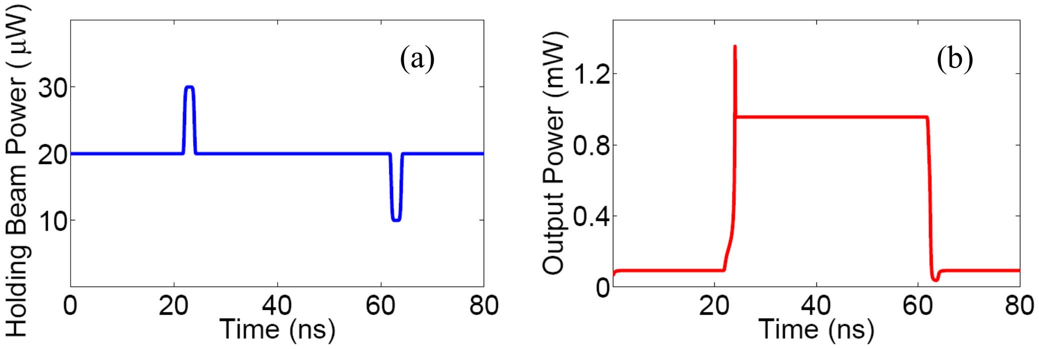

Figure 3-17 : AOFF operation in SOA-DFB using signals at same wavelength for the f device parameters $L = 300$ µm, $\kappa L = 3$, $g_0L = 1.2$. All the signals (CW holding beam and the SET/RESET signal) have an identical normalized detuning coefficient of $\delta_0L = 6.76$. The CW holding beam power is 20 µW. Super Gaussian of order two SET/RESET signal pulses with FWHM of 2 ns are used. (a) The deviation from the mean holding beam power is 10 µW. (b) Temporal dynamics of the output power.

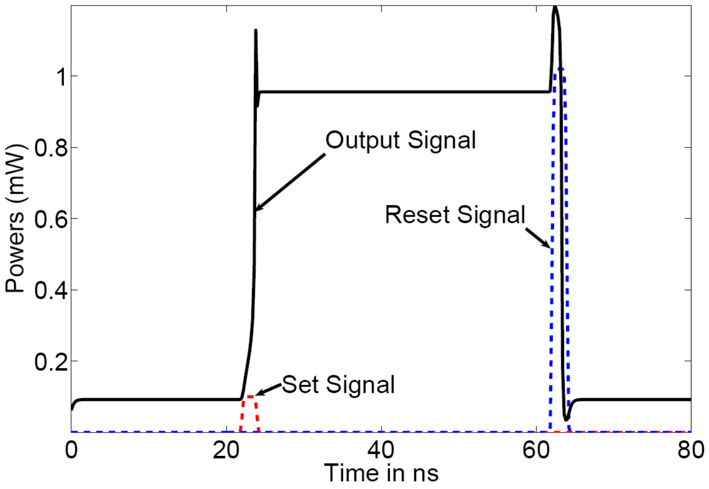

Figure 3-18 : AOFF operation in SOA-DFB using signals at different wavelength for $L = 300$ µm, $\kappa L = 3$, $g_0L = 1.2$. The CW holding beam power is 0.1 mW. Super Gaussian of order two SET (RESET) signal pulses with FWHM of 2 ns are used with peak power of 0.1 mw (1 mW). The detuning coefficient $\delta_0L = 1$ ($\delta_0L = 7.9$) is used for the SET (RESET) signals, while for the CW signal the detuning coefficient is $\delta_0L = 6.56$

We now consider an AOFF operation using signals of different wavelengths as discussed by in Ref. [48]. The working principle of such operation can be understood in a simplified way. The input signal is located inside the band gap of the structure close to the band edge. The SET and the RESET signal is situated far from the stop band at detuning coefficients $\delta_0L = 1$ ($\delta_0L = 7.9$) and hence are unaffected by the grating. The power of the holding beam is kept constant at 0.1 mW. The corresponding output is plotted in Figure 3-18. From the calculation we obtain that a smaller value of SET power is needed in comparison to the RESET power. The red dotted line shows the temporal dynamics SET signal while the blue dotted line shows the temporal dynamics of the RESET signal. The resultant output is plotted by a black line. By this process a larger dynamic range of the control signal can be chosen.

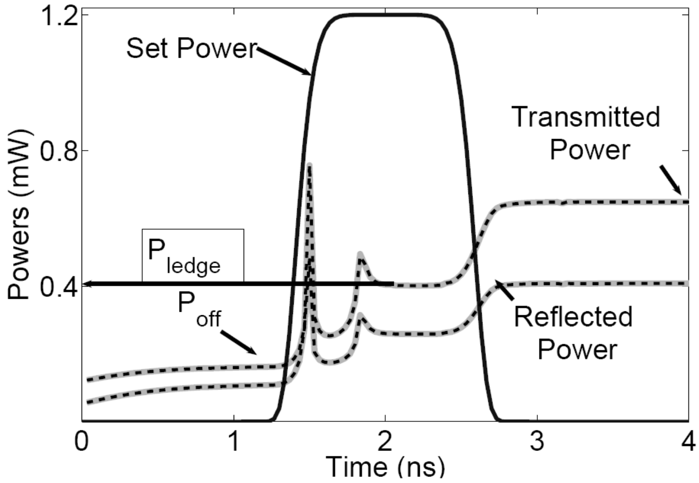

Figure 3-19 : Temporal dynamics of the low-to-high switching operation for the for $L = 300$ µm, $\kappa L = 3$, $g_0L = 1.2$. with SET peak power of 1.2 mW. The dynamic shows that the output is latched to an intermediate state during the duration of the pulse and switches to the high transmitting state.

To see the effect of the actual field dynamics we consider a multi-section time dependent model. We consider a super Gaussian pulse of order two with FWHM of 2 ns and plot the evolution of the transmitted and the reflected power in presence of the SET pulse in Figure 3-19. We observe that with the rising edge of the SET pulse both the transmitted and reflected power increases, and saturates at a power level (P_{ledge}) and are latched there till the duration of SET pulse. With the decreasing edge of the pulse the transmitted and the reflected power start increasing again and saturate at the high transmitting state even after the Set pulse is gone. It was observed by Maywar et al. [48] (but no physical explanation was given), that the ledge height decreases linearly with the SET power. To explain the phenomena we plot the hysteresis curve of the input signal in presence or absence of a constant SET power. The green curve in Figure 3-20 shows the bistable curve for the input holding beam. In presence of the SET power it is found that the bistable curve moves to lower power and the effective transmission at the operating holding beam power is reduced. Near the holding beam input power the black curve is almost linear and it moves almost linearly to the right with increasing SET power. So the ledge power should decrease near-linearly with the SET power.

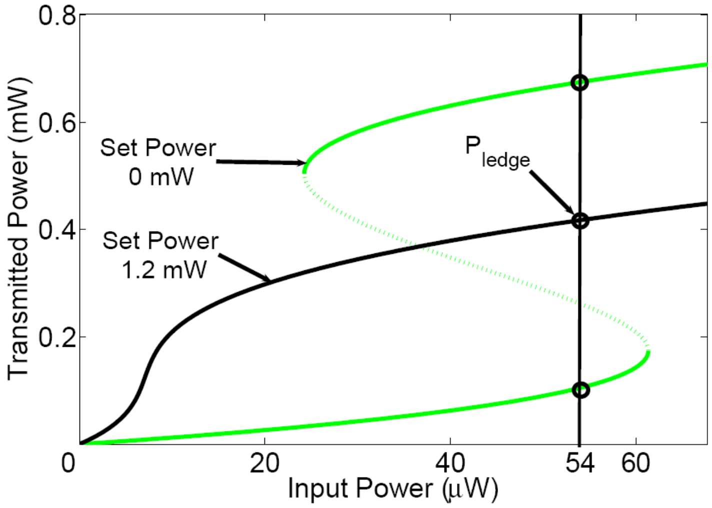

Figure 3-20 : Steady state bistable curves for $L = 300$ μm, $\kappa L = 3$, $g_0L = 1.2$. with SET peak power of 1.2 mW. with peak SET power of 1.2 mW. The green (black) curve is the bistable curve in absence (presence) of the SET pulse.

3.3 Summary

In this chapter we have described the steady state response of a nonlinear periodic structure. We have introduced the elliptic function formalism which gives an exact solution of the GNLCME for Kerr-type media. From the steady state solution we found that the output power shows bistable behaviour with respect to the input power. These types of device show a memory effect and a hysteresis, which have potential application for constructing all-optical flip-flop and switches. Further we solve the nonlinear coupled mode equation numerically to study the temporal dynamics. The results from our time-dependent calculation are verified with the analytical solutions as obtained in the steady state. The operation principle of the all-optical flip-flop is described in this chapter for passive and active waveguide gratings.

As a new result we have introduced a scheme of a co-propagating SET and a counter-propagating REST signal with respect to the CW holding beam. This scheme gives more freedom to operation of all-optical flip-flops. In this scheme the so called negative RESET pulse is not needed. We have also described the near linear decrease of ledge height in flip-flop operation with signals of different frequencies.

4 Novel isolator design

In an all-optical fiber transmission several connectorized optical components are present, and various backscattered signals are generated from the end faces of these components. This scattered light can enter the source and destabilize it creating unwanted feedback. Optical feedback degrades the signal-to-noise ratio and consequently the bit-error probability (usually called bit error "rate" BER), thus resulting in poor transmission performance. Isolators are thus indispensable devices for eliminating these backscattering. Ideally, an isolator would pass all light in one direction and block all light in the reverse direction. The common isolators explore the Faraday rotation in which the plane of polarization of a laser beam is rotated by 45° as it passes through a high Verdet constant[11] material, positioned in an axial magnetic field produced by permanent magnets. This rotation is additive for reflections passing back through the isolator giving 90° difference between the input and reflected polarization states at the input to the isolator. An input polarizer will therefore reject the back reflections.

High-speed and large-capacity optical fiber transmission systems are expanding, as a result of the development of optical amplifiers. But this leads to more backwards reflected power, hence the demand for optical isolators is also increasing. Demand is also expected to increase, as LAN and other subscriber optical fiber networks expand. It is therefore imperative that isolators and other optical components be further improved to achieve higher performance, compact size, and high integration density. The conventional isolators show extremely high isolation ratio but in general can not be integrated in a chip. So isolators which can be monolithically integrated in a chip with other optical components are of high interest. Recently researchers showed integrated AlGaInAs/InP waveguide isolators [57] with 11.4 dB isolation ratio utilizing the magneto-optic Kerr effect. Though it is a promising candidate, it poses problems in fabricating permanent magnetic material with other components in an optical chip. In view of this we propose an alternative approach exploiting the axially asymmetries in non-magnetic nonlinear periodic structures, and hence explore an "optical diode"-like functionality for active and passive devices in the following.

4.1 General theory leading to nonreciprocal behaviour

In this section we describe the general theory of a nonreciprocal device based on a simplified model of an *asymmetric Fabry–Perot resonator* (AFPR) with a nonlinear medium in the cavity (see Figure 4-1). We assume that front and back mirror of an AFPR are linear, and have a constant reflectivity[12] R_1 and R_2, respectively. For convenience we define the following parameters: L is the cavity length; λ_0 is the operating wavelength; g is the total gain (or loss) coefficient, which is expressed as a sum of the linear absorption coefficient α_{int} and the nonlinear gain (or absorption) coefficient g_{NL}; θ is half of the cavity's round-trip phase change, which is expressed as a sum of resonant phase ϕ_{res} (corresponding to resonant wavelength λ_{res}), linear phase ϕ (corresponding to operating wavelength λ_0), nonlinear phase contributions ϕ_{NL}; n_{eff} is the effective index of the waveguide, R_{eff} is the effective reflectivity, and L_{eff} is the effective length for nonlinear interaction.. The average power[13] in the cavity is defined as P_{avg}. With these definitions the reflectivity R, transmissivity T, and the power enhancement PE in the cavity of an AFPR are given by

---

[11] The Verdet constant is an optical constant that describes the strength of the Faraday effect for a particular material

[12] This simplified assumption does not strictly hold in the case of dielectric mirrors but this gives a reasonably good approximation for broad band mirrors considered here. Such mirrors are also influenced by nonlinearity but these effects are negligible near the Bragg wavelength of the mirrors as can also be seen from Figure 2-4. However, a more rigorous approach [21] can be used in defining the reflectivities of the mirrors. In this case the cavity length should be modified to include the effective penetration depth of the fields in mirrors [28]. We neglected these effects to keep a simple modelling approach in explaining the nonreciprocal phenomena.

$$T = \frac{P_{\text{Trans}}}{P_{\text{In}}} = \frac{H}{1 + F\sin^2(\theta)}, \tag{4.1}$$

$$R = \frac{P_{\text{Refl}}}{P_{\text{In}}} = \frac{E + F\sin^2(\theta)}{1 + F\sin^2(\theta)}, \tag{4.2}$$

$$\text{PE} = \frac{P_{\text{Avg}}}{P_{\text{In}}} = \frac{M}{1 + F\sin^2(\theta)}, \tag{4.3}$$

where the quantities H, E, F, and θ are defined as

$$\begin{gathered} F = \frac{4R_{\text{eff}}\exp(gL)}{\left[1 - R_{\text{eff}}\exp(gL)\right]^2}, \quad E = \frac{\left(\sqrt{R_1} - \sqrt{R_2}\exp(gL)\right)^2}{\left[1 - R_{\text{eff}}\exp(gL)\right]^2}, \quad H = \frac{\exp(gL)(1 - R_1)(1 - R_2)}{\left[1 - R_{\text{eff}}\exp(gL)\right]^2}, \\ M = \left[\frac{(1 - R_1)(1 + R_2\exp(gL))}{\left(1 - R_{\text{eff}}\exp(gL)\right)^2}\right]\frac{L_{\text{eff}}}{L}, \quad L_{\text{eff}} = \left[\frac{\exp(gL) - 1}{g}\right], \end{gathered} \tag{4.4}$$

$$g = g_{\text{NL}}\left(P_{\text{Avg}}\right) - \alpha_{\text{int}}, \ \theta = \phi_{\text{res}} + \phi + \phi_{\text{NL}}\left(P_{\text{Avg}}\right), \ \phi = \frac{2\pi L}{\lambda_0 / n_{\text{eff}}}, \ \phi_{\text{res}} = \frac{2\pi L}{\lambda_{\text{res}} / n_{\text{eff}}} \ R_{\text{eff}} = \sqrt{R_1 R_2}. \tag{4.5}$$

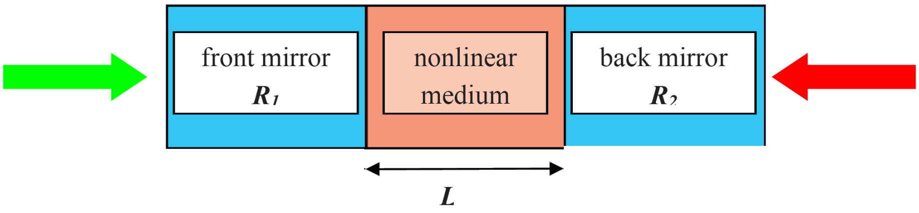

Figure 4-1 : Schematic diagram showing a nonlinear periodic structure. The green and the red arrow indicates the left-to-right and right-to-left direction of propagation. .

The transfer characteristic of an AFPR can be calculated from Eq. (4.1) and (4.2). The transmission shows a resonance at $\theta = \phi_{\text{res}} = m\pi$, were m is any integer. The quantity ϕ is the phase detuning with respect to the phase ϕ_{res} at resonance, i.e., it measures the frequency detuning from resonance ϕ_{res} in absence of nonlinearity. The quantity F is related to the cavity *finesse*

---

[13] For a detailed derivation of the average power in the cavity see ref. [28].

$\mathbb{F}$ (the cavity finesse is defined as the ratio of the resonance full width at half maximum to the free spectral range) as

$$\begin{aligned}\mathbb{F} &= \frac{\text{full width at half maxima}}{\text{free spectral range}} \\ &= \frac{\pi}{2\arcsin\left(\sqrt{(2H-1)/F}\right)} \qquad (4.6) \\ &\approx \frac{\pi\sqrt{F}}{2}, \quad \text{for} \quad F \gg 1.\end{aligned}$$

The nonlinear contribution in the gain (or loss) term g_{NL} and phase ϕ_{NL} are assumed to depend on the cavity power P_{Avg}. We first discuss the linear case by neglecting any power dependence of the gain (or loss) and phase. In the linear lossless ($g = 0$) case it can be seen from Eq. (4.1) – (4.5) that the transmissivity at resonance is $T = 1$ in the symmetric case (i.e., if $R_1 = R_2$), while it is $T < 1$ for an asymmetric case (i.e., if $R_1 \neq R_2$). The resonance in both cases is at $\theta = \phi_{\mathrm{res}} = m\pi$.

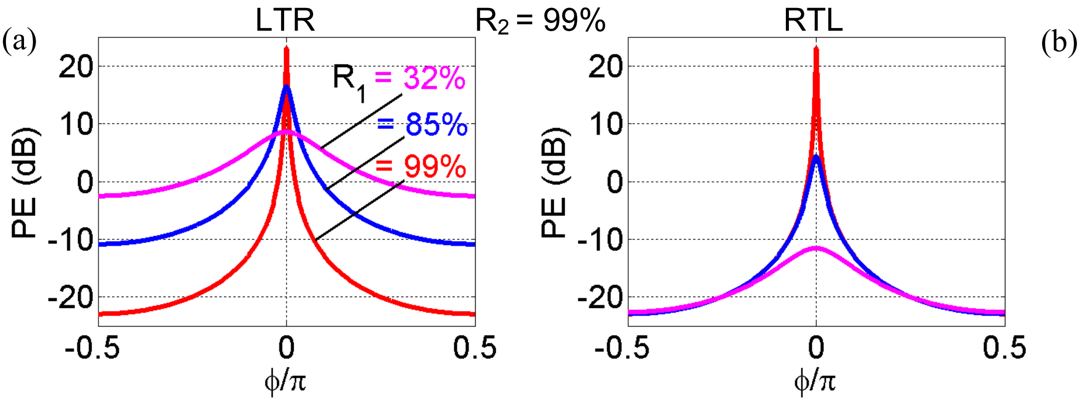

Figure 4-2 : Variation of power enhancement (PE) in the cavity as a function of phase detuning ϕ. Linear lossless case, $\alpha_{\mathrm{int}} L = 0$, for different values of $R_1 = 0.99$ (red), 0.85 (blue), 0.32 (magenta), with $R_2 = 0.99$. (a) LTR & (b) RTL propagations.

Linear lossless cavity: We first look at the effect of different mirror reflectivities on the linear transmission characteristics. We assume that the same input power is injected into the AFPR in *left-to-right* (LTR) direction (see the green arrow in Figure 4-1) or in *right-to-left* (RTL) direction (see the green arrow in Figure 4-1). Changing the launching direction of the input signal can be simply modelled by swapping the quantities R_1 and R_2 in Eq. (4.1) – (4.5). The calculated power enhancement in the cavity PE for the linear, lossless case, and for different combinations of R_1 and R_2 are plotted in Figure 4-2. Some observations can be made from the plots. (i) As the resonator becomes asymmetric ($R_1 \neq R_2$) the PE at resonance decreases (see the PE at $\phi = 0$ in Figure 4-2). (ii) Interestingly the average power coupled to the cavity[14] is different even if the same input power is injected from the LTR direction or from the RTL direction. The origin of this different average power in the cavity can be understood with the help of equation (4.3) and the quantity M therein. In the asymmetric case (i.e., $R_1 \neq R_2$), interchanging R_1 and R_2 leads to different values of M for different direction of propagations, leading to different average powers inside the cavity. Owing to the asymmetry of the structure, if the incoming signal sees a highly reflecting mirror first, most of the power is reflected, while in the reverse direction the same signal sees a low-reflecting mirror and can couple more power to the cavity. For a dielectric mirror the input field decays exponentially along the incident direction according to its associated penetration depth [80]. Mirrors with different reflectivities have different penetration depths, and the effective cavity length changes if the direction of incidence is reversed. However, the reflectivity and the transmissivity of the AFPR in this case are identical for LTR and RTL direction of propagation

---

[14] PE is a measure of the average power coupled to the cavity.

Linear lossy cavity: In the linear case with a lossy cavity the situation becomes different but it retains similar features, as can be seen from Figure 4-3. Here also the PE in the cavity is different for LTR and RTL propagating cases. The PE decreases with the increasing loss in the cavity. It is interesting to note that the reflectivity of the device is different for different directions of propagation in this case (see (a) & (b)). This type of direction dependent reflectivity is also predicted by others [12]. So for identical incident powers the reflected power is

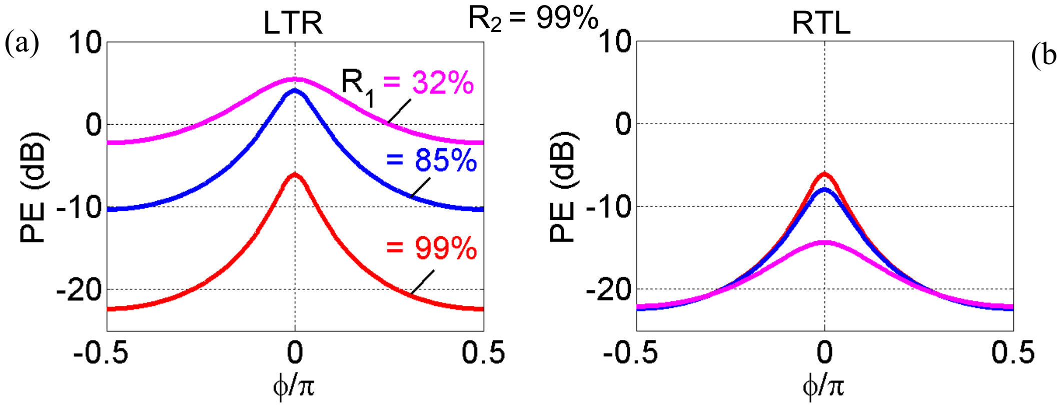

Figure 4-3 : Variation of power enhancement (PE) in the cavity as a function of phase detuning ϕ. Linear case with linear loss coefficient, $\alpha_{\text{int}} L = -0.3$, for different values of $R_1 = 0.99$ (red), 0.85 (blue), 0.32 (magenta), with $R_2 = 0.99$. (a) LTR & (b) RTL propagations.

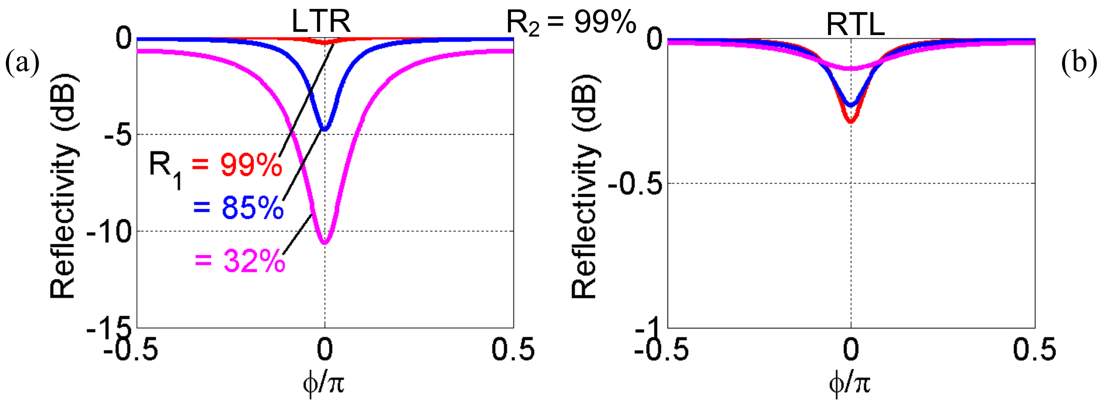

Figure 4-4 : Variation of reflectivity R of AFPR as a function of phase detuning ϕ. Linear case with linear loss coefficient, $\alpha_{\text{int}} L = -0.3$, for different values of $R_1 = 0.99$ (red), 0.85 (blue), 0.32 (magenta), with $R_2 = 0.99$. (a) LTR & (b) RTL propagations.

different in presence of loss if the device is asymmetric. However, the transmitted power is identical for LTR and RTL propagations.

Non-linear lossless cavity: Now we focus on the case in which the material in the cavity is made out of nonlinear material. In such a case the refractive index and gain (or loss) of the material in the cavity is no longer constant but is dependent on the cavity power. As the average power in the cavity P_{Avg} is different for different directions of propagation in the asymmetric case (i.e., $R_1 \neq R_2$), the nonlinearly induced change in the material properties (i.e., either gain or phase or both, depending on the type of nonlinearity used) is different. This leads to a nonreciprocal transmission with respect to the direction of propagation.

In view of the discussions in the previous paragraphs we can generalize the nonreciprocal phenomena. For any nonlinear resonator if any material or structural property $\psi(z)$[15] satisfies $\psi(z) \neq \psi(-z)$ then the *inversion symmetry* is broken and the average power coupled to the resonator is different for different direction of propagations. In presence of nonlinearity this leads to a nonreciprocal transmission with respect to the direction of propagation.

This type of "optical diode"-like behaviour is also observed in different nonlinear resonator structure [15][16][18][20][32][41][43][45][53][62][63][73]. All of these apparently different structures have inherent violation of the *inversion symmetry*. This simple model of a nonlinear AFPR can describe these different observations in a same framework.

Though we have used a linear resonator characteristics in explaining the non-reciprocal phenomena, our arguments are valid even for the nonlinear cases. In the following sections we explore some detailed calculations on some specific type of nonlinearities. We have considered the following type of nonlinear media in the cavity:

(i) Kerr-type material

(ii) Semiconductor optical amplifier (SOA).

We choose for our simulation a silicon-on-insulator (SOI) waveguide structure for the passive devices and InP based structure for active devices. The mirrors of the AFPR are realized by two distributed Bragg reflectors (DBR), with a sidewall corrugation [18] (see Figure 4-5). We note that these dielectric mirrors show some wavelength dependence both in phase and amplitude, but this dependence can be neglected near the sharp resonance of the AFPR considered here[16]. For lower values of reflectivities (~32%) we can use the Si-air interface at the waveguide end as cavity mirrors. Though we have chosen some particular material systems in our explanation, these results are also applicable to different material systems with suitable scaling relations.

---

[15] The material property can be reflectivity or more generally a z dependent property of the coupling coefficient κ, the periodicity of the grating Λ, biasing current density J_c for active devices, or the nonlinear coefficient γ of the mirrors forming the resonator.

[16] See footnote [10] on page 45.

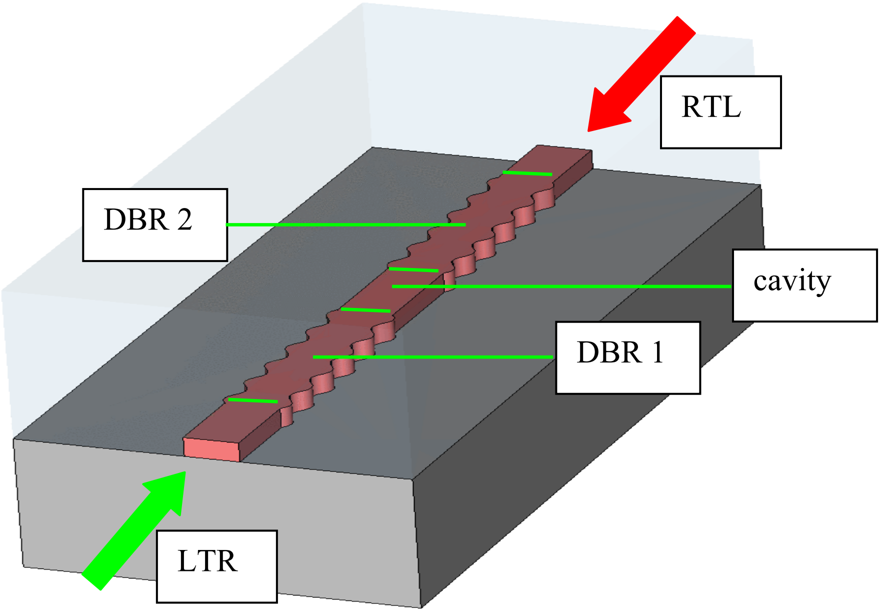

Figure 4-5 : Schematic waveguide structure with two sidewall corrugated DBR mirrors forming an asymmetric Fabry-Perot resonator.

4.1.1 Kerr-type nonlinear medium in the cavity

In this section we explore the effect of Kerr-type nonlinear material in the cavity of AFPR. As discussed in Section 2.3.1 the refractive index of a Kerr-type material is modified with the intensity of the light. Here we considered the nonlinear contribution in phase due to self-phase modulation (SPM) and relate it to the nonlinear coefficient γ according to the following expression [5]

$$\begin{aligned}\phi_{\mathrm{NL}} &= P_{\mathrm{Avg}}\gamma L \\ &= P_{\mathrm{Avg}}/P_{\mathrm{ref}}, \quad \text{with } P_{\mathrm{ref}} = 1/(\gamma L).\end{aligned} \tag{4.7}$$

Here P_{Avg} is the average power in the cavity (see Eq. (4.3)), which depends on the input power P_{in}.

We consider a silicon-on-insulator (SOI) waveguide structure as shown in Figure 4-5. The nonlinear coefficient of such a material is $\gamma = 3.5\ \mathrm{cm}^{-1}\mathrm{W}^{-1}$ [36]. The waveguide has a width of 430 nm and a height of 220 nm. This type of high index-contrast waveguide structures shows high field confinement, leading to lowering the A_{eff} to a small value [36]. The lower value of A_{eff} is favourable for enhancing the nonlinear effects. For this structure we consider $A_{\mathrm{eff}} = 0.05\ \mu\mathrm{m}^2$. By choosing different corrugation depths and lengths of the DBR section it is possible to engineer a suitable reflectivity of the mirrors. In all the results which follow the power is expressed in units of a reference power $P_{\mathrm{ref}} = (\gamma L)^{-1}$, which gives a scale factor and we can use the same results for different materials by changing this scale factor. The reference power P_{ref} can be interpreted as the average cavity power P_{Avg} required to introduce a nonlinear phase shift of 1 rad.

The set of equations (4.1) to (4.5) can be solved numerically but here we discuss a graphical solution which helps in understanding the nonlinear behaviour of the AFPR. The nonlinear phase shift ϕ_{NL} is dependent on the cavity power as expressed by Eq. (4.7). This expression together with Eq. (4.3) and (4.5) allows us to calculate the dependency of the average power in the cavity P_{Avg} on a given input power P_{In} of the signal. We neglect any loss (i.e., $g = 0$), so that the coefficient M and F as in Eq. (4.4) are constant. The right hand side of equation (4.3) can be written as a function of the cavity power. It is plotted in dB scale in Figure 4-6 for two different values of the phase detuning ϕ from the resonance phase ϕ_{res}, namely $\phi = 0$ (see the red curve in Figure 4-6 (a)), $\phi = -0.3\pi$ (see the blue curve in Figure 4-6 (b)) respectively. These curves are similar to the AFPR cavity PE spectrum (see Figure 4-2) considering the fact that the quantity in the x-axis represents the nonlinear phase term proportional to the average power P_{Avg} through Eq. (4.7).

The left hand side of (4.3) is a straight line (see black lines in Figure 4-6 (a), (b)) with its slope depending upon $1/P_{In}$. However, we note that in the semi-logarithmic scale the straight line is distorted, which is necessary to get a large dynamic range. The intersection of this "straight line" with the cavity PE spectrum (see the filled and void circles in Figure 4-6) gives the solution of Eq. (4.3).

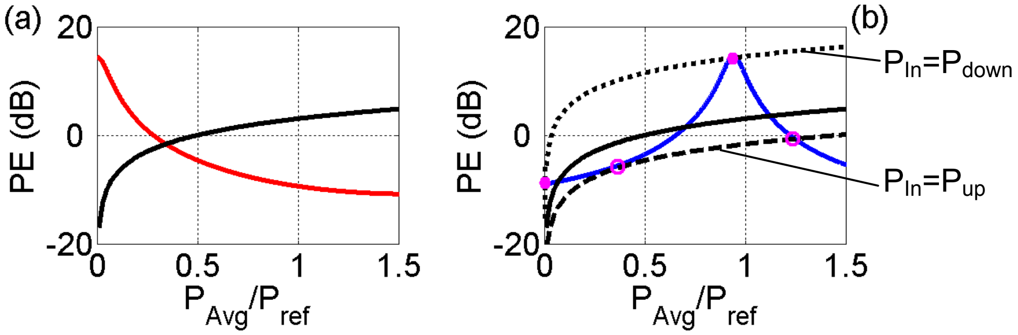

Figure 4-6 : Graphical solution of equation (4.3) for a AFPR with $R_1 = 0.85$, $R_2 = 0.95$, $L = 100$ µm, $\gamma = 3.5$ cm^{-1}W^{-1} in the lossless case $\alpha_{int}L = 0$ for (a) $\phi = 0$ and (b) $\phi = -0.3\pi$ The black dotted line is for the power corresponding to down-switching threshold, dashed line for the up-switching threshold, while the solid line corresponding to the power in the bistable region. $P_{ref} = (\gamma L)^{-1}$

Now we consider different values of the input powers P_{In}. At low input power both curves intersect at one point only leading to a single real solution of Eq. (4.3). As the input power is increased the slope of P_{Avg}/P_{In} changes, and eventually the curves intersects the cavity PE spectrum at two points (see the filled circles at the intersection of black dotted line and blue curve in Figure 4-6(b)). In that case we have two solutions of Eq. (4.3). The corresponding input power gives the down-switching threshold. If we further keep on increasing the power the "straight line" intersects the cavity spectrum at three points[17] (see the intersection of solid black line and blue curve in Figure 4-6 (b)), two of which give the two stable solution of the said equation, while the other gives as unstable solution. If we still keep on increasing the input power, the curves again intersect at two points (see the void circles at the intersection of black dashed line and blue curve in Figure 4-6 (b)). The corresponding input power gives the down-switching threshold. Beyond this point we get again a single valued solution even if the input power is increased. So by changing the input power we can trace out an S-shape hysteresis curve.

---

[17] In general it can be multivalued but here we discuss only the first bistable region.

Some physical insight can be gained from this graphical solution. In the bistable region the cavity has two stable states: a) low cavity power for an off-resonance condition, and b) high cavity power for an on-resonance condition. At any temporal instance the device can be either in the state "on-resonance" or in the state of "off-resonance" as also described in Section 3.1.1. For different values of the phase detuning, the resonance peak of the cavity PE spectrum (see the blue curve in Figure 4-6 (b)) changes both in location and height. This leads to a change in the value of the switching thresholds. Also we can see that for certain critical values of the phase detuning ϕ the solution of (4.3) is always single valued, whatever the input power may be. This is a common phenomenon is nonlinear resonators and is discussed by [66][77].

"AFPR" with inversion symmetry: We now specialize to the symmetric case of equal mirror reflectivity $R_1 = R_2$. We choose $R_1 = R_2 = 0.99$, 0.95, 0.90 and 0.75 respectively. In Figure 4-7 we plot the dependence of the output power on the input power of the structures for LTR (see Figure 4-7 (a)), and for RTL (see Figure 4-7 (b)) propagating signals, with loss coefficient $\alpha_{\text{int}} = 1$ dB/cm. We choose an operating point at a relative phase detuning of $\phi = -0.1\,\pi$. From these figures we cannot distinguish between the LTR or RTL propagating cases. This justifies our explanation of reciprocal transmission also in the case of a *nonlinear* resonator having *inversion symmetry*.

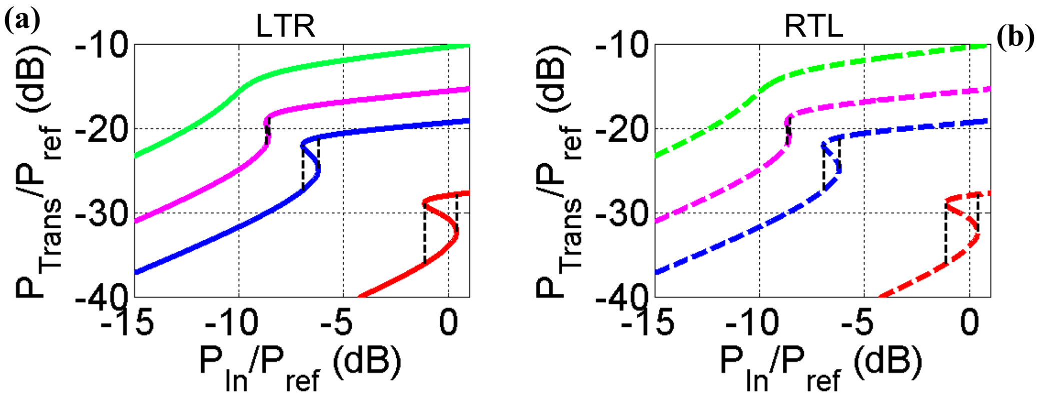

Figure 4-7 : The variation of the output power with respect to the input power of an AFPR with $L = 100\ \mu\text{m}$, $\gamma = 3.5\ \text{cm}^{-1}\text{W}^{-1}$, and $R_1 = R_2 = 0.99$ (red), 0.95 (blue), 0.90 (magenta) and 0.75 (green), $\alpha_{\text{int}} = 1$ dB/cm, $\phi = -0.1\pi$ for (a) LTR and (b) RTL propagating signals. $P_{\text{ref}} = (\gamma L)^{-1}$.

To generalise this we calculate the up-switching and down-switching thresholds for each value of the operating point P_{In}, and for two different linear loss coefficient ($\alpha_{\text{int}} = 0$, $\alpha_{\text{int}} = 1$ dB/cm), and both operation directions and plot in the Figure 4-8(B) and (b) for $R_1 = R_2 = 0.99$ and $R_1 = R_2 = 0.95$, respectively. The shaded region represents the bistable region bounded by the up-switching and the down-switching threshold. From this filled curves we see that bistability is observed only below certain value of the phase detuning ϕ[18]. As mentioned before this feature is common to Kerr-based nonlinear resonators.

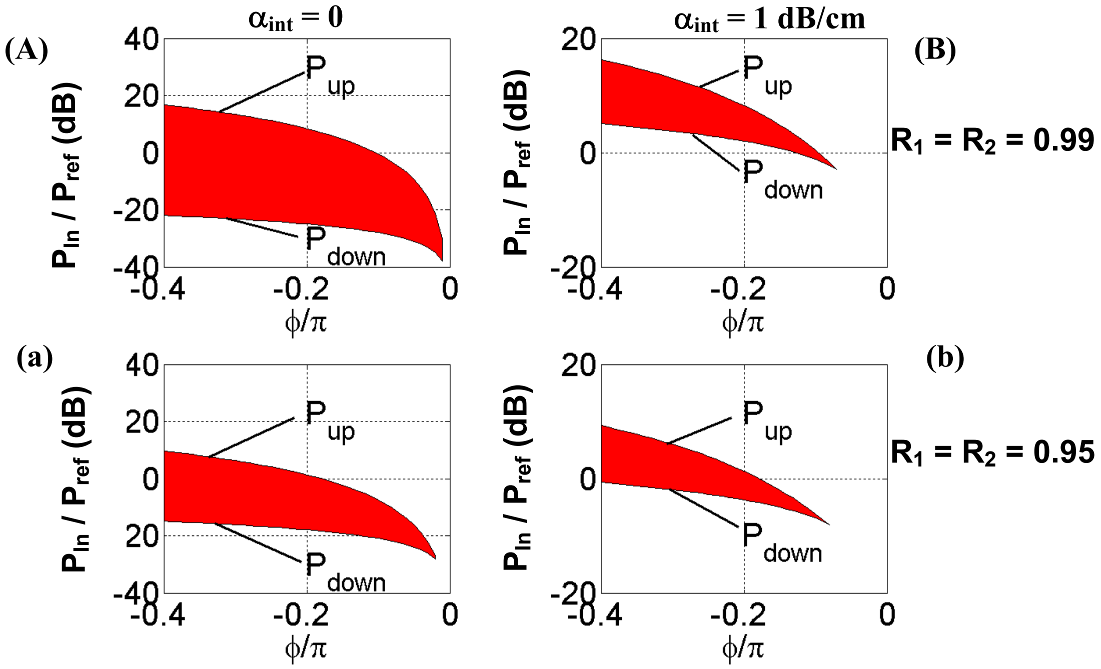

Figure 4-8 : Variation of the input power and detuning (corresponding to the offset from frequency resonance), specifying a bistable (shaded) region which is bounded by the up- and down-switching thresholds for different reflectivity combinations, and for different linear loss coefficients. The left column shows the lossless case, $\alpha_{int} = 0$ for (A) $R1 = R2 = 0.99$; (a) $R1 = R2 = 0.95$. The right column represents the lossy case with linear loss coefficient $\alpha_{int} = 1$ dB/cm (B) $R1 = R2 = 0.99$; (b) $R1 = R2 = 0.95$. In all the curves the following device parameters are valid $L = 100$ µm, $\gamma = 3.5$ cm^{-1}W^{-1}, the reference power is $P_{ref} = (\gamma L)^{-1}$.

AFPR without inversion symmetry: Now we consider structures in which the inversion symmetry is broken, i.e., in the case of $R_1 \neq R_2$. We calculate the input-output characteristics for different reflectivity combinations, and for LTR and RTL propagation. We plot the up-switching and the down-switching threshold for different values of ϕ for the LTR and RTL direction of propagations of an AFPR in Figure 4-9. We observe that the transmission curves for LTR and RTL propagation deviate from each other as the asymmetry[19] increases. Further we can see that for certain range of the input power and operating range the down-switching threshold of the RTL curve is higher than the up-switching threshold of the LTR curve. In the region in-between them the LTR path is always higher transmitting while the RTL path is always lower transmitting. In this region the device essentially work as an all-optical diode, which transmits the signal in the forward direction while attenuates the signal in the backward directions.

---

[18] This can be seen as the point the up and the down switching threshold converge to a single point.

[19] We consider the structure to be more asymmetric if the value of R_1 and R_2 deviates stronger.

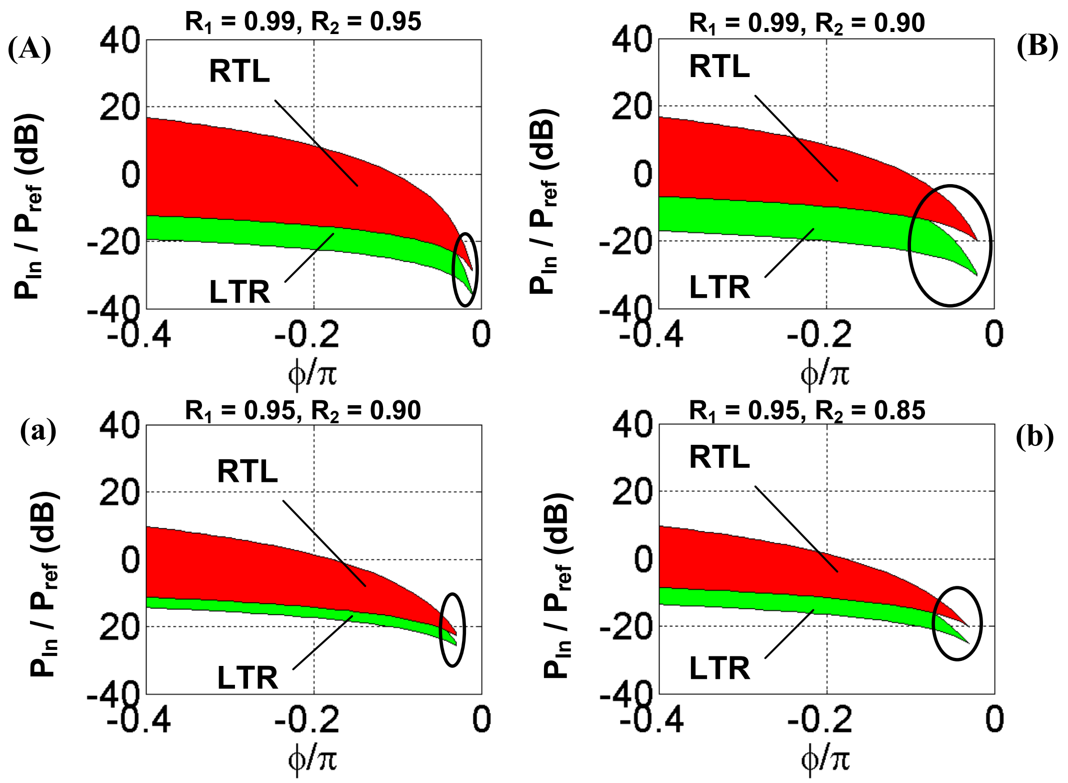

Figure 4-9 : Variation of the input power and detuning ϕ (corresponding to the offset from frequency resonance), specifying a bistable (shaded) region which is bounded by the up- and down-switching thresholds. Lossy case, with loss coefficient $\alpha_{\mathrm{int}} = 1$ dB/cm, $L = 100$ μm, $\gamma = 3.5$ cm^{-1}W^{-1}. The reference power is $P_{\mathrm{ref}} = (\gamma L)^{-1}$. for (A) $R_1 = 0.99$, $R_2 = 0.95$; (B) $R_1 = 0.99$, $R_2 = 0.90$; (a) $R_1 = 0.95$, $R_2 = 0.90$; (b) $R_1 = 0.95$, $R_2 = 0.85$. The LTR and RTL propagating cases are depicted by green and red shaded areas, respectively. The marked regions show the isolation region.

In Figure 4-10 the RHS of (4.3) has been depicted for three different phase detuning parameter ϕ (i.e., for threes different frequency offsets from the resonance of the linear resonator). Again, the LHS of (4.3) has been depicted for an input power of $P_{\mathrm{In}} = P_{\mathrm{ref}}$ (see black dotted line in Figure 4-10). As can be seen by the different intersection points, the power enhancement PE, the transmissivity T, and the reflectivity R are different for various input frequencies (phase detuning ϕ). Similarly, LTR and RTL operation are different with respect to PE, R, and T.

In Figure 4-11 the dependence of output power P_{Trans} on the input power P_{In} is to be seen for various values of RTL and LTR operation. The up-switching and the down-switching thresholds (as schematically marked in Figure 3-1 on page 23) are seen to be different for LTR and RTL operations, indicating a nonreciprocal transmissivity.

We plot similar cases in Figure 4-12 considering linear loss $\alpha_{\mathrm{int}} = 1$ dB/cm [28]. We found that with an increase in loss the peak of the cavity resonance decreases, which is accompanied by an increase of the down-switching threshold. This narrows the hysteresis. The separation of the LTR and RTL curves increases correspondingly (see Figure 4-13). However, the extinction ratio as defined by (3.1) of the each of the hysteresis curves decreases with the increase of loss. The up-switching threshold does not change significantly. So for a real device with non-zero but moderate loss, the non-reciprocal behaviour is enhanced.

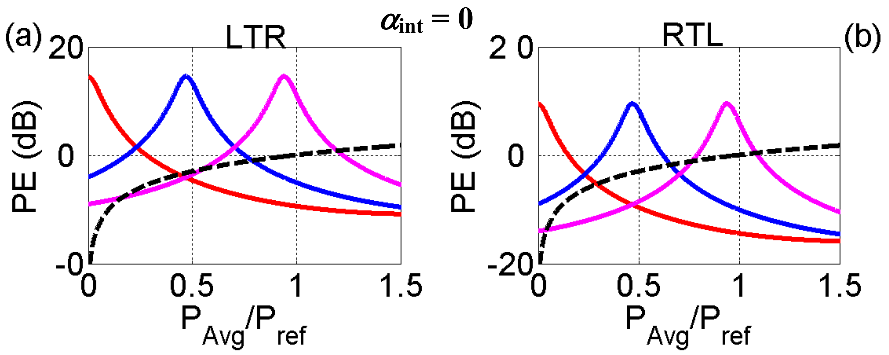

Figure 4-10 : Graphical solution of NL-AFPR for a specific input power of $P_{in} = P_{ref}$ (black dotted line) in absence of linear loss, $\alpha_{int} = 0$ with $R_1 = 0.85$, $R_2 = 0.95$, $L = 100$ μm, $\gamma = 3.5$ cm^{-1}W^{-1} for three different phase detuning, $\phi = 0$ (red), -0.15π (blue), -0.3π (magenta). (a) LTR and (b) RTL propagating cases.

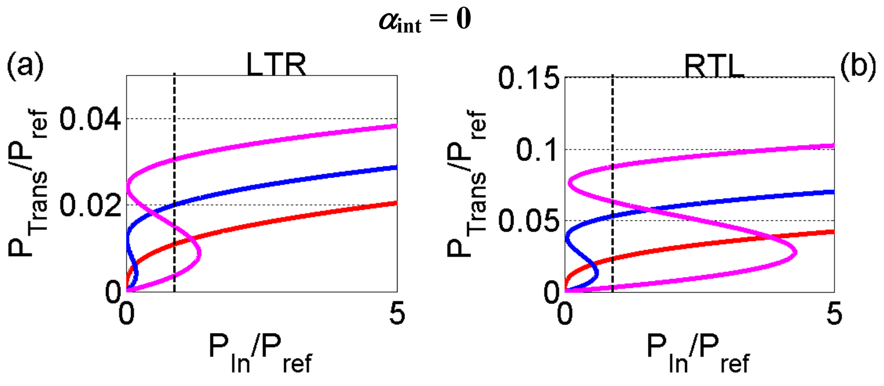

Figure 4-11 : Bistable curves of a NL-AFPR in absence of linear loss, $\alpha_{int} = 0$ with $R_1 = 0.85$, $R_2 = 0.95$, $L = 100$ μm, $\gamma = 3.5$ cm^{-1}W^{-1} for three different phase detuning, $\phi = 0$ (red), -0.15π (blue), -0.3π (magenta). (a) LTR and (b) RTL propagating cases. The black dotted line correspond to a certain input power of $P_{in} = P_{ref}$

We plot the hysteresis curves for LTR and RTL propagating signals for a phase detuning $\phi = -0.15\pi$ in Figure 4-14. The marked region shows the isolation region where the device shows high forward transmission (LTR) and low backward (RTL) transmissions. In this region the device works as an isolator. The maximum isolation ratio in this case is 6 and is relatively low, but we can increase this ratio with a proper choice of nonlinear material and cavity.

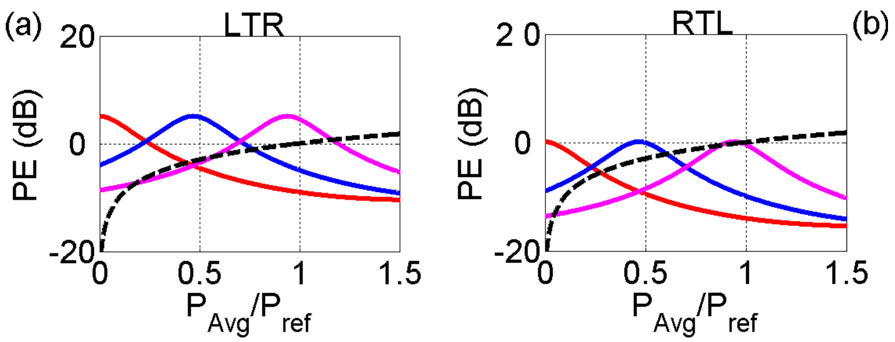

Figure 4-12 : Graphical solution of NL-AFPR for a specific input power of $P_{\text{in}} = P_{\text{ref}}$ (black dotted line) in presence of linear loss, $\alpha_{\text{int}} = 1$ dB/cm with $R_1 = 0.85$, $R_2 = 0.95$, $L = 100$ μm, $\gamma = 3.5$ cm^{-1}W^{-1} for three different phase detuning, $\phi = 0$ (red), -0.15π (blue), -0.3π (magenta). (a) LTR and (b) RTL propagating cases.

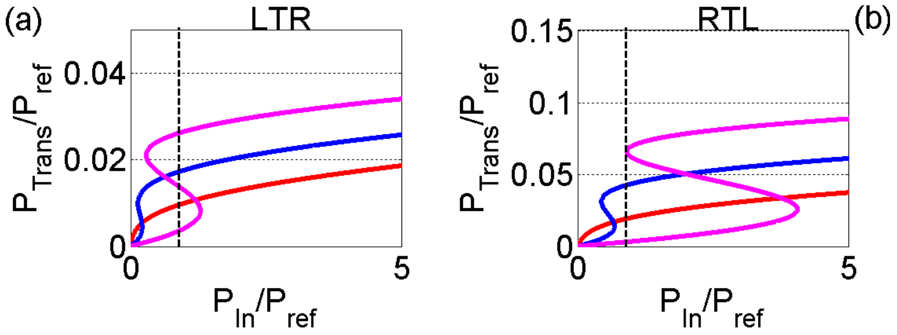

Figure 4-13 : Bistable curves of a NL-AFPR in presence of linear loss, $\alpha_{\text{int}} = 1$dB/cm with $R_1 = 0.85$, $R_2 = 0.95$, $L = 100$ μm, $\gamma = 3.5$ cm^{-1}W^{-1} for three different phase detuning, $\phi = 0$ (red), -0.15π (blue), -0.3π (magenta). (a) LTR and (b) RTL propagating cases. The black dotted line correspond to a certain input power of $P_{\text{in}} = P_{\text{ref}}$.

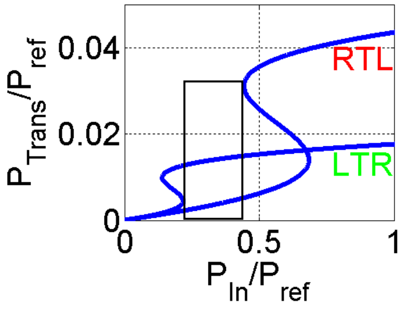

Figure 4-14 : Isolator behaviour for phase detuning $\phi = -0.15\pi$ with parameter as on Figure 4-13. if the device is operated at input power lying inside the rectangular box, then for RTL operation the transmissivity T is low, and is high for LTR operation.

Effect of two photon absorption (*TPA*): In certain semiconductor materials two-photon absorption (TPA) [36] contributes significantly to losses. TPA loss can be written similar to equation (4.7) as

$$g_{NL} = -\gamma_{\mathrm{TPA}} P_{Avg}. \tag{4.8}$$

For silicon-based structures which we consider here we use $\gamma_{\mathrm{TPA}} \sim 1.58\ \mathrm{cm^{-1}W^{-1}}$ [36]. We consider now the influence of TPA in the bistable characteristic of the AFPR. To find the relative effect of TPA it is instructive to define a figure of merit [36] for TPA as

$$\mathrm{FOM}_{\mathrm{TPA}} = \frac{n_2^I}{\alpha_2 \lambda}, \quad \gamma_{\mathrm{TPA}} = \frac{\gamma}{2\pi \mathrm{FOM}_{\mathrm{TPA}}} \tag{4.9}$$

For silicon-based devices the $\mathrm{FOM}_{\mathrm{TPA}}$ varies from 0.35 to 1.56 as has been reported by [36]. We use $\mathrm{FOM}_{\mathrm{TPA}} = 0.35$ and discuss the same structures as before to see the effect of TPA on the isolation behaviour.

Neglecting the effect of TPA

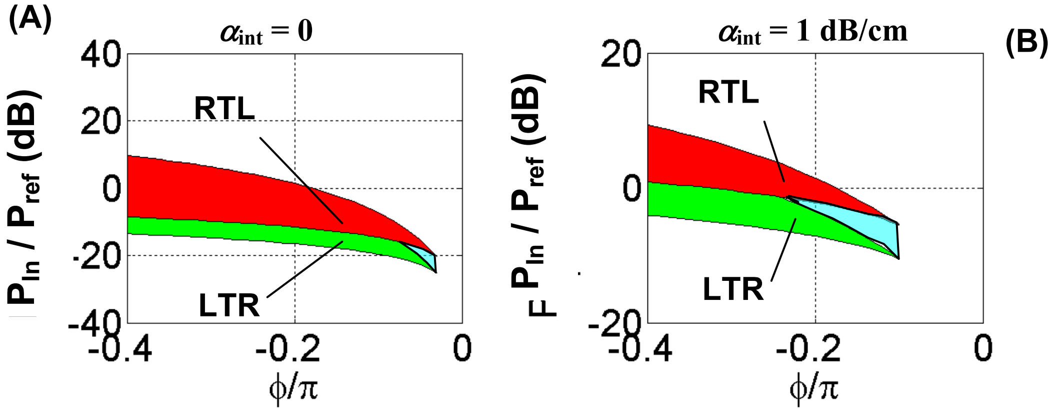

Including the effect of TPA

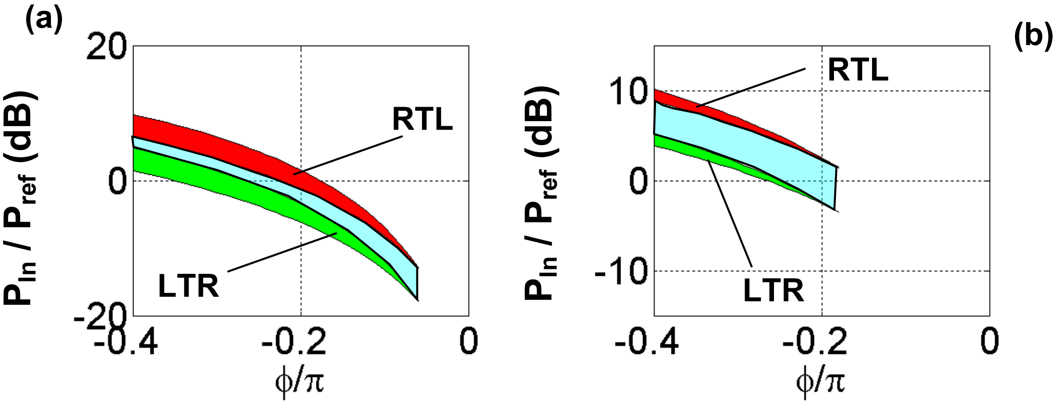

Figure 4-15 : Influence of TPA on the transmission properties of a NL-AFPR. Variation of the input power and detuning ϕ (corresponding to the offset from frequency resonance), specifying a bistable (shaded) region which is bounded by the up- and down-switching thresholds. with $R1 = 0.85$, $R2 = 0.95$, $L = 100$ µm. The red and green shaded region represents the bistable region for RTL and LTR propagating signals. TPA is neglected in (A) and (B) while in (a), and (b) TPA is included. The left column is for the lossless (linear) case, $\alpha_{\mathrm{int}} = 0$ dB/cm, while the right column is for linear loss of $\alpha_{\mathrm{int}} = 1$ dB/cm. $P_{\mathrm{ref}} = (\gamma L)^{-1}$

In Figure 4-15 we plot the variation of the input power and phase detuning, specifying a bistable (shaded) region which is bounded by the up- and down-switching thresholds for different linear loss. The upper boundary of the green (red) shaded area gives the up-switching threshold, while the lower boundary represents the down switching threshold, both for LTR, and RTL operations. The marked in-between regions in Figure 4-15 specify the region where LTR and RTL operation leads to a different transmissivity. We observe that in presence of loss the isolation region increases (compare Figure 4-15(A) with Figure 4-15(B)). We found that with stronger TPA in comparison to Kerr-effect, i.e., low value of $\mathrm{FOM}_{\mathrm{TPA}}$ the input power range showing isolation increases (compare Figure 4-15(A) and (a)). However the isolation ratio is found to decrease.

Simplified expressions for a cavity with large finesse $\mathbb{F}$: For a resonator with a large finesse the expressions (4.1) to (4.5) can be simplified near resonance assuming $\sin^2\theta \approx \theta^2$, $\phi_{\mathrm{res}} = m\,\pi$. So we can write

$$1 + F\sin^2(\theta) \approx 1 + F\,\theta^2. \tag{4.10}$$

All the expressions (4.1) to (4.5) can thus be written in simplified form as

$$\frac{P_{\mathrm{Trans}}}{P_{\mathrm{In}}} \approx \frac{H}{1 + F\,\theta^2}, \tag{4.11}$$

$$\frac{P_{\mathrm{Refl}}}{P_{\mathrm{In}}} \approx \frac{E + F\,\theta^2}{1 + F\,\theta^2}, \tag{4.12}$$

The expressions for reflectivity and transmissivity can be further simplified for the lossless case by eliminating θ with $\phi_{\mathrm{res}} + \phi + \phi_{\mathrm{NL}}$, $\phi_{\mathrm{NL}} = \gamma L\, P_{\mathrm{Avg}}$ from Eq. (4.5), This results in a cubic equation in $\mathrm{P}_{\mathrm{Trans}}$,

$$\frac{P_{\mathrm{Trans}}}{P_{\mathrm{In}}} \approx \frac{H}{1 + \left[\dfrac{P_{\mathrm{Trans}}}{P_0} - \sqrt{F}\phi_0\right]^2}, \tag{4.13}$$

$$\frac{P_{\mathrm{Refl}}}{P_{\mathrm{In}}} \approx \frac{E + \left[\dfrac{P_{\mathrm{In}} - P_{\mathrm{Refl}}}{P_0} - \sqrt{F}\phi_0\right]^2}{1 + \left[\dfrac{P_{\mathrm{In}} - P_{\mathrm{Refl}}}{P_0} - \sqrt{F}\phi_0\right]^2}. \tag{4.14}$$

A so-called characteristic power is defined by

$$P_0 = \frac{H}{2(\gamma L) M \sqrt{F}}. \tag{4.15}$$

The above expression (4.13) for the transmissivity resembles the expression described by Soljačic′ et al. [66]. We can see that we can associate different characteristic power for different directions of propagation because from Eq. (4.4) the quantity M is different for LTR and RTL propagations (i.e. by swapping R_1 and R_2). Hence this device with $R_1 \neq R_2$ will show non-reciprocal transmission/reflection behaviour if nonlinearity is present.

4.1.2 SOA type nonlinear medium in the cavity

In this section we consider the SOA as a nonlinear medium in the cavity of an AFPR. Similar to the analysis in section 2.4 we can write the gain and the nonlinear phase in the cavity as

$$g_{\mathrm{NL}} = \frac{\Gamma_{\mathrm{conf}} g_0}{1 + P_{\mathrm{Avg}} / P_{\mathrm{sat}}}, \tag{4.16}$$

$$\phi_{NL} = \frac{\alpha g_0 L}{2} \left(\frac{P_{\mathrm{Avg}} / P_{\mathrm{sat}}}{1 + P_{\mathrm{Avg}} / P_{\mathrm{sat}}} \right). \tag{4.17}$$

Comparing with equations (4.7) and (4.8) we see that that the nonlinear contribution to the gain and phase depends differently on the power in the cavity. So we expect different influence on the input-output characteristics of the AFPR in comparison to the Kerr + TPA type nonlinear devices. Like before we define the scaling factor for power as P_{sat} and all the results shown are in the normalized in units of $P_{\mathrm{ref}} = P_{\mathrm{sat}}$.

We first consider the NLAFP with the cavity length of $L = 300$ µm, $R_1 = 0.85$ and $R_2 = 0.95$. Further we use $\Gamma_{\mathrm{conf}} = 0.25$, alpha-factor $\alpha_{\mathrm{H}} = 5$, linear loss $\alpha_{\mathrm{int}} = 50\ \mathrm{cm}^{-1}$. The gain is chosen to be 95% of the lasing threshold of the resonator. In Figure 4-16(a) we plot the variation of the input power and detuning ϕ (corresponding to the offset from frequency resonance), specifying a bistable (shaded) region which is bounded by the up- and down-switching thresholds of an NL-AFPR for LTR and RTL propagations. For this set of parameter values the shaded regions almost overlap for all values of the detuning ϕ considered. However, for lower value of detuning we have a small separation between. The isolation ratio in this region is plotted in Figure 4-16(b). Here we found the maximum isolation ratio to be ~ 6.5.

To see the influence of alpha factor α_{H}, we consider a low value of $\alpha_{\mathrm{H}} = 1$ keeping rest of the parameters same as before for LTR and RTL propagations are plotted in of Figure 4-16(c). For this case we found a large separation of the hysteresis curves showing a large isolation range. The corresponding maximum isolation ratio variation is plotted in Figure 4-16(d). The maximum isolation ratio is ~ 6 in this case but the isolation ratio variation with the detuning shows near flat top variation.

To see the effect of the mirror reflectivity we now reduce the reflectivity of the front mirror $R_1 = 0.32$. Here we consider the alpha-factor to be $\alpha_{\mathrm{H}} = 5$. The variation of the up- and down-switching threshold is for LTR and RTL propagations are depicted in Figure 4-16(e). Reducing the mirror reflectivity increases the asymmetry. So the hysteresis curves separates more from each other in comparison with Figure 4-16(a). The isolation ratio is found to be higher (~ 8) in comparison to the previous two cases.

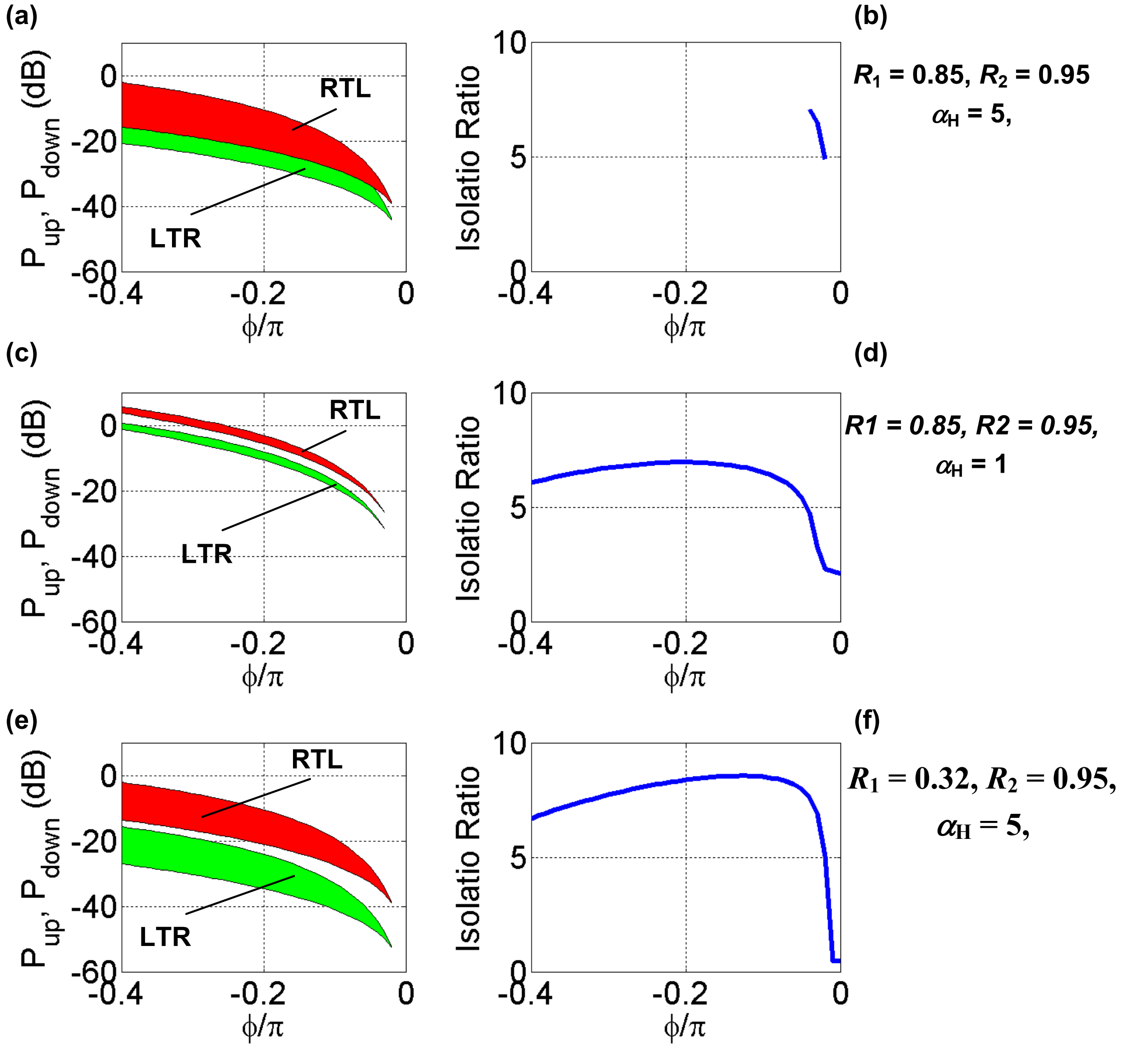

Figure 4-16 : Nonreciprocal behaviour of a SOA-based AFPR. The left column show the variation of the input power and detuning ϕ (corresponding to the offset from frequency resonance), specifying a bistable (shaded) region which is bounded by the up- and down-switching thresholds of an NL-AFPR with SOA in the cavity. The right column show the corresponding variation of maximum isolation ratio with detuning ϕ.

.

4.1.3 Comparison of different types of nonlinearity

In the previous two sections we have discussed the effect of two different types of nonlinear media in the cavity. Here in this section we want to make a comparative study of these two types of nonlinearities with devices having same length. First, we assume an InP SOA gain variation and amplitude-phase coupling via the Henry-factor α_H, but disregard other sources of nonlinearities. Second, we assume for a passive semiconductor that loss depends on TPA, and have a Kerr-type phase nonlinearity. The following parameters are used for actual power calculations:

$$\begin{aligned} \Gamma_{\text{conf}} &= 0.35, \quad L = 300\,\mu\text{m}, \quad g_0 = 150\,\text{cm}^{-1}, \quad \lambda = 1.54\,\mu\text{m}, \\ \alpha_H &= 5, \quad \alpha_2 = 0.8\,\text{cmGW}^{-1}, \quad n_2^I = 0.45\times10^{-4}\,\text{cm}^2\text{GW}^{-1}, \\ \text{FOM}_{\text{TPA}} &= 0.35, \quad P_{\text{sat}} = 10\,\text{mW}. \end{aligned} \tag{4.18}$$

In Figure 4-17(a) we plot the dependence of the nonlinear gain coefficient on the cavity power. Here we have assumed that the linear loss is zero. As expected the gain coefficient g_{NL} decreases monotonously and approaching zero as shown by the red curve. The TPA-induced loss increases linearly with the cavity power. The variation of the nonlinear phase change ϕ_{NL} in the cavity is also plotted in Figure 4-17(b) for a similar case. In the power range considered here the influence of the Kerr-effect induced phase change is relatively weak in comparison to the SOA type nonlinear medium. Comparing the different effects from Figure 4-17 we can conclude that the SOA-type nonlinearity is useful in designing a low power bistable device. The change of gain and phase are both strongly influenced by a small variation of the cavity power. Thus the input power required to observe switching operation can be further lowered by a suitable choice of resonator structures which can efficiently couple more power into the cavity. For a resonator of quality factor Q and volume V it can be shown that the switching power scales with (Q/V) [77]. So a high-Q resonator with highly confined fields should be preferred. Photonic crystal based resonators can offer some of the best available solutions.

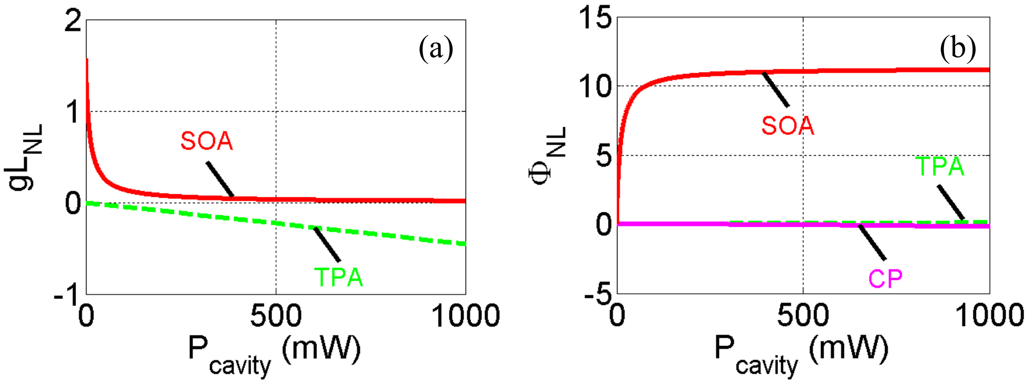

Figure 4-17 : Influence of different types of nonlinearity on (a) the nonlinear gain/loss and (b) the nonlinear phase shift for different values of cavity power.

4.2 Asymmetric periodic structures

In this section we discuss about the nonreciprocal phenomena of some complex structures. We focus the structurally variation properties of a periodic structures in which the inversion symmetry is broken in which case they behave in a nonreciprocal way.

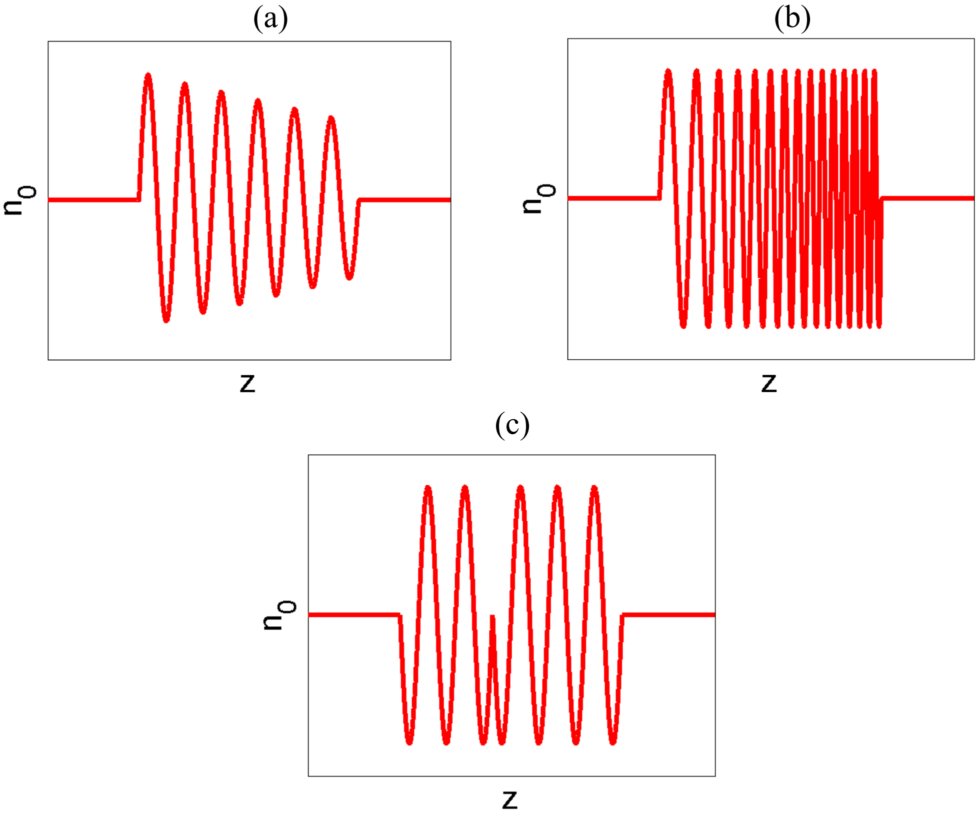

Figure 4-18 : Different type of asymmetries in grating structures. (a) Stopband tapered; (b) Chirped; (c) Asymmetrically placed phase shifted structure.

In a periodic structure there are many possibilities to introduce asymmetry like a tapered periodic structure (see Figure 4-18 (a)), chirp periodic structure (see Figure 4-18 (b)), or an asymmetrically placed phase shift (see Figure 4-18(c)). It is also possible to vary the nonlinear coefficient along the length [52], [15], or to combine them.

4.3 Stopband tapered waveguide Bragg grating [16][43][44]

We consider a grating design of length L, where the effective refractive index $n(z)$ changes both with z according to $n(z) = n_0 + \Delta n_G(z) \cos[(2\pi z / \Lambda(z)) + \Omega(z)]$ (see Figure 4-18) [42]. The grating amplitude $\Delta n_G(z)$ is varied linearly along z. From (2.27) we find that in this case the coupling coefficient κ decreases linearly along the direction of propagation (see Figure 4-1). This leads to a linear decrease of the stopband along the direction of propagation, while the centre of the stopband remains constant at the Bragg wavelength. We define the tapering coefficient $\Delta\kappa$ for a grating of length L by the following expression: The coupling coefficient κ is assumed to vary linearly as a function of z according to

$$\kappa(z) = \kappa(0)\left[1 + \Delta\kappa \frac{z}{L}\right]. \tag{4.19}$$

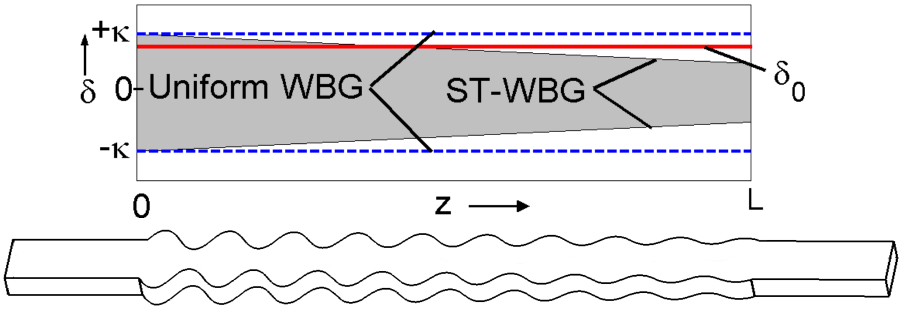

Figure 4-19 : (a) Stopband-tapered waveguide Bragg grating (ST-WBG) of length L. Schematic stopband dependence on z with band edges for uniform grating (– – –), and for ST-WBG (upper and lower boundaries of shaded region), and detuning parameter δ_0 of CW input signal (——). (b) Schematic ST-WBG with varying sidewall corrugations.

Gratings for which $\Delta\kappa < 0$ holds we refer to as negatively tapered (see the shaded region in Figure 4-19), while those for $\Delta\kappa > 0$ holds are positively tapered. The case $\Delta\kappa = 0$ gives the uniform WBG with no tapering (see the region between the dashed lines in Figure 4-19). Here we consider only negative tapering.

4.3.1 Numerical simulations of an active structure [43]

We numerically study the steady state solutions of the generalized nonlinear coupled mode equations (2.60) and (2.61). For steady state calculation we have used transfer matrix method (TMM) (see Appendix B.1 and B.2). In this section we discuss the effect of stopband tapering in an active waveguide grating.

We consider an InP-based WBG with $n_0 = 3.4$, an effective cross section area 0.36 μm^2, a length $L = 300$ μm, and a Bragg wavelength $\lambda_B = 1.55$ μm ($k_B = 2\pi\, n_0 / \lambda_B = \pi / \Lambda$, $\Lambda = 228$ nm). We use $g_0 L = 1.2$, and an alpha-factor $\alpha_H = 5$. The stopband tapering introduces an asymmetry in the structures, and to explore the nonreciprocal behaviour we numerically evaluate (2.60) and (2.61) together with the equation (4.19) for different values of $\Delta\kappa$. We plot the variation of the up- and down-switching threshold as a function of the detuning coefficient in Figure 4-20 for the LTR and RTL propagating cases, for (a) $\Delta\kappa = 0$ %; (b) $\Delta\kappa = -10$ %; (c) $\Delta\kappa = -20$ %; (d) $\Delta\kappa = -30$ %. As the asymmetry increases the curves for LTR and RTL propagations separates from each other, and for relatively high asymmetry of $\Delta\kappa = -30$ % the two curves are completely separated showing a distinct region showing non reciprocity. The hysteresis curves for two directions and for a detuning coefficient of $\delta_0 L = 5$ in plotted in Figure 4-21. The isolation region is marked by shaded filled areas. The RTL input power is found to be 2.7 mW, the output power is 6.8 mW according to Figure 4-20, while the same input power of 2.7 mW for LTR operation leads to an output power of 0.62 mW with an associated isolation ratio of 11.

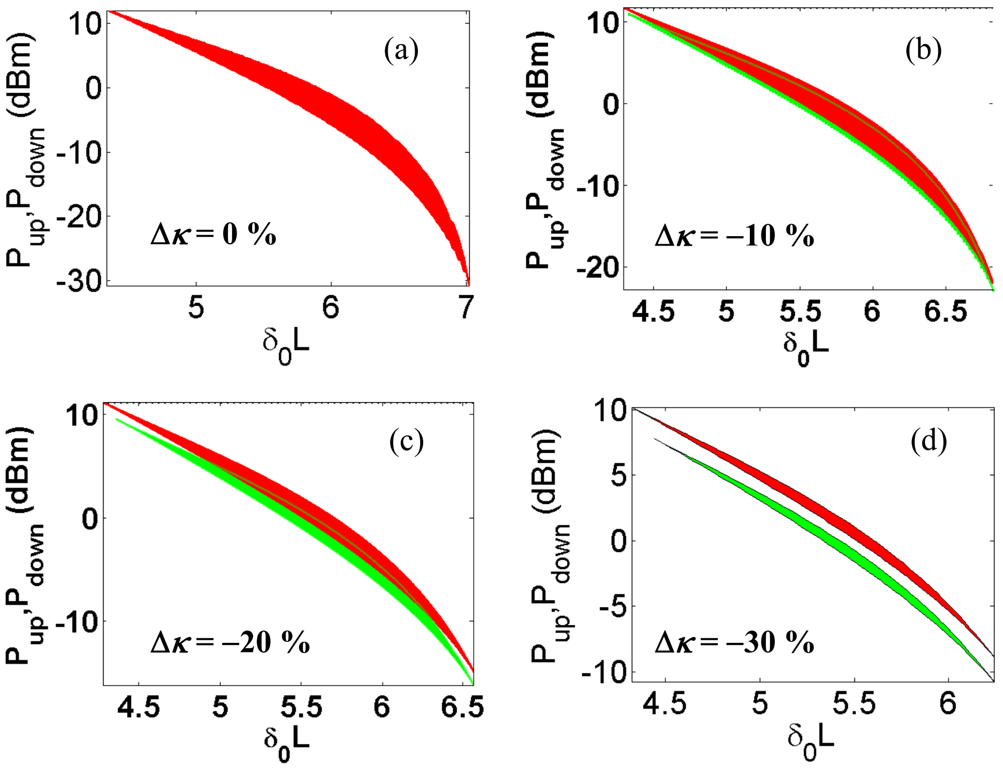

Figure 4-20 : Variation of the switching up and down switching thresholds for (a) $\Delta\kappa = 0$ %; (b) $\Delta\kappa = -10$ %; (c) $\Delta\kappa = -20$ %; (d) $\Delta\kappa = -30$ %. The red and the green curves are for the LTR and RTL propagating cases respectively.

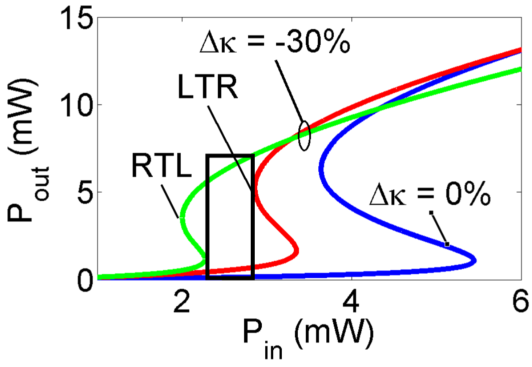

Figure 4-21 : Nonreciprocal behaviour for an active device with $\Delta\kappa = -15$ % and $\delta_0 L = 4.75$

4.3.2 Numerical simulations of passive structure [16]

Also in the passive case we find that with an increase of the negative tapering coefficient the hysteresis curves move away from each other as can be seen from Figure 4-20. Here we have considered a similar structure as in the active case with $\kappa L = 5$, and $\delta_0 L = 4.75$. We have used $\Delta\kappa = -15$ %. We numerically study both the steady state and the time dependent solutions of the generalized nonlinear coupled mode Eq. (2.60). For the steady state calculation we used GTMM (see Appendix B.2) and for the time-dependent solutions we used implicit finite difference scheme (see Appendix B.4). From the numerical simulations we found for the RTL propagation input power of is found 130 mW. The output power is 120 mW according to Figure 4-22, while the same input power of 130 mW for LTR operation leads to an output power of 15 mW with an associated isolation ratio of 8.

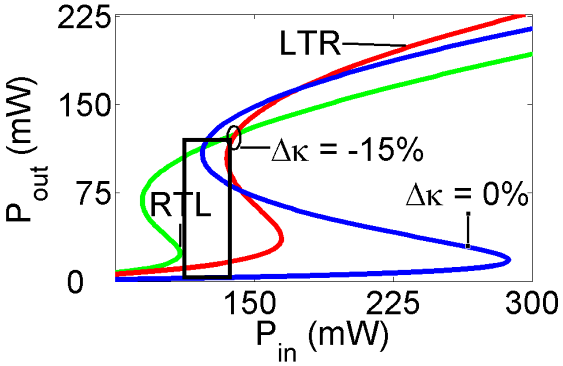

Figure 4-22 : Nonreciprocal behaviour for an passive device with $\Delta\kappa = -15$ % and $\delta_0 \boldsymbol{L} = 4.75$

To get a better understanding of passive ST-WBG we solve the time dependent equations for CW input power of 110 mW which is in the isolation region just above the up-switching threshold of the bistable curve for RTL propagations. We apply a CW signal with smooth transition (see the black curve in Figure 4-23(c)). For RTL propagating case the device goes to the high transmitting state (see the green curve in Figure 4-23 (c)), while for LTR propagation is in the low transmitting state. The field distribution for the LTR and RTL propagating cases is also plotted in Figure 4-23 (a) and (b) respectively. It is to be seen that for RTL propagations the power inside the grating is substantially high, in comparison to the LTR propagating case.

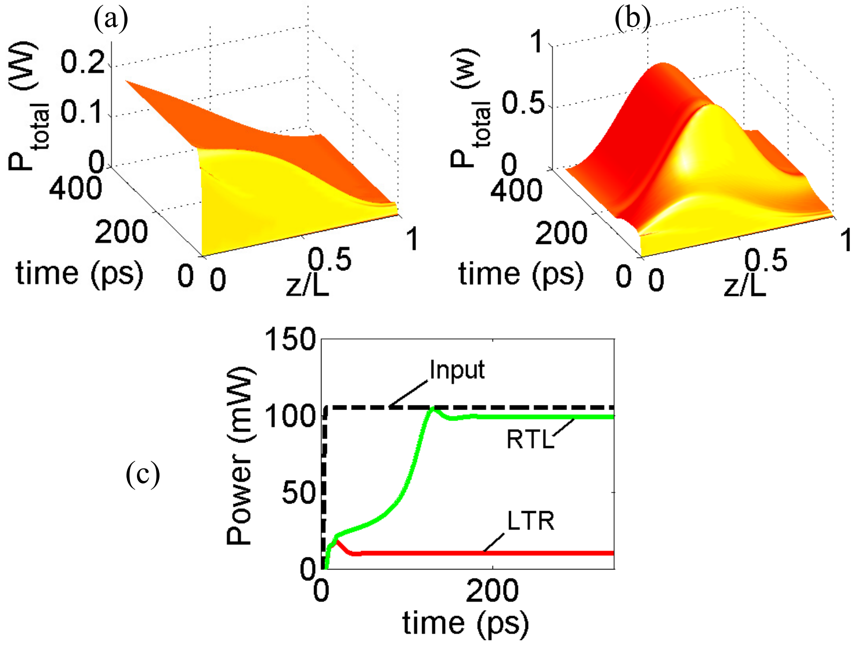

Figure 4-23 : Nonreciprocal behaviour for a passive device with $\Delta\kappa = -15\ \%$ and $\delta_0 L = 4.75$ showing nonreciprocal transmission behaviour. (a) and (b) shows the temporal and spatial variation of intensity inside grating for a the LTR and RTL propagating cases. (c) Temporal dynamics of the transmitted power for LTR and RTL propagations.

Figure 4-24 displays the impulse response of the passive grating with the same detuning $\delta_0 L = 4.75$ as before (within the stopband near its upper edge at $z = 0$) and for an input peak power of 170 mW, either for LTR or RTL operation. The average input power of 85 mW is close to the RTL up-switching threshold in Figure 4-24. For RTL propagation the transmitted impulse is larger (and more compressed because of the high dispersion near the band edge) than for the LTR direction (where the carrier frequency is farther away from the band edge and dispersion is lower). For spectrally broader impulses, a careful optimization of the grating and its operation point are required.

ST-WBG structures essentially are asymmetric structures and all the explanations in section 4.1 qualitatively hold for grating structures. Here we try to give an alternative picture more relevant to periodic structures. We consider the schematic dependencies at $\omega_0 = \omega_T^{\mathrm{RTL}}$ in Figure 4-26. For low input powers the effective local-average index $n_{\mathrm{la}} \propto \Delta n_G$ decreases linearly along the tapered grating (linear Δn_G). Its spatial average n_{avg} over the total grating length is given by the lowest horizontal dashed line (ω_T), where ω_T denotes the associated transmission resonance frequency (lower-left inset). For larger input powers, $n_{\mathrm{la}} \propto \Delta n_G + n_2|E|^2$ increases and shows a hump, upper-most solid line. n_{avg} increases (ω_T^{RTL}), and the transmission resonance is down-shifted from ω_T to ω_T^{RTL} (lower-left inset). The resonant field intensity is shown in the upper-right inset (←). For LTR operation, the field still "sees" a stopband due to the band edge shift and therefore decays exponentially, Figure 4-26 upper-right inset (→). The average refractive index n_{avg} and the transmission resonance still "sees" a stopband due to the band edge shift and therefore decays exponentially, Figure 4-26 upper-right inset (→). The average refractive index n_{avg} and the transmission resonance ω_T^{LTR} (lower-left inset) do not deviate so strongly from ω_T as for RTL operation, so for the same ω_0 the LTR transmission is less than for the RTL case.

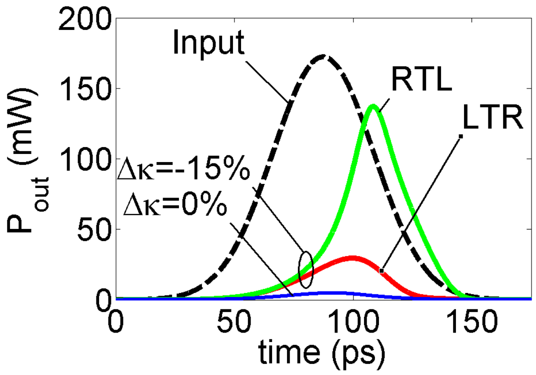

Figure 4-24 : Impulse responses showing nonreciprocal behaviour for a passive device with $\Delta\kappa = -15$ % and $\delta_0 L = 4.75$.

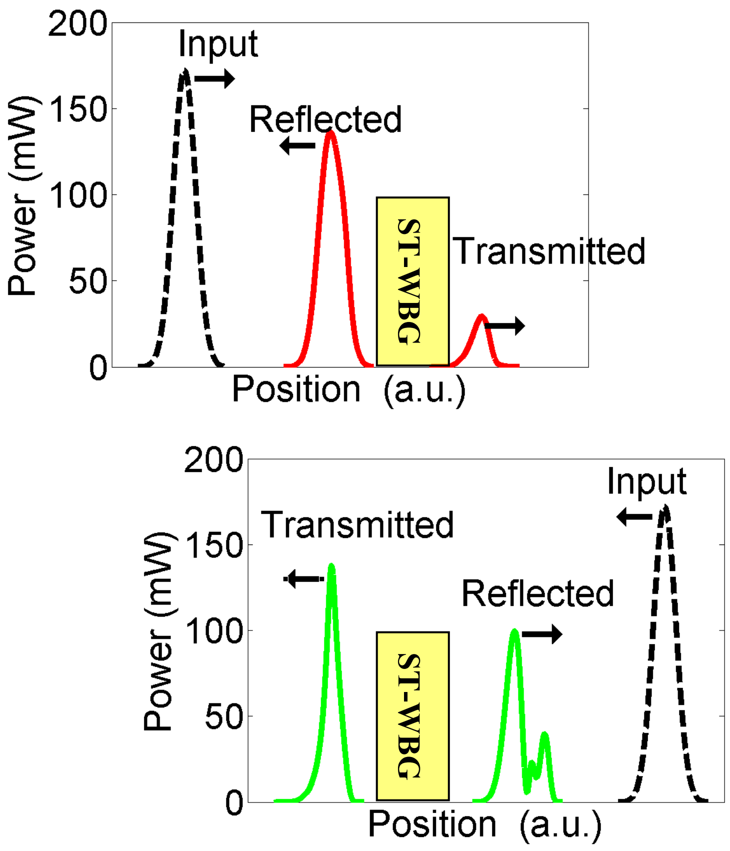

Figure 4-25 : Impulse responses showing nonreciprocal behaviour for the same parameters considered in the Figure 4-24.

The threshold power can further reduced by highly confined structure of SOI. Also from the scaling relation of coupled mode equations (see Section 2.3.1.1 on page 15) we can see that by increasing the length of the device reduces the threshold switching power, but it increases the response time of the device. The isolation ratio and bandwidth can be further enhanced by introducing chirp in conjugation with tapering. We will discuss the effect of chirp and other type of asymmetry in the subsequent sections. In chapter 6 we will show some rigorous numerical calculation based 2D nonlinear FDTD simulation. More complicated variation of the stopband can be also included to optimize the isolation ratio and bandwidth of the nonreciprocal device.

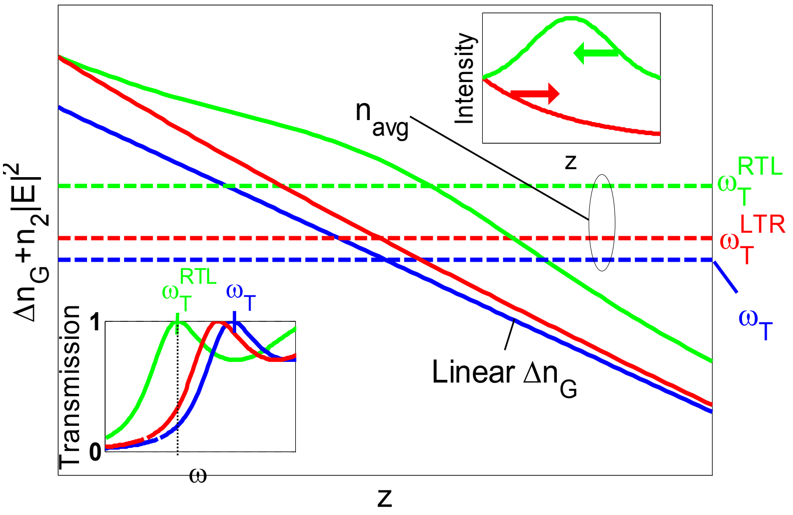

Figure 4-26 : Schematic of locally-averaged refractive index as a function of *z*, CW frequency $\omega_0 = \omega_T^{RTL}$. Low power (—, Linear Δn_G), nonlinear RTL (—) and LTR operation (—). Horizontal dashed lines for spatial average navg over total grating length labelled with respective transmission resonance frequencies ω_T (– –), ω_T^{LTR} (– –), ω_T^{RTL} (– –). Lower-left inset: Power transmission near upper band edge. Top right inset: Intensity for RTL (←) and LTR (→) operation.

4.4 Effect of chirp and other asymmetries in an active device

In this section we consider the effect of chirp and a tapered current density in an active device. Here we introduce C_Λ as a chirp coefficient for a linear variation of the periodicity (see Figure 4-18(b)) along the direction of propagation according to the following expression,

$$\Lambda(z) = \Lambda(0)\left[1 + C_\Lambda \frac{z}{L}\right]. \tag{4.20}$$

Similarly a biased current density of an SOA can also be tapered linearly along the direction of propagation with the help of current taper coefficient ΔJ [76],

$$J_c(z) = J_c(0)\left[1 + \Delta J \frac{z}{L}\right]. \tag{4.21}$$

For the set of parameters $\Delta\kappa = +30\ \%$, $C_\Lambda = -30\ \%$ and $\Delta J = 0\ \%$, $\delta_0 L = 5.5$, $g_0 L = 1.2$. we found a large separation between LTR and RTL propagations. The maximum isolation ratio in this case is 22 from Figure 4-27. In Figure 4-27 the LTR case is represented by the green curve and the RTL case is represented by the red curve.

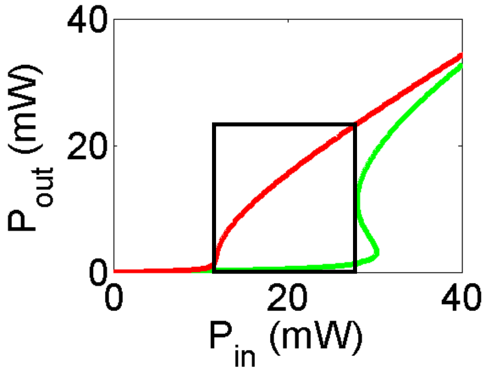

Figure 4-27 : Nonreciprocal behaviour for an active device with $\Delta\kappa = +30$ %, $C_\Lambda = -30$ % and $\Delta J = 0$ %, $\delta_0 L = 5.5$, $g_0 L = 1.2$

We calculate the hysteresis curve for different combinations of $\Delta\kappa$, ΔJ and C_Λ in Figure 4-28. From Figure 4-28 (a) and (b) we observe that by changing C_Λ from +20 % to +30 % the isolation region increases but the range of δ_0L to observe bistability reduces. The negative tapering coefficient and positive chirp coefficient together increases the isolation region (Figure 4-28 (c)) and isolation ratio. The positive current tapering increases the bandwidth but reduces the isolation region (Figure 4-28 (d)).

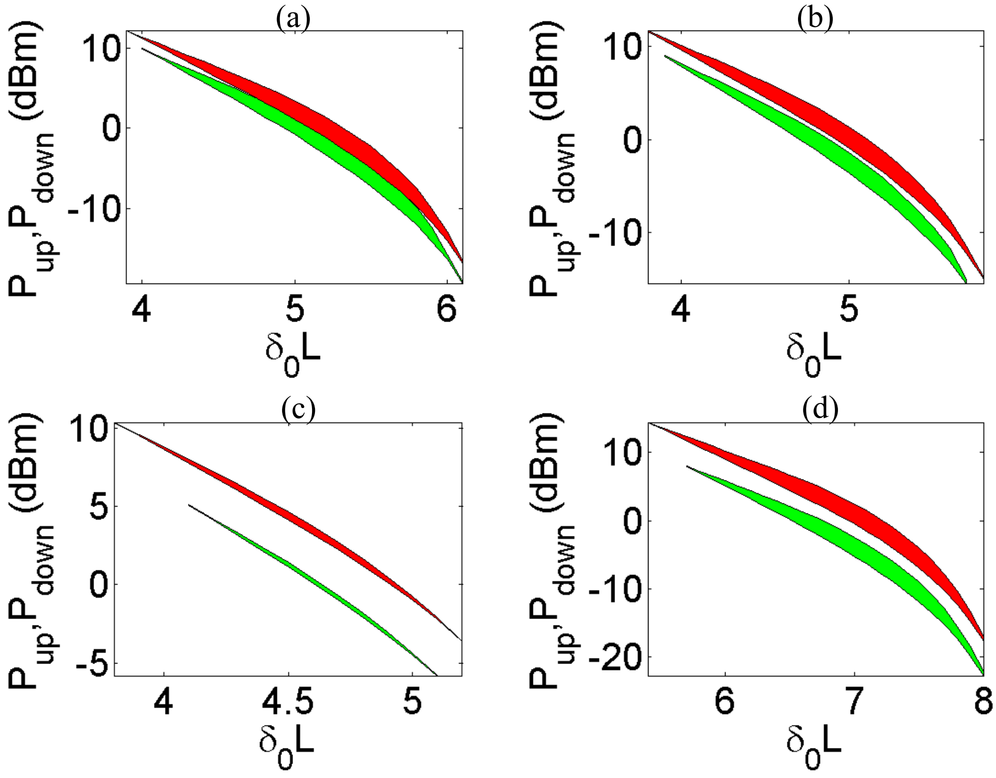

Figure 4-28 : Variation of the up and down switching threshold for an active device with (a) $\Delta\kappa = -10$ %, $C_\Lambda = +20$ % and $\Delta J = 0$ %. (b) $\Delta\kappa = -10$ %, $C_\Lambda = +30$ % and $\Delta J = 0$ %. (c) $\Delta\kappa = -30$ %, $C_\Lambda = +30$ % and $\Delta J = 0$ %. (d) $\Delta\kappa = -10$ %, $C_\Lambda = +20$ % and $\Delta J = -10$ %, $g0L = 1.2$.

4.5 Asymmetrically phase shifted structure [45]

In this section we present an asymmetry placed λ/4 phase shift as another non-reciprocal Kerr-type nonlinear periodic structure (see Figure 4-29) on the basis of an exact solution of the nonlinear coupled mode equations in the steady state. We have discussed the method of GTMM in Appendix B.2. For a λ/4 phase shifted structure the expressions can be simplified and can be written in terms of analytic expressions. We note that this kind of structure is similar to the AFPR discussed in Section 4.1. The phase shift can be introduced by a point defect or by an extended region bounded by two DBR regions.

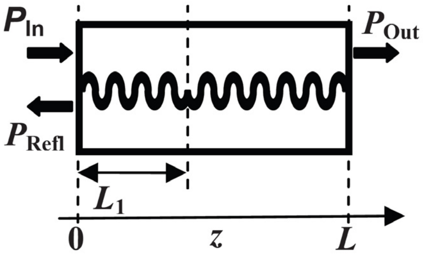

Figure 4-29 : Schematic of periodic structure with a $\lambda/4$ phase-shift at location $z = L_1$

4.5.1 Exact solution of NLCME

We re-write the NLCME for Kerr type of nonlinear Bragg gratings with unit step phase-shift Ω introduced in the grating [52],

$$\begin{aligned}+\frac{\mathrm{d}A_f}{\mathrm{d}z} &= \mathrm{i}\left[\Gamma\left(\left|A_f\right|^2+2\left|A_b\right|^2\right)\right]A_f+\mathrm{i}\kappa\exp\left[-\mathrm{i}\left(2\delta z-\Omega(z)\right)\right]A_b,\\ -\frac{\mathrm{d}A_b}{\mathrm{d}z} &= \mathrm{i}\left[\Gamma\left(\left|A_b\right|^2+2\left|A_f\right|^2\right)\right]A_b+\mathrm{i}\kappa\exp\left[+\mathrm{i}\left(2\delta z-\Omega(z)\right)\right]A_f.\end{aligned} \tag{4.22}$$

The above nonlinear coupled mode equations (NLCME) describe the field distribution in a nonlinear periodic structure. They are a powerful tool in analyzing the response of finite-length uniform or complicated structures, while avoiding the difficulties involved in solving the fully-vectorial wave equations. In general, the coupled mode equations must be solved numerically. In certain limits it is possible to find an analytic solution. Here we use the so called generalized transfer matrix method as described by Radic et al. [60], were the steady state solutions are obtained in terms of the elliptic function formalism [59][60][75]. We consider the phase-shifted structure (Figure 4-29), having uniform periodic regions ($0 \le z \le L_1$ and $L_1 \le z \le L$) with the length of each section given by $L_1 = x\,L$ and $L_2 = (1-x)\,L$. The quantity $x = 0.5$ describes the situation of a symmetrically placed phase shift.

To solve the equations we start with a given value of transmitted field at the output and calculate the corresponding input field. We treat each uniform section denoted by $m = 1, 2$ separately and enforce proper boundary conditions at $z = L_1$. By separating the amplitude and the phase factor of both the forward and backward propagating waves $A_{f,\,b} = A_\pm \exp(\mathrm{i}\phi_\pm)$, it is possible to find two conserved quantities for each section. We introduce a critical intensity

$A_c^2 = 4\lambda n_0/3\pi n_2 L$, and define the normalized forward flux as $J(z) = [A_+(z)/A_c]^2$. The conserved quantities can thus be written in normalized form,

$$\begin{aligned}
\bar{F}_{T,m} &= \left(A_+^{\,2} - A_-^{\,2}\right)\big/A_c^{\,2}, \qquad\qquad m = 1,2 \\
G_m &= \kappa L\sqrt{J\left(J - \bar{F}_{T,m}\right)}\cos\psi_m + \left[\delta L + 2\left(J - \bar{F}_{T,m}\right)\right]J, \\
\frac{\mathrm{d}\bar{F}_{T,m}}{\mathrm{d}z} &= 0, \quad \frac{\mathrm{d}G_m}{\mathrm{d}z} = 0, \\
\psi_m &= 2\delta z + \phi_+ - \phi_- - \Omega\,.
\end{aligned} \tag{4.23}$$

The conserved quantity $\bar{F}_{T,m}$ can be readily identified as the transmitted flux in each section. The conservation of the transmitted flux is justified for a medium without any loss or gain. It can be further shown that the transmitted flux is conserved throughout the structures. So we drop the index 'm' in the $\bar{F}_{T,m}$ and write $\bar{F}_{T,1} = \bar{F}_{T,2} = \bar{F}_T$. In the present study we consider only $\lambda/4$ phase-shifted structures, i.e., in our case we use the change of Ω as π. Using the conserved quantities we write the equation describing the forward intensity inside each of the uniform grating sections as

$$\left(\frac{L}{2}\frac{\mathrm{d}J}{\mathrm{d}z}\right)^2 = (\kappa L)^2 J\left(J - \bar{F}_T\right) - \left[G_m - (\delta L)J - 2\left(J - \bar{F}_T\right)J\right]^2 = P_m(J), \qquad m = 1,2. \tag{4.24}$$

The forward flux can be obtained by integrating the above equation in each section,

$$\int_{J(z)}^{F_T} \frac{\mathrm{d}J}{\sqrt{P_m(J)}} = 2\frac{L_m}{L}. \tag{4.25}$$

The integral on the left hand side is a standard elliptic integral [8] whose solution depends on the parameters κL, δL, G_m, and on the integration limits $J(z)$ and $\bar{F}_T$. The solution can be written in terms of the roots of the 4th-order polynomial $\mathrm{P}_m(J)$. We consider the most frequently encountered case in which all the roots J_i^m (i = 1, 2, 3, 4) of the polynomial $P_m(J)$ are real, and $J_1^m \geq J(z) \geq F_T \geq \mathrm{J}_2^m > J_3^{\mathrm{m}} > J_4^m$ is valid. Since we are interested in the input-output characteristics of the structure, we start with a given value of transmitted intensity $I^{(2)} = F_T$ and calculate the intensity at the section boundary denoted by $I^{(1)} = J(L_1)$. Enforcing proper boundary conditions at $z = L_1$ and using a similar method as above, the input intensity $I^{(0)} = J(0)$ can be calculated. Thus we write the expression for the input intensity in each section boundary in compact notation as

$$\begin{aligned}
I^{(m-1)} &= J_3^{\,m} + \frac{\left(J_2^{\,m} - J_3^{\,m}\right)}{1 - \dfrac{J_1^{\,m} - J_2^{\,m}}{J_1^{\,m} - J_3^{\,m}}\mathrm{sn}^2\left(u^{(m)};k^{(m)}\right)}, \qquad m = 1,2 \\
u^{(m)} &= \mathrm{F}\left(\varphi^{(m)},k^{(m)}\right) - \frac{4L_m}{g^{(m)}L}, \quad g^{(m)} = 2\left[\left(J_1^{\,m} - J_3^{\,m}\right)\left(J_2^{\,m} - J_4^{\,m}\right)\right]^{-1/2}, \\
k^{(m)} &= \frac{g^{(m)}}{2}\left[\left(J_1^{\,m} - J_2^{\,m}\right)\left(J_2^{\,m} - J_4^{\,m}\right)\right]^{1/2}, \quad \sin\varphi^{(m)} = \left[\frac{\left(J_1^{\,m} - J_3^{\,m}\right)\left(I^{(m)} - J_2^{\,m}\right)}{\left(J_1^{\,m} - J_2^{\,m}\right)\left(I^{(m)} - J_3^{\,m}\right)}\right]^{1/2}.
\end{aligned} \tag{4.26}$$

Here, sn($u^{(m)}$; $g^{(m)}$) is a Jacobian elliptic function, sine modulus, defined by the argument $\sin\varphi^{(m)}$ and the modulus $g^{(m)}$, and F($\varphi^{(m)}$, $k^{(m)}$) is the incomplete elliptic integral of first kind. The above expressions can be greatly simplified for the special case $\delta_0 L = 0$,

$$I^{(1)} = \frac{F_T}{2}\left[1 + \mathrm{nd}\left(u^{(2)}, k^{(2)}\right)\right],$$

$$u^{(2)} = \sqrt{{F_T}^2 + (\kappa L)^2}, \quad k^{(2)} = \left[1 + \left(\frac{F_T}{\kappa L}\right)^2\right]^{-1/2}, \tag{4.27}$$

$$I^{(0)} = {J_3}^1 + \frac{\left({J_2}^1 - {J_3}^1\right)}{1 - \frac{J_1^1 - J_2^1}{J_1^1 - J_3^1}\,\mathrm{sn}^2\left(u^{(1)}; k^{(1)}\right)} = f\left(\kappa L, \delta L, F_T, x\right),$$

$$u^{(1)} = \mathrm{F}\left(\varphi^{(1)}, k^{(1)}\right) - \frac{8x}{g^{(1)}}, \quad g^{(1)} = 2\left[\left(J_1^{(1)} - J_3^{(1)}\right)\left(J_2^{(1)} - J_4^{(1)}\right)\right]^{-1/2}, \tag{4.28}$$

$$\sin\varphi^{(1)} = \left[\frac{\left(J_1^1 - J_3^1\right)\left(I^{(1)} - J_2^1\right)}{\left(J_1^1 - J_2^1\right)\left(I^{(1)} - J_3^1\right)}\right]^{1/2}.$$

So we can calculate the input-output characteristics of the structure for $\delta_0 L = 0$ using the analytic expression given in Eq. (4.28). For $\delta_0 L \neq 0$, equations (4.26) should be used. With this formulation it is also possible to calculate the fields inside the grating structure.

4.5.2 Non-reciprocal behaviour

We now consider the case in which the same incident signal is propagating either from left-to-right (LTR) or from right-to-left (RTL). It is interesting to note that in an asymmetric structure with $L_1 \neq 0.5L$, and if the same input power is injected from LTR or from RTL direction, the transmitted powers are different (see Figure 4-30). This effect can be physically understood by looking at the penetration depth of the input field, which is different if the light is incident from different directions. Different penetration depths result in different nonlinear shifts in the resonance frequencies, which in turn lead to a non-reciprocal behaviour. Different signal propagation directions, LTR or RTL can be easily implemented using $L_1 = x\,L$ and $L_1 = (1 - x)\,L$, respectively. It is evident that for a symmetrically placed phase shift with $x = 0.5$ and for a given value of $\bar{F}_T$ the solution of $I^{(1)}$ and subsequently $I^{(0)}$ are the same for RTL and LTR propagation. For $x \neq 0.5$ the value of $I^{(1)}$ and subsequently $I^{(0)}$ is different for LTR or RTL propagation as can be seen in Figure 4-30 shows the variation of the transmissivity with respect to the normalized input power for a structure with $\kappa L = 4$ and a signal detuning coefficient of $\delta_0 L = 0$. The solid line and the broken lines represent structures with $L_1 = 0.5L$ and $L_1 = 0.4L$, respectively. Figure 4-30 (c) displays the bistable transmission curves for LTR (– · –) and RTL (– –) operation. We use $P_{\mathrm{ref}} = 1.3$ W as a reference power for an InP based structure with L = 600 µm and operating wavelengths near $\lambda = 1.55$ µm. The shaded region in Figure 4-30 (c) shows the isolation regime, in which the device is in the high transmission state for an LTR propagating signal, while it is in the low transmission state for an RTL propagating signal. It is to be also observed that for $\delta_0 L = 0$ the effect is reversed, i.e., RTL transmission is always higher than the LTR transmission as can be seen from Fig. 1b. This non-reciprocal effect can be utilized for optical isolation.

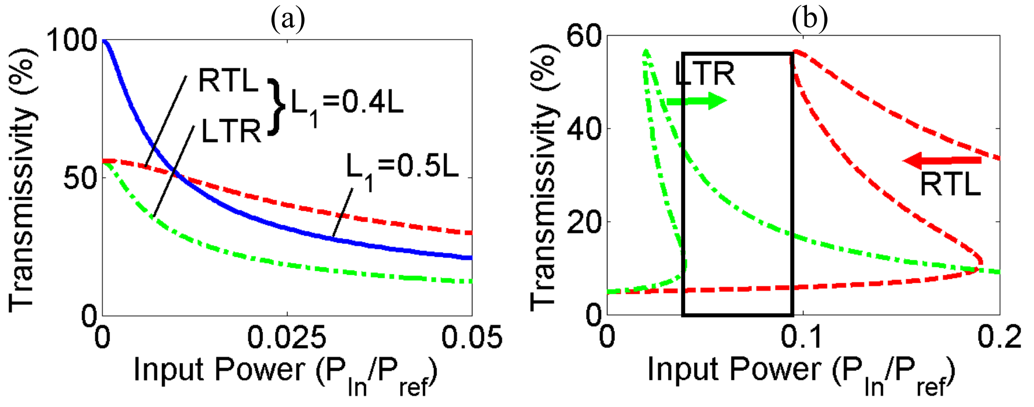

Figure 4-30 : (a) Variation of the transmissivity with normalized input power for $\kappa L = 4$ and $\delta_0 L = 0$, and for symmetric (solid line) and asymmetric $\lambda/4$ phase-shifted structures (broken lines). (b) Bistable curves for the same structure with $\delta_0 L = -0.70$. Reference power $P_{\text{ref}} = 1.3$ W.

•

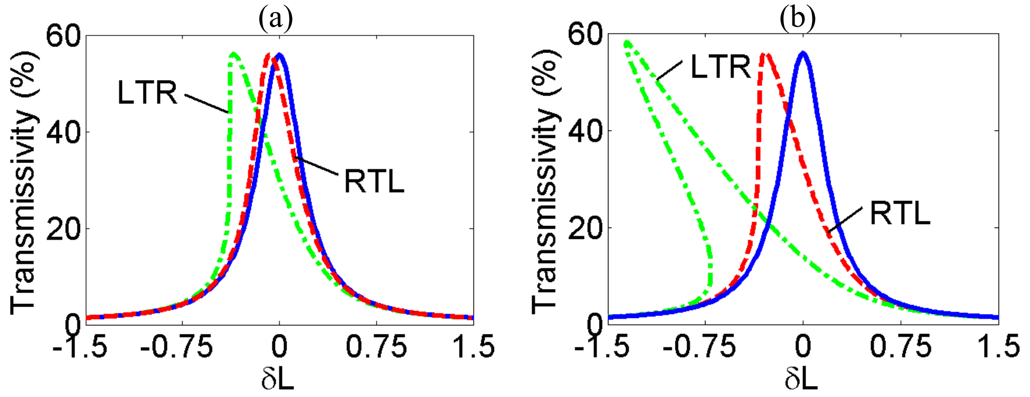

Figure 4-31 : Transmission curve for a $\lambda/4$ phase-shifted structure at location $z = L_1$ for different values of input power showing a direction dependent bending of the transmission curve. (a) Variation of the transmissivity with normalized detuning for $\kappa L = 4$ with $P_{\text{In}}/P_{\text{ref}} = 0.01$, and (b) with $P_{\text{In}}/P_{\text{ref}} = 0.04$. The solid blue line represents the transmissivity of the structure in the linear case. Reference power $P_{\text{ref}} = 1.3$ W.

From Figure 4-30(b) we find a maximum isolation ratio of 3 and 7, respectively. This isolation ratio is less in comparison to standard Faraday-effect based isolators, but it is possible to improve this extinction ratio by optimizing different axial asymmetries (e.g. bandgap taper, chirp, and phase-shift).

The dependence of the refractive index on the input power leads to a power dependent change in the shape of the transmission curve as can be seen from Figure 4-31. Here we plot the transmission curve for LTR (– · –) and RTL (– –) operation for two different values of input powers, namely (a) $P_{\text{In}}/P_{\text{ref}} = 0.01$, and (b) $P_{\text{In}}/P_{\text{ref}} = 0.04$. The solid line represents the transmission curve for the linear case. It is observed that with increasing input power the resonant frequency shifts more towards the lower frequency side. Above a certain threshold power, the transmission curve becomes bistable. The shift in the resonance frequency for LTR operation is more pronounced than the one for RTL operation.

From the above results it is evident that due to a nonlinear shift in the resonance frequency bistability is observed in the input-output power characteristic and in the transmission curve. For a phase-shifted structure the bandwidth is usually small due to the high Q-factor at resonance.

4.6 Summary

In this chapter we have introduced a general theory of nonreciprocal transmission in a nonlinear periodic structure. In presence of nonlinearity any resonator structure lacking inversion symmetry shows a non-reciprocal behaviour. The general description of the theory enables us in designing a device which shows a isolation or “optical diode” like phenomena. We have studied this phenomena for asymmetric Fabry-Perot resonator, stopband tapered Bragg grating, asymmetrically phase shifted isolator phaseThis theory is applicable to wide variety of nonlinearity like Kerr, SOA, TPA, carrier-plasma effects, thermal nonlinearity. This formulation can be extended to negative index material, saturable absorber or all combined nonlinear effects. This simplified formulation is applicable to photonic crystal based resonator and can be also extended to ring resonators.

5 Lowering of switching threshold

Compact all-optical switches and logic gates are of high interest in view of their applications in future packet-switched networks. A leading candidate for such devices are resonator structures based on nonlinear materials[72] [33], which shows bistable behaviour [61] with regard to the intensity of the input beam. In this device switching between the low and high transmission states can be achieved within a very small length scale, which allows a compact design. However, owing to the very small value of the nonlinear coefficient in most optical materials (including silica fibers), the power required to observe any detectable shift in the stopband (the switching threshold) is very high [5]. Unless the power requirement can be somehow reduced, these devices will remain unsuitable for commercial applications.

To overcome this difficulty a few remedies have been proposed [51][59][38][47], that either use materials with higher nonlinearities or some sort of field enhancement to increase the nonlinear effects. In particular it was observed [51][59][38] that the threshold power can be reduced substantially by using a $\lambda/4$ shifted grating, where a defect is created in the grating's interior. This opens a narrow transmission band within the stopband. Owing to the reduced group velocity for this transmission band, the interaction time increases and nonlinear effects are more pronounced, leading to a reduction of the threshold switching power. However, the price paid for this improvement is a lowering of the extinction ratio for this design.

Here we propose an alternative approach based on asymmetry in the resonator structures as discussed in the previous chapter. This design significantly reduces the switching power, while retaining a serviceable extinction ratio over a wide range of parameters. In this section we discuss the possibility of lowering switching threshold by a proper geometric design.

5.1 Passive stopband tapered waveguide Bragg grating [43][16]

The stopband tapered waveguide Bragg grating (STWBG) (see Figure 5-1) is introduced in section 0. Here we focus on the issues of lowering the switching threshold for bistable operation. We first consider the passive structure as considered in Section 4.3.2. Here we use the same parameters as discussed in Section 3.2.1. As discussed before the refractive index at each point in the grating is modified by the field intensity through the nonlinear refractive index, which leads to the variation of the band edges. For non-zero tapering there is an additional modification of the local band edges that comes from the changing grating amplitude (see Figure 5-4 and Figure 5-5). Different regions of the bistable curve can be understood by considering the dynamic behaviour of these local band edges within the grating. We will review the bistable switching phenomena again here with comparison to the uniform grating to explain the physics of lowering the switching threshold.

In the low intensity limit, an incoming wave does not appreciably alter the position of the local band edges, and decays exponentially (see Figure 5-4(a)) if its frequency lies within the stopband ($|\delta| < \kappa$). In a finite grating structure the exponential tail reaches the back of the grating, leading to non-zero but low transmission. For negative tapering the stopband is wider at the front of the grating than at the back of the structure (see the dashed curves in Figure 5-1 with reference to the dotted CW line), and a larger negative tapering coefficient Δκ leads to a proportional increase of the "transparent" region (see Figure 5-1) near the back of the structure for the CW signal. For relatively high magnitudes of the negative tapering coefficient |Δκ| the CW wave can propagate outside the stopband near the rear of the structure even for low intensities. This leads to generally higher transmissions, in the low-intensity case, for negatively tapered gratings, as can be seen in Figure 5-2.

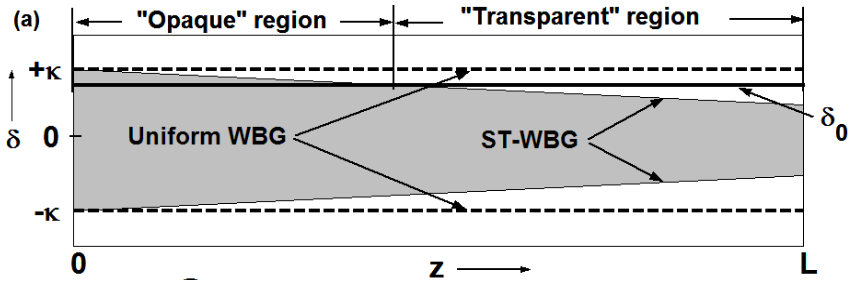

Figure 5-1 : Schematic diagram showing the variation of the stopband as a function of position *z* inside the grating of length *L*. The dashed lines give the band edges for a uniform grating. The lines bounding the shaded region show the stopgap variation for a ST-WBG. The solid line gives the detuning parameter of the CW input signal. The marked regions show the so called "opaque" and "transparent" regions of the grating, corresponding to the CW signal.

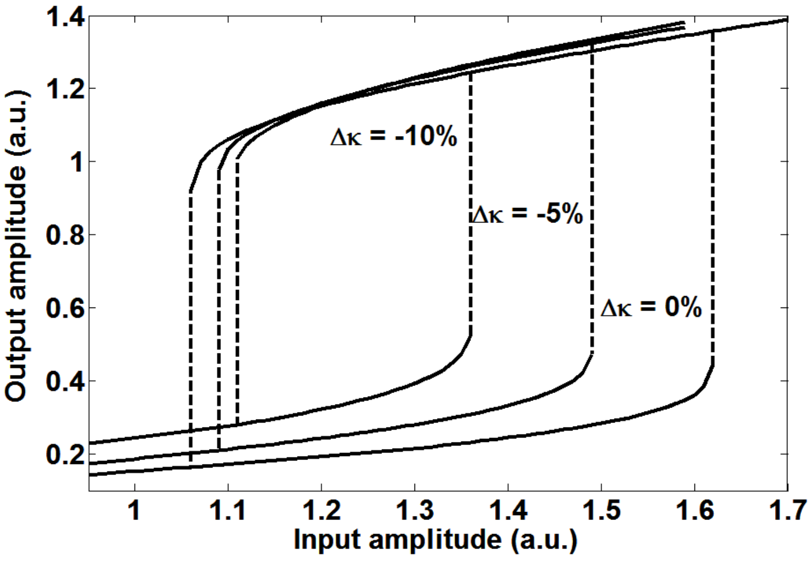

Figure 5-2 : Bistable curves for different tapering coefficients.

With the increase in input intensity, the local band edges are shifted to a lower frequency (see Figure 5-4), and so the penetration depth of the signal into the stopband increases, leading to an increase in the transmission coefficient. Near the up-switching threshold, where the frequency of the local upper-band edge at the rear of the grating equals the frequency corresponding to the detuning parameter of the CW signal, and the wave is able to propagate outside the gap over the entire length of the grating. With an increase in the tapering magnitude, the size of the transparent region at the rear of the grating is increased proportionally, and so the up-switching threshold is reached at a lower intensity. The result is a near-linear decrease in the up-switching threshold with respect to tapering magnitude, as observed in Figure 5-3. This effect is more prominent if the detuning is chosen close to the upper-band edge.

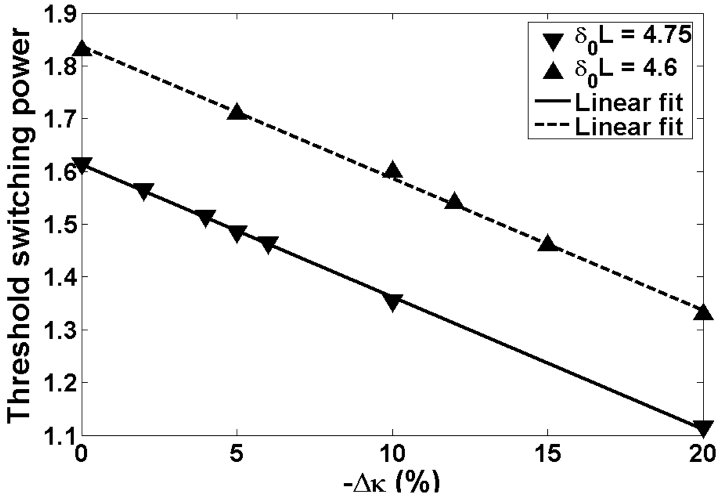

Figure 5-3 : The threshold switching power for the ST-FBG, which decreases linearly with the negative tapering coefficient for detuning coefficients $\delta_0 L = 4.75$ and $\delta_0 L = 4.6$.

If the input intensity is then reduced the system does not directly return to the low intensity state. We observe that the high field intensity creates a local "barrier" (see Figure 5-5(b), (c)) near the front end of the structure. With a gradual decrease of the input intensity, it is observed that the local barrier is lowered and the output intensity decreases. At the down-switching threshold this barrier disappears, and the system switches back to the low transmitting state. Because the barrier occurs at the front of the grating where the influence of the tapering is small, its height and extension are not significantly affected by the tapering, and so the down-switching threshold is close to that of the uniform grating.

To estimate the required intensity levels for bistable operation we consider a standard single mode fiber of effective area $A_{\mathrm{eff}} = 50\ \mu\mathrm{m}^2$ at a wavelength of 1.55 μm. The up-switching threshold intensity for a grating with $\kappa = 5\ \mathrm{cm}^{-1}$, $L = 1$ cm is found to be 2.6 GW/cm^2 (corresponding to a power level of 1.28 kW). The tapered design ($\Delta\kappa = -10\%$) can reduce the threshold intensity to 1.7 GW/cm^2 (corresponding to a power level of 0.8 kW). This power level is still too high for actual device application. The power levels can be reduced in a highly nonlinear fiber where the effective nonlinearity $\gamma = \omega_0 n_2^I/(cA_{\mathrm{eff}})$ is of the order of 10^3 larger ($\gamma \sim 1360\ \mathrm{W}^{-1}\mathrm{km}^{-1}$) [70] than in a standard silica based fiber ($\gamma \sim 2.7\ \mathrm{W}^{-1}\mathrm{km}^{-1}$). Photonic crystal fibers with higher nonlinearity ($\gamma \sim 675\ \mathrm{W}^{-1}\mathrm{km}^{-1}$) [52] could also be used to reduce the threshold switching power. Semiconductor DFB structures having higher nonlinear coefficients could also be employed. For example, in InP the nonlinear coefficient is $\sim 10^4$ times larger than in silica [23], and the effective area for a pedestal waveguide is in the order of 0.4 μm^2. A linearly tapered Bragg grating structure in InP will operate at a switching power level of the order of $\sim 10^6$ lower (i.e. in the order of a few tens of mW) than in a silica-based device. For this power level the two-photon absorption in InP is still quite low ($\sim 0.01\ \mathrm{cm}^{-1}$) [23]and can be neglected in comparison to the loss in a real device.

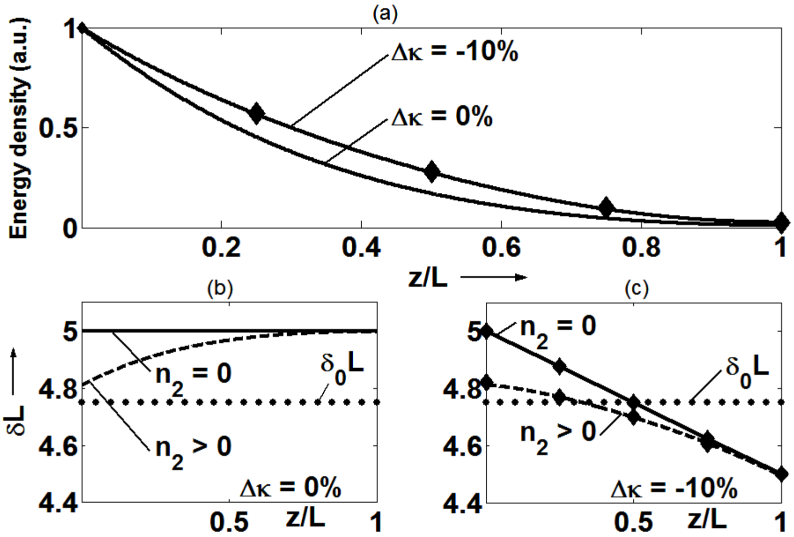

Figure 5-4 : Low transmission state: a) Energy density inside the grating for different tapering coefficients, $\Delta\kappa = 0\%$ (—) and $\Delta\kappa = -10\%$ (–♦–). The energy density is normalised to the peak value. (b) *Upper-band edge* of the stopgap for the uniform grating, with $\Delta\kappa = 0\%$. The solid line gives the upper-band edge for $n_2^I = 0$, the dashed line shows the local band edge. c) upper band edge for the ST-WBG, with $\Delta\kappa = -10\%$. The horizontal dotted line shows the detuning $\delta_0 L$.

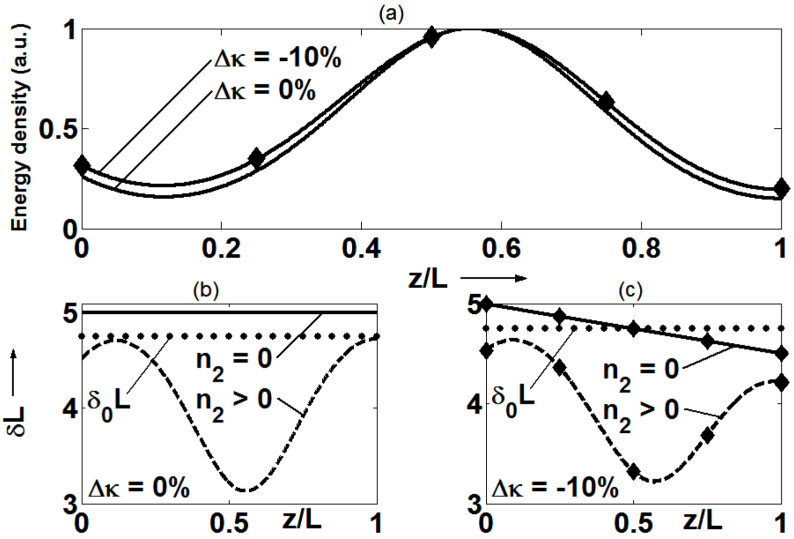

Figure 5-5 : High transmission state: a) Energy density inside the grating for different tapering coefficients, $\Delta\kappa = 0\%$ (—) and $\Delta\kappa = -10\%$ (–♦–). The energy density is normalised to the peak value. (b) *Upper-band edge* of the stopgap for the uniform grating, with $\Delta\kappa = 0\%$. The solid line gives the upper-band edge for $n_2^I = 0$, the dashed line shows the local band edge. c) upper band edge for the ST-WBG, with $\Delta\kappa = -10\%$. The horizontal dotted line shows the detuning $\delta_0 L$.

Using gratings of longer length increases the interaction time and is another option for the reduction of switching power. The switching time is also increased with increase in the length. In SOI based structure the high field confinement enhances the nonlinearity

($\gamma = 3.5\ \mathrm{W}^{-1}\mathrm{cm}^{-1}$[36]) is reported. But the TPA can degrade the switching threshold significantly in SOI based devices.

5.2 Active Stopband tapered waveguide Bragg grating [43]

For active device we solve the steady state NLCME with the same parameter as given in section 3.1.3.1. We use the normalized coupling coefficient $\kappa(0)L = 3$, the normalized gain coefficient $g_0L = 1.2$, the normalized internal loss $\alpha_{\mathrm{int}}L = 0$, and the linewidth enhancement factor $\alpha_H = 5$. Figure 5-6 shows the bistable behaviour of the ST-DFB-SOA over a range of tapering coefficients $\Delta\kappa$. By comparison with the uniform DFB-SOA (given by the curve $\Delta\kappa = 0\%$ in Figure 5-6) it is observed that tapering decreases the up-switching threshold significantly. The down-switching threshold also decreases with increasing $|\Delta\kappa|$, however the variation is relatively small. It is also observed that the extinction ratio remains high over a large range of tapering coefficients. We plot the variation of the up-switching threshold and down- switching threshold with the detuning coefficient in Figure 5-7. We see that for all values of detuning the switching threshold is reduced with high magnitudes of the negative tapering coefficient $|\Delta\kappa|$.

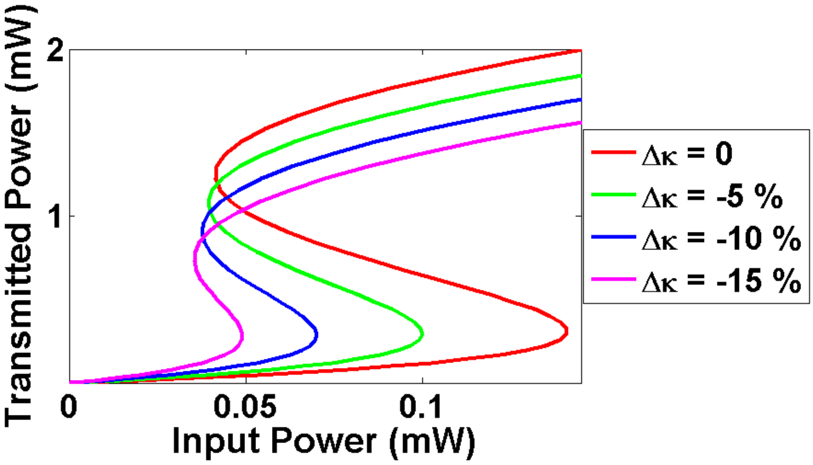

Figure 5-6 : S-curves of ST-DFB SOA for different tapering coefficients Δκ, where the normalized gain coefficient $g_0L = 1.2$, the normalized internal loss $\alpha_{\mathrm{int}}L = 0$, and the normalized detuning coefficient $\delta_0L = 6.5$.

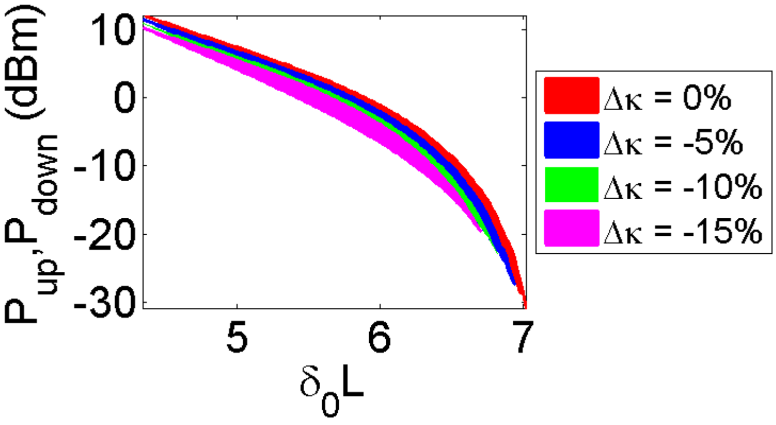

Figure 5-7 : Variation of the up and down switching threshold with the detuning coefficient for the same parameters consider in Figure 5-6

5.3 Asymmetrically phase shifted structure [45]

The asymmetrically phase shifted structure (See 4.5 for details) also reduce the switching threshold. We plot for different the Transmission bistable curve for different location of asymmetric phase shift in Figure 5-8. In this type of device the increasing asymmetry reduces the switching threshold accompanied by strong reduction of extinction ratio.

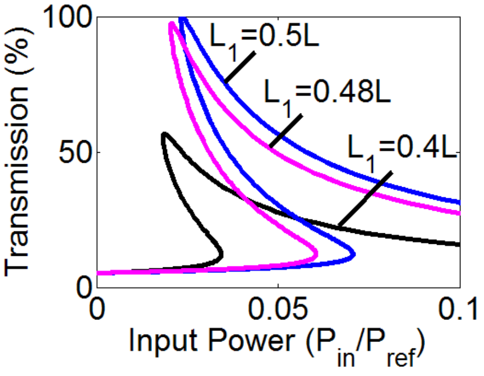

Figure 5-8 : S-curve of asymmetrically phase shifted structure for different value of L_1 for RTL propagation.

5.4 Asymmetric Fabry-Perot resonator

To explain the effect in terms of the simplified model of asymmetric Fabry-Perot resonator as in section 4.1. We look in the graphical solution for the symmetric case of $R_1 = R_2$ and for the asymmetric case of $R_1 \neq R_2$ in Figure 5-9. The red line represents the symmetric case, while the blue and green line represents the case $R_1 > R_2$ and $R_1 < R_2$ respectively. The black dotted line shows the case $P_{avg} = P_{in}$. We see that for $R_1 > R_2$ the up switching threshold is much lower than symmetric case. The asymmetrically phase shifted structure also show the similar behaviour.

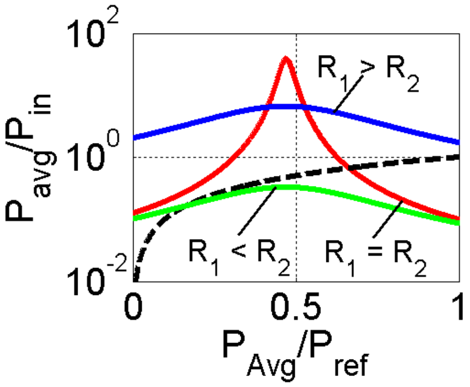

Figure 5-9 : Graphical solution of NL-AFPR with $L = 100$ µm, $\alpha_{\text{int}} = 0$ dB/cm. The red line represents the case of $R_1 = 0.95$, $R_2 = 0.95$. The blue line represents the case of $R_1 = 0.95$, $R_2 = 0.32$. The green line represents the case of $R_1 = 0.32$, $R_2 = 0.95$. The black dotted line corresponding to $P_{\text{In}} = P_{Avg}$. TPA is neglected.

5.5 Summary

In this chapter we have introduced different type of asymmetries in the resonator structures. We found in all cases the up-switching threshold is reduced in comparison to the symmetric structure. In phase shifted structure and AFPR we can observe strong reduction of the extinction ratio. For ST-WBG we found that with the increase in negative tapering coefficient the extinction ratio remain high for a large range of parameters. Other structural variation like chirp and current density taper also reduce the switching threshold. With proper optimization with all this asymmetry it is be possible to reduce the switching threshold further. We could also use an all optical limiter [64] after this bistable device to increase the extinction ratio.

6 Nonlinear FDTD simulation

6.1 Introduction[20]

Compact and integrated optical devices are of particular importance for the realization of faster and more affordable communication technologies. Among various optical devices, all-optical switches and logic gates are the key components for the ultra-fast optical signal processing [73][44][16]. It is well known that these functionalities are realized by optical bistability in periodic nonlinear media [10][68][67][63][15] and its asymmetric variations [32]. However, previous literature address one-dimensional (1D) simple structures having weak perturbation and those analyzed by either a transfer-matrix method or coupled mode equations.

Some authors apply the pseudo-spectral time domain method to a 1D left-handed multilayer system [15]. Others apply the nonlinear finite-difference time-domain (FDTD) method to a 1D weakly modulated multilayer structure [40], and also to asymmetrically arranged photonic crystal defects in a slab waveguide [41]. However, the light intensity required for the nonlinear switching operation is nevertheless found still orders of magnitude higher than are in real with widely available experimental setups. Recently, very low switching-threshold operation has been achieved in photonic crystal bistable nano-cavities by employing two-photon absorption (TPA) in Si [54]. A disadvantage of TPA is that the switching speed is much slower than that of the nonlinearity of electronic origin [67]. It would therefore be desirable to clarify possible conditions with which minimum switching power is achieved for particular realistic device structures and materials while retaining a sufficient speed of operation.

Here we investigate numerically an optical Schmitt trigger [64] operation in a longitudinally asymmetric WBG. These WBGs have also the property of non-reciprocal transmission where the switching threshold in one direction is lower than that in the other direction. The analyzed WBG has a structure that can be actually fabricated by employing an optical planar circuit technology based on a InGaAsP/InP system with strong nonlinearity [17] [35]. The sidewall modulation of this structure is strong, and the coupled mode equations may not be directly applied due to the strong coupling between the forward and the backward waves [44] [67]. Therefore, analysis has been performed fully numerically with the nonlinear finite-difference time-domain (FDTD) method that inherently deals with the necessary coupling and guiding effects of the WBGs; the code has been developed by the authors, and it runs effectively on parallel cluster computers [17]. Some authors have addressed an instability issue in nonlinear periodic structures [67][15][32]. In this respect we have investigated the field inside the grating using either the simple optical Kerr nonlinearity and damped Lorentz dispersion [17] [35], or the soft-core Coulomb potential as a stable numerical model of the saturable nonlinear mechanism of bound electrons [34]. The behaviour of the chaotic states in the nonlinear WBG is discussed qualitatively.

---

[20] The numerical simulation discussed in this chapter has been performed by the first author of [19]. However the design of such waveguide and the idea was proposed by the author of this thesis.

6.1.1 Asymmetric waveguide Bragg grating

The asymmetric WBG has been modelled such that the stopband of the grating has a nearly linear profile along the waveguide. The grating is realized by a sidewall periodic perturbation of a dielectric waveguide whose top view and cross section are shown in Figure 6-1(a) and (b), respectively. The sidewall modulation is expressed by a function of distance z as

$$x(z) = \pm\left[\frac{W}{2} + \frac{W_g}{2} g(z/L) \sin\left(\frac{2\pi z}{\Lambda}\right)\right], \tag{4.29}$$

where Λ is the period of the grating chosen to be $\Lambda = 0.241$ µm for this paper, and L_0 is the total length of the grating. The averaged width of the waveguide was chosen to be $W = 0.4$ µm such that it supports only the dominant propagation mode at the operating frequency. The maximum amplitude of the sidewall modulation is determined by $W_g/2$. The nearly linear variation of the band edge frequency is described by a 3rd-order polynomial in terms of the normalized distance $z' = z/L_0$ as $g(z') = a(z')^3 + b(z')^2 + c(z') + d$, whose coefficients have been found by fitting the polynomial to some FDTD results of stopbands for uniform waveguide gratings as shown in Figure 6-2; they are chosen to be $a = -0.4856$, $b = -0.0009$, $c = 0$, and $d = 1$, and the resulting profile of the upper band-edge frequency for $W_g = 0.1$ μm is shown in Figure 6-1 (c). With this profile the sidewall modulation amplitude varies nonlinearly from $W_g/2$ at the left-hand-side of the waveguide to $W_g/4$ at the right-hand-side of the waveguide.

For the numerical model, the actual variation of the band-gap frequency is approximated by a stair-cased finite-difference discretization. Due to the restriction of the computational resource, the cell sizes have been chosen to be $\Delta x = 0.025$ µm and $\Delta z = \Lambda/10 = 0.0241$ μm. Note that Δx is comparable to the side wall modulation, and it may appear too coarse to resolve the depth of the modulation. However, Δz is sufficiently small to resolve the periodic variation of the grating. We have therefore checked in preliminary analyses that the present cell size can resolve the side-wall modulation sufficiently for the purpose to realize the nearly linear profile of the band edge frequency.

We define the direction of light transmission as follows: when a light is transmitted from left to right (LTR), it goes through a waveguide having a negatively varying stopband (the stopband width is decreasing). In contrast, when light is transmitted from right to left (RTL), it goes through a waveguide having a positively varying stopband (the stopband width is increasing). We emphasize that the sidewall modulation chosen in this paper is much stronger than that in previous literature in order to reduce the length of the WBG and the required incident light power for switching.

The waveguide has a three-dimensional (3D) pedestal waveguide structure as in Figure 6-1, which consists of InP (refractive index $n = 3.17$ at wavelength $\lambda = 1.55$ µm) for the upper and the lower cladding, InGaAsP ($n = 3.42$ at the same wavelength) for the core, and surrounding air. For the numerical representation, the structure is approximated by a dielectric slab of $n = 3.34$ to be analyzed by a 2D FDTD method. The polarization of the incident light is quasi-TM where the dominant electric field component is perpendicular to the substrate. We employ the same fabrication and design procedures used in [61] [44]. The third-order nonlinear susceptibility for InGaAsP core has been confirmed to be $\chi_0^{(3)} = 3.8\times10^{-18}$ m^2/V^2 by our extensive numerical and experimental investigations [17] [35].

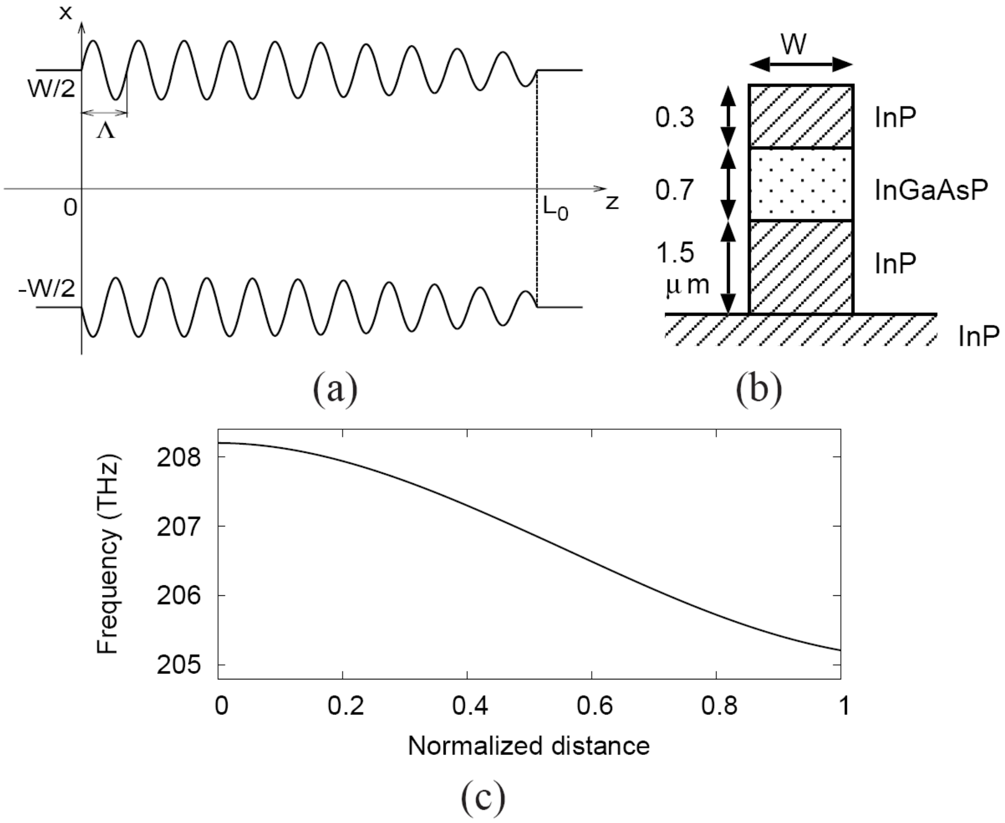

(a) (b)

(c)

Figure 6-1 : Schematic configuration of the waveguide Bragg grating having an asymmetric stop-band; (a) the top view, and (b) the cross section of the waveguide. In the analysis the structure is approximated by a slab waveguide having an effective refractive index of the stacked structure. The ports for signal detection are located at a half hight of the InGaAsP core and at $(x, z) = (0,0)$ and $(0, L_0)$. (c) An example of the upper band-edge frequency variation realized by the third-order polynomial $g(z')$ for $W_g = 0.1$ μm

6.1.2 FDTD analysis of WBG

We apply Yee's FDTD algorithm to Maxwell's equations [78] including the constitutive equation of isotropic media with Kerr nonlinearity and typical chromatic dispersion properties through the auxiliary differential equation (ADE) technique [19][71]. The optical Kerr nonlinearity is modelled with an instantaneous response, and TPA is not taken into consideration. When the incident light power is reduced to the level of 100 mW or less, this is considered to be an appropriate approximation. The relation between the field E and the light power P has been derived by numerically evaluating the effective area of the waveguide $A_{\mathrm{eff}} = 0.53$ μm^2, thus we obtain $P = A_{\mathrm{eff}}\,|E|^2/(2Z_0)$, where $Z_0 = 377\ \Omega$ is the intrinsic wave impedance of vacuum.

For the asymmetric WBG of $W_g = 0.1\ \mu$m and $W_g = 0.2\ \mu$m, the transmission spectra for weak incidence have been analyzed as shown in Figure 6-3. It is seen in this figure that each spectrum is the combined one of those found in Figure 6-2 for uniform gratings; due to the asymmetric variation of the grating modulation, the total transmission is also asymmetric with respect to frequency. In the previous 1D model e.g. in [44], both the upper and the lower band edges are changed while the stopband centre remains unchanged. In contrast, for the present waveguide model the stopband centre is chirped as well as that the upper band-edge changes largely. The operating frequency is generally chosen to be slightly lower than the upper band edge frequency.

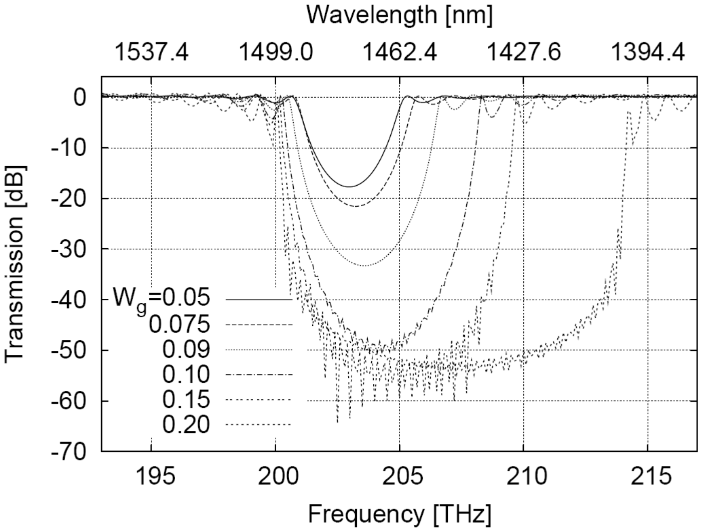

Figure 6-2 : Transmission spectra for the 100Λ-long waveguide Bragg gratings of uniform amplitudes of sidewall modulation. W_g in legend is in μm.

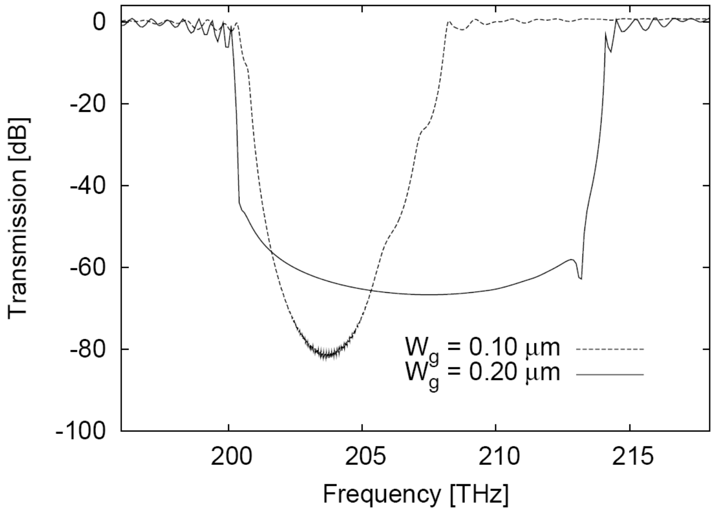

Figure 6-3 : Comparison of the calculated transmission spectra for 200-Λ-long asymmetric gratings with the maximum modulation $W_g = 0.1$ μm and $W_g = 0.20$ μm. The upper frequency band edges are 208.20 THz for $W_g = 0.1$ μm, and 214.08 THz for $W_g = 0.20$ μm

We first chose the operating frequency at 207.9 THz (or free space wavelength $\lambda_0 = 1.442$ μm) for the case of $W_g = 0.1$ μm, i.e. the frequency difference from the upper band edge was $\Delta f = 0.3$ THz, and launched a sinusoidal wave from either the left-hand-side or the right-hand side port of the asymmetric WBG. The incident light power is gradually increased, followed by a flat region such that the field in the grating establishes a stationary state. This staircase-like input is repeatedly cumulated until the incident light becomes strong enough to cause switching, and then the incident power is reduced in a similar manner until it vanishes. This allows the detection of the switch-on and -off thresholds of the WBG. The incident and the output time signals are plotted in Figure 6-4 for the WBG of $L_0 = 235\ \Lambda$; due to the rapidly oscillating sinusoidal carrier, only the envelopes of the incident and the output signals for the RTL and the LTR configurations are visible in the figure. It is observed that the switching threshold is lower for the RTL configuration than for the LTR configuration; the switch-on threshold of the electric field is $E_{th}^{(on)} = 2.6\times10^7$ V/m (equivalent light power $P_{th}^{(on)} = 480$ mW) for RTL, while it is $E_{th}^{(on)} = 3.7\times10^7$ V/m ($P_{th}^{(on)} = 950$ mW) for LTR. The switch-off threshold field is $E_{th}^{(off)} = 1.8\times10^7$ V/m ($P_{th}^{(off)} = 240$ mW) for RTL, while it is $E_{th}^{(off)} = 2.6\times10^7$ V/m ($P_{th}^{(off)} = 490$ mW) for LTR. Either of the two transmission plots show the Schmitt trigger operation, i.e. the switch turns on at a certain incident power, holding the on-state until the input passes through a lower threshold power [64]. Note also that the transition time for switching is 2 to 3 ps. Overshoot and bouncing are seen afterwards, and the signal settling time is approximately 10 ps. The right vertical axis of Figure 6-4 shows the change in normalized permittivity by the optical Kerr nonlinearity, and this is convenient when the switching threshold is compared to other results. For this case the change in normalized permittivity for the switch-on threshold is 2.2×10^{-4}, which is much smaller than those used in literature, e.g. [10].

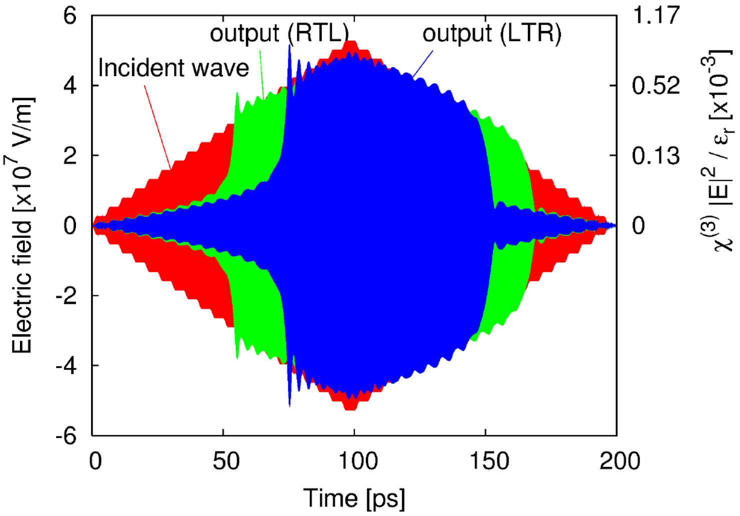

Figure 6-4 : Switching for the LTR and RTL configuration of a 235Λ-long waveguide with W_g = 0.1 μm at 207.9 THz operating frequency (Δf = 0.3 THz). Maximum incident field value is 5.25 × 107 V/m at 100 ps. Right vertical axis shows the normalized permittivity change by the nonlinearity.

The origin of the non-reciprocity and the stability is described qualitatively in [73][32]; as in these references, the behaviour of the field inside the grating is reasonably considered in view of energy diffusion. Due to the monotonic change of the band-edge frequency, for the LTR (negative) configuration, the light power injected into the grating diffuses gradually in the forward direction, which leads to a large power required for switching. In contrast for the RTL (positive) configuration, the incident light power can be built up within the grating since the light energy diffuses in the backward direction being blocked by the increasing potential barrier of the grating, which leads to a relatively smaller power required for RTL switching than for LTR switching.

In Figure 6-5 we show the snapshots of the electric field for the RTL configuration with L_0 = 200 Λ, W_g = 0.1 μm at the operating frequency 207.85 THz for (a) an off-state and (b) an on-state. Similar fields are observed for the case of the LTR configuration. From these figures it is found that the fields have a few peaks, which indicates that the mode of resonance in the grating is of higher-order. Due to both the strong grating modulation and the structural asymmetry and despite that the incident light power has been gradually increased, the fundamental mode is not generated but the higher-order mode takes over. It has been found in our results that the off-state fields are significantly different between the RTL and the LTR (not shown) configurations. For the RTL configuration the field penetrates into the waveguide, while for the LTR configuration the field is blocked at the entrance to the waveguide. When the waveguide grating switches on, the field distributions become similar for the RTL and the LTR configurations.

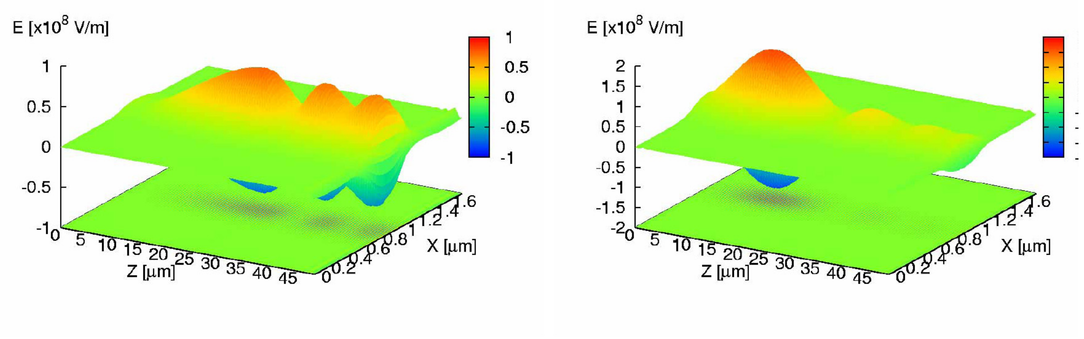

(a) (b)

Figure 6-5 : Electric field for 200 Λ-long RTL configuration (positive variation) with W_g = 0.1 μm at 207.85 THz operating frequency. (a) Off-state at 90 ps, and (b) on-state at 130 ps.

The relation between the length of the waveguide grating and the switching threshold for the RTL configuration is plotted in Figure 6-6 with different operating frequencies f_{op} = 207.85 THz, 207.9 THz and 207.95 THz for W_{g} = 0.1 μm, and f_{op} = 214.03 THz for W_{g} = 0.2 μm as discussed later. The switching threshold no longer exhibits a linear dependence on the grating length when the grating is longer than approximately 210 Λ. This behaviour of the threshold value is considered to be due to the strong modulation of the grating. This tendency applies also to other cases of different W_{g}. The minimum threshold is obtained at length around 220 Λ to 230 Λ regardless of W_{g}. The WBGs longer than 235 Λ are found unstable, causing a modulation-like field to grow rapidly, which is to be discussed in a later section. We have noted that for the minimum threshold condition at a length around 220 Λ to 230 Λ, the incident light and the light reflected from the grating become out of phase, and subsequently, the total field at the input port (right-hand-side port) becomes very small. Contrary, for shorter grating lengths the total field at the input port is observed significantly large (not shown). The total field near the input port will obviously affects the switching behaviour. Therefore, the phase difference between the incident and the reflected lights, which is determined by the total length of the asymmetric grating, could be the main reason for the fact that the threshold is not linearly dependent on the grating length.

Next we further increase the sidewall modulation to W_{g} = 0.20 μm while maintaining the longitudinal profile of the modulation, i.e. the modulation amplitude $W_{\mathrm{g}}/2$ of the grating varies according to the same polynomial, namely from 0.10 μm to 0.05 μm along the waveguide. The transmission spectra for the 200 Λ-long asymmetric grating is compared with that of W_{g} = 0.1 μm in Figure 6-3. The operating frequency for the nonlinear switching analysis was then chosen to be 214.03 THz, closer to the band edge (214.08 THz) than that of the previous case because the transmission spectrum is much steeper at the band edge, which allows the same level of extinction ratio for the nonlinear switching operation.

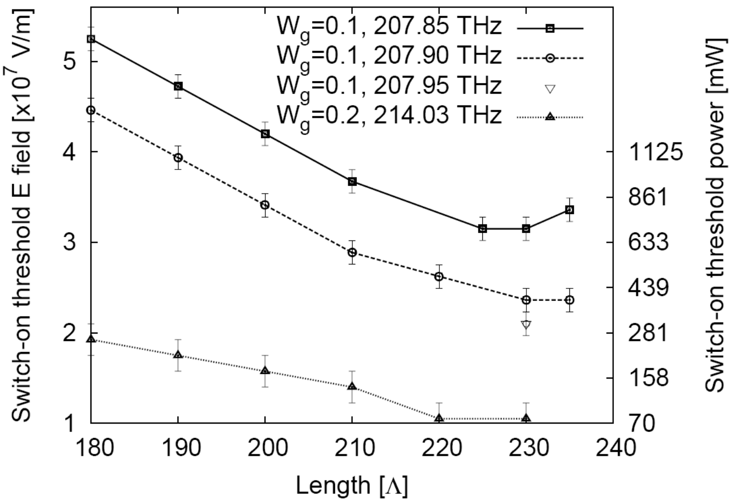

Figure 6-6 : Switch-on threshold electric field and power versus the length of the waveguide grating for the RTL (positive) configuration with $Wg = 0.1\ \mu$m and $0.2\ \mu$m. The error bars are the uncertainty due to the step increment of the incident field variation.

The results for the switching behaviour are shown in Figure 6-7. In this result the switching threshold has been reduced to $E_{\mathrm{th}}{}^{(\mathrm{on})} = 1.05\times10^7$ V/m (equivalent light power $P_{\mathrm{th}}{}^{(\mathrm{on})} = 77$ mW) for the RTL configuration, and to $E_{\mathrm{th}}{}^{(\mathrm{on})} = 1.6\times10^7$ V/m (equivalent light power $P_{\mathrm{th}}{}^{(\mathrm{on})} = 170$ mW) for the LTR configuration. In this case the switch-off threshold is not clearly visible, but it exists at around $E_{\mathrm{th}}{}^{(\mathrm{off})} = 0.35\times10^7$ V/m (equivalent light power $P_{\mathrm{th}}{}^{(\mathrm{on})} = 480$ mW) both RTL and LTR. The time evolution exhibits larger fluctuations than that of the previous case in Figure 6-4 because the operating frequency is closer to the band edge and therefore the extinction ratio is worse than that in Figure 6-4. The change in normalized permittivity for the switch-on threshold is 3.6×10^{-5}. Note that the transmission spectrum for $W_g = 0.20\ \mu$m has a very steep transition and a large dip near the band edge, in comparison to those for $W_g = 0.10\ \mu$m. However, we observe that the stability of the switching operation is not largely affected by the dip. The steep transition reduces the switch-on power significantly. If the switch turns on, the bandgap shifts to the lower frequency side, and the device can maintain the on-state like an electronic Schmitt trigger, irrespective of the fine structure of the transmission curve near the band edge.

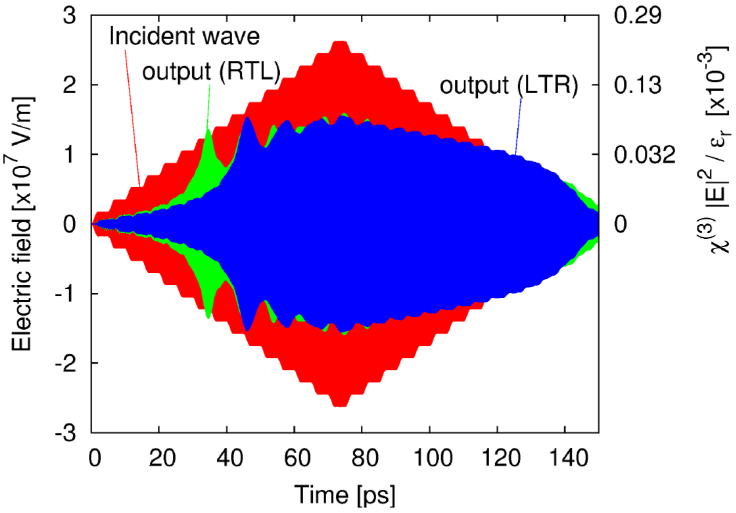

Figure 6-7 : Switching for the LTR and RTL configuration of a 220Λ-long waveguide with $Wg = 0.20$ µm at 214.03 THz operating frequency ($\Delta f = 0.05$ THz). Maximum incident field is 2.6×10^7 V/m at 75 ps. Minimum switch-on threshold is $E_{\text{th}}{}^{(\text{on})} = 1.05\times10^7$ V/m (equivalent light power $P_{\text{th}}{}^{(\text{on})} = 77$ mW) for RTL.

As expected, the stronger modulation allows the reduction of the switching threshold significantly. With the incident laser power of 77 mW, the experimental observation of the switching operation in this device seems to be feasible. One may consider an alternate candidate for the nonlinear media, which would exist in a class of organic polymers; polydiacetylene 9-BCMU has a nonlinear susceptibility $\chi_0{}^{(3)} = 1.4\times10^{-16}$ m^2/V^2 [73]. This value is approximately 36 times larger than that of InGaAsP (Q1.35) investigated in this paper, and allows to reduce the required incident light power strongly, namely down to approximately 2 mW, which would enable an actual functional device having a very low threshold.

6.1.3 Stable state of nonlinear WBG

We have investigated the dynamic stability of a uniform WBG for comparison with the previous asymmetric WBGs. We observed a stable state for $L = 200\,\Lambda$, $W_g = 0.15\,\mu$m, uniform WBG at operating frequency 209.40 THz. The upper band-edge frequency of this structure is 209.55 THz. The time evolution of the field is shown in Figure 6-8. In this case switching occurred at 40 ps with the incident threshold field $E_{\text{th}}{}^{(\text{on})} = 1.6\times10^7$ V/m (equivalent light power $P_{\text{th}}{}^{(\text{on})} = 170$ mW). For the time period between 40 ps and 50 ps, a relatively sharp pulse is observed. Further analyses showed that when the incident field is stronger the pulse becomes higher and narrower, leading to a number of soliton-like pulses generated and transmitted (not shown). After 50 ps, the incident power reduces gradually, and thereby the grating's inner field switches to a stable state, which is retained until the incident light almost vanishes at time 100 ps. The corresponding field distributions are shown in Figure 6-9(a) for an off-state at 20 ps, and in (b) for an on-state at 60 ps. These field distributions indicate that the field is of a longitudinal fundamental mode, because only a single envelope peak is observed for the on-state, which is similar to those observed in previous literature for 1D solution [40][68] [44]. Note that the field in Figure 6-9(b) for the on-state is much larger than that in (a) for the off-state. It is also interesting to note in Figure 6-8 that the on-state lasts for some picoseconds even after the incident light vanishes. This is a clear evidence of the fact that a large amount of energy is stored in the grating during the on-state, and once the incident light goes down across the switch-off threshold, the stored energy starts diffusing out of the grating. This diffusion process would take some picoseconds in this case. In addition, the switch-off threshold for this operation condition is significantly lower, which has extended the on-state duration even after the incident light has turned off. In general, for certain values of field amplitude and single-step rise-time of the input-field staircase, it is possible that the system prefers to stay in the transmitting on-state by exciting gap solitons and by radiating the excess energy as a train of pulses ([40] Figure 3). Such a gap soliton may be observed at time 60 ps in Figure 6-8, where the field distribution resembles that of a soliton, Figure 6-9(b). This stable gap soliton decays relatively slowly, even if the input pulse falls below the switch-off threshold.

6.1.4 Pulsative state of nonlinear WBG

Interestingly, for the same analysis conditions as the previous taper configuration of $W_g = 0.2\,\mu$m except that the grating modulation is uniform, the stable switching is not observed clearly even when a relatively high-power incident light is launched. Instead, a pulsative state is suddenly observed as shown in Figure 6-10. By comparison with the results for the asymmetric WBG in Figure 6-7, it is found that the asymmetric grating has an effect of stabilizing the switch-on state. Similar stability characteristics have been investigated by Jia et. al. for a weakly-modulated taper nonlinear Erbium-doped fiber Bragg grating [32]. According to their results, stability of Bragg grating structures is significantly affected by the taper configuration of the grating, and it is indeed not straightforwardly predictable. In our WBG structure the grating modulation is much stronger, and thereby the stability range is even more reduced. Without the gradual change of the electric field modulation, the transition between the stable and the pulsative states is so sudden that the stable distribution of the field is hardly retained in the WBG structure. This explanation is consistent with the transmission spectrum (Figure 6-3) that has a very steep transition and a large dip at higher-frequency side of the first peak near the upper band edge. It is therefore anticipated that the switching property would be improved by a careful design of the grating configuration.

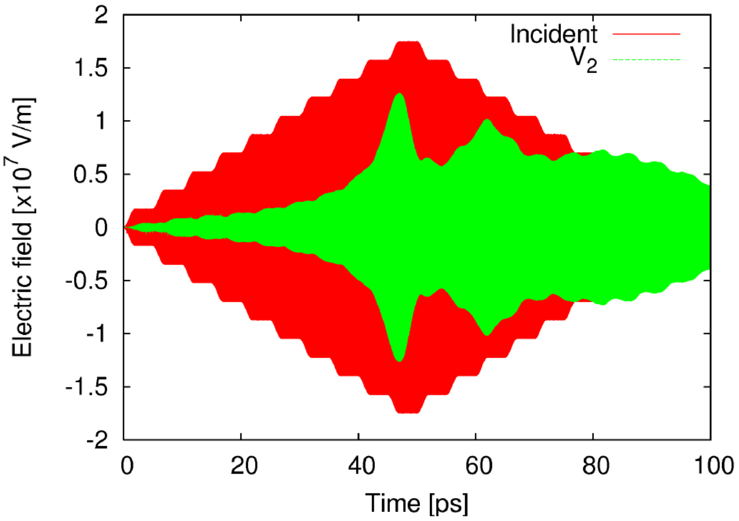

Figure 6-8 : An example of the stable switching state for a uniformly modulated WBG of 200 Λ in length, $W_g = 0.15\ \mu$m at operating frequency 209.40 THz ($\Delta f = 0.15$ THz). The maximum field is 1.75×107 V/m. Switch-on occurs at $E_{th}^{(on)} = 1.6\times107$ V/m (equivalent light power $P_{th}^{(on)} = 170$mW)

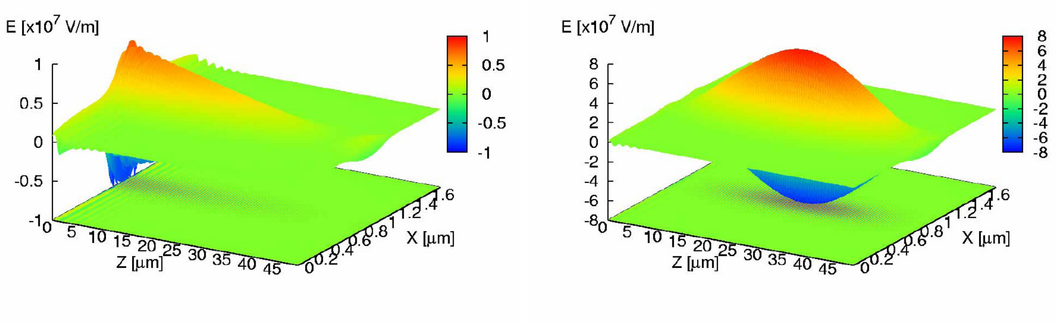

(a)

(b)

Figure 6-9 : Stable state electric field for 200 Λ-long uniform grating. Wg = 0.15 µm, 209.40 THz, 1.75×107 V/m. (a) Off-state at 20 ps, and (b) on-state at 60 ps

6.1.5 Chaotic state of nonlinear WBG

It was found that when the waveguide was longer than a certain length the nonlinear analysis tends to diverge at a relatively small incident field, resulting in a modulation-like behaviour, and finally resulting in a chaotic state. The similar phenomena have also been reported elsewhere [67][15]. In the discussion of the stability characteristics of Bragg gratings by Jia et.al. [32], it is shown that the modulation instability occurs in nonlinear Bragg gratings due to the interplay between group velocity dispersion (GVD) and nonlinear effects. This mechanism is close to that of the optical soliton propagation and self-focusing phenomena as it has been de-

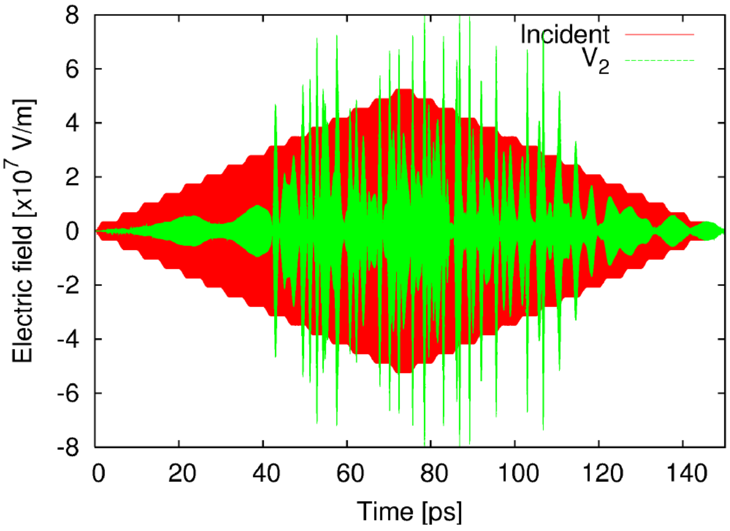

Figure 6-10 : An example of the pulsative time signal for a uniformly modulated WBG of 220 Λ in length, $W_g = 0.2\ \mu$m at operating frequency 214.03 THz ($\Delta f = 0.05$ THz). The maximum incident field is 5.25×10^7 V/m. Transition to the pulsative state occurs at incident field $E = 3.2\times10^7$ V/m (equivalent light power $P = 720$ mW).

monstrated numerically using the same FDTD algorithm [19]. Due to even stronger dispersion in a Bragg grating at a frequency close to its band edge, the onset of modulation instability occurs at a lower power level for Bragg gratings in comparison to solitons in an ordinary waveguide. The chaotic behaviour following the self-focusing of a light beam has been investigated using a softcore Coulomb potential (SCP) model of bound electrons [34]. We show here that the SCP is applicable to nonlinear Bragg gratings for the investigation of the dynamic chaotic behaviour of the grating field.

The SCP model can avoid the singularity of an instantaneous nonlinearity by employing a saturation mechanism near the core of a Coulomb potential; the binding force of an atom is derived from the so-called soft-core Coulomb potential [34]

$$U(x) = -\frac{q^2}{\sqrt{r_0^2 + x^2}}. \tag{4.30}$$

where x is the displacement from equilibrium for a bound particle having an electric charge q, and r_0 is an equilibrium radius. These parameters can be determined from desired nonlinear properties such as linear susceptibility, third-order nonlinear susceptibility, and a characteristic resonance frequency of the charged particle. In its differential equation of electron motion it has a term for the Lorentz dispersion and a term for the 3rd-order nonlinearity, which can be efficiently implemented in the FDTD algorithm through the ADE formalism [19]. We will report the detailed analysis in a forthcoming paper.

In Figure 6-11 we show the time evolution of the field detected at the input port V_1 and at the output port V_2, for a uniformly modulated WBG of 300 Λ in length; (a) is for the instantaneous Kerr nonlinearity and the Lorentz dispersion with a damping factor $\delta_p = 1.0\times10^{14}$ rad/s, and (b) for the SCP model with a damping factor $\delta_p = 1.0\times10^{13}$ rad/s. From these results one

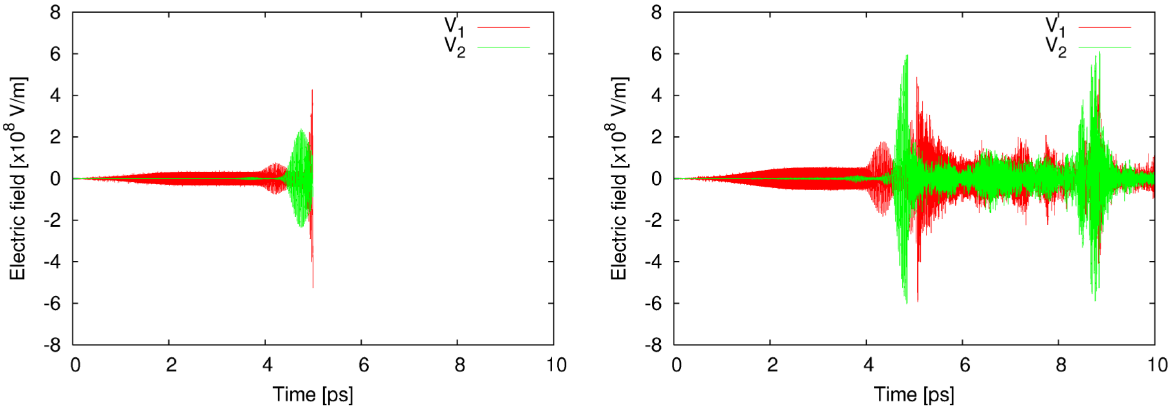

Figure 6-11 : (a) Optical Kerr model for f_{op} = 206.5 THz (Δf = 0.2 THz), with Lorentz dispersion with the damping factor $\delta p = 1.0\times10^{14}$ rad/s. Calculation stopped at 5 ps. (b) SCP model for fop = 200.3 THz (Δf = 0.2 THz), with the damping factor $\delta p = 1.0\times10^{13}$ rad/s. Calculation still continues after 10 ps

can see that the SCP model allows the observation of the chaotic behaviour, at least qualitatively, by virtue of the saturating nature of the model, while in (a) even with a larger damping factor the calculation stops due to a convergence problem of the nonlinear algorithm. Our extensive study shows that when the damping factor is increased for the Lorentz dispersion model, the modulation-like field builds up like the result in (a) at a slightly later time, and it results in the same convergence problem of the nonlinear algorithm. Figure 6-11 Time signals that exhibit the modulation-like instability. For uniform WBGs of $L_0 = 300\,\Lambda$. The incident light is a smoothly excited sinusoid with the maximum field 5.25×10^7 V/m.

6.2 Summary

We have demonstrated numerically non-reciprocal transmission and Schmitt trigger operation in asymmetric WBGs with strong sidewall modulation. The asymmetric WBG structure exhibits a stable switching region at the incident light power as small as 77 mW for the RTL configuration (positively varying stopband) and 170 mW for the LTR configuration (negatively varying stopband). This threshold power is in a level experimentally accessible in an actual functional device. We have also demonstrated the analysis of stable, pulsative, and chaotic states of the nonlinear WBG structure with the FDTD method. In particular, it is found that asymmetricity of WBGs allows a stable switching operation compared to uniformly modulated WBGs. The modulation-like instability is qualitatively investigated by using a numerically stable nonlinear algorithm based on the soft-core Coulomb potential model.

7 Signal processing in periodic structures

In all the preceding chapters we have explored the resonant structures focusing mainly on the all-optical bistable switching or direction dependent isolator behaviours. In this chapter we discuss about two other signal processing applications relevant to optical networks. First, we discuss about degenerate four-wave mixing (FWM) effects in a STWBG (see Section 0 on page 62 for description of STWBG) structures and also give some comparison with ring resonator. Next, we will discuss about a possible high extinction ratio optical switching application in an asymmetric Fabry-Perot waveguide resonator (AFPR) exploiting TPA effects.

7.1 Four-wave-mixing in ST-WBG

In degenerate FWM [4], the nonlinear interaction of two waves at frequency ω_s ("signal") and ω_p ("pump") leads to a phase-sensitive, fully transparent generation of a converted wave at frequency $\omega_c = 2\omega_p - \omega_s$. The ratio of incoming signal and outgoing converted power, normalized by the pump power squared, is the normalized conversion efficiency $\eta_\mathrm{FWM} / P_p^2$. It can be improved by exploiting the field enhancement in resonant structures.

We use the NLCME equations to model such structures (see Section 4.3 on page 62 for description of STWBG). It comprises a passive WBG with a Bragg wavelength $\lambda_\mathrm{B} = 1.5767$ µm ($\Lambda = 232$ nm). A pump at $\lambda_\mathrm{p} = 1.558$ µm ($\delta_\mathrm{p} L = 48.8$, CW power $P_p = 21$ mW) and a Gaussian "1101" signal pulse with a FWHM of 50 ps and repetition rate 250 ps at $\lambda_\mathrm{s} = 1.5746$ µm ($\delta_s L = 5.4$, close to the transmission resonance for the nonlinear case, peak power $P_s = 14$ mW) are injected, Figure 7-1a (left axis). Due to the low signal group velocity at the linear-case band edge $\delta L = 5.59$ ($\lambda = 1.5745$ µm) at $z = 0$, the nonlinear interaction is high and an enhanced FWM is observed. For $\Delta\kappa = -15\%$ and LTR propagation, we find a converted wave at $\lambda_\mathrm{c} = 1.5417$ µm ($\delta_\mathrm{c} L = 92.3$, peak power $P_c = 5$ µW), Figure 7-1a (right axis), corresponding to a conversion efficiency of $\eta_\mathrm{FWM} = -34.5$ dB; for RTL operation we have $\eta_\mathrm{FWM} = -44$ dB, and without tapering it is $\eta_\mathrm{FWM} = -38$ dB.

The reason for these differences lies in the differing phase matching and field enhancement conditions. For RTL operation and stopband tapering, the signal $\omega_\mathrm{s} = \omega_\mathrm{T}^\mathrm{RTL}$ is closest to the upper band edge (transmission resonance $\omega_\mathrm{T}^\mathrm{RTL}$), Figure 7-1b (lower-left inset, left-most transmission curve). It deviates strongest from the phase velocities of pump and converted wave, which propagate nearly unaffected from the grating's dispersion. For LTR operation the signal frequency ω_s is farther away from the band edge because of the tapering, therefore it is less influenced by dispersion, but becomes still resonantly enhanced, so the efficiency is larger. For an untapered grating ($\Delta\kappa = 0$ %) the resonant enhancement is less, Figure 7-1b (lower-left inset, right-most transmission curve), but the phase matching is good, so η_FWM takes on an intermediate value.

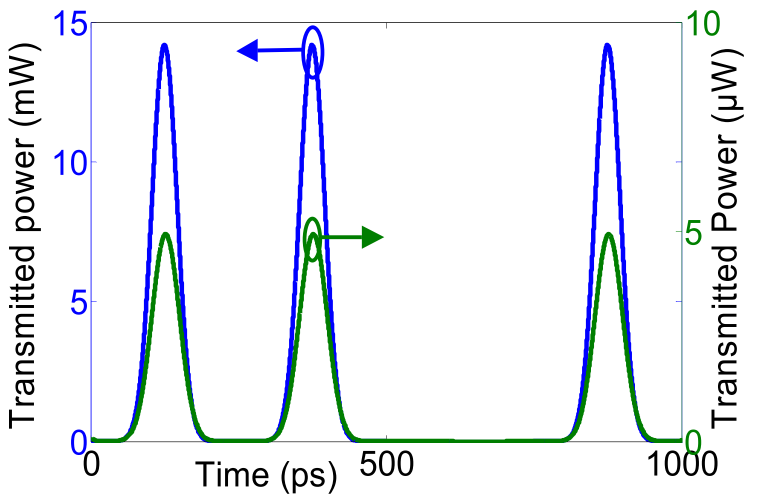

Figure 7–1a : FWM in an InP-based tapered and untapered (LTR propagation) WBG. High-power “1101” signal pulses (left axis ←), converted pulses (right axis →)

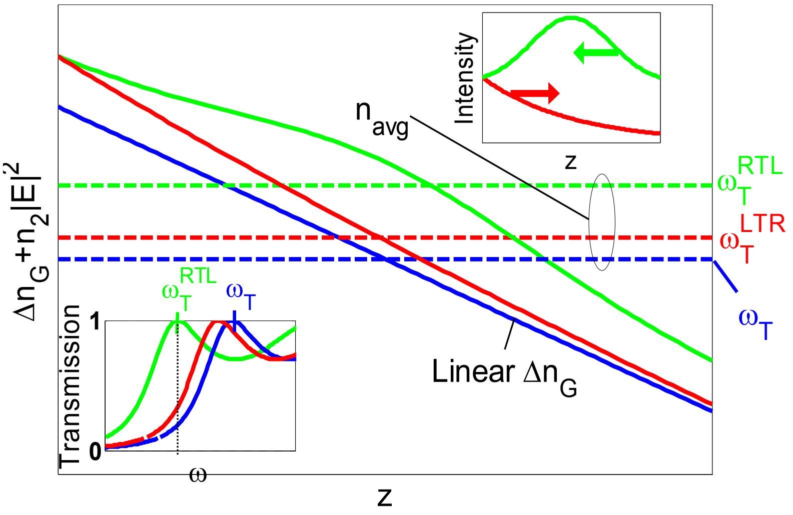

Figure 7-1b : Schematic of locally-averaged refractive index as a function of *z*, CW frequency $\omega_0 = \omega_T^{RTL}$. Low power (—, Linear Δ$n_G$), nonlinear RTL (—) and LTR operation (—). Horizontal dashed lines for spatial average navg over total grating length labelled with respective transmission resonance frequencies ω_T (– –), ωTLTR (– –), ω_T^{RTL} (– –). Lower-left inset: Power transmission near upper band edge. Top right inset: Intensity for RTL (←) and LTR (→) operation.

Here we have utilized Bragg grating based resonator structures. However for resonant field enhancement a micro ring resonator can also be used [16]. The normalized FWM efficiency as obtained from the experimentally measured value as reported [16]. is $\eta_{\mathrm{FWM}} / P_p^2 = 1.2\ \mathrm{W}^{-2}$ in the case of ring resonators. This is comparable with the Bragg grating’s normalized efficiency of 0.77 W^{-2}.

It is interesting to note that — contrary to the situation for the ring resonator below — once the signal is tuned to the band edge, the converted-wave frequency may be adjusted quite freely by changing the pump frequency.

7.2 High extinction ratio switching using two-photon absorption in a silicon waveguide resonator

Silicon has attracted a great deal of attention for optoelectronic applications due to its potential for forming inexpensive, monolithic integrated optical components. The strong optical confinement offered by silicon on insulator (SOI) waveguides enhances nonlinear optical interactions, such as Raman and Kerr effect, in a chip-scale device [31]. This opens numerous possibilities in using silicon as a material for all-optical signal processing. However, this functionality is impaired by two-photon absorption (TPA), which can severely degrade the performance of a device [39]. Recently, TPA-induced ultrafast switching was demonstrated in SOI wire waveguides [55] resulting in a relatively low extinction ratio of about 11 dB. On the other side, high extinction ratio switching has been shown in an asymmetric Fabry-Perot resonator (AFPR) with a relatively slow saturable absorber inside the cavity [58]. In this paper we combine the advantages of a high extinction ratio inherent in an AFPR with the fast TPA nonlinearity readily available in silicon. By optically tuning the reflectivity of a silicon-based AFPR through TPA inside the cavity, we switch between an impedance-matched condition with low reflectivity, and a high-reflectivity state. This leads to a high extinction ratio larger than 20 dB for the reflected signal. We describe the steady-state behaviour with a simple model and comment on possible limitations of the switching speed.

As described before an asymmetric Fabry-Perot resonator can be modelled by Eq. (4.1) – (4.5), together with Eq. (4.8). For better readability we repeat some of those equations once again here

$$R = \frac{P_{\mathrm{Refl}}}{P_{\mathrm{In}}} = \frac{E + F\sin^2(\theta)}{1 + F\sin^2(\theta)}, \tag{4.31}$$

$$\mathrm{PE} = \frac{P_{\mathrm{Avg}}}{P_{\mathrm{In}}} = \frac{M}{1 + F\sin^2(\theta)}, \tag{4.32}$$

where quantities E, F, M, and θ are defined as before (see Eq. (4.1) – (4.5))

$$\begin{aligned} E &= \frac{\left(\sqrt{R_1} - \sqrt{R_2}\exp(gL)\right)^2}{\left[1 - R_{\mathrm{eff}}\exp(gL)\right]^2}, \\ M &= \left[\frac{(1-R_1)\left(1 + R_2\exp(gL)\right)}{\left(1 - R_{\mathrm{eff}}\exp(gL)\right)^2}\right]\frac{L_{\mathrm{eff}}}{L}, \end{aligned} \tag{4.33}$$

As before we use the same parameters for the silicon-based structures considered here we use $\gamma \approx 3.5\ \mathrm{cm^{-1}W^{-1}}$, $\gamma_{\mathrm{TPA}} \approx 1.58\ \mathrm{cm^{-1}W^{-1}}$ [36] at $\lambda = 1.54\mu\mathrm{m}$.

The round-trip phase and the attenuation in the cavity depend on the average power in the cavity through Eq. (3). With increasing input power more energy is coupled into the cavity. The high cavity power introduces a nonlinear phase shift via the Kerr effect and moves the resonance to a larger wavelength. Simultaneously, the loss of the cavity increases via TPA. From Eq. (4.31) we see that the reflectivity of the AFPR becomes minimum if its input impedance is matched, i.e., if $R_1 = R_2 \exp(-2\alpha_{\mathrm{loss}}L)$ holds. So by changing the input power large changes of the AFPR reflectivity are induced; this can be used to construct a switch. In the scheme depicted in Figure 7-2 the strong power of the pump signal modulates the cavity resonance condition for the probe signal, and the information of the pump can be transferred to the probe. In general, pump and probe wavelengths are chosen to be different, and the absorption is tuned by cross-absorption modulation [55]. Here, for simplicity, we only discuss the case of identical pump and probe wavelength. In all the results which follow we normalize the power by the reference power P_{ref}. The quantity ϕ is the phase detuning with respect to the phase at resonance, i.e., it measures the frequency detuning from resonance.

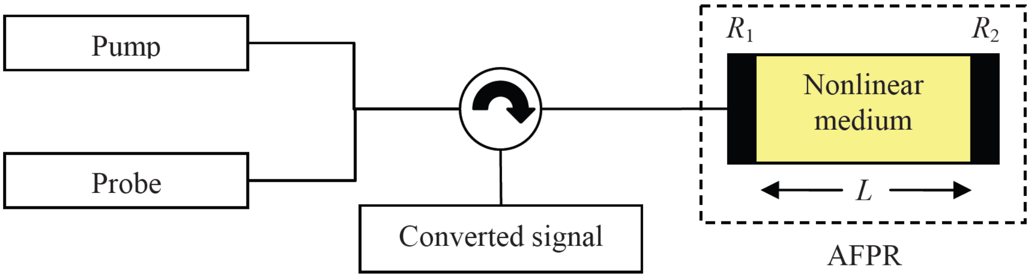

Figure 7-2 : Scheme of switching operation using reflective AFPR

We solve the set of Eq. (4.31) – (4.32) to characterize the steady state behavior of an AFPR. We consider the following set of parameters: $R_1 = 32\%$ (50%), $R_2 = 99\%$ (85%) with $L = 1\,000$ µm and a linear loss of 1 dB/cm. In Figure 7-3(a) we plot the typical variation of the frequency dependent reflectivity $R(\phi)$ with different input powers. The solid blue curve in Figure 7-3(a) shows $R(\phi)$ for $R_1 = 32\%$, $R_2 = 99\%$ in the linear case, while the red (dashed) and green (dot-dashed) curves are for an input power of $P_{\mathrm{In}} = 0.1\,P_{\mathrm{ref}}$ and $P_{\mathrm{In}} = 0.26\,P_{\mathrm{ref}}$, respectively. Due to the Kerr nonlinearity the reflectivity spectrum shifts to the higher wavelength side (negative value of ϕ). It shows a power dependent tuning of $R(\phi)$ which can be exploited for a nonlinear filter. With increasing input power the minimum reflectivity approaches zero (see green dash-dotted curve in Figure 7-3(a)). In Figure 7-3 (b) (Figure 7-3(e)) we plot the variation of the reflectivity in dB for different input powers and for different phase detuning of the AFPR having $R_1 = 32\%$ (50%), $R_2 = 99\,\%$(85 %). For certain values of the phase detuning the reflectivity falls below 20 dB, e.g., for a phase detuning of -0.195π (-0.25π) the reflectivity is below 20 dB when an input power of 0.31 P_{ref} (0.45 P_{ref}) is applied; the associated variation of the reflectivity with the input power is shown in Figure 7-3(d) by a blue (red dashed) curve. The average power inside the cavity is plotted on a dB scale in Figure 7-3(c) (Figure 7-3(f)).

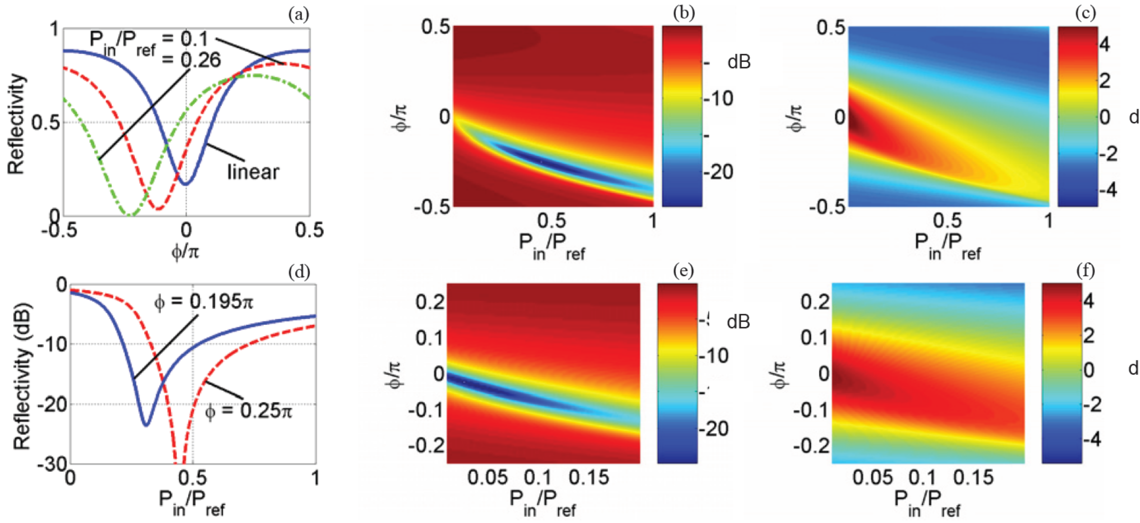

Figure 7-3 : Effect of including TPA on reflectivity of AFPR for different parameters. (a) Dependence of the reflectivity ϕ or $R_1 = 32\%$, $R_1 = 99\%$. (b) & (e) Dependence of reflectivity on the input power and for the phase detuning in an AFPR with $R_1 = 32\%$, $R_1 = 99\%$ and $R_1 = 50\%$, $R_1 = 85\%$ respectively; (c) & (f) Dependence of P_{avg} in the cavity for the parameters used in (b) & (e). (d) Dependence of reflectivity R on power for $R_1 = 32\%$, $R_1 = 99\%$.

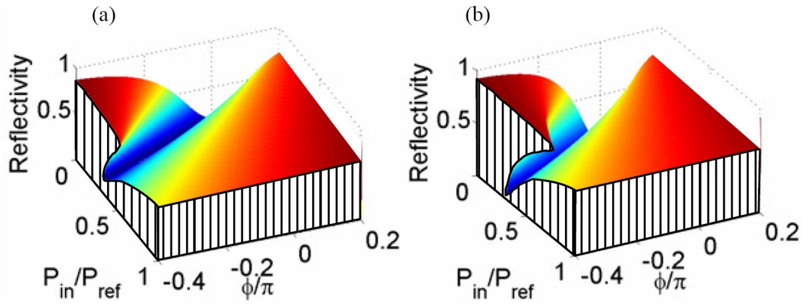

Figure 7-4 : Effect of neglecting TPA on reflectivity of AFPR for different parameters. Dependence of reflectivity on input power, and on phase detuning in an AFPR with (a) $R_1 = 32\%$, $R_2 = 99\%$; (b) $R_1 = 50\%$, $R_2 = 85\%$.

If the reflectivity of the back mirror R_2 is reduced to 85 % and the front mirror reflectivity R_1 is increased to 50 %, it is found that the power required to attain low reflectivity is reduced (see Figure 7-3(e) and (f)). The effective reflectivity $R_{\mathrm{eff}} = \sqrt{R_1 R_2}$ is increased in this case, which leads to a larger power enhancement inside the cavity. The bandwidth in is reduced as would be expected for a cavity with large finesse. The power requirements for high extinction ratio switching can be further reduced by choosing a material with lower $\mathrm{FOM}_{\mathrm{TPA}}$.

TPA neglected : It is to be noted that in absence of TPA the device shows a bistable state of operation for certain values of the input power and phase detuning as can be seen from Figure 7-4 for, say, $P_{\mathrm{In}} = 0.5\, P_{\mathrm{ref}}$ at $\phi = -0.4\,\pi$. TPA degrades the performance of bistable operation such that bistability is not observed in presence of TPA for the cavity parameters and the power range considered here.

Switching speed : Though TPA is an ultrafast process, the speed of the device is limited to the photon lifetime in the cavity, and to the relaxation time of the generated free carriers. The photon lifetime in the cavity can be reduced using a low-Q cavity, but then in turn the cavity power enhancement is reduced. So there exits a tradeoff between the photon lifetime and the switching power. The relaxation time of free carriers can be minimized by a proper design of the waveguide geometry [55]. Further, if free carriers are extracted from the cavity by forming a pin junction in the transverse direction of the waveguide, the recovery time of the device can be lowered [31].

We note that the present study is limited by the steady-state assumption, and so the switching dynamics can not be calculated. Proper optimizations of a device with suitable switching power, switching time and reasonable bandwidth are currently being investigated using a dynamical model.

7.3 Summary

In this chapter we have discuss about degenerate FWM effects in a stopband tapered waveguide Bragg grating (STWBG) structure. As a new result we have observed that the FWM efficiency can be different for an asymmetric waveguide based resonator structure. Further we have proposed a high extinction ratio switch, using two-photon absorption in an optically switched asymmetric Fabry-Perot waveguide resonator. To achieve the high extinction ratio we combine the advantages of a high extinction ratio inherent in an AFPR with the fast TPA nonlinearity readily available in silicon.

References

[1] A. B. Aceves and S. Wabnitz, “Self-induced transparency solitons in nonlinear refractive periodic media”, *Phys. Lett. A*, vol. 141(1, 2), 37 – 42, 1989.

[2] M. J. Adams, H. J. Westlake, M. J. O’Mahony, and I. D. Henning, “A comparison of active and passive optical bistability in semiconductors”, *IEEE J. Quantum Electron.,* vol. QE-21(9), 1498 – 1504, 1985.

[3] V. R. Almeida, C. A. Barrios, R. R. Panepucci, and Michal Lipson, “All-optical control of light on a silicon chip”, *Nature* 431, 1081 – 1084, 2004.

[4] G. P. Agrawal, *Nonlinear Fiber Optics*, Academic Press, San Diego, third edition, 2001.

[5] G. P. Agrawal, *Applications of Nonlinear Fiber Optics*, Academic Press, San Diego, 2001.

[6] G. P. Agrawal, and N. K. Dutta, *Semiconductor Lasers*, Van Nostrand Reinhold, New York, second edition, 1993.

[7] R. W. Boyd, *Nonlinear Optic*, Academic Press, San Diego, third edition, 1992.

[8] P. F. Byrd, M. D. Friedman, *Handbook of Elliptic Integrals for Engineers and Scientists*, Springer, Berlin, 1971.

[9] N. Calabretta, Y. Liu, F. M. Huijskens, M. T. Hill, H. de Waardt, G. D. Khoe, and H. J. S. Dorren, “Optical signal processing based on selfinduced polarization in a semiconductor optical amplifier”, *J. Lightwave Technol.*, vol. 22(2), 372 – 381, 2004.

[10] W. Chen and D. L. Mills, “Gap solitons and the nonlinear optical response of superlattices”, *Phys. Rev. Lett.* , vol. 58(2), 160 – 163, 1987.

[11] Y. Dumeige, L. Ghisa, P. Feron, “Integrated all-optical pulse restoration with coupled nonlinear microring resonators”, *Opt. Lett.*, vol. 31(14), 2187 – 2189, 2006.

[12] S. Duttagupta, and G. S. Agarwal, “Reciprocity relations for reflected amplitudes”, *Opt. Lett.*, vol. 27(14), 1205 – 1207, 2002.

[13] T. Erdogan, “Fiber Grating Spectra”, *J. Lightwave Technol.*, vol. 15(8), 1277 – 1294, 1994.

[14] B. J. Eggleton, and C. M. de Sterke, “Nonlinear puls propagation in bragg gratings”, *J. Opt. Soc. Am. B*, vol. 14(11), 2980 – 2993, 1997.

[15] M. W. Feise, I. V. Shdrivov, and Y. S. Kivshar, “Bistable diode action in left-handed periodic structures,” *Phys. Rev. E*, vol. 71(3), 037602 – 4, 2005.

[16] W. Freude, A. Maitra, J. Wang, Ch. Koos, C. Poulton, M. Fujii, J. Leuthold, “All-optical signal processing with monlinear resonant devices”, *Proc. 8th Intern. Conf. on Transparent Optical Networks (ICTON'06)*, We.D2.1, Nottingham, UK, June, 2006,

[17] M. Fujii, C. Koos, C. Poulton, J. Leuthold, and W. Freude, “Nonlinear FDTD analysis and experimental verification of four-wave mixing in InGaAsP/InP racetrack micro-resonators,” *IEEE Photon. Technol. Lett.,* vol 18(2), 361 – 363, 2006.

[18] M. Fujii, A. Maitra, C. Poulton, J. Leuthold, W. Freude, “Non-reciprocal transmission and Schmitt trigger operation in strongly modulated asymmetric WBGs”, *Opt. express,* vol. 14 (26), 12782 – 12793, 2006.

[19] M. Fujii, M. Tahara, I. Sakagami, W. Freude, and P. Russer, “High-order FDTD and auxiliary differential equation formulation of optical pulse propagation in 2D Kerr and Raman nonlinear dispersive media,” *IEEE J. Quantum Electron.*, vol. 40(2), 175 – 182, 2004.

[20] K. Gallo, G. Assanto, K. R. Parameswaran, and M. M. Fejer, “All-optical diode in a periodically poled lithium niobate waveguide”, *Appl. Phys. Lett.*, 79(3), 314 – 316, 2001.

[21] E. Germire, “Theory of quarter-wave-stack dielectric mirrors used in a thin Fabry-Perot filter”, *Applied Opt.,* vol. 42(27), 5442 – 5449, 2003.

[22] H. Gibbs, *Optical bistability: controlling light with light*, Academic Press, 1985.

[23] R. Grover, *InP based optical micro-ring resonators*, Ph.D. thesis, Dept. Elect. Eng. and Comp. Sc., Univ. of Maryland, College Park, 2003.

[24] J. He and M. Cada, "Optical bistability in semiconductor periodic structures", *IEEE J. Quantum Electron.,* 27(5), 1182 – 1188, 1991.

[25] C. H. Henry, “Theory of the Linewidth of Semiconductor Lasers”, *IEEE J. Quantum Electron.*, vol. 18(2), 259 – 264, 1982.

[26] J. Herrera, E. Tangdiongga, Y. Liu, M. T. Hill, R. McDougall, A. Poustie, G. Maxwell, F. Ramos, J. Marti, H. de Waardt. G. D. Khoe, A. M. J. Koonen, H. J. S. Dorren, “160 Gb/s all-optical packet switching employing in-band wavelength labelling and a hybrid-integrated optical flip-flop”, *Proc. ECOC’06*, Post deadline paper Th4.1.5, Cannes. France, Sept., 2006,.

[27] A. Hurtado, A. Gonzalez-Marcos, I. D. Henning and M.J. Adams, “Optical bistability and nonlinear gain in 1.55 µm VCSOA”, E*lectron. Lett.,* vol. 42(8), 483 – 484 2006.

[28] K. Ikeda, Y. Fainman, “Nonlinear Fabry-Perot resonator with a silicon photonic crystal waveguide”, *Opt. Lett.*, vol. 31(23), 3486 – 3488, 2006.

[29] T. Iizuka and C.M. de Sterke, “Corrections to coupled mode theory for deep gratings”, *Phys. Rev. E*, vol. 61(4), 4491 – 4499, 2000.

[30] J. D. Jackson, *Classical Electrodynamics,* John Wiley & Sons, New York, 2003.

[31] B. Jalali, and S. Fathpour, “Silicon photonics”, *J. Lightwave Technol.* 24(12), 4600 – 4615, 2006.

[32] X. H. Jia, Z. M. Wu, G. Q. Xia, “Analysis of bistability steady characteristics and dynamic stability of linearly tapered nonlinear Bragg grating”, *Opt. express*, vol. 12(13), 2945 – 2953, 2004.

[33] H. M. Keller, S. Pereira, J. E. Sipe, "Grating enhanced all-optical switching in a Mach-Zehnder interferometer”, *Optics Communication*, vol. 170, 35 – 40, 1999.

[34] J. Koga, “Simulation model for the effects of nonlinear polarization on the propagation of intense pulse lasers,” *Opt. Lett.*, vol. 24, 408 – 410, 1999.

[35] C. Koos, M. Fujii, C. Poulton, R. Steingrueber, J. Leuthold, and W. Freude, “FDTD-modeling of dispersive nonlinear ring resonators: Accuracy studies and experiments,” *IEEE J. Quantum Electron.*, vol. 42(12), 1215 – 1223; 2006

[36] C. Koos, C. Poulton, L. Jacome, J. Leuthold, and W. Freude, “Nonlinear silicon-on-insulator waveguides for all-optical signal processing”, *Opt. express*, vol. 15, 5976 – 5990, 2007.

[37] T. Kremp, *Split-step wavelet collocation methods for linear and nonlinear optical wave propagation*, Ph.D. thesis, Dept. Elect. Eng. and Information Eng, University of Karlsruhe, 2002

[38] H. Lee, G. P. Agrawal, "Nonlinear Switching of Optical Pulses in Fiber Bragg Gratings", *IEEE J. Quantum Electron.*, vol. 39(3), 508 – 515, 2003.

[39] T. K. Liang, and H. K. Tsang, “Efficient Raman amplification in silicon-on-insulator waveguides”, *Appl. Phys. Lett.*, vol. 85(16), 3343 – 3345, 2004.

[40] E. Lidorikis and C. M. Soukoulis, “Pulse-driven switching in one-dimensional nonlinear photonic band gap materials : a numerical study”, *Phys. Rev. E* 61(5), 5825 – 5829, 2000.

[41] X.-S. Lin and S.Lan, “Unidirectional transmission in asymmetrically confined photonic crystal defects with Kerr nonlinearity,” *Chin. Phys. Lett.*, 22, 2847 – 2850, 2005.

[42] N. M. Litchinitser, G. P. Agrawal, B. J. Eggleton, G. Lenz, “High-repetition-rate soliton-train generation using fiber Bragg grating”, *Opt. Express*, vol. 3(11), 411 – 417, 1998.

[43] A. Maitra, J. Wang, O. Hügel, C. G. Polton, W.Freude, and J. Leuthold, “All-Optical flip-flop based on an active stopband tapered DFB structure”, Optical Amplifiers and Their Applications (OAA), WD3, Aug, Budapest, 2005.

[44] A. Maitra, C. G. Poulton, J. Wang, J. Leuthold, and W. Freude, “Low switching threshold using nonlinearities in stopband-tapered waveguide Bragg gratings”, *IEEE J. Quantum Electron.,* 41(10), 303 – 1308, 2005.

[45] A. Maitra, J. Wang, J. Leuthold, and W. Freude, “Isolator behaviour in asymmetric λ/4 phase-shifted structure”, *Photonics 2006*, IOD17, Dec., Hyderabad, 2006.

[46] R. J. Manning, A. D. Ellis, A. J. Poustie, and K. J. Blow, “Semiconductor Laser Amplifiers for Ultrafast All-Optical Signal Processing”, *J. Opt. Soc. Am. B*, vol. 14(11), 3204 – 3216, 1997.

[47] D. N. Maywar and G. P. Agrawal, “Transfer-matrix analysis of optical bistability in DFB semiconductor laser amplifiers with nonuniform gratings”, *J. Quantum Electron.*, vol. 33(11), 2029 – 2037, 1997.

[48] D. N. Maywar, G. P. Agrawal, and Y. Nakano, “Robust Optical Control of an Optical-Amplifier-Based Flip–Flop,” *Opt. Express,* vol. 6(3), 75 – 80, 2000.

[49] D. N. Maywar and G. P. Agrawal, “Effect of Chirped Gratings on Reflective Optical Bistability in DFB Semiconductor Laser Amplifiers,” *IEEE J. Quantum Electron.*, vol. 34(12), 2364 – 2370, 1998.

[50] D. N. Maywar, G. P. Agrawal, and Y. Nakano, “All-optical hysteresis control by means of cross-phase modulation in semiconductor optical amplifiers”, *J. Opt. Soc, Am. B*, vol. 18(7), 1003 – 1013, 2001.

[51] A. Melloni, M. Chinello and M. Martinelli, "All-Optical Switching in Phase-Shifted Fiber Bragg Grating", *IEEE Photon. Technol. Lett*, vol. 12(1), 42 – 44, 2000.

[52] A. Mori, K. Shikano, K. Enbutsu, K. Oikawa, K.Naganuma, M.Kato, S. Aozasa, “1.5 µm band zero-dispersion shifted tellurite photonic crystal fiber with a nonlinear coefficient γ of 675 $W^{-1}km^{-1}$”, *Proceedings ECOC’04*, Th3.3.6.

[53] S. Mujumdar, and H. Ramachandran, “Use of a graded gain random amplifier as an optical diode”, *Opt. Lett.*, vol. 26(12), 929 – 931, 2001.

[54] M. Notomi, A. Shinya, S. Mitsugi, G. Kira, E. Kuramochi, and T. Tanabe, “Optical bistable switching action of Si high-Q photonic-crystal nanocavities,” *Opt. Express* 13, 2678 – 2687 (2005).

[55] L. R. Nunes et. al., “Low energy ultrafast switching in silicon wire waveguides”, *Proceedings ECOC’05*, PDP-0959.

[56] K. Otsuka, “All-Optical Flip–Flop Operations in a Coupled-Element Bistable Device”, *Electron. Lett.,* vol. 24, 800 – 801, 1988.

[57] W. Van Parys, D. Van Thourhout and R. Baets, B. Dagens, J. Decobert, O. Le Gouezigou and D. Make, R. Vanheertum and L. Lagae, “11.4dB Isolation on an Amplifying AlGaInAs/InP Optical Waveguide Isolator”, *Proceedings OFC’06*, OFA2.

[58] C. Porzi, et. al., “Impedance-detuned high-contrast vertical cavity semiconductor switch”, *Proceedings OFC’05*, OThM5.

[59] S. Radic, N. Geroge, G. P. Agrawal, “Theory of low-threshold optical switching in nonlinear phase-shifted periodic structures”, *J. Opt. Soc. Am. B*, vol. 12(4), 671 – 680, 1995.

[60] S. Radic, N. Geroge, G. P. Agrawal, “Analysis of nonuniform nonlinear distributed feedback structures: Generalized transfer matrix method”, *IEEE J. Quantum Electron.*, vol. 31, 1326 – 1336, 1995.

[61] E. G. Sauter, *Nonlinear Optics*, John Wiley & Sons, New York, 1996.

[62] M. Scalora, J. P. Dowling, C. M. Bowden, and M. J. Bloemer, “The photonic band edge optical diode,” *J. Appl. Phys,*. 76, 2023 – 2026, 1994.

[63] M. Scalora, J. P. Dowling, C. M. Bowden, and M. J. Bloemer, “Optical limiting and switching of ultrashort pulses in nonlinear photonic band gap materials”, *Phys. Rev. Lett.* 73, 1368 – 1371, 1994.

[64] O. H.Schmitt, “A thermionic trigger,” *J. Scientific Instruments*, vol. 15, 24, 1938.

[65] J. E. Sipe, L. Poladian, and C.M. de Sterks, “Propagation through nonuniform grating structures”, *J. Opt. Soc. Am. A*, vol. 11(4), 1307 – 1320, 1994.

[66] M. Soljačic′, M. Ibanescu, S. G. Johnson, Y. Fink, and J. D. Joannopoulos, “Optimal bistable switching in nonlinear photonic crystals,” Phys. Rev. E 66, 055601(R)(1-4) (2002).

[67] C. M. de Sterke and J. E. Sipe, *Gap solitons, in Progress in Optics*, vol. XXXIII, North-Holland, Amsterdam, 203 – 260, 1994.

[68] C. M. de Sterke, J. E. Sipe, ‘‘Switching dynamics of finite period nonlinear media: A numerical study’’, *Phys. Rev. A*, vol. 42(5), 2858 – 2869, 1990.

[69] C. M. de Sterke, K. R. Jackson, B. D. Robert, “Nonlinear coupled-mode equations on a finite interval: a numerical procedure”, *J. Opt. Soc. Am. A*, vol. 8(2), 403 – 412, 1991.

[70] N Sugimoto, T. Nagashima, T. Hasegawa, S. Ohara, K. Taira, K. Kikuchi, “Bismuth-based optical fiber with nonlinearity coefficient of 1360$W^{-1}Km^{-1}$”, *Proceedings OFC’04*, PDP 26.

[71] A. Taflove and S. C. Hagness, *Computational electrodynamics: The finite-difference time-domain method*, 3rd ed., chap. 9, Artech House, 2005.

[72] D. Taverner, N. G. R. Broderick, D. J. Richardson, R. I. Laming and M. Ibsen, ‘‘Nonlinear self-switching and multiple gap-soliton ation in a fiber Bragg grating’’, *Opt. Lett.*, vol. 23, 328 – 330, 1998.

[73] M. D. Tocci, M. J. Bloemer, M. Scalora, J. P. Dowling, C. M. Bowden, “Thin-film nonlinear optical diode”, *Appl. Phys. Lett.*, vol. 16, 2324 – 2326, 1995.

[74] J. Wang, A. Maitra, C. G. Poulton, W. Freude, and J. Leuthold, “Temporal dynamics of the alpha factor in semiconductor optical amplifiers”, *J. Lightw. Technol.*, vol. 25(3), 2007

[75] H. G. Winful, J. H. Marburger, and E. Garmire, “Theory of bistability in nonlinear distributed feedback structures”, *Appl. Phys. Lett.*, vol. 35, 379 – 381, 1979.

[76] Z. -M. Wu, G. –Q. Xia, X. –H. Jia, “Nonuniform DFB-SOAs: dynamic characteristics of bistability and a novel configuration based on linearly variable current Injection”, *IEEE J. Quantum Electron.,* vol. 41(3), 384 – 389, 2005.

[77] M. F. Yanik, S. Fan, and M. Soljačic′, “High-contrast alloptical bistable switching in photonic crystal microcavities”, *Appl. Phys. Lett.* 83, 2739 – 2741, 2003.

[78] K. S. Yee, “Numerical solution of initial boundary value problems involving Maxwell’s equation in isotropic media,” *IEEE Trans. Antennas Prop.*, vol. 14, 302 – 307, 1966.

[79] P. Yeh, *Optical Waves in Layered Media*. John Wiley and Sons, New York, 1988.

[80] K. Yelen, L. M. B. Hickey, M. N. Zervas, “A new approach for fiber DFB lasers with improved efficiency”, *IEEE J. Quantum Electron.,* vol. 40(6), 711 – 720, 2004.

[81] Y. Yu, C. D. Cantrell, L. S. Tamil, “Analysis of nonlinear periodic dielectric media using the finite-difference method with absorbing boundary conditions”, *J. Opt. Soc. Am. A*, vol. 13(1), 147 – 151, 1996.

[82] N-S Zhao, H. Zhou, Q. Guo, W. Hu, X-Bo Yang, S, Lan, and Xu-Sheng Lin, “Design of highly efficient optical diodes based on the dynamics of nonlinear photonic crystal molecules”, *J. Opt. Soc. Am. B*, vol. 23(11), 2434 – 2440, 2006.

[83] D. Zwillinger, *Handbook of Differential Equations,* Academic press, Second edition.

Appendix A: List of parameters used for SOA-DFB simulation

Physical Quantity	Symbol	Value
Device length	L	300 μm
Active-region width	W	2 μm
Active-region depth	d	0.15 μm
Differential gain	A	6×10^{-16} cm^2
Transparency carrier density	N_0	0.4×10^{18} cm^{-3}
Carrier lifetime	τ	0.2 ns
Saturation power	P_{sat}	10 mW
Confinement factor	Γ_{conf}	0.32
modal refractive index	n	3.4
Mode cross section	σ	10 μm^2

Appendix B: Numerical methods

In spite of the complexity of NLCME, a large set of analytic solution exists [1] [10] for certain special cases. But in general it is solved numerically. As with any numerical algorithm for solving nonlinear partial differential equations, the method must be tested for its stability and numerical accuracy. In this Appendix we discuss different numerical methods used to solve the NLCME's. We compare different methods with their relative accuracy and numerical efficiency.

B.1 Transfer matrix method

The most popular method used to simulate the steady state behaviour of a 1D complex structure with axially varying parameters is the transfer matrix method (TMM). For linear case this method gives the exact numerical solution of the PDE's. In this section we first discuss a general method for solving coupled differential equations with constant coefficients and extent it to multi-sections to include grating non-uniformity. Later we will discuss about the extension of this analysis to the nonlinear case, i.e., in the case the coefficients are no longer constant but depends weakly upon the input fields.

The pair of couple mode equations (2.40) comprises 2 × 2 system of homogeneous differential equations, we write in the general form as

$$\begin{gathered} \frac{\partial \underline{A}}{\partial z} = \mathrm{i}\underline{M}\underline{A}, \\ \underline{A} = \begin{bmatrix} A_f \\ A_b \end{bmatrix}, \quad \underline{M} = \mathrm{i}\begin{bmatrix} \delta_f & \kappa_f \\ -\kappa_b & -\delta_b \end{bmatrix}. \end{gathered} \tag{B.1}$$

In the above equation $\delta_{f,\,b}$ represents the self coupling coefficients for the forward and backward coupling waves respectively, while $\kappa_{f,\,b}$ represents the cross coupling coefficients. For the time being we assume these coefficients to be constant, representing a linear system. The standard technique to solve this type of coupled differential equations is eigenvector decomposition [83]. Applying this technique, the solution of the differential equation can be written as

$$\begin{bmatrix} A_f(z) \\ A_b(z) \end{bmatrix} = \underline{\mathrm{v}}^{-1} \begin{bmatrix} \exp(\tilde{\gamma}_1 z) & 0 \\ 0 & \exp(\tilde{\gamma}_2 z) \end{bmatrix} \underline{\mathrm{v}} \begin{bmatrix} A_f(0) \\ A_b(0) \end{bmatrix}. \tag{B.2}$$

Here $\tilde{\gamma}_{1,2}$ are the eigenvalues of matrix $\underline{M}$ with eigenvectors $\underline{\mathrm{v}}_{1,2}$, which can be explicitly written as

$$\begin{gathered} \tilde{\gamma}_{1,2} = \delta_d \pm \sqrt{\delta_m^{\ 2} - \kappa_e^{\ 2}}, \\ \text{where } \delta_m = \frac{(\delta_f + \delta_b)}{2}, \quad \delta_d = \frac{(\delta_f - \delta_b)}{2}, \quad \kappa_e = \kappa_f \kappa_b, \end{gathered} \tag{B.3}$$

The matrix comprises the column vectors of the eigenvectors are written as

$$\underline{\mathrm{v}} = \begin{bmatrix} 1 & 1 \\ -\frac{1}{\kappa_f}\left(\delta_m - \sqrt{\delta_m{}^2 - \kappa_e{}^2}\right) & +\frac{1}{\kappa_f}\left(\delta_m + \sqrt{\delta_m{}^2 - \kappa_e{}^2}\right) \end{bmatrix} \tag{B.4}$$

We apply proper boundary conditions at the input and output of a grating of length *L* and with this we can write the solutions as

$$\begin{bmatrix} A_f(L) \\ A_b(L) \end{bmatrix} = \underline{T}\,\underline{A}\begin{bmatrix} T_{11} & T_{12} \\ T_{21} & T_{22} \end{bmatrix}\begin{bmatrix} A_f(0) \\ A_b(0) \end{bmatrix}, \tag{B.5}$$

$$\begin{aligned} T_{11} &= \exp(\mathrm{i}\delta_d L)\left[\cos(\tilde{q}L) + \frac{\mathrm{i}\delta_m}{\tilde{q}}\sin(\tilde{q}L)\right] \\ T_{12} &= \frac{\mathrm{i}\kappa_e}{\tilde{q}}\exp(\mathrm{i}\delta_d L)\sin(\tilde{q}L) \\ T_{21} &= \frac{\mathrm{i}\kappa_e}{\tilde{q}}\exp(\mathrm{i}\delta_d L)\sin(\tilde{q}L) \\ T_{22} &= \exp(\mathrm{i}\delta_d L)\left[\cos(\tilde{q}L) - \frac{\mathrm{i}\delta_m}{\tilde{q}}\sin(\tilde{q}L)\right]. \end{aligned} \tag{B.6}$$

$$\tilde{q} = \sqrt{\delta_m{}^2 - \kappa_e{}^2}. \tag{B.7}$$

In the above equation matrix $\underline{T}$ represents the transfer matrix of the whole grating structure. If we divide the grating length into *m* smaller subsections, we can define a transfer matrix of each section in the similar way. The transmission or reflection characteristics can then be obtained by multiplying matrices of individual sections in the following way

$$\begin{bmatrix} A_f(L) \\ A_b(L) \end{bmatrix} = \underline{T}^{(M)}\underline{T}^{(M-1)}\cdots\underline{T}^{(1)}\begin{bmatrix} A_f(0) \\ A_b(0) \end{bmatrix} \tag{B.8}$$

Different grating non-uniformities can be introduced by choosing proper grating parameters in different sections. So in principle any complex structure (e.g. taper, chirp, discrete phase shift) can be simulated using a stair-case approach. Here we assume that these parameters remain constant over the grating subsections. A discrete phase shift can be introduced in-between any of these subsections by introducing a simple phase-shift matrix as

$$\begin{aligned} \begin{bmatrix} A_f(L) \\ A_b(L) \end{bmatrix} &= \underline{T}^{(M)}\underline{\Phi}\,\underline{T}^{(M-1)}\cdots\underline{T}^{(1)}\begin{bmatrix} A_f(0) \\ A_b(0) \end{bmatrix}, \\ \underline{\Phi} &= \begin{bmatrix} \exp(+\mathrm{i}\psi) & 0 \\ 0 & \exp(\text{-}\mathrm{i}\psi) \end{bmatrix}. \end{aligned} \tag{B.9}$$

Since we assume that no wave is incident from the back of the grating we use the backward calculation method, i.e., we specify the output and calculate the corresponding input by multiplying the inverse of individual transfer matrices in the following way

$$\begin{bmatrix} A_f(0) \\ A_b(0) \end{bmatrix} = \underline{T}^{(1)^{-1}} \underline{T}^{(2)^{-1}} \cdots \underline{T}^{(M)^{-1}} \begin{bmatrix} A_f(L) \\ 0 \end{bmatrix} \tag{B.10}$$

So we can calculate the transmissivity and the reflectivity of the above structure by the following expressions

$$\text{Transmissivity} = \left| \frac{1}{T_{22}} \right|^2, \quad \text{Reflectivity} = \left| -\frac{T_{21}}{T_{22}} \right|^2. \tag{B.11}$$

It is to be noted that these section length can not be chosen arbitrarily small. The section length is limited by the validity of slowly varying envelope approximations, which can be quantitatively written as

$$L_m \gg \beta. \tag{B.12}$$

Here L_m is the length of the m^{th} section, and β is the propagation constant in the grating. The expressions (B.6) simplifies to the standard liner problem as given by Erdogan et al. [13]

The above method is strictly valid for constant coefficients. In case of nonlinearity this coefficients are no longer constant but depends on the input fields, as can be seen from section 2.4. But this rather simple calculation method can also be applied for calculating the transmission characteristics of nonlinear structures [73]. We start with a constant distribution of power in the grating structure, i.e., we assume that all the coefficients of the transfer matrix in each section are constant. Then we calculate the field distribution of the entire structure. Then we update the coefficients (e.g. gain for active devices and effective detuning parameters for the forward and the backward waves) with the calculated average power in each section. We continue these steps until the power distribution inside the entire grating does not change any more. This type of iterative solution can be used to solve the GNLCME's in the steady state. Figure B-3 shows a flowchart for numerical solution using TMM.

B.2 Generalized transfer matrix method

The exact solution of the NLCME is useful in calculating the steady-state response of the structure. But the simplicity in the formulation rules out the possibilities to design non-uniform structures or structures with axially varying parameters. This limits the applicability of the present formulation to a wide class of complex periodic structures. However this problem can be solved by extending this method with by so-called generalized transfer matrix method (GTMM) [60]. This analysis is a powerful tool in simulating a complex grating structure, in the framework of coupled mode theory.

In GTMM a non-uniform structure is modelled as a set of M strictly periodic, uniform segments, as shown in Figure B-1. The field distribution in each section can be calculated analytically provided the boundary condition at one of its interface is given. We then can relate the field in one section to its neighbouring section with proper boundary conditions similar to the transfer matrix method (TMM) as described in Appendix B.1. We divide the entire structure of length L is into M segments, each of length L_m. The coupled mode formalism in each uniform section of length L_m is valid as long as the following condition

$$L_m \gg 2\pi / \beta_m \,, \tag{B.13}$$

is satisfied, i.e., as long as the section length is kept much longer than the period of the grating in that section.

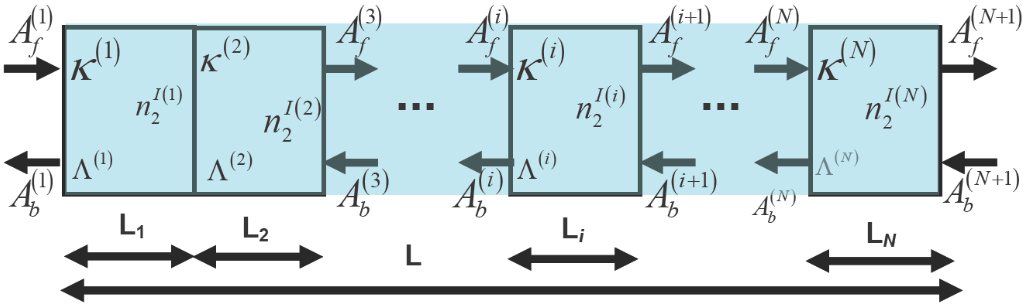

Figure B-1 : Schematic GTMM

Now we focus only on the m^{th} uniform section, which have the following set of constant parameters (κ_m , β_m, Γ_m, Ω_m , L_m). It can be shown that for a given intensity distribution for $z \geq z_{m+1}$, the field distribution within the neighbouring section (i.e., within $z_m \geq z \geq z_{m+1}$) can be calculated exactly. So we can start with the transmitted intensity distribution at the end of the structure and repeat the procedure ($M - 1$) times to get the intensity distribution at the beginning of the structure. In each section the exact solution can be obtained using the elliptic function formalism, as described in the previous section.

We follow the same procedure as used for a uniform structure and rewrite the equations (3.4) – (3.7) in the normalized form as

$$\frac{L}{2}\frac{\mathrm{d}J}{\mathrm{d}z} = +\tilde{\kappa}_m \sqrt{J\left(J - \tilde{F}_{T,m}\right)} \sin\left(\psi_m\right), \tag{B.14}$$

$$\frac{L}{2}\frac{\mathrm{d}\left(J - \tilde{F}_{T,m}\right)}{\mathrm{d}z} = +\tilde{\kappa}_m \sqrt{J\left(J - \tilde{F}_{T,m}\right)} \sin\left(\psi_m\right), \tag{B.15}$$

$$JL\frac{\mathrm{d}\phi_+}{\mathrm{d}z} = +\tilde{\kappa}_m \sqrt{J\left(J - \tilde{F}_{T,m}\right)} \cos\left(\psi_m\right) + \frac{4\eta_m}{3}\left(3J - 2\tilde{F}_{T,m}\right)J, \tag{B.16}$$

$$-L\left(J - \tilde{F}_{T,m}\right)\frac{\mathrm{d}\phi_-}{\mathrm{d}z} = +\tilde{\kappa}_m \sqrt{J\left(J - \tilde{F}_{T,m}\right)} \cos\left(\psi_m\right) + \frac{4\eta_m}{3}\left(3J - \tilde{F}_{T,m}\right)\left(J - \tilde{F}_{T,m}\right). \tag{B.17}$$

All the quantities are normalized to the dimensionless form using the reference intensity $A_c^{\,2}$ as,

$$\bar{I} = \frac{A_-^{\,2}}{A_c^{\,2}}; \quad \tilde{G}_m = \frac{G_m L}{2A_c^{\,2}}; \quad \tilde{\kappa}_m = \kappa_m L; \quad \tilde{\delta}_m = \delta_m L; \quad \eta_m = \sum_{m=1}^{M} \frac{n_{2,m}^{I} L_m}{L}. \tag{B.18}$$

The two conserved quantities (3.8) and (3.9) can be similarly written as,

$$\tilde{G}_m = \tilde{\kappa}_m \sqrt{J\left(J - \tilde{F}_{T,m}\right)} \cos\psi_m + \left[\tilde{\delta}_m + 2\eta_m \left(J - \tilde{F}_{T,m}\right)\right] J, \tag{B.19}$$

$$\tilde{F}_{T,m} = J - \bar{I}. \tag{B.20}$$

We use $\bar{I} = A_-^{\,2} / A_c^{\,2}$ and $\psi_m = 2\delta_m z + \phi_+(z) - \phi_-(z) - \Omega_m$. We define $\Delta\Omega_m = \Omega_{m+1} - \Omega_m$ as the phase difference between two adjacent sections and η_m as the average nonlinearity in the m^{th} section. It can be further shown that, the continuity of the flux at the boundary between two sections, leads to a conservation of the transmitted flux over the entire structure, i.e.,

$$\tilde{F}_{T,1} = \tilde{F}_{T,2} = \cdots \tilde{F}_{T,m} = \cdots = \tilde{F}_{T,M} = \tilde{F}_T. \tag{B.21}$$

We denote this conserved flux as $\tilde{F}_T$. The above equation is a direct consequence of the equation of continuity, which states that for a loss/gain-less medium the transmitted flux in the steady state must be conserved. Finally we eliminate ψ_m from equation (B.19) and (B.14) arrive at the equation governing the forward flux in segment m as

$$\begin{aligned}\left(\frac{L}{2}\frac{\mathrm{d}J}{\mathrm{d}z}\right)^2 &= \tilde{\kappa}_m^{\,2} J\left(J - \tilde{F}_T\right) - \left[\tilde{G}_m - \left\{\tilde{\delta}_m + 2\eta_m\left(J - \tilde{F}_T\right)\right\} J\right]^2 \\ &= P_m(J).\end{aligned} \tag{B.22}$$

The above equation can be solved in terms of standard elliptic integrals as described in previous section. For a given transmitted flux $\tilde{F}_T$ at the end of the structure and for given parameters (e.g. κ, δ, Γ) the right hand side of equation (B.22) can be represented by a polynomial of degree 4. For a piecewise uniform section assumption this polynomial has unique roots, and the solution of the above equation can be writing in the explicit form in terms of these roots. Here we discuss the most frequently encountered case in which all the roots J_i^{m} ($i = 1, 2, 3, 4$) of the polynomial $P_{\mathrm{m}}(J)$ are real, and $J_1^{\mathrm{m}} \geq J(z) \geq \tilde{F}_{T,m} \geq J_2^{\mathrm{m}} > J_3^{\mathrm{m}} > J_4^{\mathrm{m}}$ is valid. This assumption can again be justified by the qualitative analysis of motion of a particle in the quartic potential in which only $J_1^{\,m} \geq J(z) \geq J_2^{\,m}$ is real assessable solution.

We assume again a non-reflecting boundary condition, which allows us to calculate the conserved quantity G_M in the last section similar to (3.12). This defines the polynomial, hence the roots of the $P_M(J)$. With the knowledge of the solution in this section we can relate the phase ψ to the next section through the following relation

$$\cos\psi_{m+1}\left(z_{m+1}\right) = \frac{\tilde{G}_{m+1} - \left[\tilde{\delta}_{m+1} + 2\eta_{m+1}\left(J_{m+1} - T\right) J_{m+1}\right]}{\tilde{\kappa}_m \left[\left(J_{m+1} - T\right) J_{m+1}\right]^{1/2}}. \tag{B.23}$$

We can include a discrete phase shift also at the segment interface by

$$\psi_m\left(z_{m+1}\right) = \psi_{m+1}\left(z_{m+1}\right) - \Delta\Omega_m. \tag{B.24}$$

In the similar way we can apply the same procedure successively to get the field distribution of the entire structure. Figure B-2 shows the flowchart of the method described here.

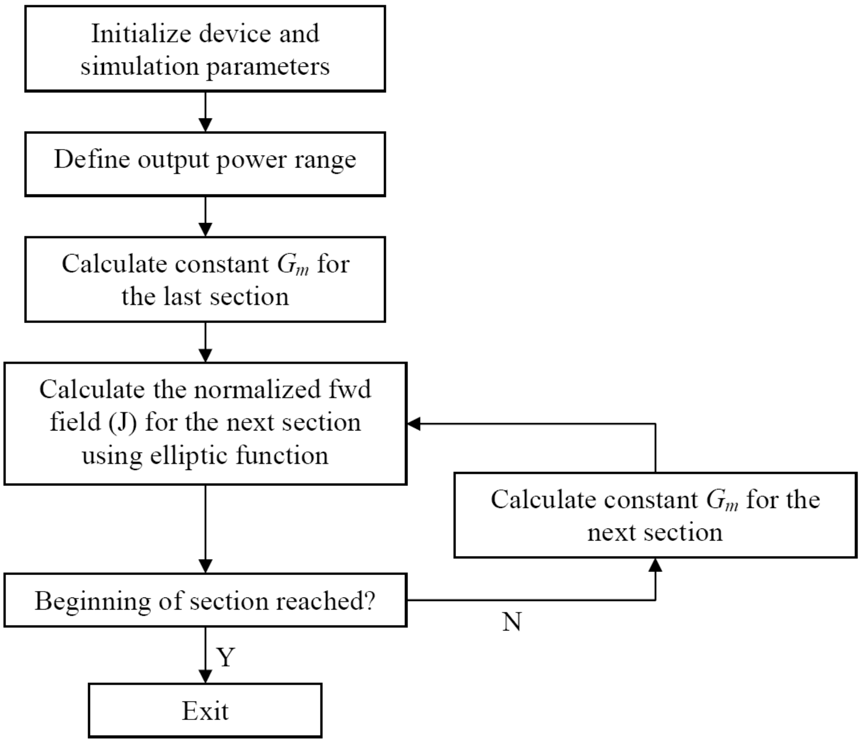
Initialize device and simulation parameters
Define output power range
Calculate constant G_m for the last section
Calculate the normalized fwd field (J) for the next section using elliptic function
Calculate constant G_m for the next section
Beginning of section reached?
N
Y
Exit

Figure B-2 : Flowchart for calculation of the field distribution using GTMM for passive device.

For each section we can integrate the equation (B.22) and get the similar result like[21] in SEction 3.1.2.1

$$J(z) = J_3 - \frac{J_3 - J_2}{1 - \frac{J_1 - J_2}{J_1 - J_3}\mathrm{sn}^2(\tilde{u}, s)}. \tag{B.25}$$

Here $\tilde{u}$ is given by the following expression[22]

$$\tilde{u} = \mathrm{sn}^{-1}(J_{m+1}, s) - \frac{4\eta_m (z_{m+1} - z_m)}{L}. \tag{B.26}$$

This completes the solution of NLCME with axial variation of grating parameters. In the subsequent sections we will use GTMM for calculating the steady state response of axially varying passive nonlinear grating structures.

---

[21] Here we again consider the frequently encountered case that all real roots of the polynomial $P_i(J)$ are real. For a more general description see Byrd and Freidman [8]

[22] The inverse of elliptic function is multivalued; here we choose the proper branch.

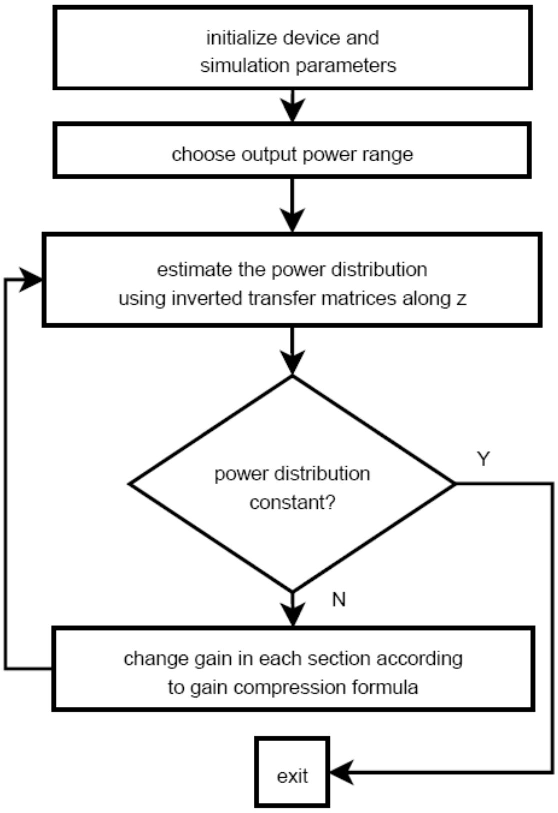
initialize device and simulation parameters
choose output power range
estimate the power distribution using inverted transfer matrices along z
power distribution constant?
Y
N
change gain in each section according to gain compression formula
exit

Figure B-3 : Flowchart for numerical solution using TMM.

B.3 Finite difference method

In this section we describe the numerical method used to solve the NLCME's using the finite difference (FD) method. In all the cases follows we use the following type of boundary conditions

$$\begin{aligned} A_f(0,t) &= A_{in,f}(t), \\ A_b(L,t) &= A_{in,b}(t), \\ A_{f,b}(z,0) &= A_{f,b}^{\text{hold}}(z). \end{aligned} \tag{B.27}$$

Here we describe a general case in which two signals are injected from the forward $A_{\text{in, f}}$ and from the backward $A_{\text{in, b}}$ direction, $A_{f,b}^{\text{hold}}(z)$ gives the initial field distribution inside the grating. So for a non-reflecting boundary conditions we have $A_{\text{in, b}} = 0$. We write the NLCME's in the following form

$$\begin{aligned} +\frac{\partial A_f}{\partial z} + \frac{1}{v_g}\frac{\partial A_f}{\partial t} &= \mathrm{i}\delta_{eff}^{f} A_f + \mathrm{i}\kappa A_b = F\left(A_f, A_b\right), \\ -\frac{\partial A_b}{\partial z} + \frac{1}{v_g}\frac{\partial A_b}{\partial t} &= \mathrm{i}\delta_{eff}^{b} A_b + \mathrm{i}\kappa A_f = G\left(A_f, A_b\right). \end{aligned} \tag{B.28}$$

Here we have introduced the two functions *F* and *G*. These quantities are general function of position and time and are expressed in terms of the local forward and backward propagating waves. Before looking at any actual numerical method, we first discretize the equations and limit their computational domain. For a device of length L we discretize our z-axis between z = 0 and $z = L$ with grid size of $\Delta z = L/N_z$, were $N_z + 1$ is the spatial grid points. Similarly we discretize the t-axis between $t = 0$ and $t = T_{\max}$ with grid size of $\Delta z = L/N_t$, were $N_t + 1$ is the temporal grid points. The grid size Δz, Δt is to be chosen carefully for each problem. The right choice of the discrete steps Δz and Δt is crucial for the numerical calculation [70]. If the steps are too large, the errors of the simulation will grow quickly and the result will be worthless whereas if they are too small, we waste computational resources and the calculations become too slow and introduce artefacts from numerical dispersion. It should be noted, that the grid points do not necessarily have to be equidistant for all methods, but in our case it makes the implementation much easier. Also the spatial discretization Δz cannot be chosen very small which is limited by the validity of the SVEA used in this thesis. Next we have to go from the continuous functions $A_{\mathrm{f,\,b}}(z, t)$ to their discrete counterparts

$$A_{f,b}\left(z,t\right)=A_{f,b}\left(m\Delta z,n\Delta t\right),\qquad m=0,\ldots N_z;n=0,\ldots N_t. \tag{B.29}$$

The discretization is shown schematically in Figure B-4. All the other structural parameters like κ, Γ, δ can also be discritized in a similar fashion. In Figure B-4 the green dots represent the initial distribution at $t = 0$. The blue and the red dots represent the front and the back of the grating. We discretize the first equation in (B.28) using Euler forward difference in time and backward differences in space. While the second equation in (B.28) using forward differences in time and forward difference in space. So we can write in our computation domain,

$$\begin{aligned} A_f^{m,n+1} &= \left(1-\frac{v_g\Delta t}{\Delta z}\right)A_f^{m,n}+\frac{v_g\Delta t}{\Delta z}A_f^{m-1,n}+v_g\Delta t\,F^{m,n}, \\ A_b^{m,n+1} &= \left(1-\frac{v_g\Delta t}{\Delta z}\right)A_f^{m,n}+\frac{v_g\Delta t}{\Delta z}A_f^{m+1,n}+v_g\Delta t\,G^{m,n}. \end{aligned} \tag{B.30}$$

To calculate the fields in the next time step at certain grid point the knowledge of the neighbouring points are needed. This type of discretization is justified as the in we have mixed boundary conditions, i.e., the forward field boundary conditions are defined at the front of the structure while the backward field boundary conditions are defined at the back of the grating.

This method gives the solution of the NLCME but is limited by the accuracy of first order method. So to get a reasonable accuracy we need to use smaller grid size leading to larger usage of computational resources. To overcome these difficulties higher order method should be tried which is discussed in the next section.

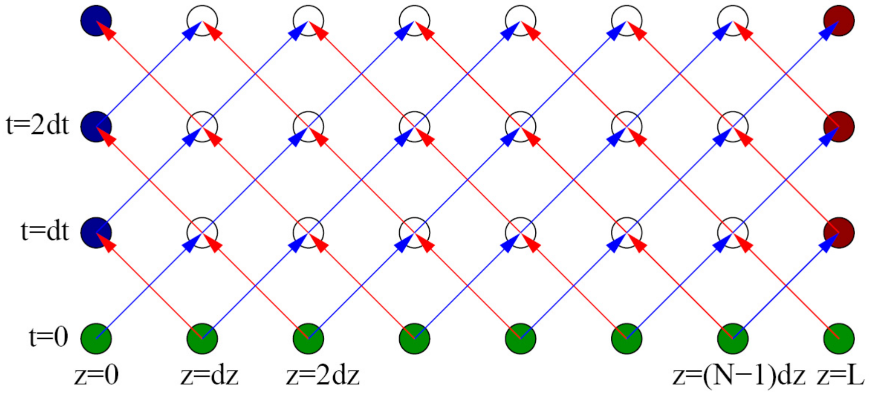

Figure B-4 : Finite difference method

B.4 Implicit Runge-Kutta method

The accuracy of the Euler method is rather low. To overcome these difficulties de Sterke et al. [69] suggested an implicit 4th-order Runge-Kutta method based on the collocation scheme.Here, we will only give a brief overview how the algorithm works and how it can implemented. For a more detailed description and the mathematical background please refer to [69] (particularly appendix A). A first step towards a more efficient integration method is to transform the partial differential equations into ordinary differential equations. This can be done by the simple coordinate transformation of which transforms the PDE's along its characteristics,

$$\begin{aligned} z &= \xi - \tau, \\ t &= \xi + \tau, \end{aligned} \tag{B.31}$$

In terms of the transformed co-ordinates the NLCME can be written as

$$\begin{aligned} \frac{\partial A_f}{\partial \xi} &= \mathrm{i}\delta^f_{eff} A_f + \mathrm{i}\kappa A_b = F\left(A_f, A_b\right), \\ \frac{\partial A_b}{\partial \tau} &= \mathrm{i}\delta^b_{eff} A_b + \mathrm{i}\kappa A_f = G\left(A_f, A_b\right). \end{aligned} \tag{B.32}$$

So we can see that this transformation reduces the PDE into ODE. It is to be noted that the co-ordinates are no longer independent but are coupled via (B.32). Each of this equation can be integrated by using higher-order efficient methods and by combining the results suitably in the grid points. The numerical procedure described by de Sterke et al. utilizes the collocation method and writes the implicit equation in the computation domain as

$$\begin{aligned} y_{n+\frac{1}{2}} &= y_n + h\left[a_{21} f\left(x_n, y_n\right) + a_{22} f\left(x_{n+\frac{1}{2}}, y_{n+\frac{1}{2}}\right) + a_{23} f\left(x_{n+1}, y_{n+1}\right)\right], \\ y_{n+1} &= y_n + h\left[a_{31} f\left(x_n, y_n\right) + a_{32} f\left(x_{n+\frac{1}{2}}, y_{n+\frac{1}{2}}\right) + a_{33} f\left(x_{n+1}, y_{n+1}\right)\right]. \end{aligned} \tag{B.33}$$

Here it is assumed that the general form of the ODE is

$$\frac{\mathrm{d}y}{\mathrm{d}x} = f\left(x, y\right). \tag{B.34}$$

Here 'y' represents either A_f or A_b in the transformed coordinate. The coefficients are listed in Table B1. An iterative method is used to solve the implicit equation (B.33). It is important to note that near the boundary this implicit equation cannot be applied in those point Euler method is used (see Figure B-5). So starting from an initial estimate the solution can be improved using iterative approach.

Table B1 : Values of the coefficients used in integration and extrapolation procedure.

$a_{21} = 5/24$ $a_{21} = 1/6$	$a_{22} = 1/3$ $a_{32} = 2/3$	$a_{23} = -1/24$ $a_{33} = 1/6$
$b_{21} = 3/8$ $b_{21} = 4/3$	$b_{22} = 0$ $b_{32} = -8/3$	$b_{23} = 9/8$ $b_{21} = 10/3$

This method can also be used to extrapolate using the collocation method to get a good estimate for the next integration step using the following expressions.

$$\begin{aligned} y_{n+\frac{3}{2}} &= y_n + h\left[b_{21} f\left(x_n, y_n\right) + b_{22} f\left(x_{n+\frac{1}{2}}, y_{n+\frac{1}{2}}\right) + b_{23} f\left(x_{n+1}, y_{n+1}\right)\right], \\ y_{n+2} &= y_n + h\left[b_{31} f\left(x_n, y_n\right) + b_{32} f\left(x_{n+\frac{1}{2}}, y_{n+\frac{1}{2}}\right) + b_{33} f\left(x_{n+1}, y_{n+1}\right)\right]. \end{aligned} \tag{B.35}$$

The coefficients are listed in Table B1. The schematic procedure can be see from the following Figure B-9

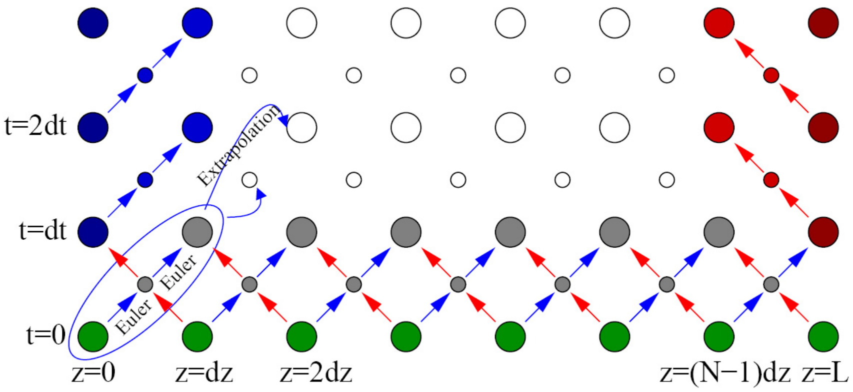

Figure B-5 : Implicit Runge-Kutta method.

B.5 Summary

In this Appendix we have discussed different numerical methods which can be used to solve the time dependent or steady state GNCLME. For steady state calculation TMM is best suited. For slowly time varying cases also TMM can be applied using iterative approach. For time dependent simulation the implicit Runge-Kutta method is more efficient than the simplified Euler method. The implicit method saves the computation resources and is more accurate. But in this procedure the temporal and spatial discretization can not be chosen independently which may pose limitation to the method. In this thesis we have used the implicit Runge-Kutta method for calculating the temporal dynamics of nonlinear periodic structures until otherwise specified.

Acknowledgements

Many people have contributed to this work in terms of their inspirations, guidance, support, and constructive criticism. The space prohibits full reckoning of my gratitude but some needs special mention.

My sincere acknowledgement is due towards my supervisor Prof. W. Freude. Working under him was a satisfying experience. His analytical acumen and penchant for perfection went a long way in refining the work to its present form. He shared a tremendous amount of time with me — I value our conversations on physics, mathematics, and on the process and techniques of writing technical papers. I am indebted to the flexibility and encouragement he provided to explore many aspects of research, and my personal life with his useful suggestions.

I would like to thank Prof. J. Leuthold for his extended support and useful comments during my stay in IHQ. I was privileged to work with him, and thank him for introducing me to the field of nonlinear signal processing using SOA, which covers a major part of my thesis. I thank him for introducing me to Dr. D. Maywar in the Univ. Rochester.

I would like to thank Prof. M. Fujii, Toyama University, for introducing me to the nonlinear FDTD algorithm. I really appreciate his valuable suggestions, and his simulating the sidewall corrugated waveguide resonators using nonlinear FDTD. I would like to thank Dr. D. Maywar for the discussions in the areas of nonlinear active DFB structures.

I would like to mention specifically Mr. J. Wang. It was really a nice experience working with him. The late hour discussions in the balcony were always most productive. I would like to thank Dr. C. G. Poulton. It was always rewarding to discuss with him and to hear his always stimulating comments, coding physics and mathematics. Among the other colleagues at IHQ I would like to thank Dr. Christian Koos, Mr. J. Brosi, Dr. G. Böttger, and Mr. A. Marculescu for the useful discussion during my stay in Karlsruhe.

I thank the German Research foundation (DFG) for the scholarship provided in the framework of the Research Training Group 786 “Mixed Fields and Nonlinear Interactions”.

Few other names should be mentioned for their help in the personal front during my stay in Karlsruhe: They are Dr. S. Kar and Dr. G. Pattanaik both presently at RPI, Troy, Dr. S. Ghosh from ICTP, Trieste. Saswat, Sidhu, Dr. V. Janardhanan, Dr. K. C. Agarwal, Dr. L. Chandra, Mohor, Krish, Dr. I. Mukhapadhaya, Dr. S. Gupta from FZK, Dr. S. K. Das from Univ. of Maryland, Dr. R. Paul at Univ. of California, Davis and Asok and Eva Kunchiwala.

I would like to thank mana, mum, didi and dadai for giving me support and encouragement during the difficult parts of my life.

Most of all, I thank my wife, Smriti. She has graced my life with her support, understanding and love. I thank her for her sacrifice as I pursued my goals. I hope to return such generosity to you in our new life together.

I am deeply grateful to my mother and father for encouraging me to pursue my education, for teaching me the value of experiences, and for their love.

Resume

Ayan Maitra

Date of birth 6th November 1975, Kolkata, India

Educational Qualification

PhD in **Electrical and Communication Engineering** from University of Karlsruhe, Karlsruhe, Germany. Thesis title "**Nonlinear resonant devices for all-optical signal processing**". Date of graduation: June 12, 2007.

M. Tech. in **Opto-electronics and Optical communication** from Indian Institute of Technology, Delhi, India in 2002.

M. Sc. in **Physics** from Jawaharlal Nehru University, Delhi, India in 2000.

B.Sc. in **Physics (Hons.)** from A. J. C. Bose College, Calcutta, India in 1997.

Awards and Achievements

- Awarded ***Rektor Scholarship*** (from June 2005, for 25 months), by University of Karlsruhe, Karlsruhe, Germany.

- Awarded doctoral research fellowship (from June 2002, for 3 years), by , in the Research Training Group 786 "Mixed Fields and Nonlinear Interactions **GKMF**" for pursuing a doctoral study in University of Karlsruhe, Karlsruhe, Germany.

- Awarded full fellowship for attending ***Enrico Fermi School of Physics,*** course ***Electron and Photon Confinement in Semiconductor Nanostructures,*** summer 2002, in Verenna, Italy, June 2002.

- Qualified ***GATE*** (India) in physics in June 2000 with 97.8 percentile.

- Qualified the ***CSIR-NET*** (India) for Junior Research Fellowship (JRF) in June 2000. Awarded Junior Research Fellowship (JRF) in Physical Sciences by the Council of Scientific and Industrial Research (CSIR).

List of Publications

Journals

1. *"Low switching threshold using nonlinearities in stopband-tapered waveguide Bragg gratings*", **A. Maitra,** C. G. Poulton, J. Wang, J. Leuthold, W. Freude. ***IEEE J. of Quantum Electron.***, vol. 41, no. 7, 1303, 2005.
2. "*Non-reciprocal transmission and Schmitt trigger operation in strongly modulated asymmetric WBGs*", M. Fujii, **A. Maitra**, C. Poulton, J. Leuthold, W. Freude, ***Opt. Exp***, vol.14, no. 26, 12782, Dec. 2006.
3. *"Temporal dynamics of the alpha factor in semiconductor optical amplifiers",* J. Wang, **A. Maitra**, C. G. Poulton, W. Freude, J. Leuthold, ***J. Lightw. Technol.,*** vol. 25, no. 3, 2007.

4. "*All-optical diode action in nonlinear asymmetric Fabry-Perot resonator with nonlinear medium in the cavity*", **A. Maitra**, J. Wang, W. Freude, J. Leuthold, in preparation.
5. "*Regeneration and noise suppression in XPM and XGM based DPSK wavelength conversion*", J. Wang, **A. Maitra**, W. Freude, J. Leuthold, in preparation.

Conference Proceedings

1. "*Fresnel-like reflection for cylindrical waves at a cylindrical interfac*e", **A. Maitra,** A. Sharma, W. Freude. School of Physics, Electron and Photon Confinement in Semiconductor Nanostructures, Verenna, Italy, June 2002.
2. "*All-optical flip-flop based on an active stopband tapered DFB structure*", **A. Maitra**, J. Wang, O. Hügel, C. G. Polton, W.Freude, J. Leuthold, ***Optical Amplifiers and Their Applications*** **(OAA)**, WD3, Budapest, Aug. 2005.
3. *"Isolator and switches based on nonlinear Bragg grating",* **A. Maitra**, J. Wang, O. Hügel, C. G. Polton, W.Freude, J. Leuthold, ***COST-P11***, Twenty, Netherlands, Oct. 2005**. (invited)**
4. "*Dynamics of linewidth-enhancement factor in semiconductor optical amplifiers*", J. Wang, C. G. Poulton, **A. Maitra**, S. Cabot, J. Jaques, W. Freude, J. Leuthold, ***Optical Amplifiers and Their Applications*** **(OAA)**, OTuC3, Whistler, Canada, June. 2006.
5. "*All-optical signal processing with nonlinear resonant device*", W. Freude, **A. Maitra**, J. Wang, C. Koos, C. G. Poulton, M. Fujii, J. Leuthold, ***International Conference of Transparent Optical Network*** **(ICTON)**, Nottingham, June 2006. **(invited)**
6. "*Isolator behaviour in asymmetric $\lambda/4$ phase-shifted structure*", **A. Maitra**, J. Wang, J. Leuthold, W. Freude, IOD17, ***Photonics 2006***, Hyderabad, India, Dec. 2006.
7. *"100 Gbit/s All-optical wavelength conversion with an SOA and a delay-interferometer"*, J. Wang , **A. Maitra**, W. Freude, J. Leuthold, ***Workshop der ITG Fachgruppe 5.3.1; "Modellierung photonischer Komponenten und Systeme",*** Technische Universität München, Germany, 12.-13. February, 2007.
8. "*Broadband slow light and nonlinear switching devices*", G. Böttger, J. –M. Brosi, **A. Maitra**, J. Wang, A. Y. Petrov, M. Eich, J. Leuthold, W. Freude, ***Progress in Electromagnetic Research*** **(PIERS)**, Beijing, March 2007. **(invited)**
9. "*Wavelet FDTD methods and applications in nano-photonics*", W. Freude, M. Fujii, C. Koos, J. Brosi, **A. Maitra**, C. G. Poulton, J. Wang, J. Leuthold, 386th WE Heraeus Seminar, Bonn, Feb. 2007. **(invited)**
10. "*Non-reciprocal transmission and low-threshold bistability in strongly modulated asymmetric nonlinear WBGs*", M. Fujii, T. Takashima, **A. Maitra**, C. Poulton, J. Leuthold, W. Freude, ***Conference on Lasers and Electro-Optics/Quantum Electronics and Laser Science Conference*** **(CLEO/QELS)**, CThFF, Baltimore, May 2007.
11. *"High extinction ratio switching using two-photon absorption in a silicon waveguide resonator",* **A. Maitra**, J. Wang, J. Leuthold, W. Freude, JWA9, ***Nonlinear Photonics*** **(NP)**, Quebec City, Canada, Sept. 2007.
12. *"Regenerative properties of interferometric cross-gain and cross-phase modulation DPSK wavelength converters",* J. Wang, **A. Maitra**, W. Freude, J. Leuthold, NtuB2, ***Nonlinear Photonics*** **(NP)**, Quebec city, Canada, Sept. 2007.
13. "*Ultra-fast optical processing with chirping semiconductor optical amplifier*", J. Wang, **A. Maitra**, W. Freude, J. Leuthold, submitted to ***Asia Pacific Optical Conference*** **(APOC)**, Wuhan, China, Nov. 2007.

Karlsruhe Series in Photonics & Communications, Vol. 2
Edited by Prof. J. Leuthold and Prof. W. Freude

Universität Karlsruhe (TH)
Institute of High-Frequency and Quantum Electronics (IHQ)
Germany

All-optical signal processing devices are likely to be used in future communication networks. Of particular interest are all-optical flip-flops, logic gates, and wavelength converters using semiconductors. These devices might find applications in optical packet header processors, for optical signal monitoring or for signal regeneration.

This book discusses a new and generic scheme for all-optical signal processing. The basic configuration comprises an asymmetric resonator within an active or passive nonlinear medium. It is shown that such a device enables all-optical flip-flop operation and all-optical switching. In addition, a novel optical isolator concept not based on magnetic materials is introduced.

A simple model is established to describe the transmission and reflection behaviour of a resonator having structural asymmetries. It is predicted that any nonlinear resonator without inversion symmetry will exhibit “optical diode”-like nonreciprocal transmission. Further it is shown that resonator asymmetries reduce the switching threshold for bistable operation. The model is also applicable to photonic crystal based resonators.

About the author

Ayan Maitra was born in 1975 in Kolkata, India. In 2000 and 2002 he was awarded the M.Sc. and M.Tech. degree from Jawaharlal Nehru University and Indian Institute of Technology, respectively, both Delhi, India. Since 2002 and for three years he held a fellowship in the Research Training Group 786 “Mixed Fields and Nonlinear Interactions” funded by Deutsche Forschungsgemeinschaft (DFG). In 2008 he received the Dr.-Ing. (Ph.D.) degree in Electrical Engineering from University of Karlsruhe, Germany. His research is focused on the design and application of nonlinear resonant structures.

ISSN: 1865-1100
ISBN: 978-3-86644-150-7

www.uvka.de